INTERACTION BETWEEN A SPOOLABLE COMPLIANT GUIDE AND A COILED TUBING DURING SUBSEA WELL INTERVENTION IN DEEP WATER

Simon Falser
(Dipl.-Ing.)

A THESIS SUBMITTED FOR THE DEGREE OF

MASTER OF ENGINEERING

DEPARTMENT OF CIVIL ENGINEERING

NATIONAL UNIVERSITY OF SINGAPORE

2009

Acknowledgement

I am very grateful to Professor Andrew Palmer for many things, especially for his faith, his constant guidance, encouragement and support within and beyond the frame of this project. The words he uses to describe Bob Brown are more than applicable to himself: “working with him gets never boring”, and I appreciate to be his student.

Many thanks to Dr. Chris Bridge; his effort and inside knowledge made such an efficient collaboration possible. He helped me saving much time in post-processing the numerical data by providing me his subroutines. Besides, it was pleasant to work with him.

Thanks to Schlumberger, namely Yves Le Moign, for financing the project and myself. Thanks also to Professor Choo Yoo Sang for bridging the fund and therefore allowing us to work financially independent.

Thanks to the NUS Structural Lab, namely Ms. Annie Tan for her diligent help in many ways, to Mr. Martin Loh and Mr. YK Koh for their technical assistance, and to Ms. Norela Bte Buang for her administrative support.

Furthermore I would like to thank my friends from Innsbruck and NUS for all the discussions and their encouragements, in particular Stefan Rainer, Barbara Rotter, Stefano Fiori, Katherina Reich, Gerd Wieland, Tammy Chan, Cheng Ti Gan, Michael Windeler, Eddie Hu, Kar Lu Teh, Kee Kiat Tho, Shen Wei and Jimmy Ng.

I owe a special debt of gratitude to my parents Martina and Günter, who supported and guided me in all this years, and would like to dedicate this thesis to my treasured grandmother Helga.

Contents

Summary

Subsea well intervention in deep water is generally being conducted from Mobile Offshore Drilling Units, using conventional drilling risers. Schlumberger proposes the new idea to replace the conventional riser by a Spoolable Compliant Guide (SCG) which could be installed on a smaller vessel, which would increase flexibility and reduce cost.

In order to compensate heave motions, the guide is intended to form an elongated S-shape by offsetting the vessel to one side. After the guide is installed, coiled tubing is run through the riser and inserted into the well for conducting well intervention. During operation, this inner pipe is tensioned which compresses the outer pipe due to geometric interaction. A major concern is that this mechanical interaction could cause local failure or reduce the design-lifetime of the guide to a significant extent.

The aim of this model test is to investigate this pipe-in-pipe interaction. The tests focus specifically on how the interradial gap between the two pipes and the bending angle affects the load transfer between them. In order to do so, four test phases each with different diameter ratios have been conducted, two with a pipe-in-pipe system and two others with a cable replacing the inner pipe. For each phase the setup is bent into different S-shapes with inclination angles of 30°, 45° and 60° by displacing one of its ends. The inner pipe or cable has been tensioned by steadily increasing load, while the stress on the outer pipe has been measured by attached strain gauges. Axial force as well as global- and local bending moment was obtained from the reading, and has subsequently been compared with a finite element calculation.

The test results show that the load transfer between the two pipes is almost independent of the inclined angle. The local bending moment, which is the moment caused only by the applied load, shows proportionality to interradial gap, whereas the axial force remains almost constant for different diameter ratios. The shape of the setup does not change with increasing load, and governs the global in-plane bending moment of the outer pipe.

All results are given normalised in respect to the yield force/moment of the outer pipe. It was observed that the outer pipe was in its plastic range for all twelve tests. The maximum axial force and local bending were measured as 0.52- and 0.22 of the outer pipe's yield capacity respectively. The load transferred into axial force in the guide pipe can be estimated as maximum 1.3 times the load applied. The local bending moment can be estimated as 0.81 times the load times the radial gap normalised by the inner diameter to the power of 0.25. The test results match the numerical results within an acceptable order of magnitude.

List of tables

List of figures

Abbreviations

A_c	cross-section area
CT	Coiled Tubing
CVAR	Compliant Vertical Access Riser
FPSO	Floating Production Storage and Offloading vessel
g_r	interradial gap
HCR	Highly Compliant Riser
ID	inner diameter
JIP	Joint Industrial Project
MODU	Mobile Offshore Drilling Unit
OD	outer diameter
SCG	Spoolable Compliant Guide
SCR	Steel Catenary Riser
SMYS	specific minimum yield stress
TTR	Top Tension Riser
VIV	Vortex Induced Vibration
WT	wall thickness
y.c.	yield capacity

Symbols

c_{TT}	factor for top tension
c_{TT}	factor for top tension
E	Young’s modulus
F_{yield}	yield force
M_{yield}	yield moment
S	section modulus
Y	yield stress
α	inclination angle
ε	strain
σ	stres

1 Introduction

1.1 From the Origin into Deep Water

The modern oil and gas industry was initiated in the early 1859 with the first recorded oil findings through drilling in Titusville, Pennsylvania, USA. The potential for huge profits, drove many people quickly into the oil and gas business. The industry grew fast and a powerful energy industry was established. Large and easily accessible reservoirs were found, and the global oil reserves were theoretically secure for many decades. However, new findings together with constantly changing regulations and much political gambling dominated the global petroleum market ever since (Yergin, 1990), and the oil price quickly established itself to an important index of the world economy's wellbeing.

Over many decades, the steadily increasing demand of petroleum was met by increasing production from onshore and shallow water reservoirs, and as a result the oil price had no technical reason to rise. As most of the easily accessible resources started to decline, however, oil became more expensive, since oil companies were forced to produce from reservoirs in deeper water, which required new and costlier technology.

1.2 Change in Technology

Fixed platforms on jackets or compliant towers were soon replaced by floating structures as more than 600 m water depth were reached. Floating production rigs such as Semisubmersibles, Tension Leg Platforms (TLP's), Spars and Floating Production Storage and Offloading vessels (FPSO's) as illustrated in Figure 1.1 are expensive, since they have to be designed to withstand harsh offshore environment for their entire

design lifetime, some such as Spars and TLP's without being brought back to shore. At the same time though, their payload capacity had to be maximise for drilling or production. More about offshore structures can be found in Chakrabarti (2005).

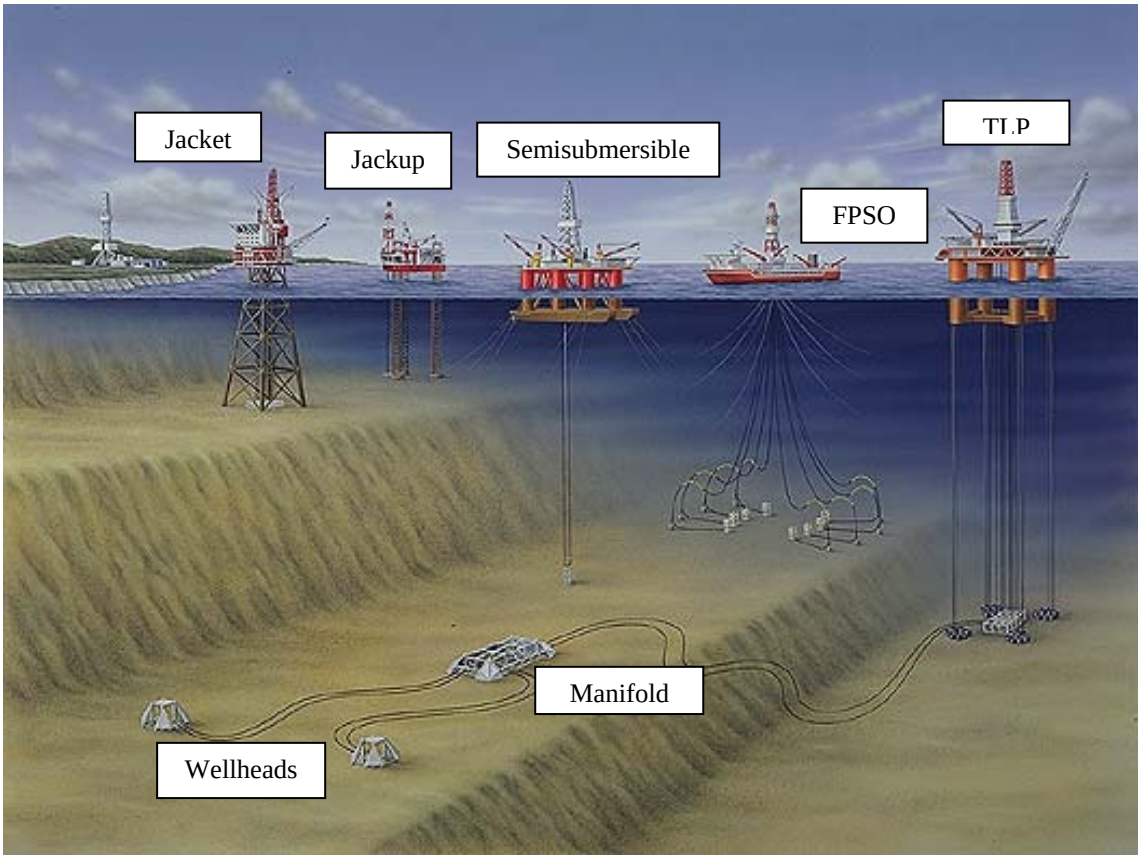

Figure 1.1: Illustration of different offshore structures and subsea equipment

The number of production hubs per oilfield was kept at its minimum, which, depending on the form and dimensions of the reservoir, makes the platform to a central hub for several square kilometres above the produced field.

Oil and gas reach the seabed through drilled wells into the reservoir. A subsea (wet) tree on top of the wellhead connects each well to a manifold, which in simple terms gathers the product from a few wells, and pumps it through production risers to the floating platform (Figure 1.1). There are several types of risers, and their principal distinction is between drilling- and production riser on fixed- or floating structures.

Drilling riser are purely vertical and have the purpose to guide the drilling string and to keep the drilling mud and cuttings in a closed system. They have to be installed from a specially equipped drilling rig, by joining several pipes together and connecting it to the preinstalled wellhead.

Production risers on the other hand can be designed in different ways, each with a different method to compensate heave motions. Depending on the water depth, the maximum heave amplitude, the production rate and therefore the riser's diameter, as well as the type of floater they are connected to are influential for the choice and design of production risers: A Top Tension Riser (TTR) works similar to the drilling riser, which is vertically connected to the wellhead with a heave compensator on deck. Steel Catenary Riser (SCR) form a catenary shape between a horizontal tangent on the seabed and a vertical at its connection on deck, whereby heave motion is compensated by a controlled cyclic lifting of the riser in its touch-down-zone on the seabed (Bai, 2001). An alternative method is the Compliant Vertical Access Riser (CVAR), where the steel riser takes up a buoyancy supported, stretched S-shape which itself compensates heave motion. Flexible risers and umbilicals are also being used in various shapes such as lazy- or steep wave and lazy- or steep S, depending on their method of buoyant support as shown in Figure 1.2. Lazy S risers generally differ from the lazy wave risers as their buoyancy support is moored to the seabed.

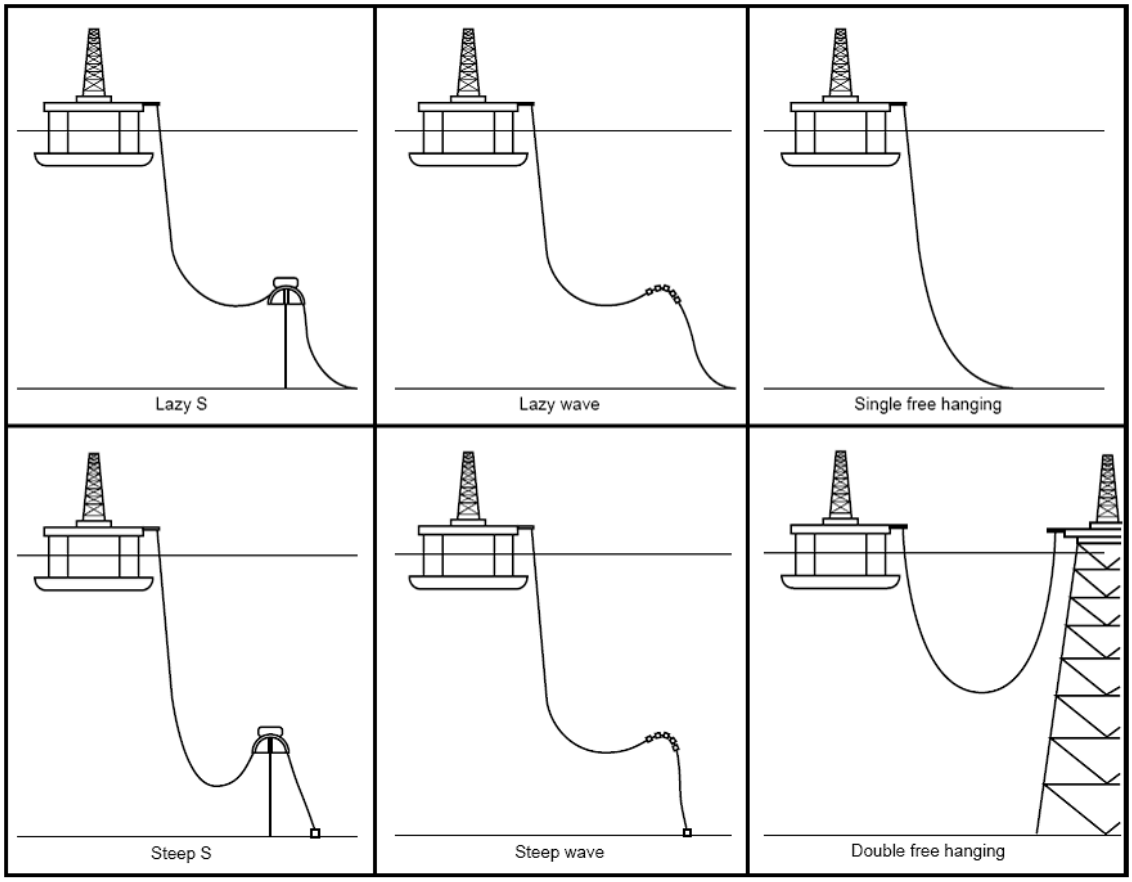

Figure 1.2: Different flexible riser shapes and catenary riser (upper right picture), not to scale (API-RP-2RD)

As one might expect, riser design for floating structures is much more challenging than for fixed platforms. The riser is free hanging or partially supported by buoyancy over the whole water column, and is exposed to much larger hydrodynamic forces compared to a riser attached to a jacked leg in shallow water.

1.3 Well Intervention

Production wells need maintenance, since either sand flows into the well or oil residuals are getting stuck on its wall. Both have to be removed in order to guarantee flow assurance and not to jeopardise the production rate, which is the core piece of any petroleum production. Enhanced recovery is another aspect in which well intervention is necessary. Thereby coiled tubing is run into the well and the reservoir rock's

permeability is increased either locally due to chemicals (acidizing), or due high pressure with which the rock is being fractured (fracturing). For heavy oil recovery, however, the oil's high viscosity has to be decreased by either heating due to steam flooding or local combustion, before a conventional production is possible. Further information about enhanced- or tertiary recovery can be found in Archer and Wall (1986).

Most well interventions require a separate connection between the well and the vessel from where the intervention is being conducted, except for TTR and CVAR riser, where the intervention can be conducted through the installed production riser, but the first is not applicable for deep water and the latter is not much used either. Therefore for well intervention, the same riser as for drilling is generally being used, where an equipped Mobile Offshore Drilling Unit (MODU) has to be installed above the well as illustrated in Figure 1.3. The vessel's heave motions are thereby compensated by a telescopic riser section at its connection to the vessel. Figure 1.3 also shows a flexible lazy-S production riser connected to a FPSO.

With the oil price at record heights in recent years, several oilfields became suddenly economical to explore and eventually to be produced from. That boom toward exploration caused a sudden shortage in drilling rigs, and fabrication yards worked on their limits to coup with the demand. Since most new fields were either in deep water or arctic environment, drilling rigs had to be designed more robust which obviously increased cost. A combination of the shortage and the newly build high end drilling rigs or drillships pushed their leasing rates up to several hundred thousand US-dollar per day, and made well intervention unnecessarily expensive.

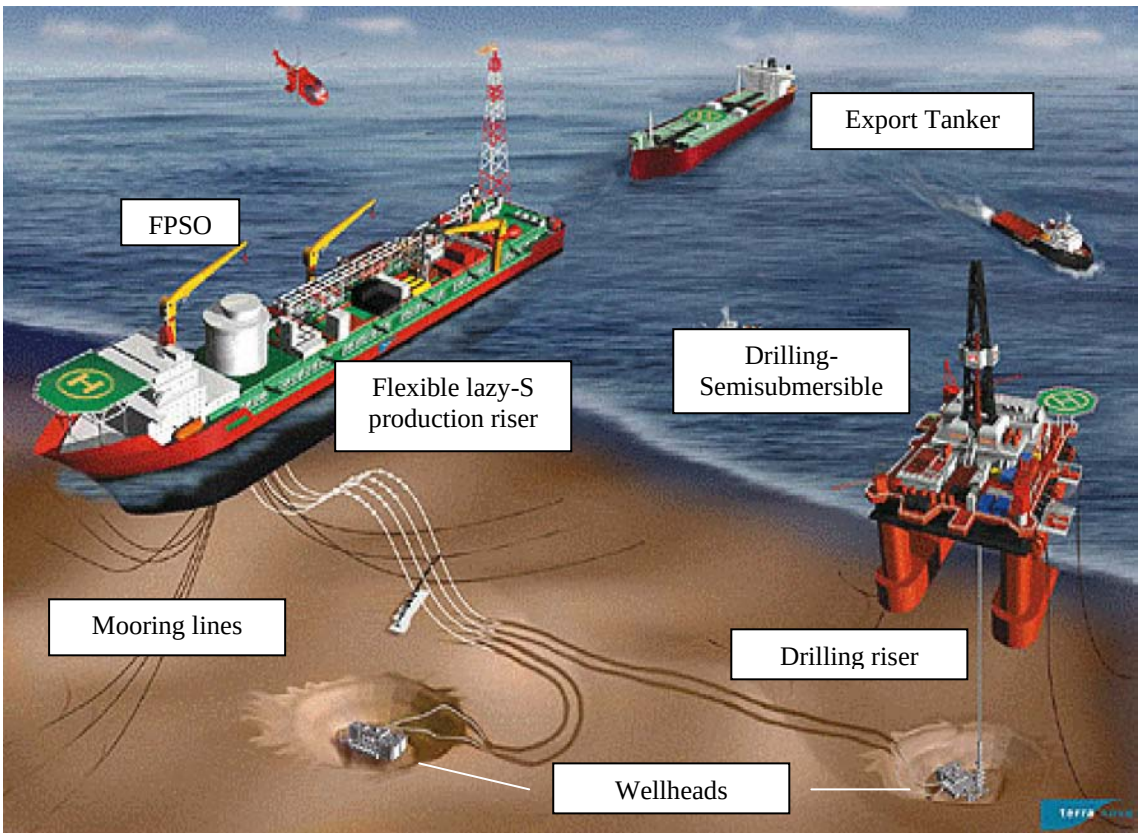

Figure 1.3: Schematic of simultaneous production by an FPSO (left) and drilling or well intervention by a semisubmersible (MODU) (right) (courtesy of Petro Canada)

1.4 The new Concept

Schlumberger sees a potential to make well intervention cheaper and more flexible, as they are developing a new device which does not require a drilling vessel.

The new idea is a Spoolable Compliant Guide (SCG), which is a small diameter steel riser reeled onto a wheel and installed on a small conventional vessel. On site, the guide gets unreeled and connected to the wellhead. Similar to the CVAR, the riser will form an elongated S-shape to compensate heave motion, as can be seen in Figure 3.1. After installation coiled tubing is run into the guide ready to operate the intervention package pre-located on top of the wellhead. A Coiled Tubing (CT) is also a small diameter steel pipe reeled onto a wheel, and is used in many different kinds of downhole-operations throughout the oil and gas industry. After the well intervention is carried out, the CT

and subsequently the SCG are being recovered by reeling up, and the vessel can sail on. Another advantage compared to the conventional workover system is that the dynamic seal, which seals the coiled tubing inside the riser, is located subsea in the upper intervention package, and not on vessel deck as it is in conventional systems, which is possibly beneficial for design and safety.

The idea is promising. There are some uncertainties and questions, none of them critical, as is common for innovative designs. One potential problem area is wear between the two pipes, in terms of durability of the residual bent guide and of load transfer between the inner and the outer pipe during operation. Since the guide is inclined, the friction forces are higher than in conventional vertical drilling risers, and therefore the wear of the guide has to be quantified. A conservative value of the contact force between the two pipes is used for conducting wear tests on the prototype's material, which consequently allows an estimation of the SCG's durability. A lubricant could be used to reduce friction and minimise wear on the inner wall of the guide. The residual bend is not expected to have much influence on the guide's shape, and since the inner pipe is lowered after the guide is installed, residual bending does not affect the pipe-in-pipe interaction and has therefore only to be checked to make sure that low-cycle fatigue will not occur.

1.5 Objectives of Study

This study intends to reduce uncertainties of load transfer during operation. For different well interventions it is necessary to run the coiled tubing deep into the well to the reservoir, whereas its dead load combined with the weight of the intervention package tensions the inner pipe significantly. This load is partially transferred to the

guide pipe at the inclined section, shown in Figure 4.1 and is termed geometric interaction.

Previous numerical calculations indicated large response forces in the guide pipe, to an extent that local buckling due to large local moments became a concern. When the interaction simulation was repeated numerically, it was found that local buckling might not occur, but the load transfer due to geometric pipe in pipe interaction and friction is nevertheless highly complex, and hence a physical model test is needed to benchmark these results.

This research focuses in particular to which extent the pulling force compresses the outer pipe, and how it affects the outer pipe's global and local bending moment. The effect of the interradial gap g_r on the load transfer will also be investigated. Furthermore it will be examined how the response changes with varying inclination angle of the pipe configuration.

The aim is to elaborate some equations to estimate the axial force and moment in the guide for the corresponding load applied onto the inner pipe. Figure 1.4 gives an overview of the test setup.

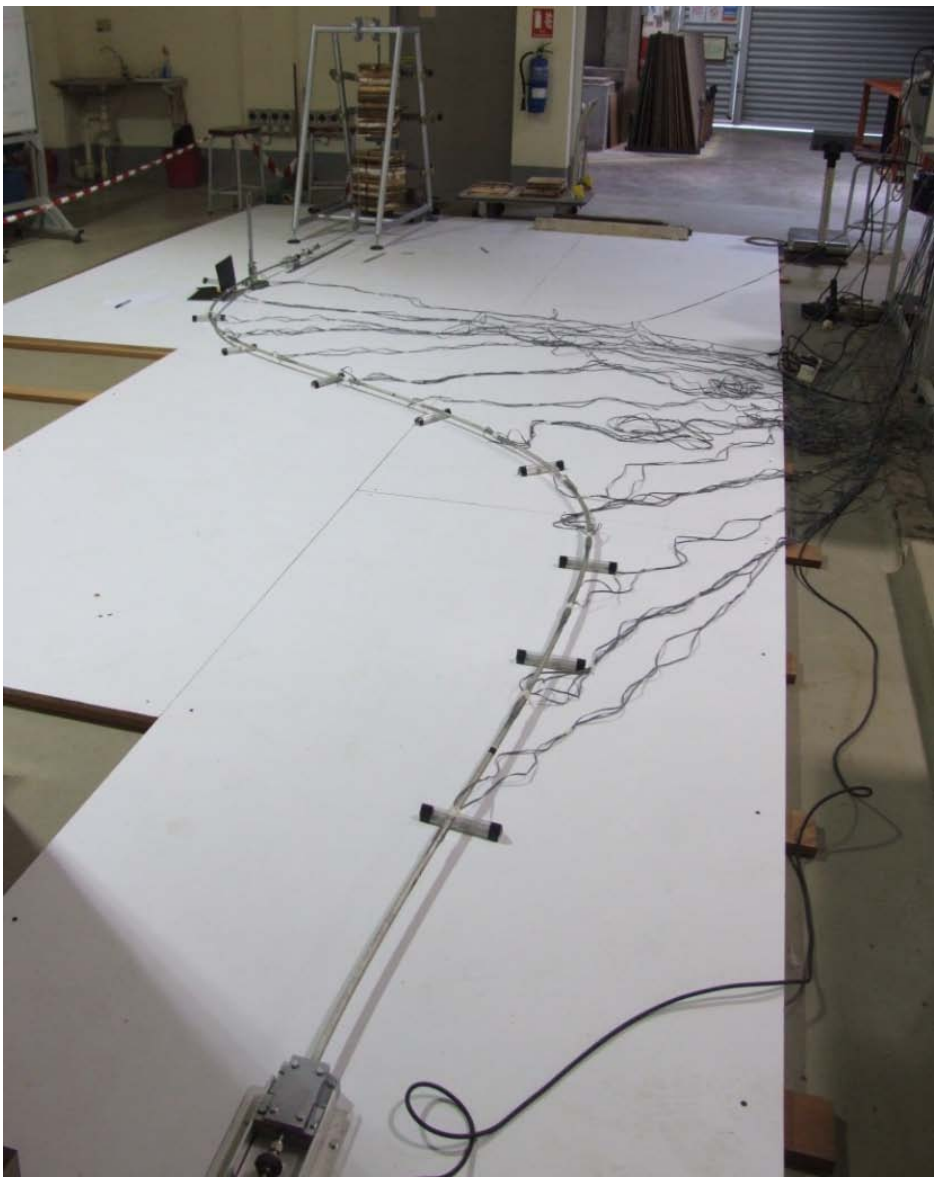

Figure 1.4: 60° inclined system during Phase 1 test

1.6 Layout of Thesis

Chapter 1, Introduction, leads the reader to the topic. It intends to explain why well intervention is necessary and how it could become cheaper with the new system Schlumberger proposes.

Chapter 2, Literature review, aims to give some background information to the addressed problem of geometric pipe-in-pipe interaction

Chapter 3, Subsea Intervention System, gives a brief overview of the state of the art design of the Spoolable Compliant Guide including its technical specifications.

Chapter 4, Physical Model Test, describes the model scaling, the model setup as well as the different tests conducted. It intends to visualise and explain the reason for the setup and test focus to the reader.

Chapter 5, Data Processing, describes how the gained data has been processed in order to achieve in plane reaction forces. An example aims to show how the normalised graphs can be used to obtain real scale responses.

Chapter 6, Model Test Results, provides and explains the most significant results obtained from the model test. This might be the core chapter of this thesis, which contains all research findings of the conducted study.

Chapter 7, Numerical Test Results, as in chapter 6, it provides and explains the most significant results from the numerical calculation. In addition it intends to support the findings from the physical model test.

Chapter 8, Comparison of Test- and Numerical Results, shows and explains similarities and differences of the measured and calculated results.

Chapter 9, Conclusion, summarises the research finding and concludes their effect.

Chapter 10, Limitations and Future Research, highlights the limitations of the conducted tests and gives an outlook to possible future research.

2 Literature Review

2.1 Introduction

Pipe-in-pipe systems are widely used in the offshore industry. Pipe-in-pipe interaction during drilling has been carefully researched, since the anxiety that the drilling string may buckle within the casing and lock up is always at present.

Another subject of much research are thermally insulated pipes: As the industry moves towards deeper water, concerns about flow assurance increase as distances from shore increase; Heat losses along export pipelines are therefore minimised by installing pipe-in-pipe flowlines with thermal insulated annulus, to prevent hydrate and wax formation in keeping the thermal conductivity high, and at the same time to save ethanol injection. Their interaction is clearly different from the one in the SCG, but nevertheless the contact between the two pipes during installation has been modelled by the same Finite Elements (FE) as were used for the SCG (Daly and Bell, 2002).

In 1998 a Joint Industrial Project (JIP) was initiated to analyse Highly Compliant Rigid (HCR) risers in large scale model tests and to compare its results with different riser analysis software (Grant et al., 1999). One of the key objectives of this project was to determine whether riser buckling, as predicted by some software, really occurs. Three different risers (CVAR, SCR, Lazy Wave SCR) were modelled in a 1:4 scale in 280 m water depth. All risers were cyclic actuated in heave motion and stress was recorded along its axis. Results have shown that in-plane response depends on the excitation period, whereas out-of-plane response is at the Vortex Induced Vibration (VIV) frequency. Grant et al. show that the tension variation is highly non-linear due intermittent occurring VIV and riser-seabed interaction for SCR's. Furthermore the

SCR riser was observed to buckle out-of-plane, which only software with out-of-plane degrees of freedom were able to predict. The study concludes that at present the most severe limitations of riser analysis software are their inability to model intermittent VIV and their low accuracy modelling of deep water clays.

However, little work has yet been done to investigate the addressed question of load transfer due to geometric interaction in a pipe-in-pipe system.

2.2 SCG System

Schlumberger provided all state of the art specifications for the SCG design, which were necessary to scale the model and helped to identify the key factors which had to be investigated.

In the report “Forces Along the Spoolable Compliant Guide” (Schlumberger, 2008) the friction force along the SCG, the build-up rate of the inclination as well as the von Mieses stress is plotted against the vessel’s offset. It was found out that for installation of the CT, the build up rate of the guide should be less than 5°/33m, which corresponds to a vessel offset of 220 m. That, on the other hand, causes high stress in the upper and lower stress joint which connect the riser, and therefore it is recommended to change the vessel positions during the CT runs through different sections of the guide. Within 0 - 50 m offset the von Mises stress in the guide reaches 80% SMYS, whereas in all other positions ± 275 m the working stress of 67% SMYS is not reached.

Simultaneously to the tests presented here, Schlumberger conducted a separate numerical study of the real scale pipe in pipe system, which results are presented in the report “Pipe-in-Pipe Interaction using ABAQUS” (Schlumberger, 2009). These results match the numerical results of the here presented model well. Schlumberger’s calculation was carried out with- and without friction between the pipes, and the results

show that friction reduces the local effective compression in the S-shape significantly, as it is illustrated in Figure 2.1. It was also found that the differential load increase into axial force is equal to -1.0 times the load applied, which reflects the result in chapter 7 and those by Kuroiwa et al. (2002).

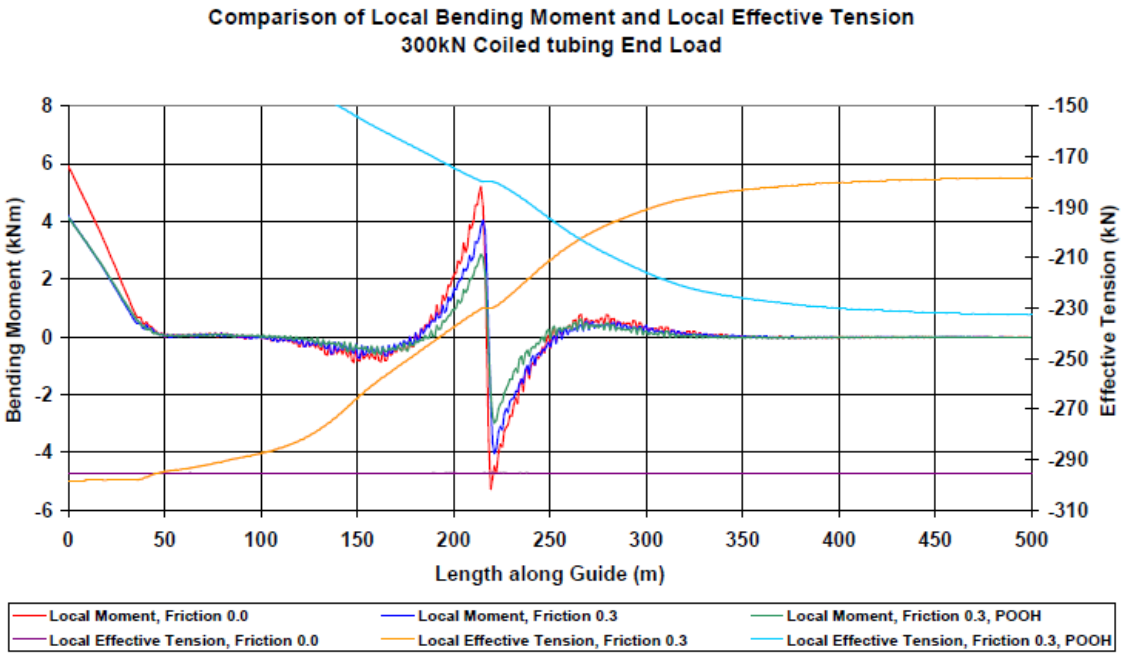

Figure 2.1: Local moment and local effective tension for real scale pipe-in-pipe analysis (Schlumberger, 2009)

The local moment was determined by Schlumberger as the load applied times the interradial gap:

$$M_{L0} \approx T_B r \tag{2.1}$$

where

M_{L0} is the local moment in the guide

T_B is the load applied onto the inner pipe

r is the interradial gap

The test results in this study, however, indicate that the differential increase in local moment $dM_{y,l}/dT$ is a function of the gap normalised by the inner pipe diameter to the

power of 0.25 (equation (6.6)), but had to be limited for a certain ratio of gap to inner pipe diameter. Unfortunately it was not possible to derive the same equation for local moment from the numerical results in this study, since unlike in the model test, they were not consistent with the interradial gap as it is explained in section 7.3.

Previous pipe-in-pipe interaction tests have been conducted by Oceanide (2007). In a vertical model setup, they investigated the dynamic response of the SCG due to heave and surge motions. Static analysis was performed by applying weights up to 338 N. Results show that the load transfer causes an axial compression of up to the load applied and decreases due acting friction gradually with height. Local moment data is not provided since the tests focused more on the dynamic behaviour. A limitation might be though, that the maximum applied load was too little compared to the guides capacity, and that therefore the guide's response was not representative. Oceanide conducted also a real scale friction test, which indicate that the friction coefficient between the CT and SCG varies in air between 0.24 and 0.27, whereas in water it was determined in the range of 0.28 and 0.30. Therefore, the used friction coefficient of 0.3 in the numerical calculation of the model presented here is justified.

The report "Pipe-in-Pipe Interaction using ABAQUS" (Schlumberger, 2008) emphasises that the load transfer is a combination of geometric- and friction interaction, and provides the modified capstan equation with which the friction force along a defined distance can be calculated:

$$T_{n+1} = T_n e^{-\mu \Delta\alpha} - m_s g \Delta L \qquad (2.2)$$

where

T_n is the tension at point 'n' along the coiled tubing

T_{n+1} is the tension at point 'n+1' along the coiled tubing, below point 'n'

μ is the friction coefficient

$\Delta\alpha$ is the difference in angle between points ‘n’ and ‘n+1’

m_s is the submerged unit weight of the coiled tubing

g is the acceleration due to gravity

ΔL is the length of coiled tubing between points ‘n’ and ‘n+1’

Equation (2.4) implies that the more the SCG is bent the more friction acts between the two pipes. It is not possible to prove that by the model test, since friction and geometric interaction cannot be divided, but the results of this study have shown that it load transfer is not influenced by inclination angles between 30° and 60°.

2.3 CVAR Riser

Compliant Vertical Access Risers (CVAR) are steel risers taking up a buoyancy supported, stretched S-shape with vertical connections at both ends. Due to their geometry, pipe-in-pipe interaction in CVAR risers is comparable to the one in the SCG guide as presented here.

Well intervention is either conducted through in place TTR- or CVAR production riser or through deliberately installed drilling risers from MODU’s. Just for CVAR risers geometric pipe-in-pipe interaction is significant, since for all other systems both pipes are almost vertical and hence only friction between them has to be considered. Due to their shape and usage, CVAR risers have similarities to the proposed SCG, and therefore the greatest relevance to the tests conducted.

CVAR risers are a new development especially attractive for FPSOs and Spars due to their relatively small heave motions. They combine both advantages of TTR and SCR or flexibles, as their dry trees allow conducting well interventions through the CVAR riser and heave motion are being compensated by its compliant shape (Ishida et al,

2001). Mungall et al. (2004) investigate CVAR riser on a semisubmersible in 3000 m deep water in the Gulf of Mexico. Numerical calculations of riser interference, extreme response and fatigue due Vortex Induced Vibration (VIV) have been undertaken, and results have shown that CVAR riser can theoretically be installed on a semisubmersible if its heave response can be kept in a certain order of magnitude.

An interesting cost comparison between an FPSO with conventional riser system, an FPSO with CVAR risers spread moored in the West of Africa, and one with CVAR risers and weathervaning hull offshore Brazil has been conducted by Okamoto et al. (2002). Not surprisingly the spread moored FPSO with CVAR risers costs much less than a conventional weathervaning FPSO does, but also the weathervaning with CVAR risers costs 30 M$ less according to the author. The major cost differences are workover equipment (which only FPSOs with CVAR risers require), trees, since wet trees are more expensive, and subsea equipment such as manifolds, control systems and flow lines, which are only counted for conventional FPSOs. The study, however, fails to mention that CVAR risers have disadvantages due to their limited radius of operation, and can therefore not being used for an oilfield with widespread wells, in which only FPSOs with wet trees are applicable.

A similar test series as it is presented in this thesis was conducted by Kuroiwa et al. (2002). He studied the load transfer during well intervention through a CVAR with a comparable test setup, and verified the results numerically. In contrast to the here presented study, he did neither examine the influence of interradial gap nor that of the inclination angle.

The outer pipe was modelled by an acrylic pipe whereas a steel wire was used to represent the inner pipe. The model scale is stated as 1:19.52, and the shape of the 5.8 m long model pipe was obtained by displacing one end 0.9 in y- and 0.1 in x direction,

which yielded to an inclination angle of 17°. It is not clear however, why this relatively small inclination angle was chosen, since the authors claim that the middle section of the compliant riser has to be nearly vertical in order to absorb heave motions.

Despite the differences in modelling and inclination angle, Kuroiwa's test results match well with those presented in chapter 6: His applied tension of 196 N onto the inner wire caused a relative tension in the guide of the same magnitude, and the differential load increase can be expressed as follows:

$$\frac{dT_{CVAR}}{dT_{CT}} \approx -1.00 \tag{2.3}$$

It confirms that the load transfer in a wire-in-pipe system into axial force is around one, which is in good agreement with the wire-in-pipe results in Table 6-2 (phase 2 and 4) which are -1.03 and -1.04 respectively. In this test the total declination angle as defined in chapter 5 is twice the inclination angle (34°) and therefore significantly smaller as 83° obtained in the 30° inclined tests of the presented study. Since for smaller declination angles less load transfer due friction can be assumed, the result of Kuroiwa et al. (2002) indicates that the total load transfer is governed by the pipes geometric interaction and is less influenced by friction. The authors do not provide the local moment, but which can be obtained by subtracting the two global moment graphs with and without loading which leads to 0.32 Nm for 196 N loading. Regrettably the wire diameter and the outer pipe's material specifications are not provided. The interradial gap r_G and the maximum elastic moment are therefore unknown, and equation (6.5) to estimate the load transfer into local moment cannot be verified.

2.4 Numerical Pipe-in-Pipe Simulation

Numerical calculations of the real scale pipe-in-pipe interactions have shown that uniform distributed buoyancy over the lower half of the CVAR riser lead to intolerable high stress at the top, bottom and middle section of the riser (Kuroiwa et al., 2002). The authors found that a gradually decreasing buoyancy from the wellhead upwards is most beneficial for the stress distribution, and the same buoyancy distribution has been designed for the SCG (Schlumberger, 2008)

In the presented study, numerical calculations were conducted using the FE software ABAQUS, since previous numerical work by Schlumberger (2008) was also conducted with the same and therefore a direct comparability is given. The inner and outer pipe was model with B31 elements, which are 3-D beam elements in ABAQUS. Pipe-in-pipe interaction was simulated by the contact elements ITT31, which allow sliding of deformable bodies (ABAQUS 6.7-1) and are allocated between the two pipes. The same element has been used to simulate the interaction between a TTR and its buoyancy can within a spars centrewell (Luk and Rakshit, 2009), as shown in Figure 2.2:

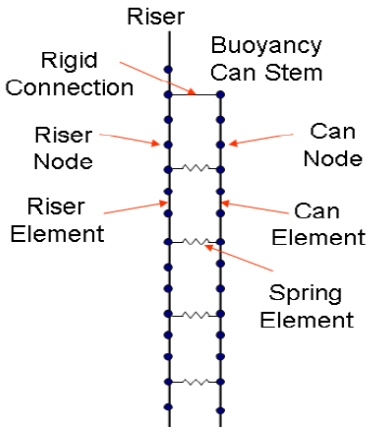

Figure 2.2: ITT31 FE-contact element modelling a riser-buoyancy can interaction (Luk et al., 2009).

The contact element ITT31 is based on non linear springs. The interradial gap is simulated by allowing a specified displacement (see input file in Appendix D) of the

inner pipe from its centralised position (Daly and Bell, 2002). The same element has been used to simulate the interaction between a flowline and a carrier during a reeled installation of a SCR, where the integrity of the insulation material critical is, but which could be modelled successfully (Daly and Bell, 2002). The ITT31 element can also be used to model pipeline-gravity anchor contact behaviour, where sliding due to thermal expansion and contraction of the pipeline can occur (O Zeitoun et al., 2009).

The correct simulation of the pipe-in-pipe contact was the most critical point in the conducted calculations, but the stated references have shown that the used element is appropriate for the here addressed problem.

Another numerical calculation has been undertaken to investigate real scale pipe-in-pipe interaction of the SCG system. Results of dynamic simulations with 10, 40, and 80% loading have shown that the outer pipe is only stable for a 10% capacity loading, and that for higher loadings buckling might occur (Principia, 2008). To estimate the maximum applicable load, the equation (2.4) for pipe-in-pipe sinusiodal buckling of the inner pipe was rearranged for the buckling force of the outer pipe, by replacing the inner pipe's weight by the contact force between the two pipes.

$$F_c > 2\sqrt{\frac{EIw_{bp}}{g_r}} \tag{2.4}$$

where

F_c is the buckling force

EI is the flexural rigidity of the inner pipe

w_{bp} is the inner pipe's submerged weight per arbitrary length

g_r is the interradial gap

This rather unexpected result initiated further research of pipe-in-pipe buckling and is described in the following section.

2.5 Pipe-in-Pipe Buckling

Inner pipe buckling and the effect of friction has been studied since many decades, and at present much understanding seems to be available. The reverse case where the outer pipe buckles due to compressing stress transferred from a tensioned inner pipe has not yet been studied, and is a potential subject for further research.

The transformation of equation (2.2) to estimate the outer pipe's buckling force, as it was undertaken by Principia (2008), leads to the same equation as for buckling load for the inner pipe in curved wellbores published by Mitchell (2007) but originally from He and Kyllingstad (1995) where the contact force w_c is defined as:

$$w_c = \sqrt{\left(w_{bp}\sin(\varphi) + F_c\varphi'\right)^2 + \left(F_c\sin(\varphi)\,\vartheta'\right)^2} \qquad (2.5)$$

where

φ is the well's inclination angle

ϑ is the azimuth

' indicates the derivative with respect to depth

The angles φ and ϑ define the trajectory of the inner pipe within the guide, but in the reverse case where the inner pipe is in tension only the inclination angle is relevant, since the inner pipe is assumed to be in plane and hence the azimuth does not change with length. By inserting the contact force w_c of into the buckling force equation (2.4), an implicit equation results.

Initially it was thought, however, that in numerical calculations the contact force can be extracted as node-contact forces directly from the software (Principia, 2008), but later it was found out that the obtained result is not independent of the number of elements and therefore just partially usable. The above stated buckling model, however, does not implement friction, and it is unclear whether it is applicable to outer pipe buckling.

The axially loaded inner pipe buckles above the critical buckling load first laterally within the surrounding guide pipe or casing, and with increasing load helically. Mitchell (1997) gives a descriptive overview of how the different buckling forces can be quantified:

No buckling:
$$F_c > -2\sqrt{\frac{EIw_{bp}}{r_G}} \tag{2.6}$$

Lateral buckling:
$$-2.83\sqrt{\frac{EIw_{bp}}{r_G}} < F_c < -2\sqrt{\frac{EIw_{bp}}{r_G}} \tag{2.7}$$

Lateral or helical buckling:
$$-5.66\sqrt{\frac{EIw_{bp}}{r_G}} < F_c < -2.83\sqrt{\frac{EIw_{bp}}{r_G}} \tag{2.8}$$

Helical buckling:
$$F_c < -4\sqrt{2}\sqrt{\frac{EIw_{bp}}{r_G}} = -5.66\sqrt{\frac{EIw_{bp}}{r_G}} \tag{2.9}$$

As can be seen, the change from lateral- to helical buckling can only be quantified within a certain range, which definition varies in different publications (Aasen et al., 2002). The respective upper limit where the lateral configuration of the buckled pipe is expected to be still stable is given in Table 2-1:

Table 2-1 Buckling coefficient at helical buckling (Aasen et al., 2002)

Author	limit
Chen,Y.C., Lin,Y.H., Cheatham,J.B. (1990)	-2.83
He,X., Kyllingstad,A. (1995)	-2.83
Lubinski,A., Woods,H.B. (1953)	-2.85
Lubinski,A., Althouse,W.S., Logan,J.L. (1962)	-2.4
Qui,W., Minska,S., Volk,L. (March 1998)	-3.75
Qui,W., Minska,S., Volk,L. (May 1998)	-5.66
Wu,J., Jukam-Wold,H.C. (1993)	-3.66
Wu,J., Jukam-Wold,H.C. (1995)	-4.24

The coefficient by Qui et al. (May 1998) is twice the one found by Chen et al. or He and Kyllingstad, and therefore Mitchell (1997) expresses the change from lateral into helical buckling in that range as shown in equation (2.8).

The reader might at first think that this is not relevant for the addressed question of load transfer due to geometric interaction, but if in future a similar experiment is being conducted in a vertical setup and therefore the outer pipe is free to move in both horizontal axes, the outer pipe could possibly take up a helical shape following similar principles as presented here.

This study intends to reduce uncertainties of load transfer during operation. The aim is to elaborate some equations to estimate the axial force and moment in the guide for the corresponding load applied onto the inner pipe.

3 Subsea Intervention System

According to the Schlumberger Report 'SCG Design Basis', Rev. 2 (2008), the subsea well intervention riser, shown in Figure 3.1, is designed so that the lower section is supported by buoyancy modules (the thicker section in Figure 3.1), which form the characteristic S-shape of the guide and allows a vertical connection to the tree. Unlike reeled pipelines, the SCG is intended to be unreeled and installed without being straightened, which leads to a residual bend along the guide.

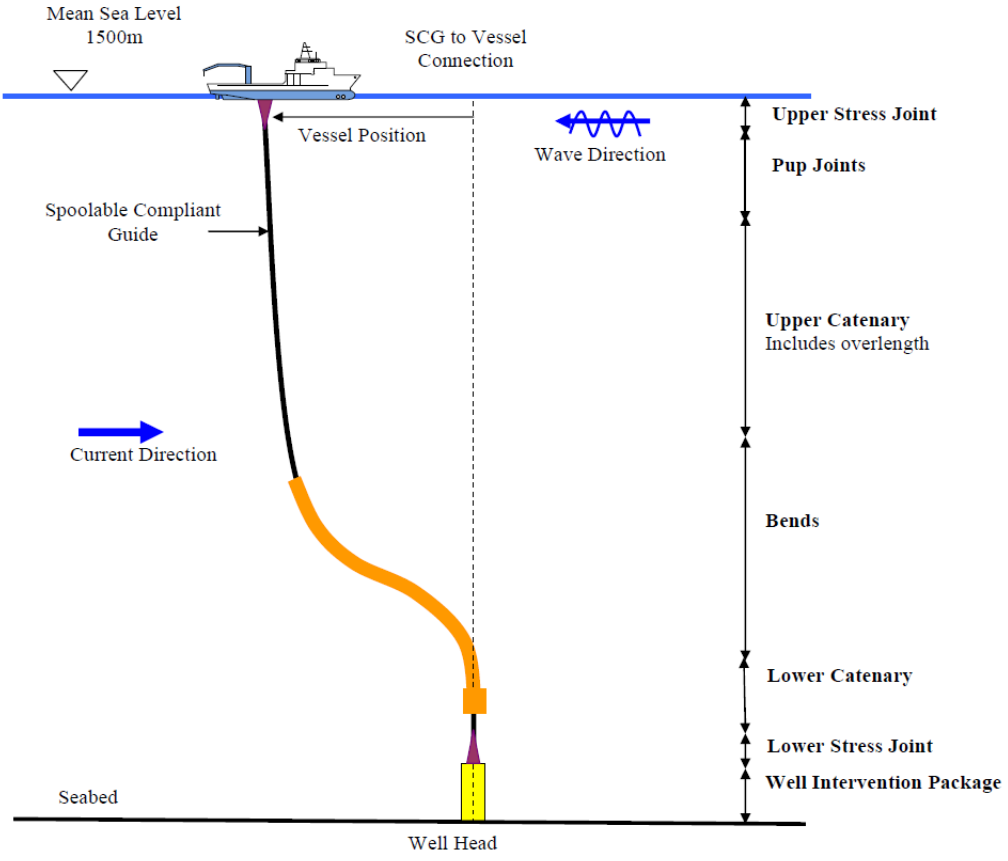

Figure 3.1: System overview of subsea well intervention due an SCG (courtesy of Schlumberger)

Typical SCG shapes with different vessel positions from over-the-wellhead position to the far vessel position are shown in Figure 3.2.

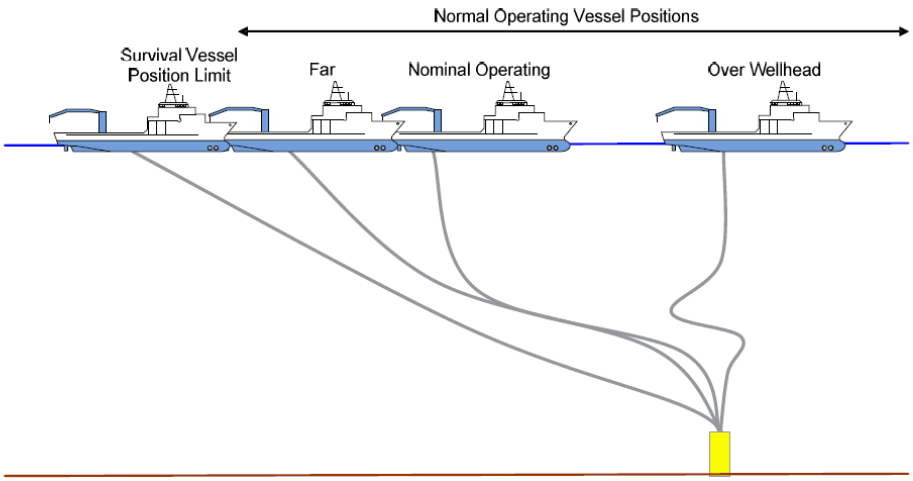

Figure 3.2: possible vessel positions and SCG shapes during operation (courtesy of Schlumberger)

3.1 SCG – Structural properties

3.1.1 Guide Pipe (Outer Pipe)

The guide pipe is a 4 ½ inch standard size coiled tubing with properties shown in

Table 3-1:

Table 3-1: Guide Pipe (Outer Pipe) properties

OD	ID	WT	Dry weight, empty	Submerged weight, Water Filled	Axial Stiffness	Bending Stiffness
[mm]	[mm]	[mm]	[kg/m]	[kg/m]	[kN]	[kNm^2]
114.3	98.36	7.6	20	17.4	528600	756

3.1.2 Coiled Tubing (Inner Pipe)

The coiled tubing which makes up the inner pipe is a 2 3/8 inch standard size coiled tubing with properties shown in Table 3-2:

Table 3-2: Coiled Tubing (Inner Pipe) properties

OD	**ID**	**WT**	**Dry weight, empty**	**Submerged weight, Water Filled**	**Axial Stiffness**	**Bending Stiffness**
[mm]	[mm]	[mm]	[kg/m]	[kg/m]	[kN]	[kNm^2]
60.3	50	5.2	7.05	6.14	130000	54

3.1.3 Material

The material properties of the guide pipe and the coiled tubing are shown in Table 3-3:

Table 3-3: Guide Pipe and Coiled Tubing Material charachteristics

symbol	*Parameter*	**Guide**	**CT**
E	Young's modulus	207 x 10^9 Pa	207 x 10^9 Pa
ρ_s	density	7850 kg/m^3	7850 kg/m^3
y_s	Yield stress	552 MPa *(80 ksi)*	758 MPa *(110 ksi)*
ν	Poisson's ratio	0.3	0.3

The conducted model tests are purely static. Therefore no environmental loads have been taken into consideration and are hence not listed here. The same applies to the buoyancy modules and the vessel dimensions. The reader can find them in the Schlumberger Report 'SCG Design Basis' (2008).

4 Physical Model Tests

4.1 Aim of Model Tests

The aim of this model test is to quantify the load transfer from the inner to the outer pipe. The tensioned inner pipe tries to straighten the outer pipe within its S shape – section (Figure 4.1), which causes compressive stress in the guide as its axial motion is constraint by the vessel on top and the well head on the seabed.

More specifically, the test focuses on how the interradial gap g_r between the two pipes and the bending angle affects the geometric interaction. In order to do so, four test phases each with different diameter ratios have been conducted, two with a pipe-in-pipe system and two others with a cable replacing the inner pipe. For each phase, the setup is bent into different S-shapes with inclination angles of 30°, 45° and 60°, by displacing one of its ends.

Schlumberger is interested in knowing the following relations:

1. To which extent the pulling force compresses the SCG
2. How the pulling force affects the SCG's global and local bending moment
3. Which effect the interradial gap g_r on the local bending moment has
4. How point 1-3 changes with varying inclination angle of the pipe configuration

Model tests at the National University of Singapore have been undertaken. To compare and to benchmark the test-results provided in chapter 6, a numerical calculation using the FE software ABAQUS has been conducted for every test, which results are examined in chapter 7. Details of each test are provided in and Appendix D to E.

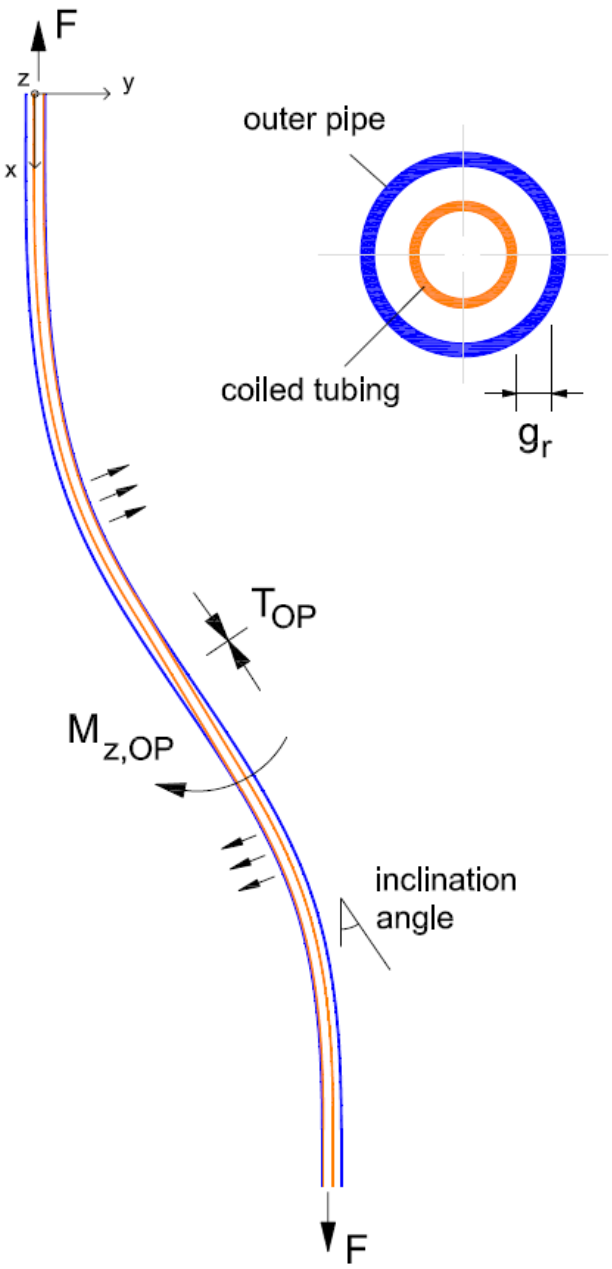

Figure 4.1: Mechanical interaction between SCG and CT

4.2 Model Test Scaling

A physical model can be scaled in different approaches. The geometry, the acting forces as well as the structure's stiffness have to be in proportion between the prototype, p, and the model, m.

Palmer et al. (1974) and Palmer (1975) define the scale factor for tubular model tests as shown in equation (4.1). The pipe's rigidity EI divided by its weight per arbitrary length w accounts for its structural properties as well as for the pipes environment. This is particularly important when subsea structures are modelled in air, as it is in this case.

$$s_L = \frac{\left(\left(\frac{EI}{w}\right)_p\right)^{\frac{1}{3}}}{\left(\left(\frac{EI}{w}\right)_m\right)^{\frac{1}{3}}} \tag{4.1}$$

where

s_L is the length - scaling factor of the model

EI_p is the flexural rigidity of the prototype

w_p is the weight per arbitrary length of the prototype

EI_m is the flexural rigidity of the model

w_m is the weight per arbitrary length of the model

In agreement with Schlumberger these tests are being conducted horizontally. It was chosen just to focus on the mechanical pipe-in-pipe interaction at the installed system. A vertical model test would have required scaffolding and several safety measurements to satisfy "working in height" regulations.

The pipe's dead load is therefore acting normal to its axis and not axially as in the real case; however this can be seen as insignificant for the investigated pipe-in-pipe reaction forces, since the model's outer- and inner pipe weight are respectively 0.64% and 0.18% of the maximum applied load of 400 kg.

4.2.1 Scaling of Pipe in Pipe Model

It is important that both, the guide pipe and the coiled tubing are equally scaled. Due to the extensive slenderness of the intervention riser designed for up to 1500 m of water depth, it is not possible to model the entire prototype conventionally, and hence only the

bend section near the wellhead is been represented as shown in Figure 3.1. Combining equation (4.1) with the locally available material small scale representations of the guide pipe and coiled tubing have been sourced. These are a small diameter pipe and a large diameter pipe to represent the guide pipe and an inner pipe with properties as scale factors shown in Table 4-1, Table 4-2 and Table 4-3 respectively.

Table 4-1: Scaling of outer pipe representing the SCG used in phase 1 and 2

SCG (1-2)	**OD**	**WT**	**Weight w**	**EI**	**EI/w**
	[mm]	[mm]	[kg/m]	[kNm^2]	[m^3]
Prototype	114.3	7.62	17.4	756	4420.64
Model	12.7	1.65	0.45	0.185	41.94
Power	*1*	*1*	*2*	*5*	*3*
Scale factor	9.00	4.62	6.22	5.28	**4.72**

Table 4-2: Scaling of outer pipe representing the SCG used in phase 3 and 4

SCG (3-4)	**OD**	**WT**	**Weight w**	**EI**	**EI/w**
	[mm]	[mm]	[kg/m]	[kNm^2]	[m^3]
Prototype	114.3	7.6	17.4	756	4420.64
Model	25.4	1.6	0.94	1.761	191.19
Power	*1*	*1*	*2*	*5*	*3*
Scale factor	4.50	4.75	4.31	3.36	**2.85**

The 2 mm wire representing the inner pipe in phase 2 and 4 has a negligible flexural rigidity, and is therefore not being scaled in respect of EI/w. It's outer diameter is 30.15 times smaller as the prototype's coiled tubing. Since the prototype pipes are submerged when in operation but the model-tests are conducted in air, the pipe´s environment has to be taken into consideration as explained in section 4.2.

This is incorporated in the scale factor of the EI/w in Table 4-1 toTable 4-3: the prototype's weight is submerged whereby the model pipe's weight its dry weight is.

Table 4-3: Scaling of inner pipe representing the CT used in phase 1 and 3

CT (1,3)	**OD**	**WT**	**Weight w**	**EI**	**EI/w**
	[mm]	[mm]	[kg/m]	[kNm^2]	[m^3]
Prototype	60.3	5.2	6.14	71.34	1183.76
Model	6	1	0.12	0.0106	8.74
Power	*1*	*1*	*2*	*5*	*3*
Scale factor	10.05	5.20	7.15	5.83	**5.14**

The scale of the pipes used in phase 1 match to an accuracy of 8% and hence the mechanical interactions of the pipe in pipe system during the phase 1-model tests can be recalculated to real life loads with relatively high accuracy. The pipes used in the model test have a length of 5.75 m. A longer section is in this case not necessary since the test focuses just on the load transfer between the pipes in its curved section above the mudline. The material specifications of the test specimens are given in Table 4-4.

Table 4-4: specimen material

specimen		**6 mm pipe**	**12.7 mm pipe**	**25.4 mm pipe**	**2 mm wire**
Material	[-]	SS316	SS316	SS304	steel wire
yield strength	[Mpa]	235	235	235	-
breaking load	[kN]	-	-	-	2.9

4.3 Test Phases

The tests started with the 12.7 mm outer pipe and 6 mm inner pipe setup, in which both pipes are in proportion to the prototype. After the first tests using the 30° inclined shape, the pipe's lower end has been shifted further to achieve a shape of 45° and 60°, where the loading has been repeated. After the 60° test was completed, the 6 mm pipe has been replaced by the 2 mm wire without making any changes on the outer pipe. Therefore,

the bending sequence of the Phase 2 tests with the 12.7 mm outer pipe and the 2 mm wire was from 60° over 45° to the remaining 30°. That is relevant since the outer pipe was already plastically bent from the 60° inclination angle, and hence the global bending moment at 45° and 30° was higher compared to those in phase 1, but has no influence on the local bending moment.

After completing all tests of phase 1 and 2 with the 12.7 mm outer pipe, this has been replaced by a 25.4 mm pipe for conducting phase 3 and 4. The length and the strain gauge arrangement were the same as for the smaller pipe, which allows a direct comparison of the results. This time the 6mm inner pipe and the 2 mm wire have been exchanged for every inclined angle starting from 30° to 45° and 60°. That eliminated the higher global in-plane bending moment for the consequent phase due to residual bending from the predecessor phase. The sequence of the test phases is given in Table 4-5.

Table 4-5: Test Phases

PHASE		**Outer Pipe**	**Inner Pipe / Wire**	**Interradial Gap g_r**
No.	**Name**	OD [mm]	OD [mm]	[mm]
1	12.7 mm Outer Pipe, 6 mm Inner Pipe	12.7	6	1.7
2	12.7 mm Outer Pipe, 2 mm Wire	12.7	2	3.7
3	25.4 mm Outer Pipe, 6 mm Inner Pipe	25.4	6	8.1
4	25.4 mm Outer Pipe, 2 mm Wire	25.4	2	10.1

The tests conducted in each phase and the corresponding load on the prototype are shown in Table 4-6 shows. The applied load is normalised with respect to the guide pipe, so that the highest load achieved in phase 1 was 29 % SMYS of the outer pipe.

The wire breaking load in a straight alignment was determined to be 308 kg by conducting a breaking test, and hence the maximum applied load has been chosen as 200 kg.

Table 4-6: Conducted model tests with their corresponding prototype load

SCG yield capacity	Phase 1 : 12.7 mm Outer Pipe, 6 mm Inner Pipe	Phase 2: 12.7 mm Outer Pipe, 2 mm Wire	Phase 3: 25.4 mm Outer Pipe, 6 mm Inner Pipe	Phase 4: 25.4 mm Outer Pipe, 2 mm Wire	**Model Test Load Phase 1 and 2 12.7 mm Outer Pipe**	**Model Test Load Phase 3 and 4 25.4 mm Outer Pipe**	**Corresponding Prototype Load**
[%]	[°]	[°]	[°]	[°]	[kg]	[kg]	[kN]
2%			30°, 45°, 60°	30°, 45°, 60°		50	28.2
3%	30°		30°, 45°, 60°	30°, 45°, 60°	30	100	42.3
4%	45°, 60°	30°, 45°, 60°			50		56.4
5%			30°, 45°, 60°	30°, 45°, 60°		150	70.4
7%	30°, 45°, 60°	30°, 45°, 60°	30°, 45°, 60°	30°, 45°, 60°	100	200	98.6
9%			30°, 45°, 60°			250	126.8
10%			30°, 45°, 60°			300	140.9
11%	30°, 45°, 60°	30°, 45°, 60°			150		155.0
12%			30°, 45°			350	169.1
14%			30°			400	197.3
15%	30°, 45°, 60°	30°, 45°, 60°			200		211.3
18%	30°, 45°, 60°				250		253.6
22%	30°, 45°, 60°				300		310.0
25%	30°, 45°, 60°				350		352.2
29%	30°, 45°, 60°				400		408.6

In phase 4 the 200 kg maximum applied load correspond to 7 % SMYS of the 25.4 mm outer pipe. Since the same 7 % SMYS match the tests with 100 kg load on the 12.7 mm outer pipe, it has been decided to compare all four test phases with each other. This comparison shows the influence of the interradial gap on the load transfer, whereas the

influence of the bending angle can be displayed by comparing the results of the three bending angles for each phase independently of the applied load.

4.4 Model Setup

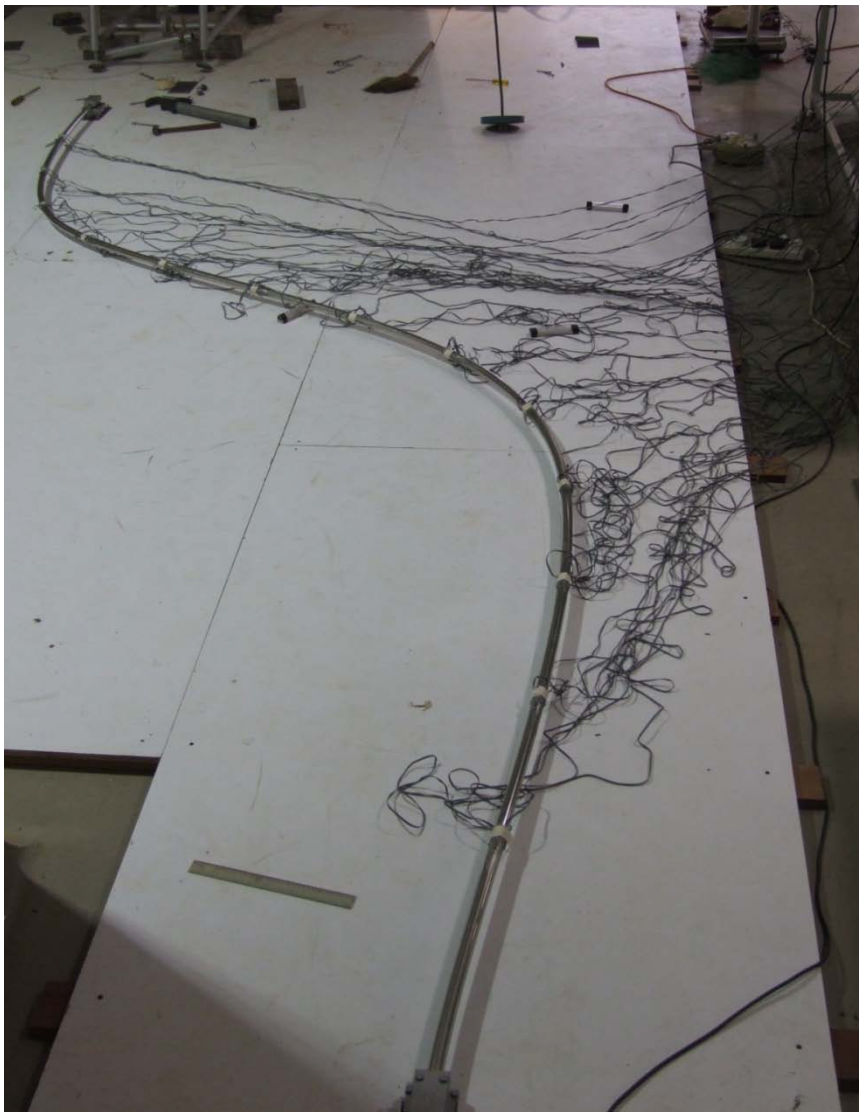

Figure 4.2: 60° inclined 25.4 mm pipe during test phase 3 and 4

The equipment used to conduct the model tests consists of two clamps to hold the outer pipe in place (Figure 4.4) a structure to tension the inner pipe, weights and some wire and clamps to connect these pieces together. In addition, the pipe is supported at nine locations with 0.575 m centres along its axis in order to minimise contact with the

surface. Detailed drawings and system overviews can be found in Appendix G: Physical Model Test: Equipment Drawings.

The principle set-up and definition of the pipe orientation is shown in Figure 4.3. The investigated inclination angles of 30º, 45º and 60º are achieved by shifting the left clamp to the coordinates given in Table 5-1.

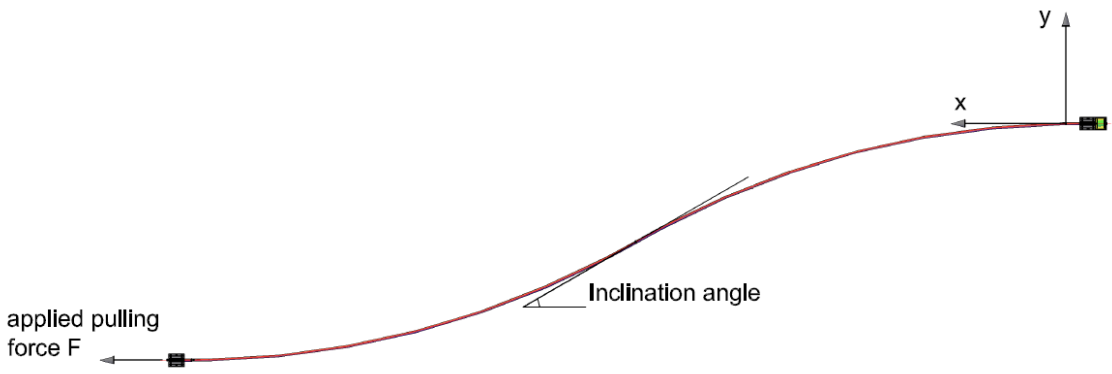

Figure 4.3: plan of principle model set up

To tension the CT, weights are hung onto the loadhanger and are connected to the pipe through a wire. Each weight is of 10 kg and its geometry allows a total weight of 400 kg, which already exceeds the model CT's elastic capacity for Phase 1 and 3 by 6%.

To measure the stress along the SCG, 38 and 52 strain gauges were attached onto the 12.mm pipe and 25.4 mm pipe respectively to measure tension and bending moment. The strain measurements were conducted using a data logger. A load cell is connected to the coiled tubing to measure the resultant force at the fixed end, and therefore the resultant friction force along the outer pipe. The measurement as well as the alignment of the strain gauges is described in section 5.2 strain gauging.

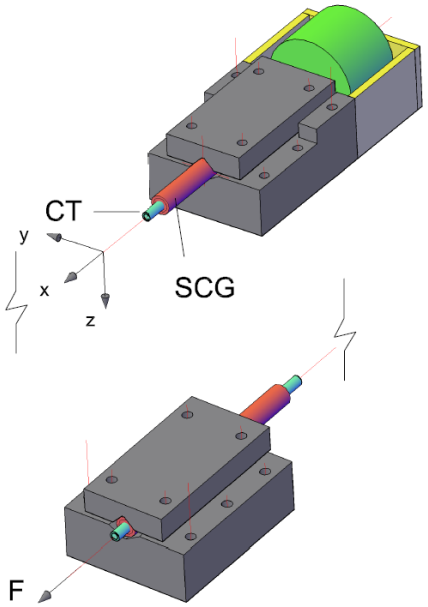

Figure 4.4: clamps to fix the SCG at its respective ends

4.4.1 Strain gauge configuration

On the 12.7 mm outer pipe used in Phase 1 and 2, 38 single element strain gauges with 5 mm in length have been aligned in axial direction. Each gauge is separately connected to the data logger, which allows a simultaneous measurement of bending moment and axial force. The spacing of 0.4 m for paired- and 0.8 m for a four –gauge (see Figure 4.5) configuration results in 13 measurement points along the outer pipe. First results have shown that a four strain gauge configuration is advantageous. It enables to differentiate pure axial strain from bending strain more accurately, as the strain at every reading point can be averaged twice as can be seen in equation (5.3). Consequently for phase 3 and 4, 52 strain gauges have been attached onto the 25.4 mm outer pipe, all four gauge configurations with a spacing of 0.4 m to measure and to quantify the out-of-plane moment. A detailed drawing of the strain gauge arrangement can be found in Appendix G: Physical Model Test: Equipment Drawings.

Figure 4.5: four gauge configuration

5 Data Processing

The required pipe shapes to achieve the 30°, 45° and 60° inclination angles were determined by trial and error using finite element analysis in ABAQUS. One end of the pipe was moved along the pipe axis (x axis) and horizontally across the pipes axis (y axis) so that the centre of the pipe had the required inclination angle, as shown in Figure 5.1. Pipe end displacements and the determined inclination angles are given in Table 5-1. The total declination angle quantifies the total change in angle along the pipe. It was observed that the total declination angle was generally greater than twice the inclination angle.

Table 5-1: Test steps for each phase; coordinates refer to their definition in Figure 4.3

Step	Inclination Angle	Total Declination Angle	ΔX	ΔY
	[º]	[º]	[m]	[m]
1	30	83	-0.25	-0.8
2	45	100	-0.6	-1.7
3	60	137	-1	-2

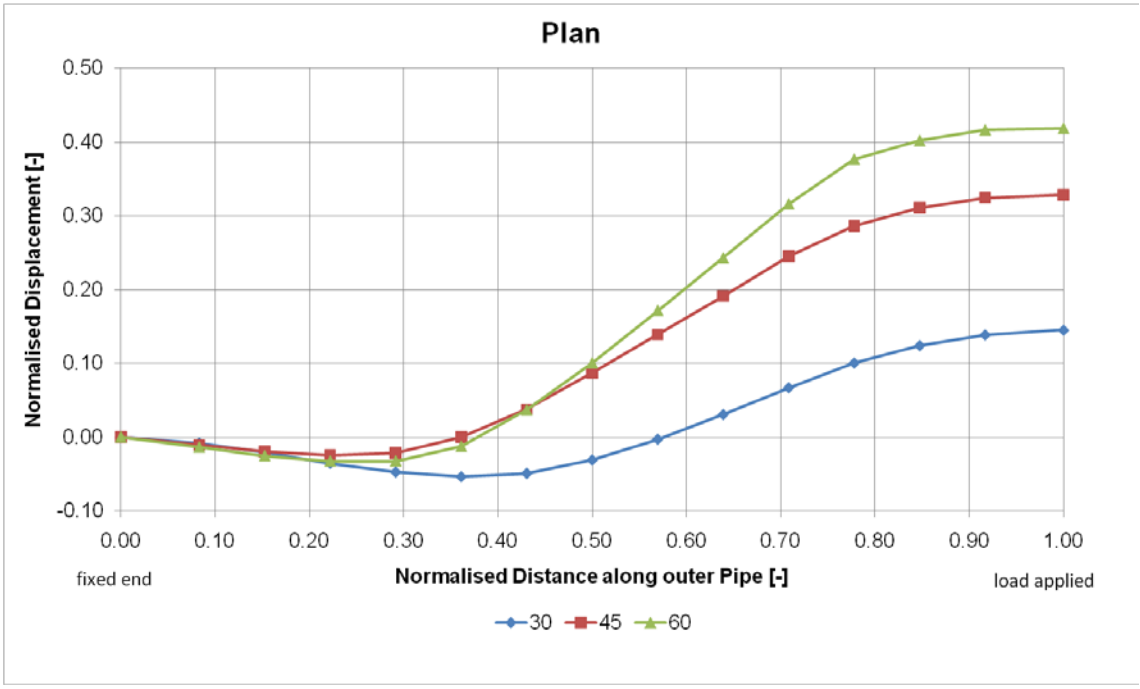

Figure 5.1: Formed shapes for different inclination angles

As can be seen in Figure 5.2, the pipe bends out of its constraint axis due to the overlength. This is particularly obvious for the 30° test, because there the displacement ratio ΔX/ΔY is higher than for the other bending anlges. For all tests conducted this so called bend out occured at the fixed side of the S-shape, whereas in the numerical calculations it was formed either at the displaced pipe's end, at the fixed end or split equally between them as it is illustrated in Figure 7.1.

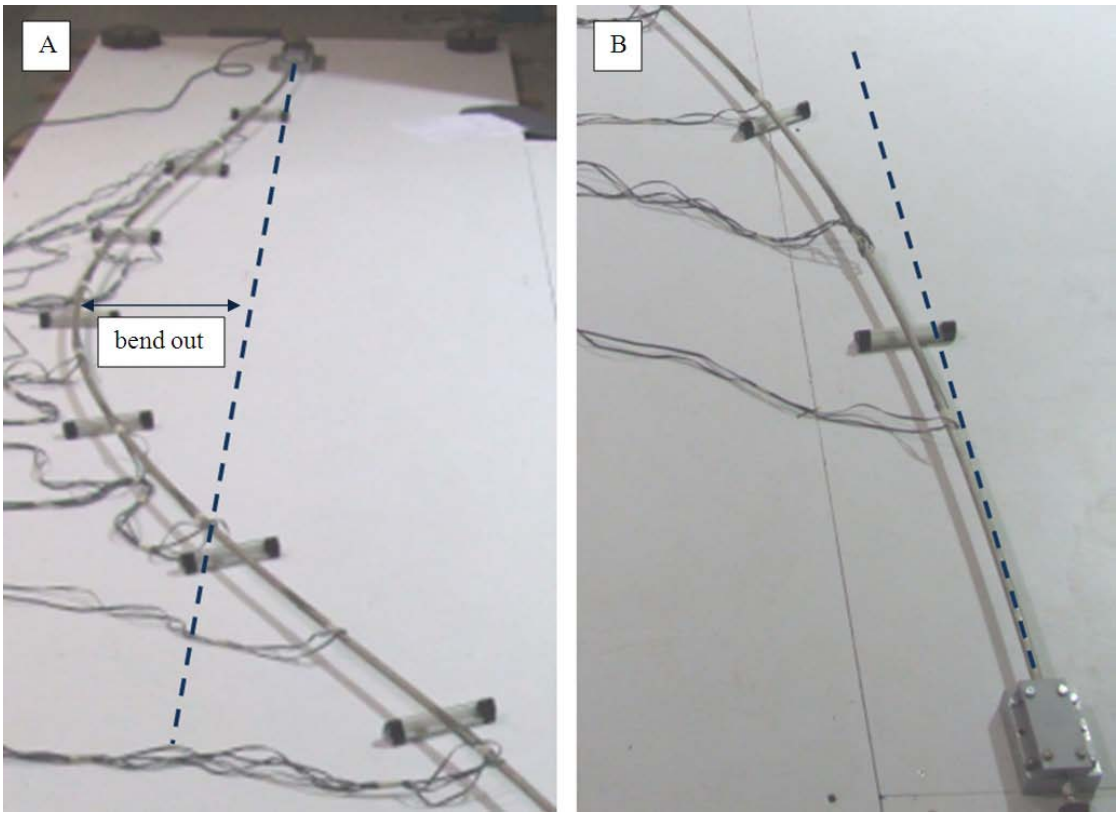

Figure 5.2: picture A shows the section where the pipe bends out of its constraint axis; picture B shows the end where the pipe follows its constraint axis before forming the S-shape

Since this shape difference affects the global- and the local bending moment of the test- and numerical results, some had to be mirrored about the x-axis when compared with the numerical plots.

Although the load is applied on the inner pipe, for consistency reasons it is normalised with respect to the outer pipes yield capacity F_y, which can be obtained from equation (5.1). That shows the direct correlation between load and measured stress along the outer pipe.

$$F_y = Y * A_c \tag{5.1}$$

where

Y is the yield stress

A_c is the cross section area

5.1 Example of how to use the results

The measurements from each test were summarised using test summary plots which contained plots of all of the measured data on a single A4 sheet. The test summary plots include the respective shape, axial force, relative axial force, global in-plane bending moment, local in-plane moment, global out-of-plane moment, local out-of-plane moment, the increase in top tension- and the increase in local in-plane bending moment with increasing load. An example result sheet in actual values can be seen in Figure 3.3, whereas Figure 5.4 shows the same test results normalised.

The relative tension is the axial force measured for a specific applied load minus the initial axial force without any load. The same applies to the local bending moment, which is the difference between the bending moment measured during load was applied and the initial bending moment when no load was yet applied to the inner pipe. The global bending moment as well as the initial axial force is due to the formed shape of the pipe in pipe system. For all twelve tests conducted, the outer pipe was already plastically bent before any load was applied. Only subtracting this initial stress from the actual stress during loading allows a quantification of the load transfer due to the increase in tension of the inner pipe.

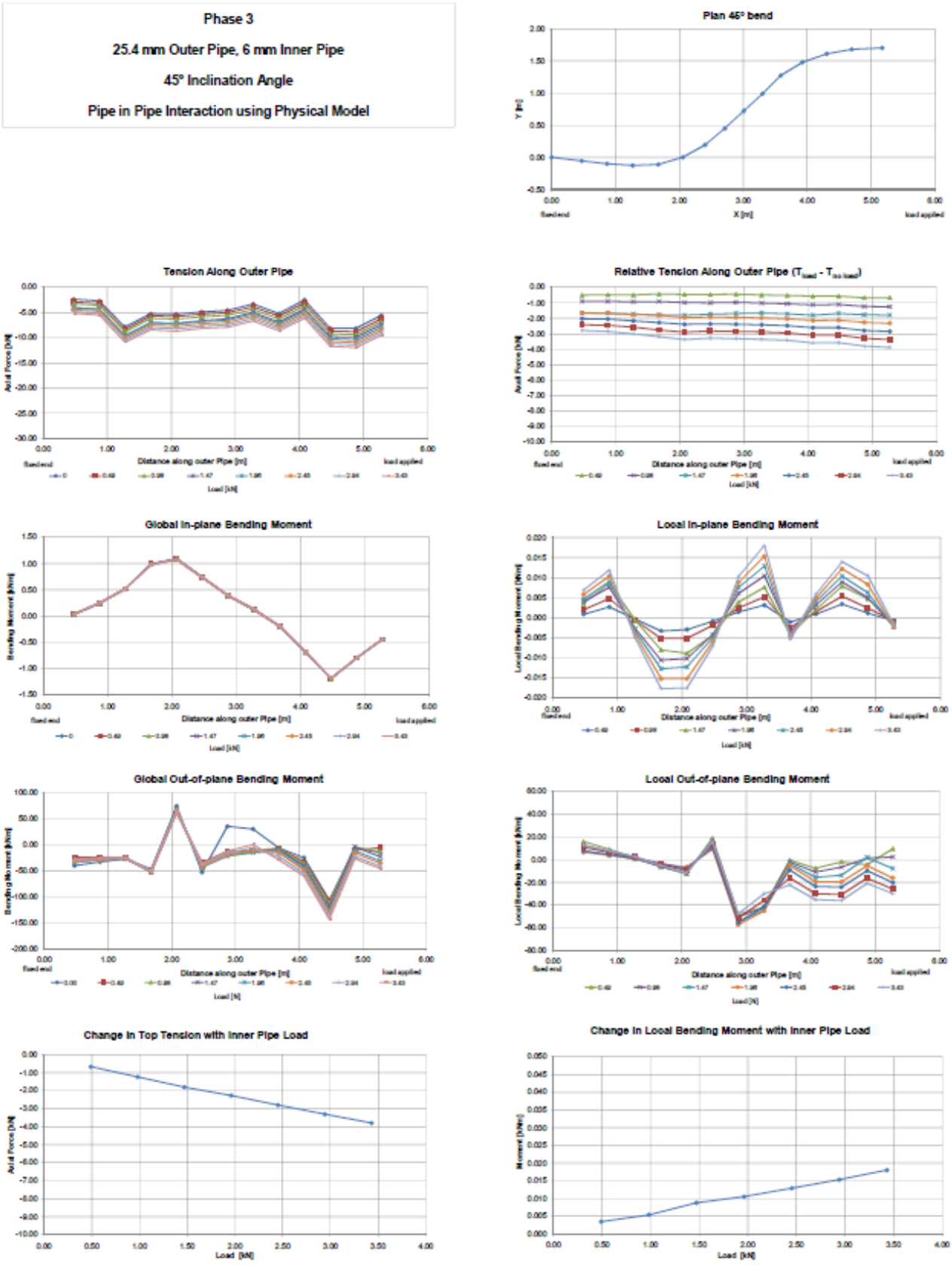

Figure 5.3: example result sheet of physical model test in dimensional values

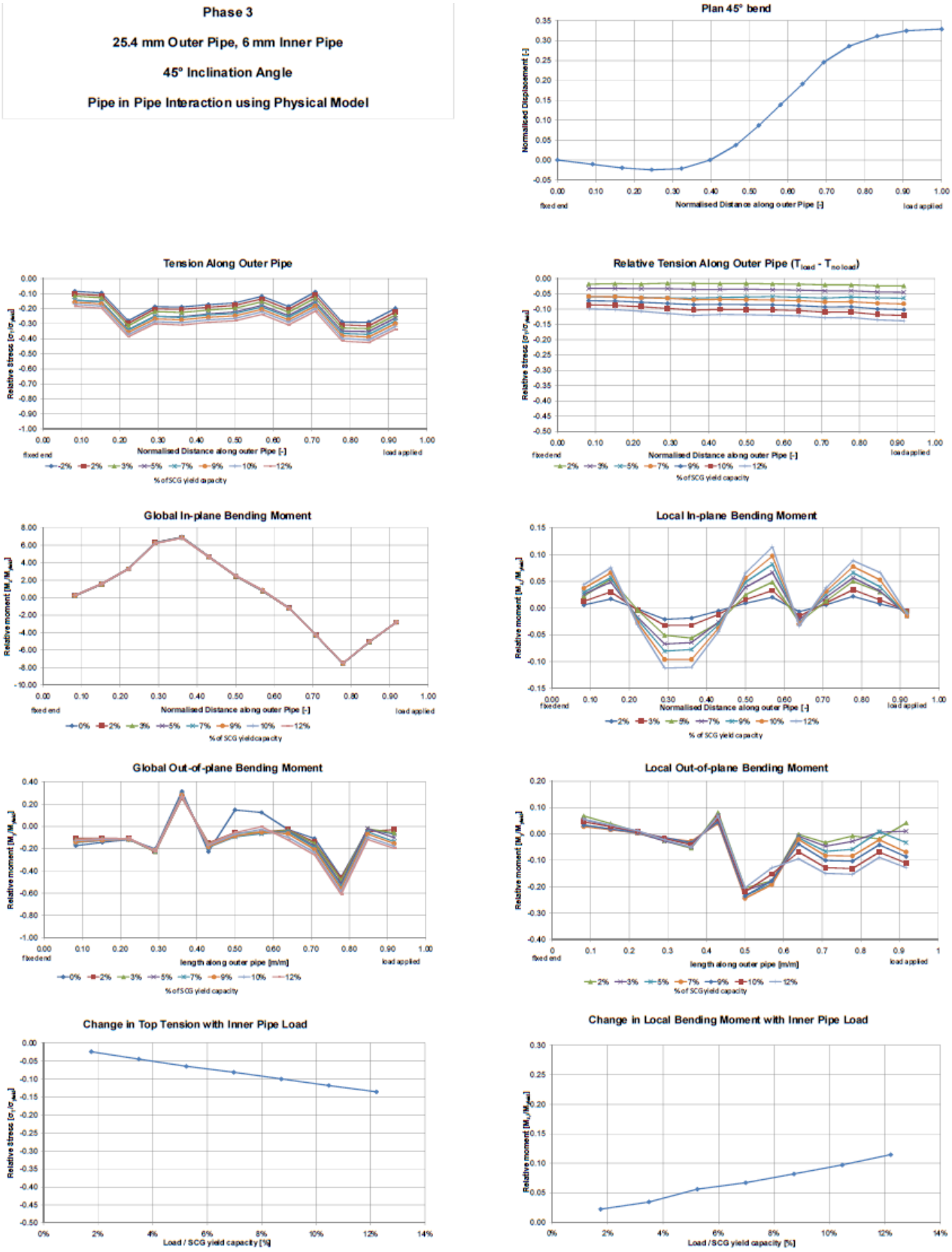

Figure 5.4: typical result sheet of physical model test in normalised values

All the results in this report are given in normalised plots, and therefore the following exercise is to show how these graphs can be used. Using the SCG and CT dimensions provided by the Schlumberger Report 'Properties of Coiled Tubing' (2008), the input parameter can be calculated as following:

Table 5-2: Prototype characteristics

	OD	**ID**	**A**	**S**	**Y**	**F_{yield}**	**M_{yield}**
	[m]	[m]	[m^2]	[m^3]	[Mpa]	[kN]	[kNm]
SCG	0.1143	0.0983	2.56×10^{-3}	6.62×10^{-5}	552	1409.61	36.55
CT	0.0603	0.0500	0.89×10^{-3}	1.13×10^{-5}	758	492.54	6.27

where

A is the cross section area
S is the section modulus
Y is the yield stress (also known as $SMYS_{100\%}$)
F_{yield} is maximum force in the elastic range
M_{yield} is the maximum moment in the elastic range

According to the Schlumberger Report 'SCG Design Basis', Rev. 2 (2008), the buoyancy tanks are intended to be installed over the riser length of 390 m above the wellhead. After installation these tanks will form the S-shape within this section. Therefore the right side of each table corresponds to the connection to the wellhead (load applied), whereas the left side (fixed end) corresponds to the end of the S-shape, which is in this case 390 m above the wellhead.

Assuming the CT is axially loaded by 400 kN and the vessel position leads to an expected inclination angle of 30°, it can be determined to what extent and where the load affects the riser. 400 kN corresponds to 27% of the SCG's yield capacity.

The maximum axial force in the guide can be expected to be 44% of its yield capacity in compression and is located at 100-43 = 57% above its connection to the subsea tree as

shown in Figure 5.5. In absolute numbers the compression is therefore 0.44*1470 = 647 kN at 0.57*390 = 222 m riser length. The same approach applies for global and local bending, except that the relative value has to be multiplied by the SCG's yield moment provided in Table 5-2.

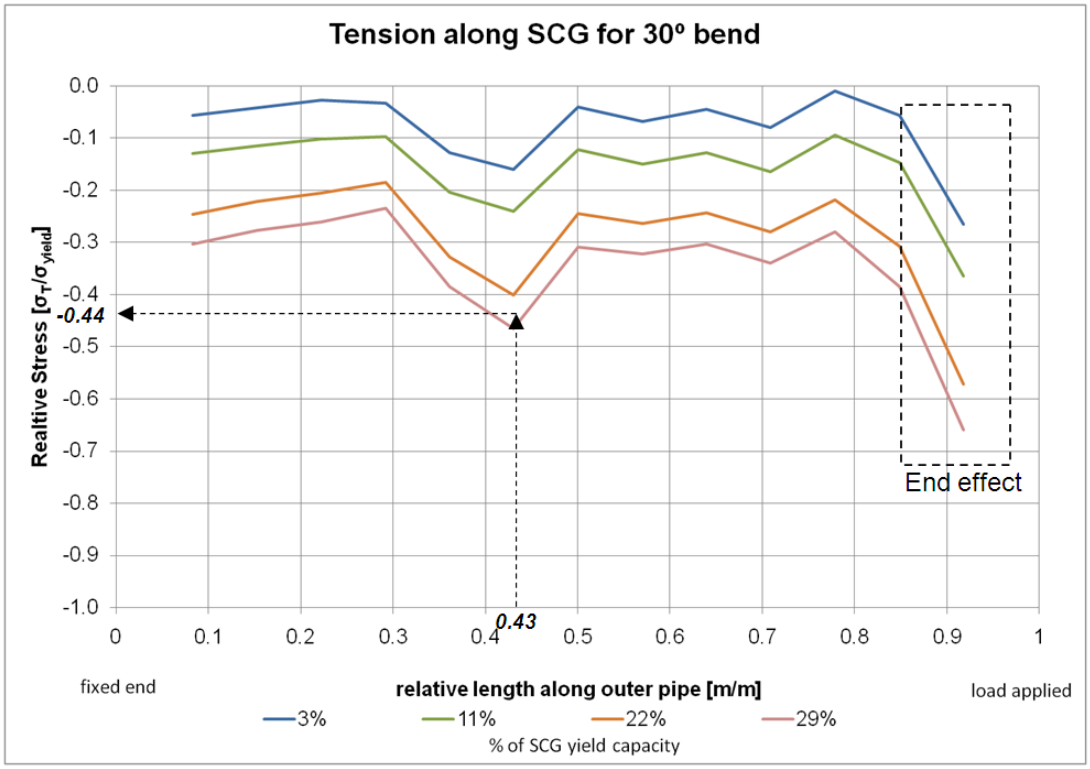

Figure 5.5: graph-use example

As every model test also this has its limitations; a slight eccentrically load can distort the result at the model pipe's end. Those results can be neglected as end effect (Figure 5.5). The linear interpolation between the graphs is valid and can easily be checked by interpolating between the given graphs.

5.2 Strain gauging

To measure bending moment and tension along the outer pipe, electrical resistance-strain gauges have been attached. Strain gauging is a common way to measure the

relative elongation of a specimen for varying loading. Strain ε is measured by changes in electrical resistance R due to the elongation of the strain gauge's grid:

$$\varepsilon = \frac{\Delta l}{l} = \frac{\Delta R/R}{K} \tag{5.2}$$

Where K is the gauge factor is and depends on the gauge's geometry.

Since the applied forces on the inner pipe are horizontally, tension and bending moment in the outer pipe are also purely horizontal; the only vertical force is gravity which is small compared to the load applied. Therefore the collateral aligned gauges (M_i) are expected to measure the minimum/maximum of the respective strain. The top and bottom gauges (T_i) should give pure axial force. However, a small M_y compared to M_z has been observed and therefore the axial force has been calculated from 4 gauges wherever possible. As can be seen in Figure 5.6 the measured strain (b) at the specimen (a) is divided into pure axial strain ε_T (c) and pure moment strain ε_M (d).

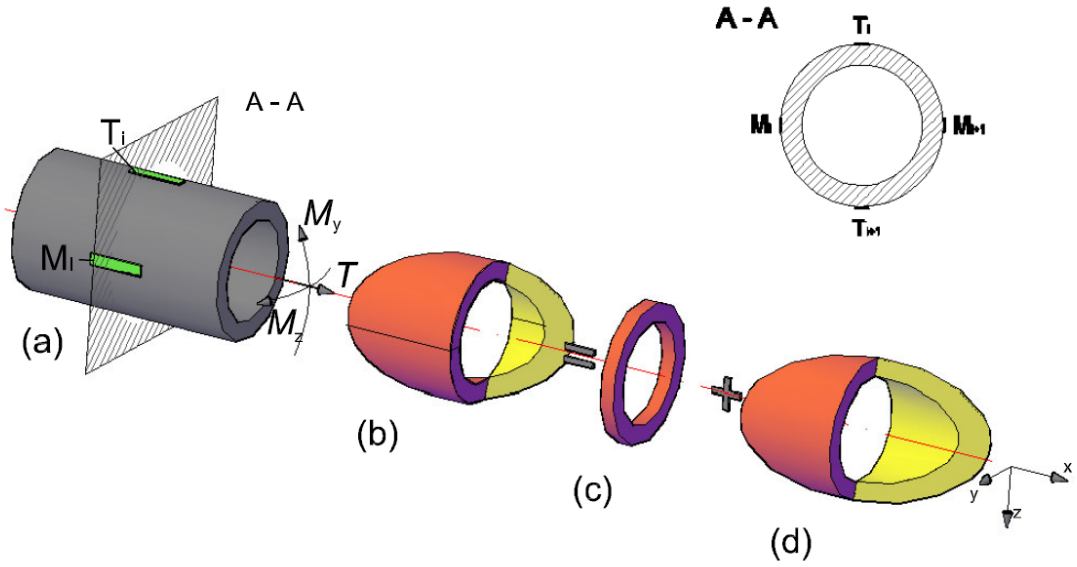

Figure 5.6: Split of real stress (b) into axial force stress (c) and pure bending (d)

Axial strain is calculated by using equation (5.3). The moment is further subdivided into M_y and M_z. using equation (5.4) and (5.5) respectively.

$$\varepsilon_T = \frac{1}{2}\left(\frac{1}{2}\sum_{i=1}^{2} T_i + \frac{1}{2}\sum_{i=1}^{2} M_i\right) \tag{5.3}$$

$$\varepsilon_{M_z} = \frac{\max(M_i; M_{i+1}) - \min(M_i; M_{i+1})}{2} * sign(M_{i+1}) \tag{5.4}$$

$$\varepsilon_{M_y} = \frac{\max(T_i; T_{i+1}) - \min(T_i; T_{i+1})}{2} * sign(T_{i+1}) \tag{5.5}$$

Section 5.2.1 describes how this split strain is been converted into stress and further into Axial force T and bending moment M.

5.2.1 Strain – Post Processing

In this experiment the important stress component is axial stress. Hoop stress is negligible, since the pipe is not exposed to pressure, and radial stress is zero at the pipe's surface where strain is measured. The linear relation of Hook's law shown in equation (5.6) has therefore been used.

$$\frac{\partial u}{\partial x} = \varepsilon = \frac{\sigma}{E} \tag{5.6}$$

The Young's modulus E was determined by a tensile test for the 12.7 mm outer pipe used in Phase 1 and 2. The reader finds a stress-strain diagram Figure G.10 at page 151.

$$\sigma_M = \varepsilon_M * E$$
$$\sigma_T = \varepsilon_T * E \tag{5.7}$$

The axial force along the SCG can therefore be calculated by multiplying the stress σ_T with the SCG's cross section area. In this case the axial force is expressed normalised to its yield stress σ_{yield}, which by convention corresponds to the 0.5% strain ε as it is indicated in Figure G.10 point A.

The bending moment can be determined by multiplying the stress by the pipe's section modulus as shown in equation (5.8).

$$M = \sigma_M * S \tag{5.8}$$

The section modulus S of a pipe is defined as:

$$S = \frac{\pi}{32} * \frac{OD^4 - ID^4}{OD} \tag{5.9}$$

In the following the resultant moment is normalised to the SCG's yield moment as given in equation (5.10).

$$M_{yield} = \sigma_{yield} * S \tag{5.10}$$

5.2.2 Normalisation Parameters

The axial force in the outer pipe is given normalised in respect to its maximum elastic capacity σ_T/σ_{yield}. To obtain the effective axial force in the guide pipe, the reading from the graph has to be multiplied by the guide's yield capacity σ_{yield} and cross sectional area A_c, which is the maximum axial force F_y as provided in Table 5-2.

The bending moment in the guide is given normalised in respect to its maximum elastic moment M/M_{yield}. The effective moment in the prototype guide can be calculated by multiplying the value from the diagram by M_{yield} which can also be found in Table 5-2.

6 Model Test Results

In this chapter the most relevant results are shown and discussed. The reader can find the complete set of model test results in Appendix A to C.

6.1 Independent axial behaviour of Inner- and Outer Pipe

To show the independent axial behaviour of both pipes, a test on the straight system has been conducted. The outer pipe was straight and the inner pipe inserted into the outer pipe and fixed at one end. The free end was loaded with 50 kg (490.5 N) and the tension along the pipe was measured and recorded by a loadcell at the fixed end (Figure 6.1)

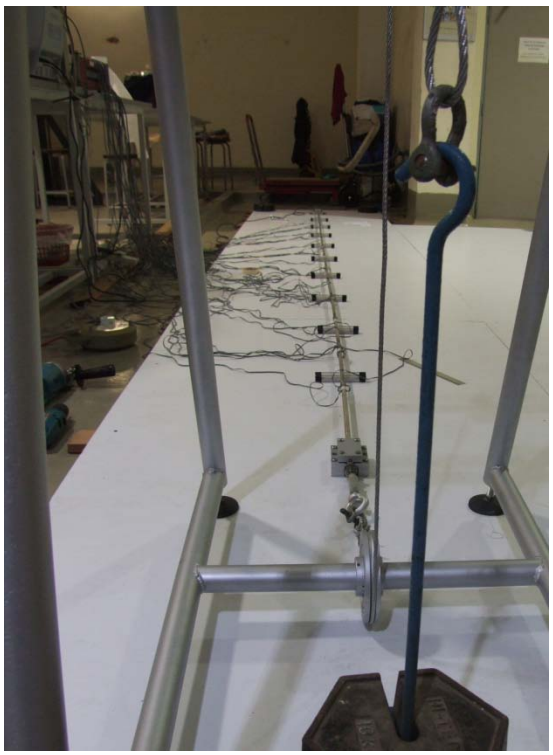

Figure 6.1: Test to show axial independence of both pipes in straight alignment

The loadcell recorded a tension of 437 N, and hence the remaining 11% of the applied load were transformed into friction along the pipe's interface. The tension distribution

along the outer pipe is shown in Figure 6.2. The fact that 89% of the applied force were transmitted to the loadcell fixed at the other end, leads to the conclusion that both pipes have an axially independent behaviour, and that the load transfer in the following inclined shapes is entirely due to their geometric interaction and acting friction.

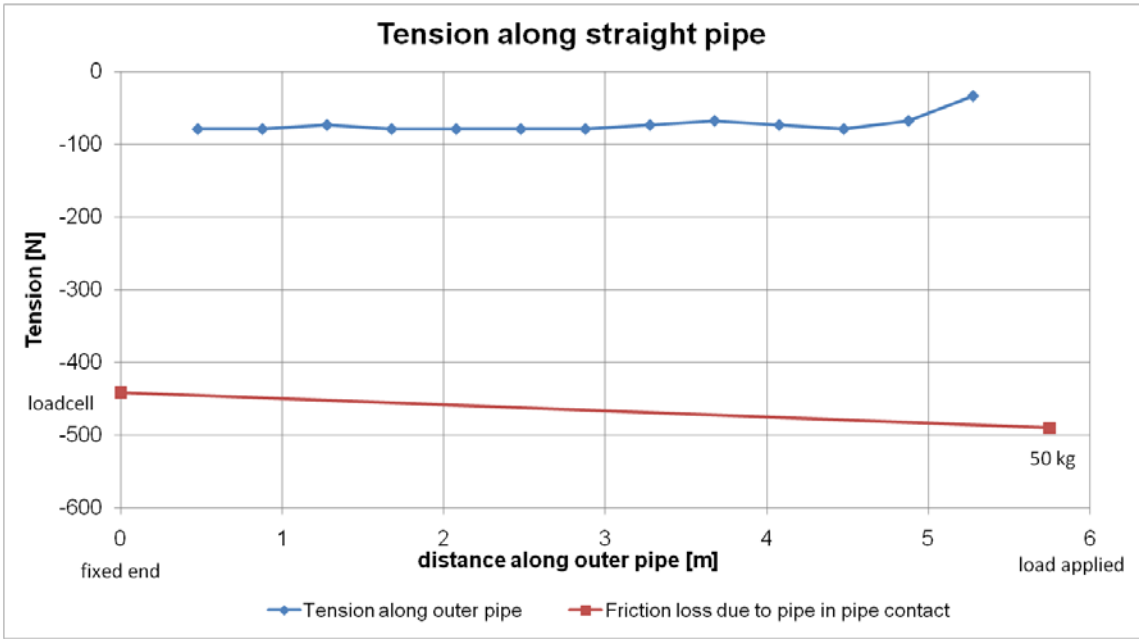

Figure 6.2: Axial force along the straight pipe in pipe system

6.2 Tension along Outer Pipe

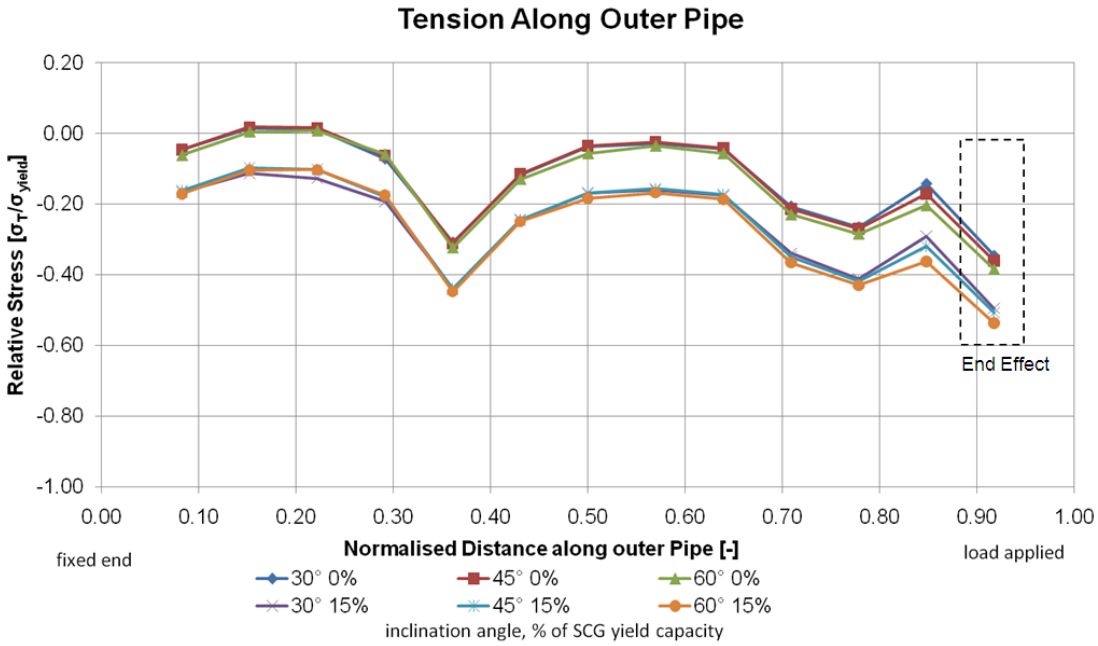

Figure 6.3: Phase 2, Tension along the SCG for different inclination angles

The initial axial force is displayed in the upper graph bundle in Figure 6.3, and the tension for the loading corresponding to 15 % of the outer's pipe yield capacity (lower graph bundle) for each inclination angle in phase 2. As can be seen, the tension along the guide pipe remains constant for the three investigated bending angles, and can hence be treated as independent of bends between 30° and 60°. The right most reading point can again be treated as an end effect. The difference between the axial force with and without loading has been defined previously as relative tension and is shown in Figure 6.4. The increase in top tension with increasing load is given in Figure 6.5. It shows an almost linear increase for the three bending angles.

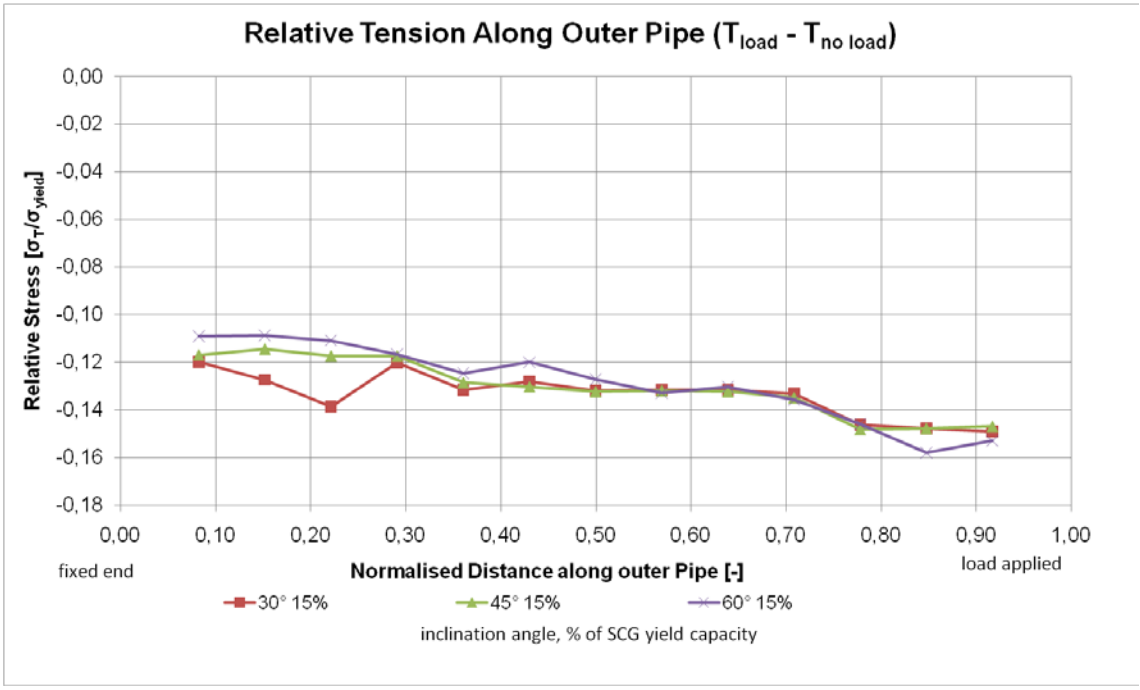

Figure 6.4: Phase 3, Tension evolution in outer pipe for different inclination angles

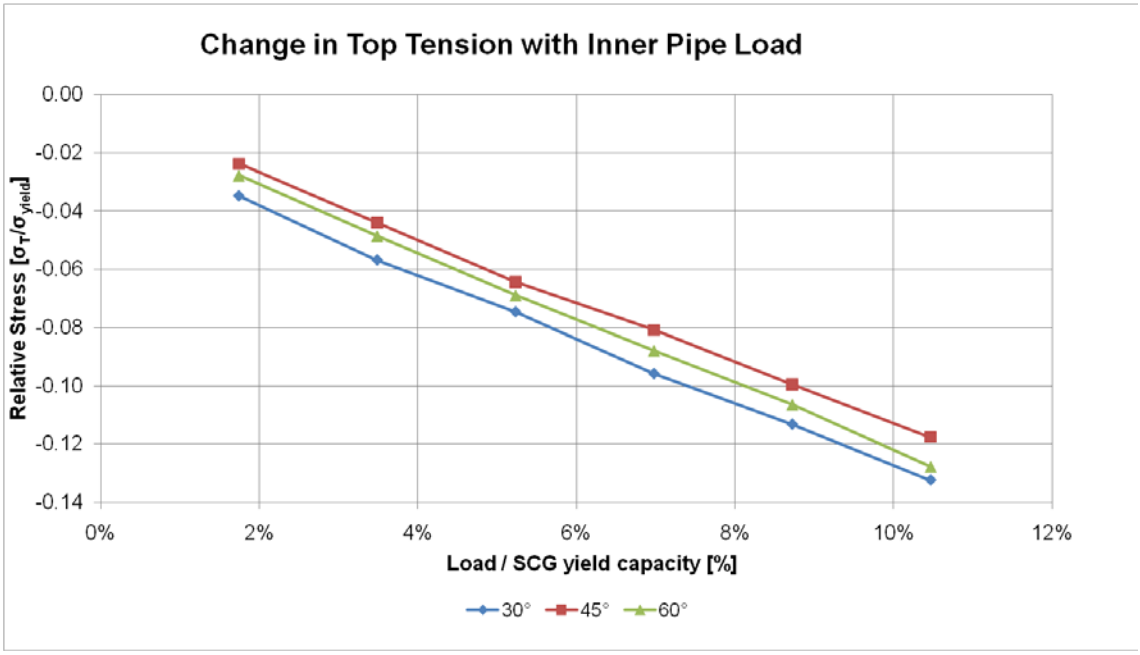

Figure 6.5: Phase 3, load-response for different inclination angles

In order to simplify further analysis of load-response data such as shown in Figure 6.5, a table with the explicit values is provided for each such diagram.

Table 6-1: graph values of Figure 6.5

Load	2%	3%	5%	7%	9%	10%
30°	-0.035	-0.057	-0.075	-0.096	-0.113	-0.132
45°	-0.024	-0.044	-0.064	-0.081	-0.100	-0.118
60°	-0.028	-0.048	-0.069	-0.088	-0.106	-0.128

Averaging the readings for the three inclination angles and each phase, a correlation between the applied load and the response can be elaborated individually for each phase. It was found that the tension in the outer pipe increases almost linearly in proportion to the applied load.

$$\frac{dT_{SCG}}{dT_{CT}} \cong c_{TT} \qquad (6.1)$$

Where

dT_{SCG} is the increase in maximum axial force in the SCG

dT_{CT} is the load applied to the CT's lowest end

c_{TT} constant factor for increase in top tension with loading

The value for c_{TT} in equation (6.1) is given in table Table 6-2:

Table 6-2: Parameters to calculate the axial force in the guide pipe

PHASE		**Outer Pipe**	**Inner Pipe / Wire**	**Interradial Gap g_r**	**dT_{SCG} / dT_{CT}**
No.	**Name**	ID [mm]	OD [mm]	[mm]	c_{TT} [-]
1	12.7 mm Outer Pipe, 6 mm Inner Pipe	9.4	6	1.7	**-1.29**
2	12.7 mm Outer Pipe, 2 mm Wire	9.4	2	3.7	**-1.03**
3	25.4 mm Outer Pipe, 6 mm Inner Pipe	22.2	6	8.1	**-1.13**
4	25.4 mm Outer Pipe, 2 mm Wire	22.2	2	10.1	**-1.04**

This result clearly indicates that a pipe in pipe configuration (phase 1 and 3) transfers more load into the guide than a wire in pipe does, which is due to higher contact forces of the pipe in pipe system and hence due to higher friction forces.

A general conservative estimation of the axial load response due to the applied load can therefore be made, and equation (6.1) can be expressed as:

$$\frac{dT_{SCG}}{dT_{CT}} \cong -1.30 \tag{6.2}$$

This at first surprising conclusion can be interpreted as follows: The load is transferred due to radial contact forces in the bends of the S-shape section (see Figure 4.1) as well as friction forces in axial direction. This geometric interaction is trying to push the outer pipe straight, which results in combination with the acting friction force in higher axial compression in the guide than load is applied on the inner pipe.

Since both pipes of the prototype are modelled proportionally by the setup in phase 1, the factor of -1.30 in equation (6.2) is not over-conservative.

The change in top tension with increasing load for all four phases is given in Figure 6.6. The almost parallel graphs confirm the claim that the transfer function of the load into axial force in the outer pipe is independent of the interradial gap.

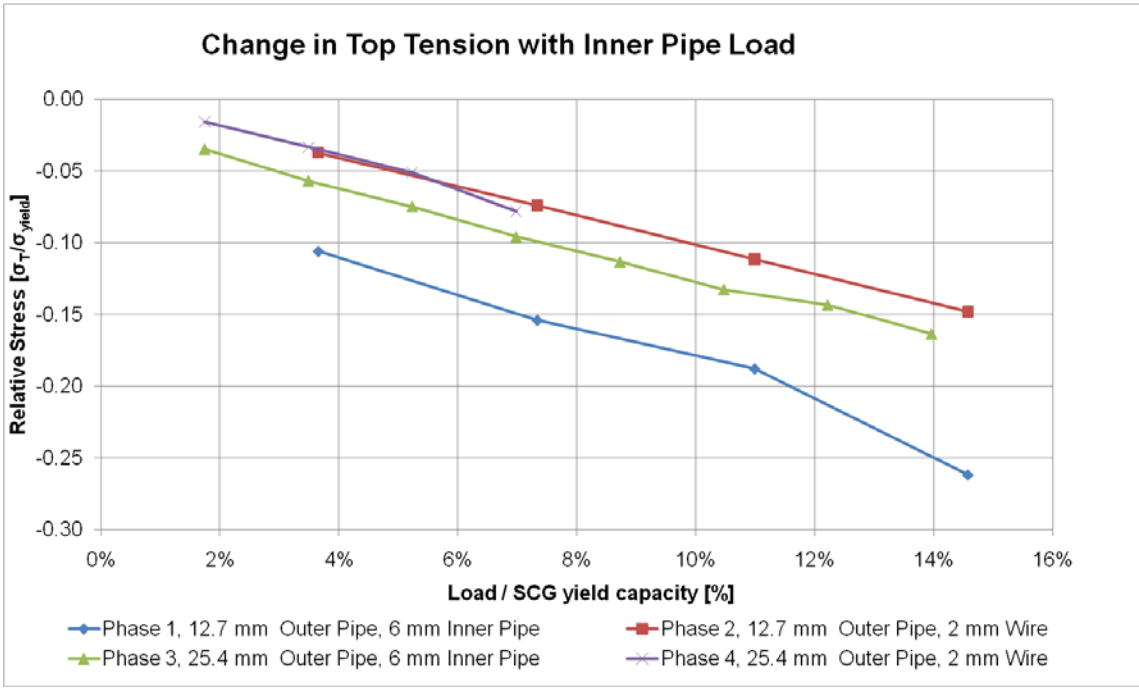

Figure 6.6: Tension evolution in outer pipe for different diameter ratios all bent 30°

Table 6-3: graph values of Figure 6.6

Load	2%	3%	4%	5%	7%	9%	10%	11%	12%	14%	15%
Phase 1			-0.106		-0.154			-0.188			-0.262
Phase 2			-0.037		-0.074			-0.111			-0.148
Phase 3	-0.035	-0.057		-0.075	-0.096	-0.113	-0.132		-0.143	-0.163	
Phase 4	-0.016	-0.033		-0.051	-0.078						

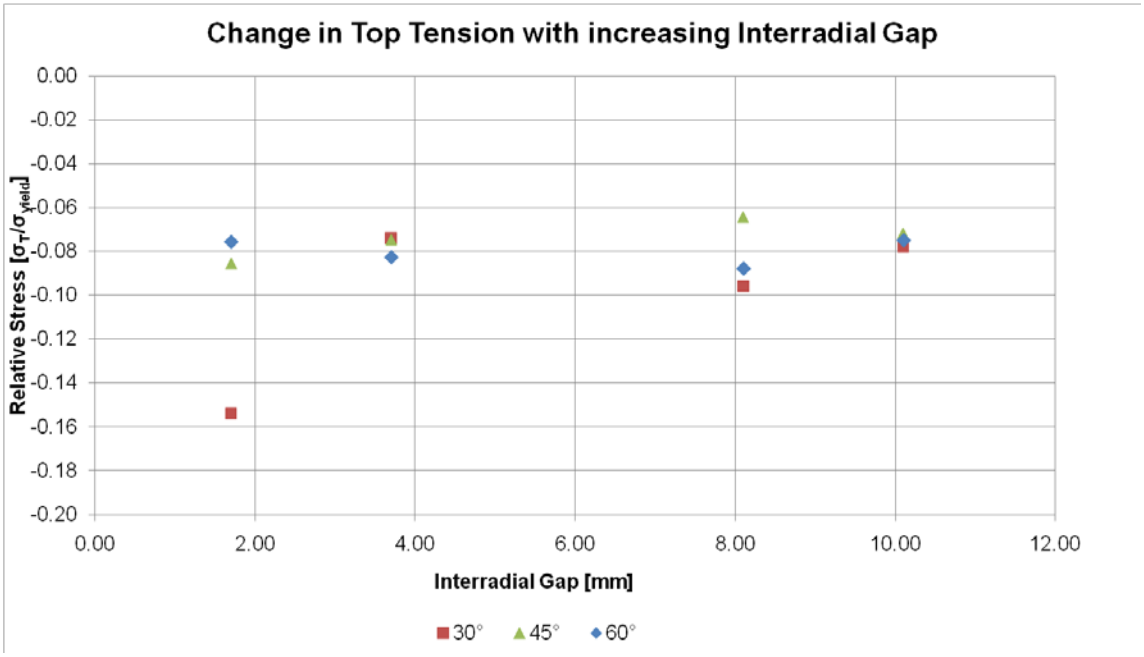

Figure 6.7: Change in top tension for all bending angles with increasing interradial gap for 7 % loading.

The relative stress in the guide pipe with respect to the interradial gap between the outer and inner pipe is shown in Figure 6.7. Again, it can be seen that there is no change in magnitude of the top tension as the interradial gap increases. Treating the 30° degree reading of phase 1 (1.7 mm gap) as outlier, the average of the given values is around -0.08 relative stress. Equation (6.2) gives for a 7 % loading a relative stress of -1.30 x 0.07 = -0.091 σ_T/σ_{yield}, which is at the safe side of the average obtained from the graph.

6.3 Global in-plane Bending Moment M_z

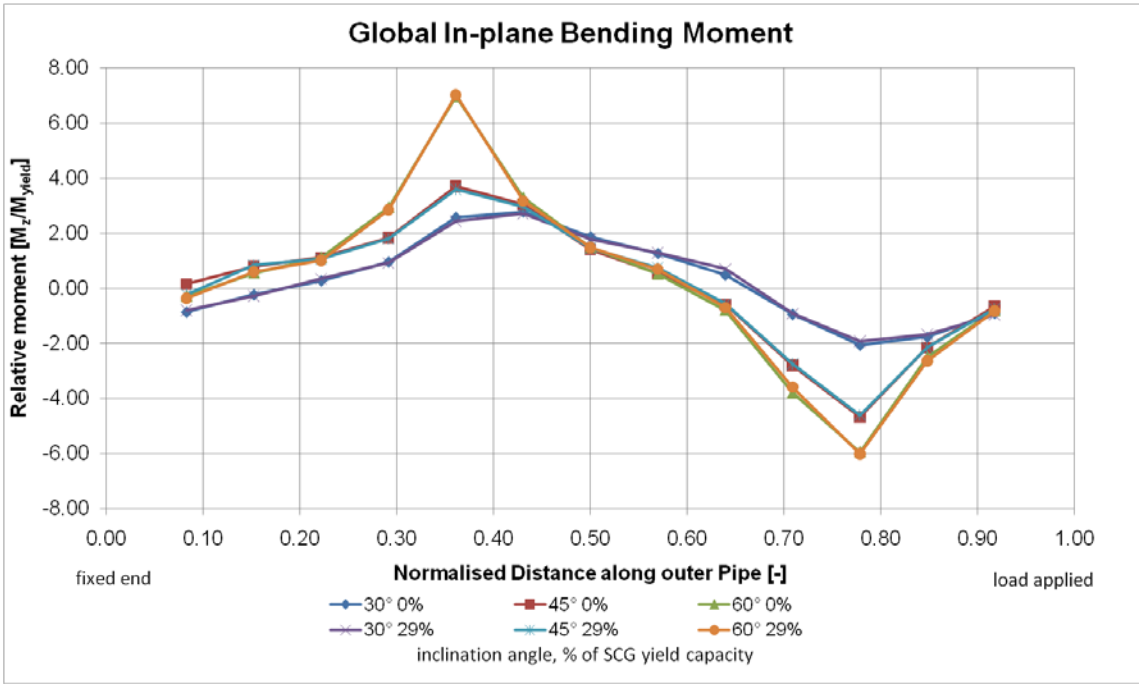

Figure 6.8: Phase 1, global in-plane bending moment M_z along outer pipe for different inclination angles

The global bending of the outer pipe depends purely on the geometry of the formed shape and does not change with the loading of the inner pipe. This can be seen in Figure 6.8, where the moment curve without loading overlays the one with loading. Since the radius of curvature decreases as the pipe gets bent further to higher inclination angles, the global bending moment increases. Figure 6.9 contains the bending moment curves for all phases in their 45° position. The moment for the 25.4 mm pipe used in phase 3 and 4 has a higher moment for the same shape because of its higher flexural rigidity. The difference in peak moment between the phase 1 and 2 graph is due to the residual bending the pipe has obtained from the previous 60° position, as it has been explained in section 4.3.

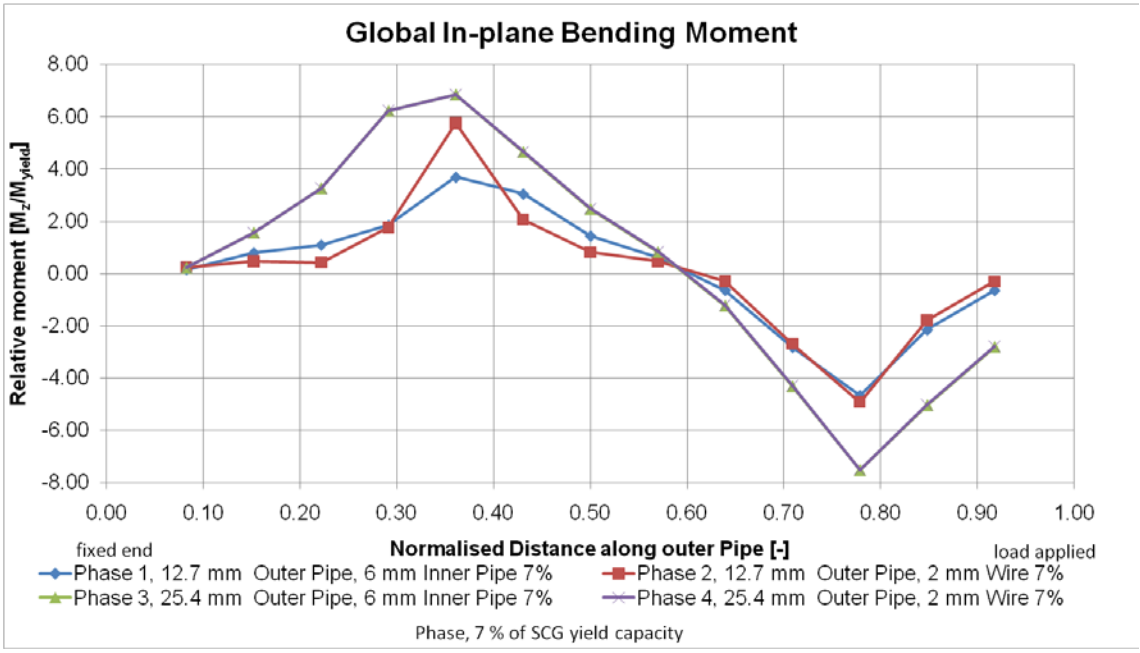

Figure 6.9: Global in-plane bending moments for 45° bend

Using equation (6.3) the outer pipe is expected to yield at a radius of curvature of 5.25 m. Neglecting the end parts of the pipe, the minimum radius of curvature for the 30° bend numerical model has been calculated to 5.4 m.

$$R_{CV} = \frac{E * OD}{2Y * f_D} \tag{6.3}$$

where

- R_{CV} is the elastic limit radius of curvature
- E is the Young's modulus
- OD is the pipe's outer diameter
- Y is the yield stress
- f_D is a safety factor, and in this case not considered

However, due to the different formed shape the actual R_{cv} is lower in the physical model than was predicted numerically, and hence the pipe is in the plastic range for all 12 tests. The minimum actual R_{cv} is therefore the minimum elastic radius divided by the absolute maximum relative moment which is shown in equation (6.4):

$$R_{CV,actual} = \frac{R_{CV,el.\ limit}}{\max\left|\frac{M_z}{M_{yield}}\right|} \quad (6.4)$$

For the 60° test for example, that gives $R_{cv,actual}$ = 5.25/7.03 = 0.75 m, which is close to the radius of 0.80 m measured at the model.

6.4 Local in-plane Bending Moment $M_{z,l}$

The graphs given in Figure 6.10 show the local bending moment along the outer pipe. In the 60° test, the maximum local moment seems to get split into two peaks of comparable magnitude. This tendency cannot be observed in any other result of a different phase, which might be due to the fact that other setups could not be loaded until 29 % of its outer pipe yield capacity, since the load is either limited by the wire-breaking load (phase 2), or the maximum weights correspond only to a smaller fraction of the guide's capacity (phase 3 and 4).

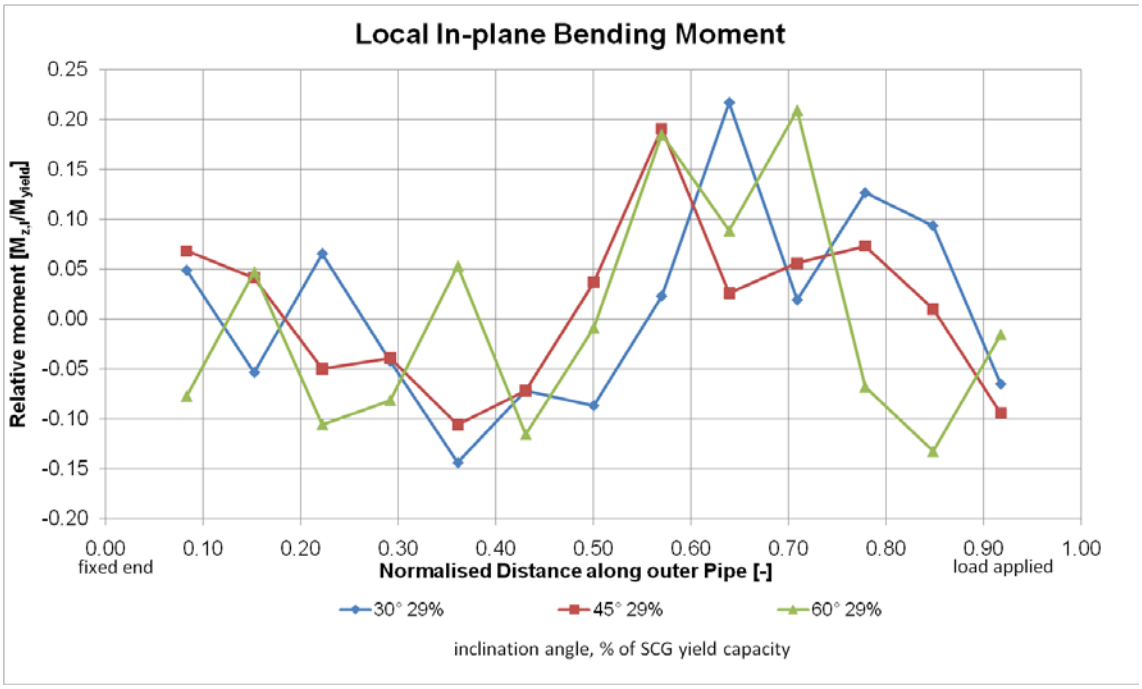

Figure 6.10: Phase 1, Local moment $M_{z,l}$ along the SCG for different inclination angles

The maximum local moment did not change for inclination angles between 30° and 60°, as shown in Figure 6.11.

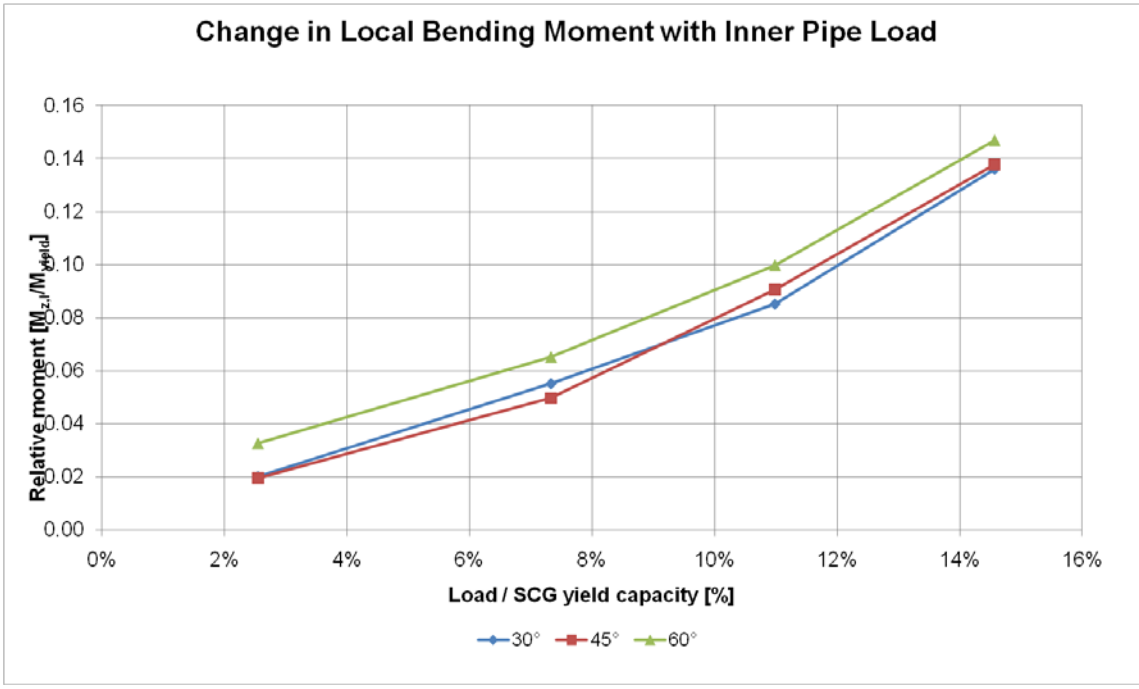

Figure 6.11: Phase 2, Increase in local moment along the SCG for different inclination angles

Table 6-4 graph values of Figure 6.11

Load	3%	7%	11%	15%
30°	0.020	0.055	0.085	0.136
45°	0.020	0.050	0.091	0.138
60°	0.033	0.065	0.100	0.147

Some evidence is given by Figure 6.12 and Figure 6.13 that the local bending moment for the same applied load (7 %) increases with increasing radial gap. The first plots the change in local bending moment with increasing load for all four test setups. Theses relation between load and local moment seems to linear, whereas the proportionality of the interradial gap to the moment has been determined as following:

The relation between load and response remains the same as for the differential increase in tension, just that a function of the interradial gap has been added in equation (6.5):

$$\frac{dM_{SCG}}{dT_{CT}} \cong c_{BM} * f(g_r) \tag{6.5}$$

where

dM_{SCG} is the measured increase in maximum local moment in % of M_{yield}

dT_{CT} is the difference in load applied to the CT in % of F_{yield}

c_{BM} is the slope of the linearised graphs for each phase

$f(g_r)$ is a function of the interradial gap

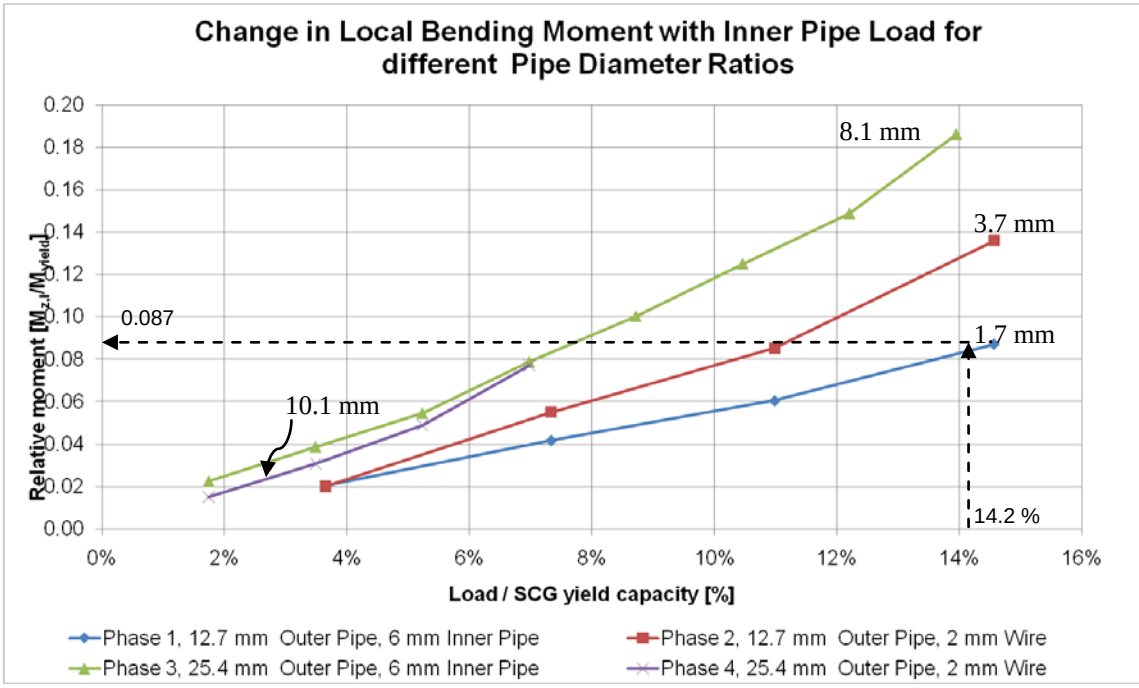

Figure 6.12: Change in local bending moment with change in inner pipe load for different interradial gaps as stated in mm, all bent 30°

Table 6-5: graph values of Figure 6.12

Load	2%	3%	4%	5%	7%	9%	10%	11%	12%	14%	15%
Phase 1			0.020		0.042			0.061			0.087
Phase 2			0.020		0.055			0.085			0.136
Phase 3	0.022	0.039		0.055	0.079	0.100	0.125				
Phase 4	0.015	0.031		0.049	0.077				0.149	0.186	

The factor c_{BM} can be read from Table 6-6. The interradial gap divided by the outer diameter of the inner pipe gives a normalised value which correlates the magnitude of the gap with the scale of the pipe.

Table 6-6: Parameters for local bending moment calculation

PHASE		Outer Pipe	Inner Pipe / Wire	Interradial Gap g_r	dM_{SCG} / dT_{CT}	g_r / OD_{CT}	$(dM_{SCG} / dT_{CT}) / (g_r / OD_{CT})^{1/4}$
No.	**Name**	ID [mm]	OD [mm]	[mm]	c_{LM} [-]	[-]	[-]
1	12.7 mm Outer Pipe, 6 mm Inner Pipe	9.4	6	1.7	0.59	0.28	**0.814**
2	12.7 mm Outer Pipe, 2 mm Wire	9.4	2	3.7	0.96	1.85	**0.820**
3	25.4 mm Outer Pipe, 6 mm Inner Pipe	22.2	6	8.1	0.88	1.35	**0.810**
4	25.4 mm Outer Pipe, 2 mm Wire	22.2	2	10.1	0.95	5.05	**0.621**

For the interradial gaps in phase 1 to 3, this ratio g_r/OD_{CT} to the power of 0.25 has been determined to be proportional to the differential load transfer between the two pipes. The diameter ratio in phase 4, where the interradial gap is 5 times larger than the diameter of the inner pipe, seems to be out of the valid range of this approach. Equation (6.5) can therefore be rewritten more specifically to:

$$\frac{dM_{SCG}}{dT_{CT}} \cong 0.81 * \sqrt[4]{\frac{g_r}{OD_{CT}}} \qquad (6.6)$$

$$\text{for } \left\{0.28 \leq \frac{g_r}{OD_{CT}} \leq 1.83\right\}$$

where

OD_{CT} is the outer diameter of the inner pipe

g_r is the interradial gap between the two pipes

If the prototype system gets for example loaded with 200 kN, the expected maximum local bending moment can be estimated as follows:

g_r = 19.03 mm; OD_{CT} = 60.3 mm

$$\frac{dM_{SCG}}{dT_{CT}} \cong 0.81 * \sqrt[4]{\frac{19.03}{60.3}} = 0.61$$

since the ratio g_r / OD_{CT} = 0.31 is closest to that in phase 1 (0.28), and the loading of 200 kN corresponds to 14.2 %, the maximum local bending is estimated as

$$\frac{M_{Z,l}}{M_{yield}} \cong 0.61 * 0.142 = 0.087$$

This can be checked by the graphs in Figure 6.12, where the line for phase 1 gets slightly exceeded since the g_r / OD_{CT}-ratio in this case is a little higher. The local moment ratio read from the vertical axis matches the one obtained in the previous calculation, which shows that equation (6.6) is valid for the stated range.

The results in Figure 6.13 confirm the above statement, and show also that the phase 4 results (g_r = 10.1 mm) do not match the trend of increase in local bending moment with increasing radial gap.

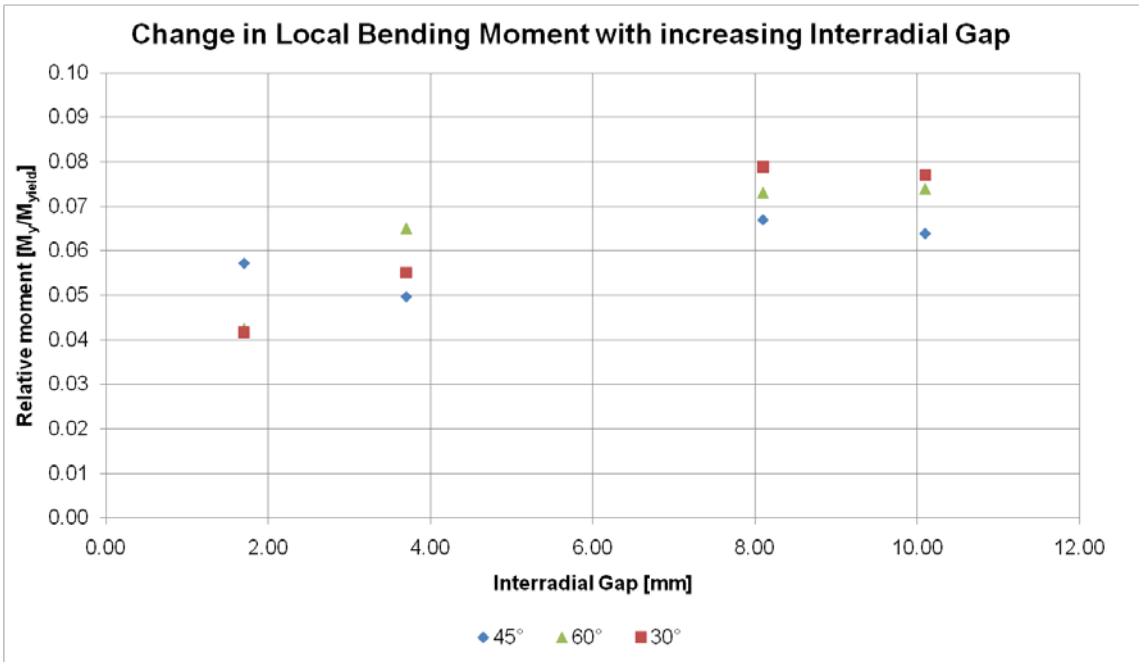

Figure 6.13: Change in local bending moment for increasing diameter ratio for all investigated inclination angles

6.5 Global out-of-plane Bending Moment M_y

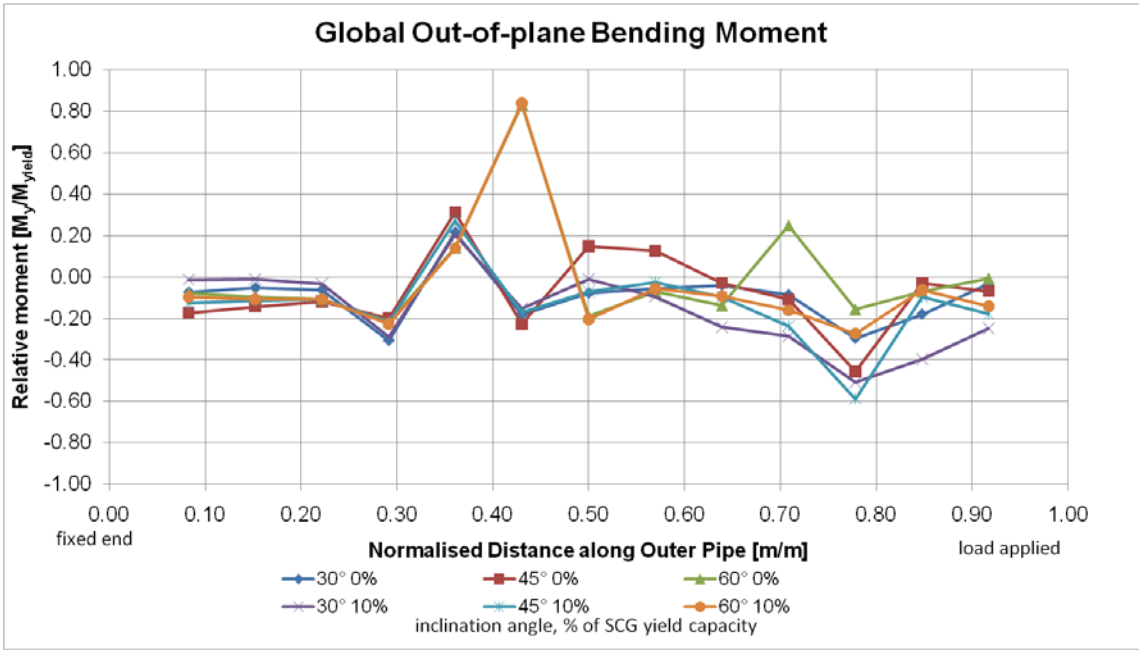

Figure 6.14: Phase 3, Global out-of-plane bending moment M_y along the outer pipe for different inclination angles

The global moment M_y about the horizontal axis y is plot in Figure 6.14. The increase in moment with increase in load and inclination angle could imply, that the steeper the riser is bent, the more it tends to move out-of-plane, but that would have to be checked by a model test which allows 3D movement of the guide pipe. Since the setup is designed to measure in-plane interactions, the out-of-plane bending moment is not the main focus of these tests. As described in section 6.7, M_y is not much influenced by the lifting, but rather by the upwards or downwards shifting of the inner pipe in the curved sections of the guide pipe.

6.6 Local out-of-plane Bending Moment $M_{y,l}$

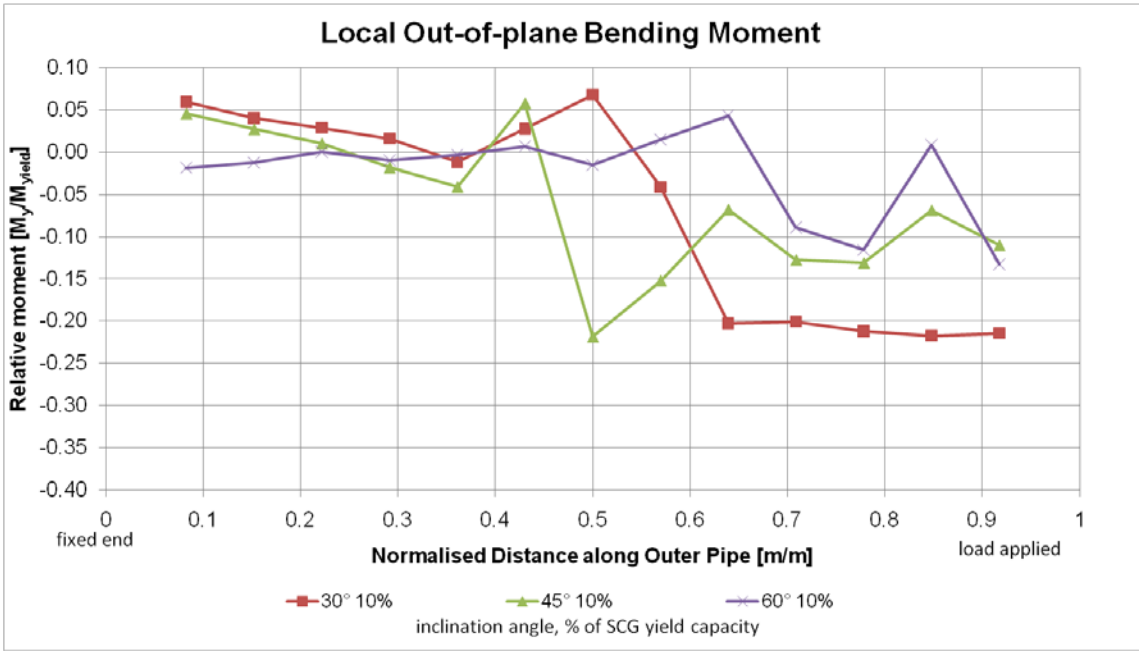

Figure 6.15: Phase 3, Local out-of plane bending moment for different inclination angles

The results contain also a local out-of-plane bending moment as it was requested by Schlumberger. A sample is given in Figure 6.15, where it can be seen that the out-of-plane bending occurs mainly in the lower- and middle section of the system. Eccentricity in loading may also influence this moment to a certain extent.

6.7 Lifting of Outer Pipe

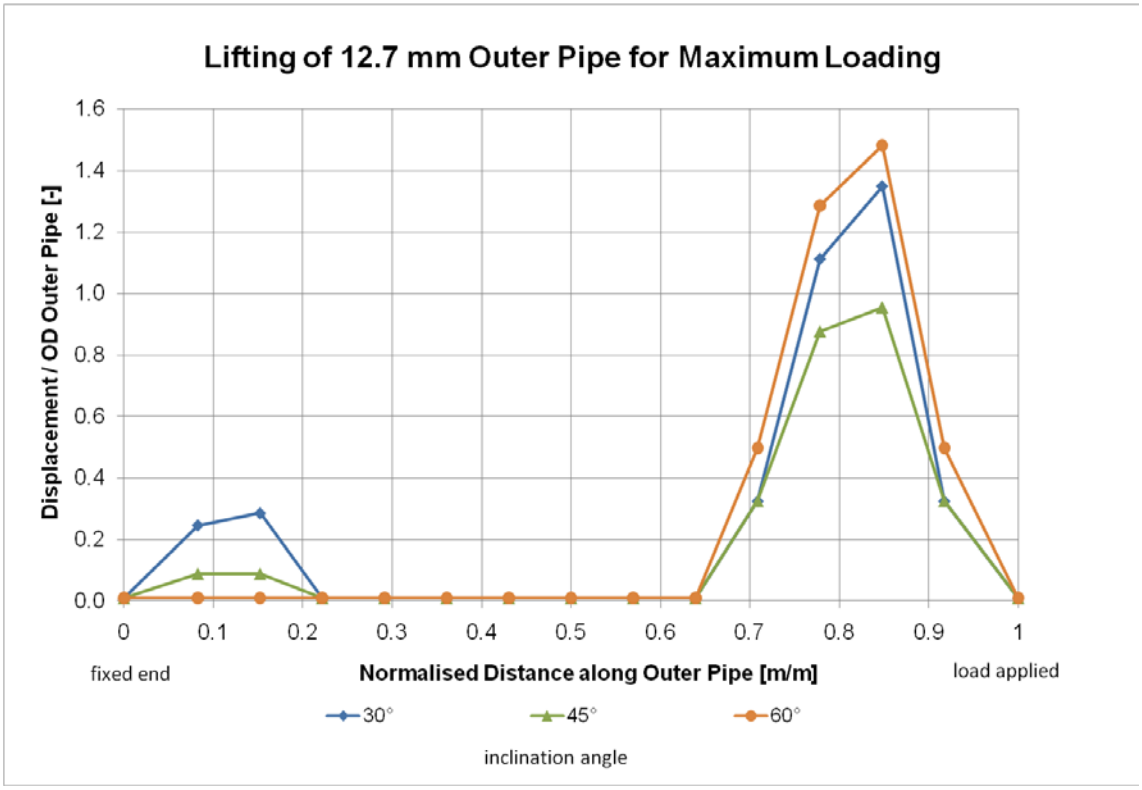

Figure 6.16: Phase 1, lifting of SCG for 29% loading

To what extent the bending moment M_y is caused by the lifting can be calculated as following: Assuming the shape of the lifted pipe as a circular segment, its radius for the 60° test and 29% loading is therefore 3.55 times the pipe length. Taking equation (6.3) and replacing the yield stress Y by ε*E (see equation (5.7)) and rearranging for it for strain, equation (6.7) is obtained. In this case an elongation of 0.03 % has been calculated. The M_y-equivalent strain for the same test at the lifted section is 0.318 %, which shows that for the maximum loading around 10 % of the M_y are resulting from the lifting.

$$\varepsilon = \frac{OD}{2R_{CV}} \tag{6.7}$$

6.8 Residual Bending

Referring to the Schlumberger Report 'Properties of Coiled Tubing, Figure 4.5' (2008) the minimum radius of curvature for a 4-½" pipe is 32 m for a maximum stress of 434 MPa (67% SMYS). With equation (6.3) the minimum radius of curvature is calculated to 25.3 m for the pipe's elastic limit of 550 MPa.

Residual bending of the model-SCG was already observed after conducting the 30° test. In order to quantify the curvature, the strain ε in equation (6.7) is replaced by the strain ε_{Mz} of the pure bending moment about z (see section 4.4.1). The resulting radii of curvature are shown in Table 6-7:

Table 6-7: Phase 1, bending radii, residual bending radii and curvature for the scaled model pipe

Phase	OD Outer Pipe [mm]	Test	Radius R_{CV} [m]	Curvature [m^{-1}]
1	12.7	30°	2	0.5
1	12.7	Residual R_{CV} after 30° bend	4.03	0.25
1	12.7	45°	1.22	0.82
1	12.7	Residual R_{CV} after 45° bend	1.48	0.68
1 and 2	12.7	60°	0.8	1.25
1 and 2	12.7	Residual R_{CV} after 60° bend	1.06	0.94
2	12.7	45°	0.96	1.04
2	12.7	Residual R_{CV} after 45° bend	1.03	0.97
2	12.7	30°	1.08	0.93
3 and 4	25.4	30°	1.92	0.52
3 and 4	25.4	Residual R_{CV} after 30° bend	3.06	0.33
3 and 4	25.4	45°	1.49	0.67
3 and 4	25.4	Residual R_{CV} after 45° bend	2.24	0.45
3 and 4	25.4	60°	0.9	1.11
3 and 4	25.4	Residual R_{CV} after 60° bend	1.19	0.84

Noticeable is that the 25.4 mm pipe, with a much higher flexural rigidity compared to the 12.7 mm pipe, has a significantly higher residual bending after each test. That is in agreement with the higher global bending moment for phase 3 and 4.

The whole set of results obtained from the physical model test can be found in Appendix A. Appendix B intends to show the influence of the bending angle by comparing the graphs for each phase separately. The effect of interradial gap is highlighted in Appendix C, where the results for the same bending angles of all four phases are compared.

7 Numerical Results

Numerical calculations using the FE software ABAQUS have been made to compare and to validate the results of the physical model test. In order to limit the degrees of freedom and hence calculation time to an acceptable order, a purely 2D model has been used.

The outer- and the inner were modelled with beam elements, while the contact between the two pipes has been simulated by sliding contact elements (Schlumberger Report 'Analytical Investigation of Pipe in Pipe interaction', 2009). All numerical simulations where conducted with acting friction, and the general steel to steel friction coefficient of 0.3 has been chosen. The type of elements and their number is given Table 7-1, whereas a complete input file sample is provided in Appendix D.

Table 7-1: Finite element type and number used

NUMERICAL CALCULATION	Outer Pipe	Inner Pipe / Wire	Contact Element
Type	B31	B31	ITT31
No. of Elements	575	575	575

As previously mentioned, ABAQUS tends to form different shapes for the same displacement and boundary conditions. This not controllable phenomena is shown in Figure 7.1, where for four different phases in 30°, three different shapes have been formed. For higher bending angles the difference is not that significant, since the x/y displacement ratio and hence the bend out is lower as it is for 30°. The shape divergence at the right end of the shapes in Figure 7.1 is due to inaccuracies in normalising, with a negligible effect on the result.

To straighten both pipes and to stabilise the calculation, a pre tension of 100 N for phase 1 and 3, and 10 N for phase 2 and 4 have been applied before the lower end was shifted into position.

The boundary condition were the same as in the model test: at one end both pipes fully fixed, and at the other the outer pipe fixed whereas the inner pipe has one degree of freedom in x-direction.

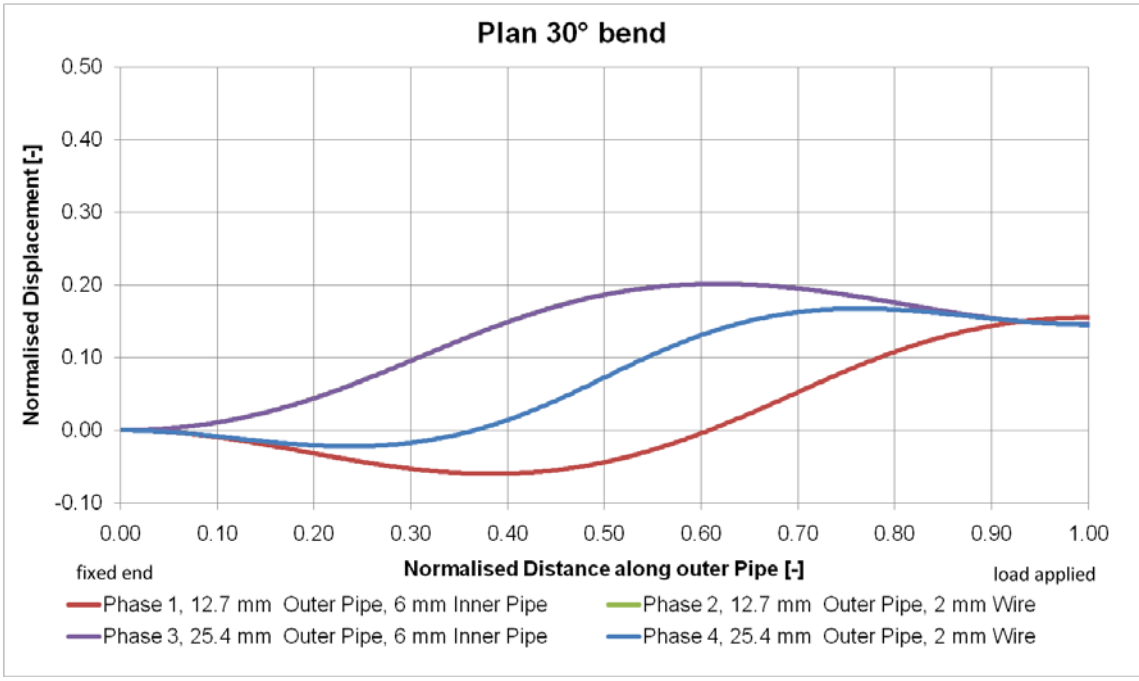

Figure 7.1: Plan view of 30° bend numerical model for all phases

7.1 Axial Force

The axial force progression along the outer pipe depends on the bending angle, as can be seen in Figure 7.2; a steeper bent guide absorbs more axial force than a less bent one does.

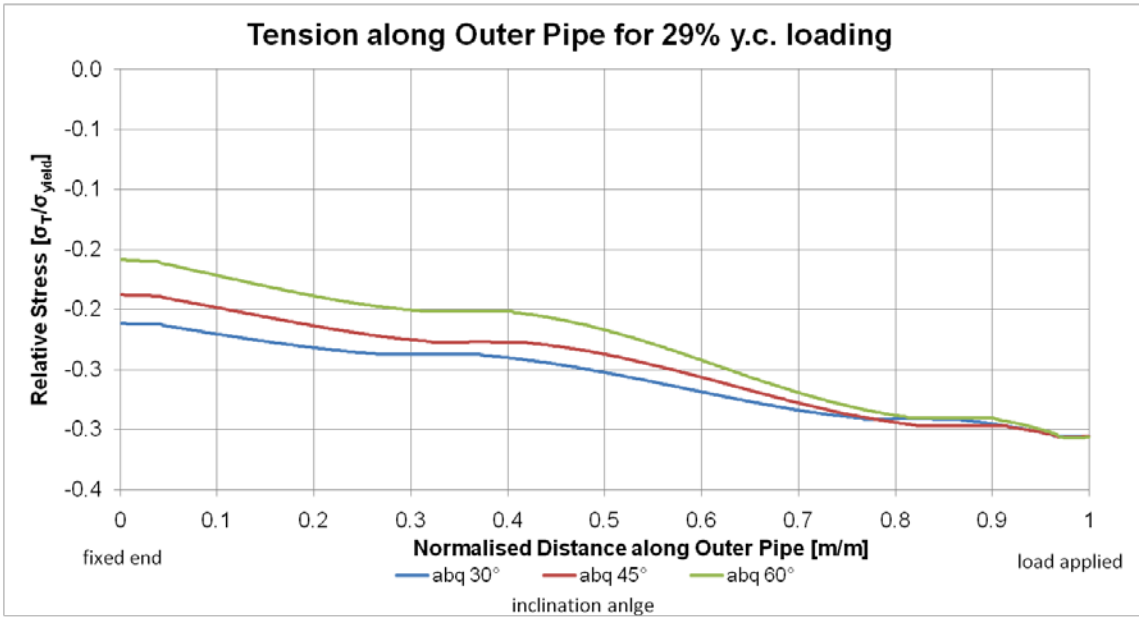

Figure 7.2: Phase 1, numerical tension along outer pipe for different inclination angles

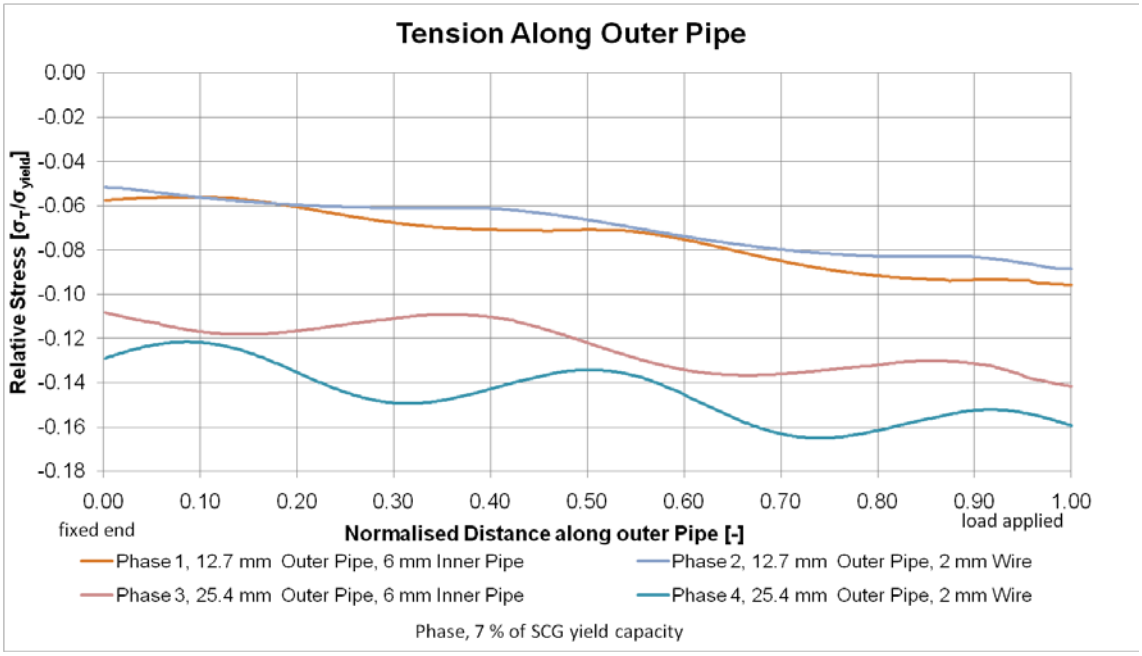

Figure 7.3: Numerical tension along outer pipe for all phases 60° bend

Interesting is the curvy evolution of axial force in Figure 7.3 for phase 3 and 4. That shows similarities to the peaks in tension observed in the model test result, just that the numerical plots are smoother as those displaying measured results.

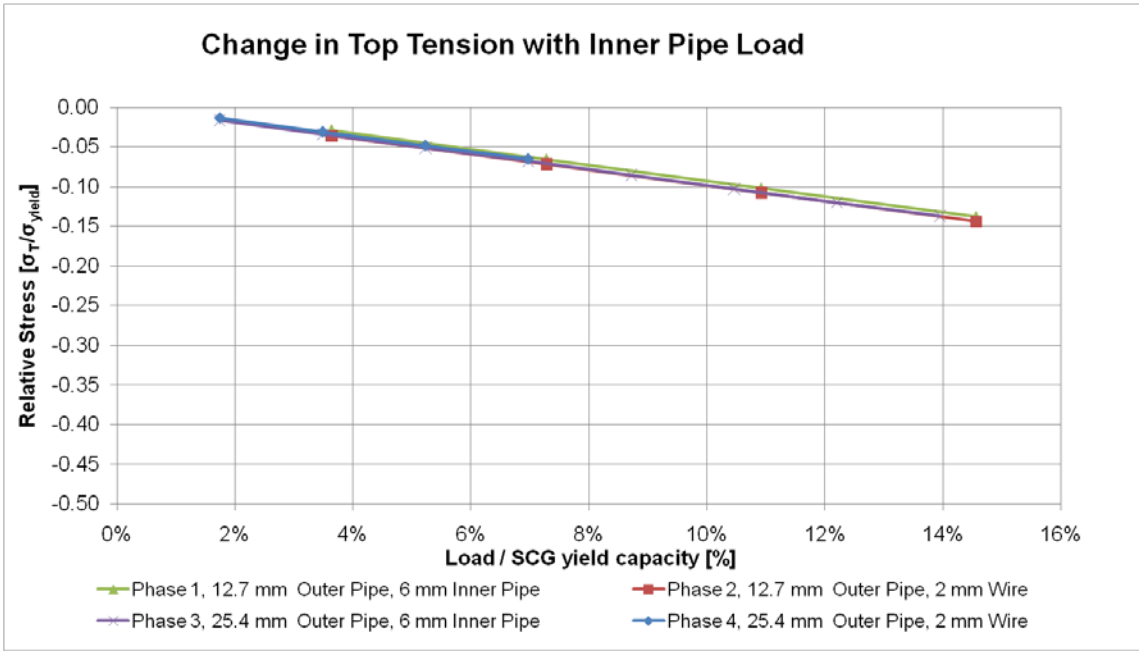

Figure 7.4: Numerical change in top tension with increasing load and different diameter ratios all 45° bend

Table 7-2: graph values of Figure 7.4

Load	2%	3%	4%	5%	7%	9%	10%	11%	12%	14%	15%
Phase 1			-0.029		-0.066			-0.102			-0.138
Phase 2			-0.036		-0.072			-0.108			-0.144
Phase 3	-0.017	-0.034		-0.051	-0.068						
Phase 4	-0.014	-0.031		-0.048	-0.065	-0.085	-0.102		-0.120	-0.137	

The claim that the tension in the outer pipe does not change for different diameter ratios is confirmed by Figure 7.4.

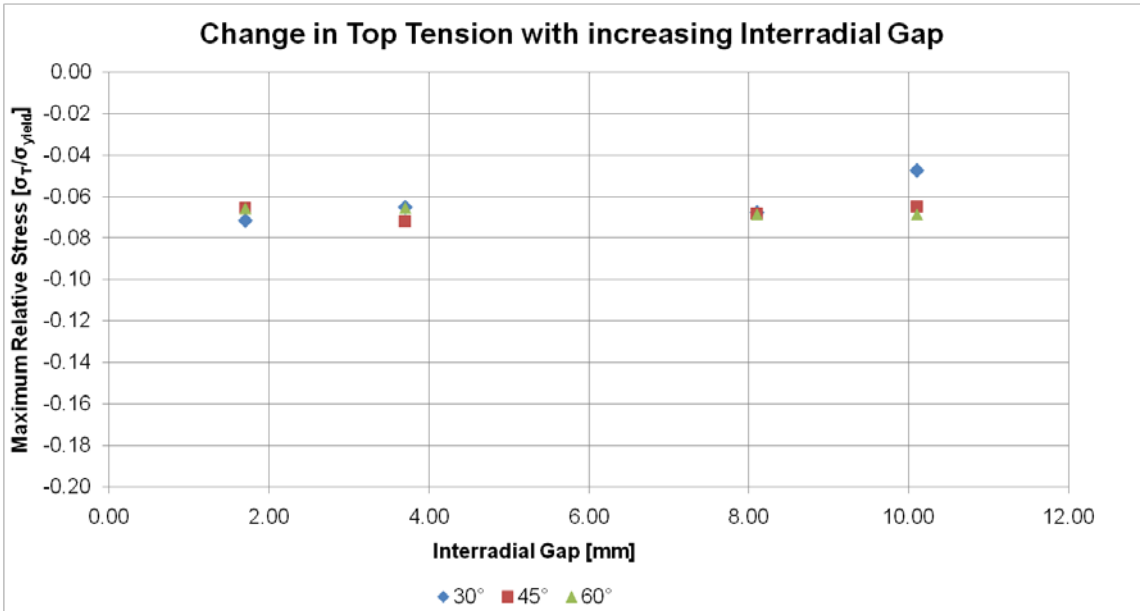

Figure 7.5: Numerical change in top tension with increasing interradial gap for all investigated bending angles and 7 % y.c. loading of the respective outer pipe

The data in Figure 7.5 show a high consistency in the numerical calculation for axial force, as the top tension for each bending angle is almost the same for the respective interradial gap.

The same approach as for the physical test results can be made for the numerical results to calculate the tension response for a specific load. Equation (7.1) indicates a smaller numerical increase in tension as it was elaborated with the results obtained by the physical model test.

$$\left(\frac{dT_{SCG}}{dT_{CT}}\right)_{num} \cong -0.995 \tag{7.1}$$

The equation can again be checked with Figure 7.5: 0.07 x 0.995 = 0.07 $\sigma_T/\ \sigma_{yield}$ is the same as the average of the results displayed.

7.2 Global Bending Moment M_z

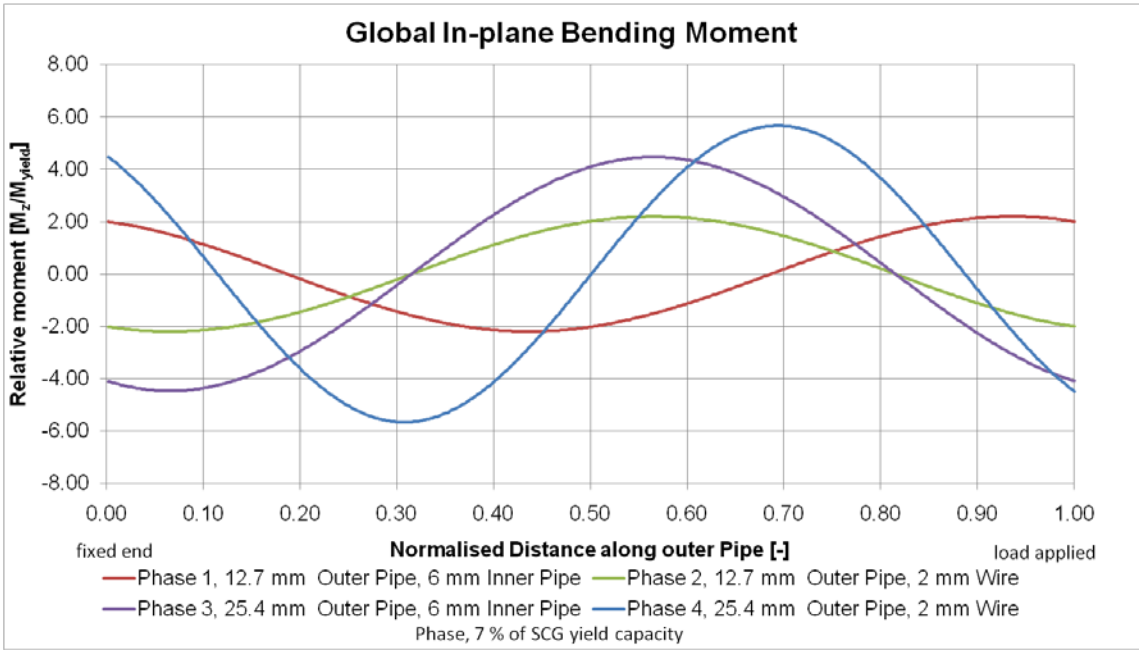

Figure 7.6: Numerical global in-plane bending moment M_z for different diameter ratios all 30° bend

Figure 7.6 plots the global bending moment of the same test whose shapes are given in Figure 7.1. That is to illustrate that depending on the section where the pipe forms the bend out, the global moment can be symmetrical about the x-axis (compare phase 1 and 2). As already discussed in chapter 6.3, the global bending moment does not increase with increasing load.

7.3 Local Bending Moment $M_{z,l}$

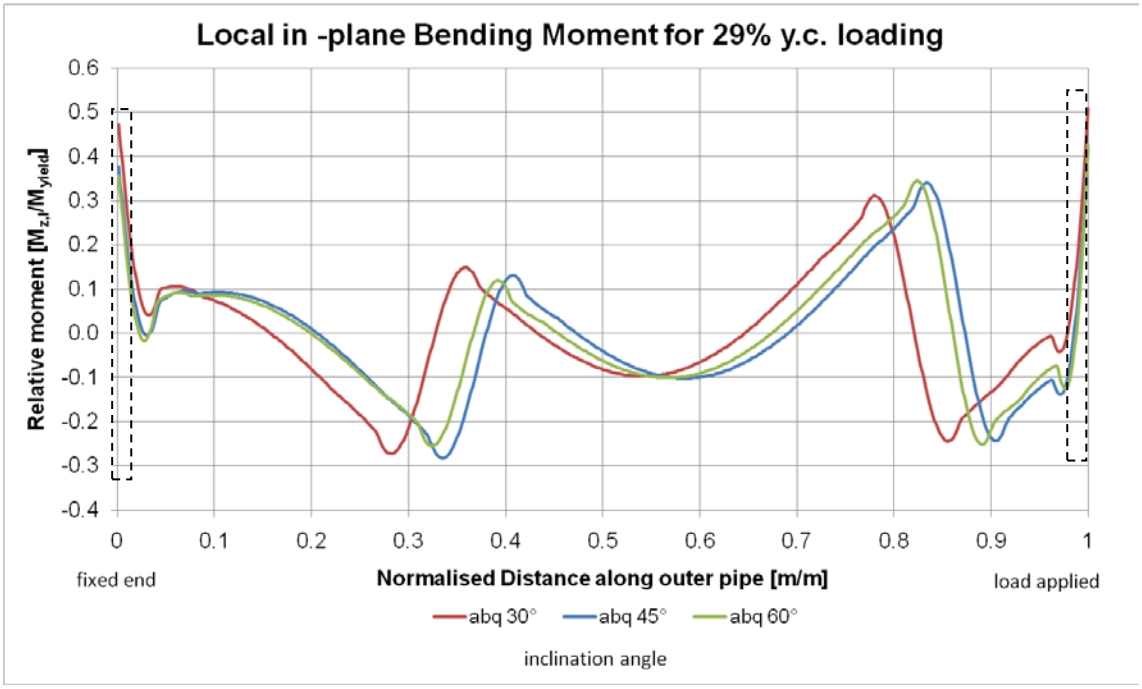

Figure 7.7: Phase 1, numerical local moment $M_{Z,l}$ along the SCG for different inclination angles

The local bending moment $M_{z,l}$ is similar for different bending angles as shown in Figure 7.7. Ignoring the most extreme readings, it can be seen that the peak of the 30° and 45° curve shifts rightwards, analogous but though opposite in direction as it was observed in the model test. This trend seems to be consistent with the location where the SCG's overlength bends out, but might not be of great relevance. Numerically, a split in the maximum local moment for 60° cannot be observed, as it was the case in the model test results.

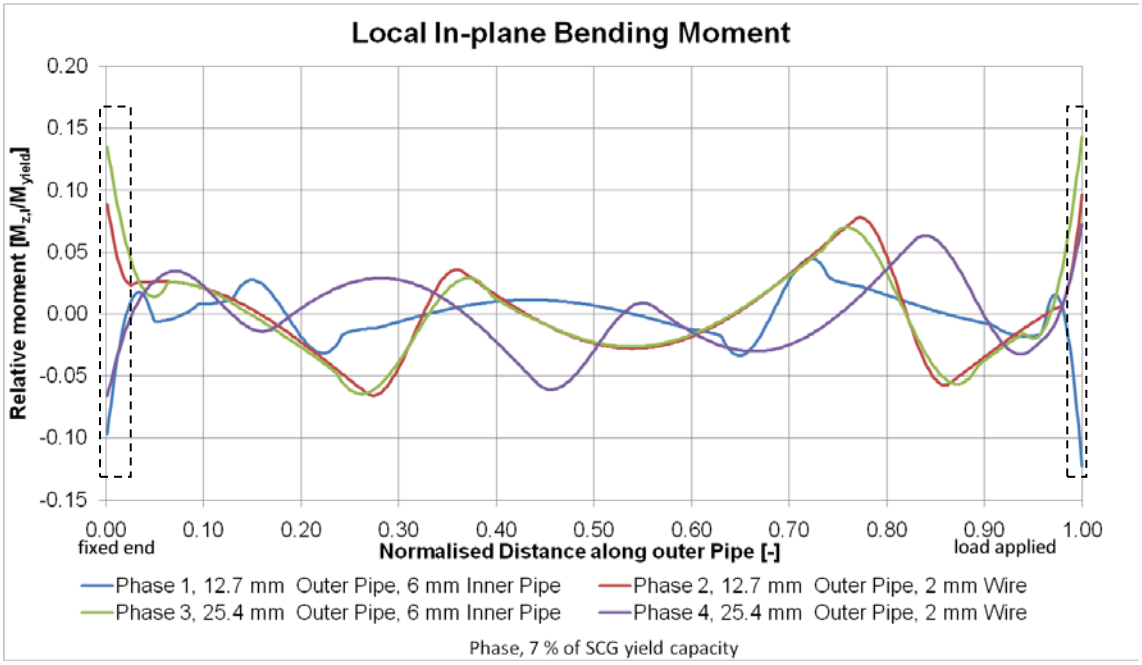

Figure 7.8: Numerical in-plane bending moment

The local bending moment graphs in Figure 7.8 show that the magnitude of local bending moment is different for each phase. The most extreme left and right results are considered as end effect and hence neglected.

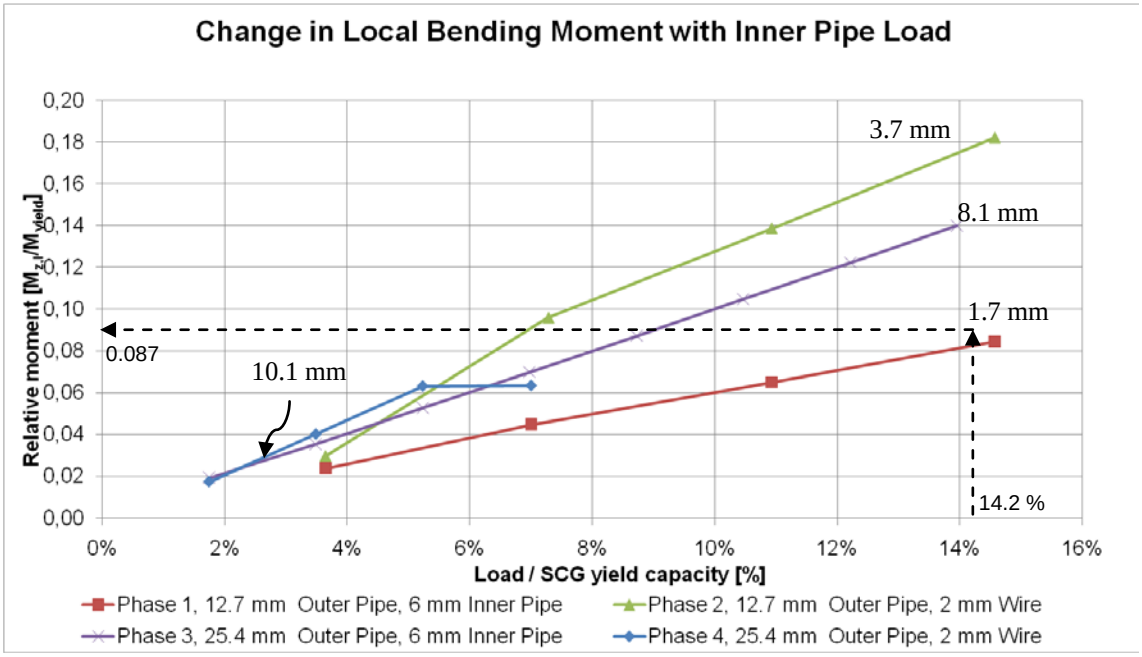

Figure 7.9: Numerical change in numerical local bending moment with change in inner pipe load for different interradial gaps as stated in mm, all bent 30°

Table 7-3: graph values of Figure 7.9

Load	2%	3%	4%	5%	7%	9%	10%	11%	12%	14%	15%
Phase 1			0.021		0.073			0.112			0.151
Phase 2			0.055		0.111			0.169			0.229
Phase 3	0.021	0.041		0.060	0.080	0.099	0.119		0.139	0.159	
Phase 4	0.018	0.041		0.064	0.088						

The same example as has been elaborated in section 6.4 on page 62 can also be checked by the numerical results. Using Figure 7.9, the same result can be obtained as it was in the previous exercise.

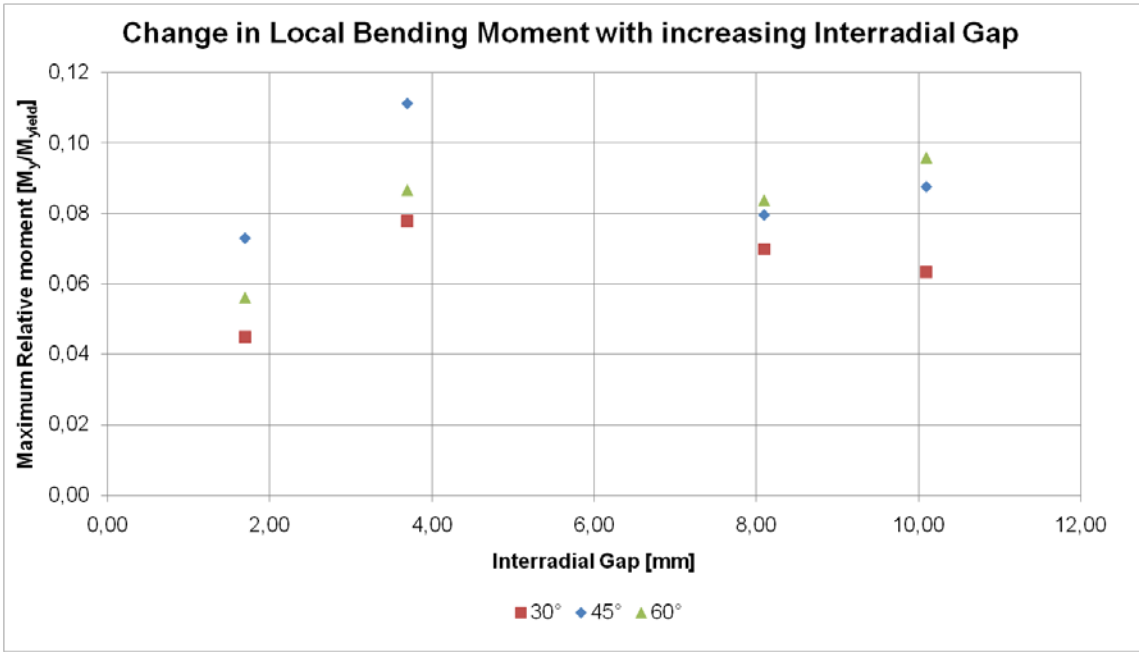

Figure 7.10: Numerical change in local bending moment with increasing interradial gap

Surprisingly, the numerical results are not as consistent as the test results are. Figure 7.10 shows relatively high discrepancy between results of the same interradial gap but different inclination angles. That doesn't allow the same approach to define a similar curve fitting equation as it was done in section 6.4. It clearly shows that phases where a wire was used (2 and 4), are leading to higher local bending moments regardless of their interradial gap.

All numerical results can be found in Appendix D,, whereas the results of how the interradial gap affects the numerical model are given in Appendix E.

Chapter 8 intends to compare the numerical- with the physical results and to highlight some of the discovered differences.

8 Comparison of Test- and Numerical Results

In the following section, the results of one particular physical- and numerical model test are compared and commented, but most of the discussed differences apply to all twelve conducted tests, which results are provided in Appendix F.

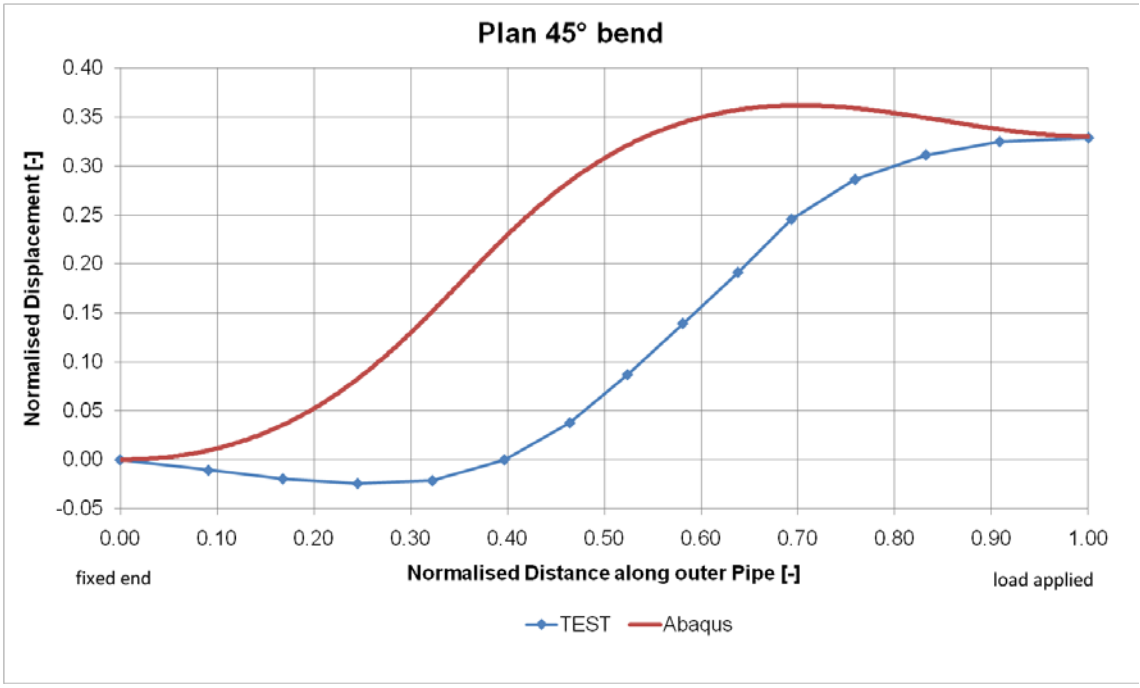

Figure 8.1: Phase 3, shape comparison between the physical and numerical model for 45° inclination angle

The shapes of the physical- and numerical model are displayed in Figure 8.1: Though not as evident as for the 30° position, it can clearly be seen that the pipe bends out at different locations for each model, which as a consequence will affect their comparability.

8.1 Axial Force

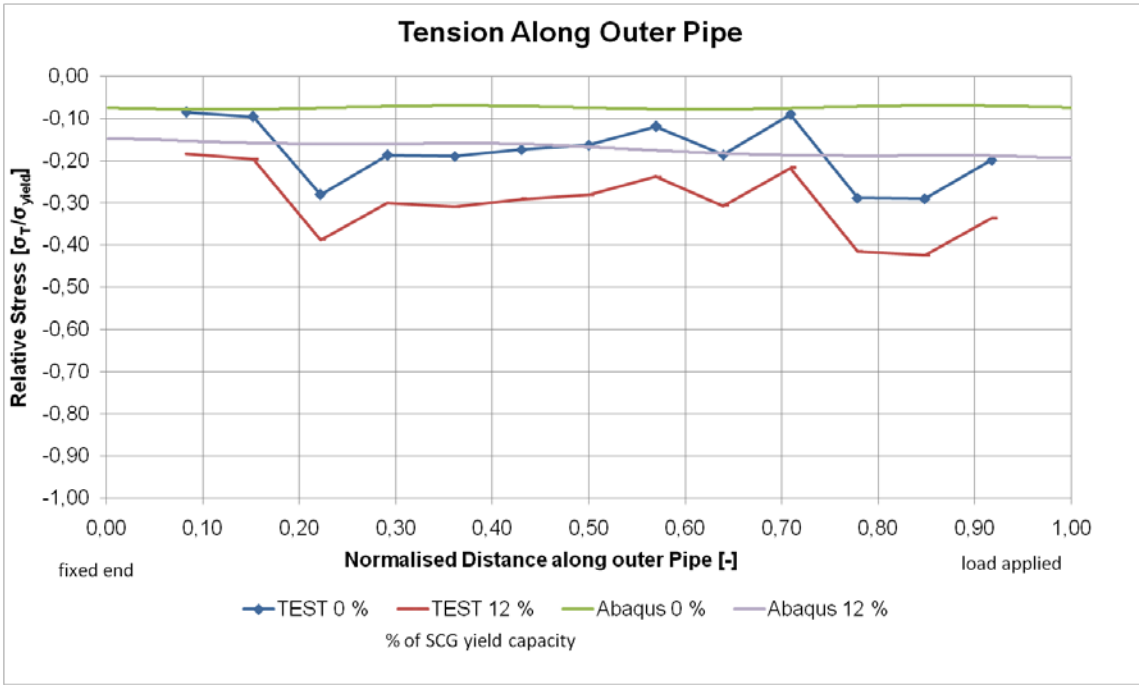

Figure 8.2: Phase 3, comparison of global moment for 45° bend and 12% y.c. loading

The measured axial compression along the outer pipe is generally higher than it was calculated numerically, as it was already discovered when comparing the factor of c_{TT} =1.3 in equation (6.2) with the factor of 1.0 obtained numerically.

It is not fully understood what causes this local increase in compression, but it could be due to locally high contact forces between the inner and outer pipe in the vicinity of the bends.

As can be seen in Figure 8.3, the maximum axial force in the outer pipe increases in both - the model test and the numerical calculation - at a comparable rate with increasing load. The divergence in magnitude is consistent with the other test results, and shows that ABAQUS tends to underestimate the load transfer in terms of tension.

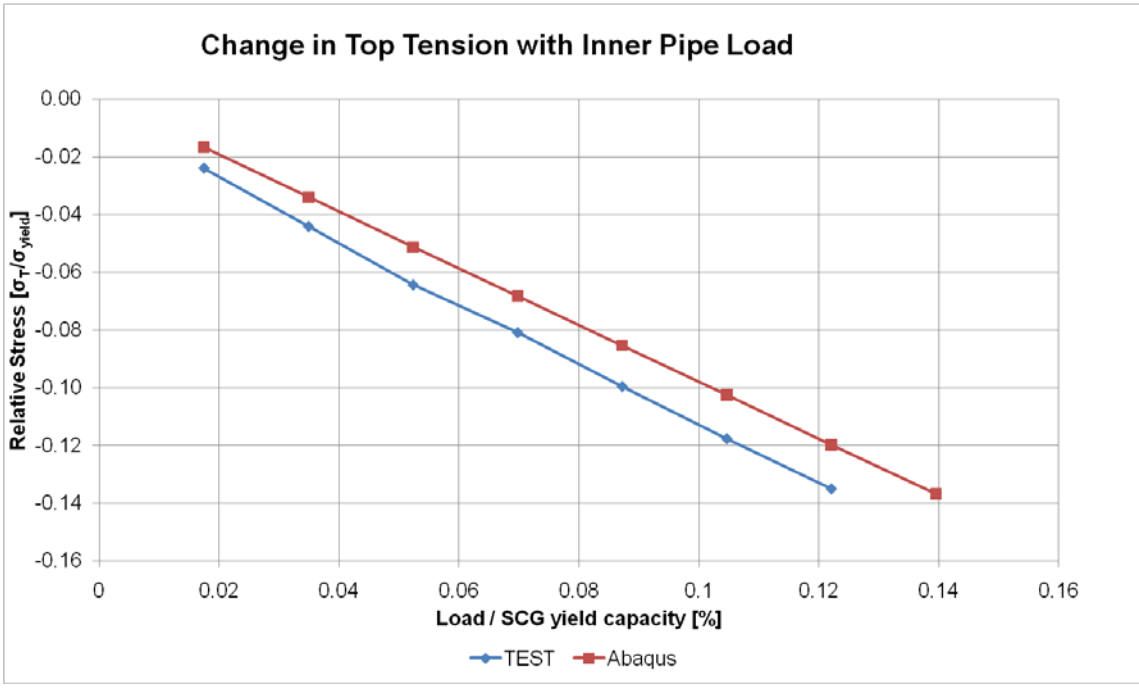

Figure 8.3 Phase 3, comparison of increase in top tension with increasing load between the physical- and numerical model for 45° bend

Table 8-1: graph values of Figure 8.3

Load	2%	3%	5%	7%	9%	10%	12%	14%
abq	-0.017	-0.034	-0.051	-0.068	-0.085	-0.102	-0.120	-0.137
test	-0.024	-0.044	-0.064	-0.081	-0.100	-0.118	-0.135	

8.2 Global Bending Moment M_z

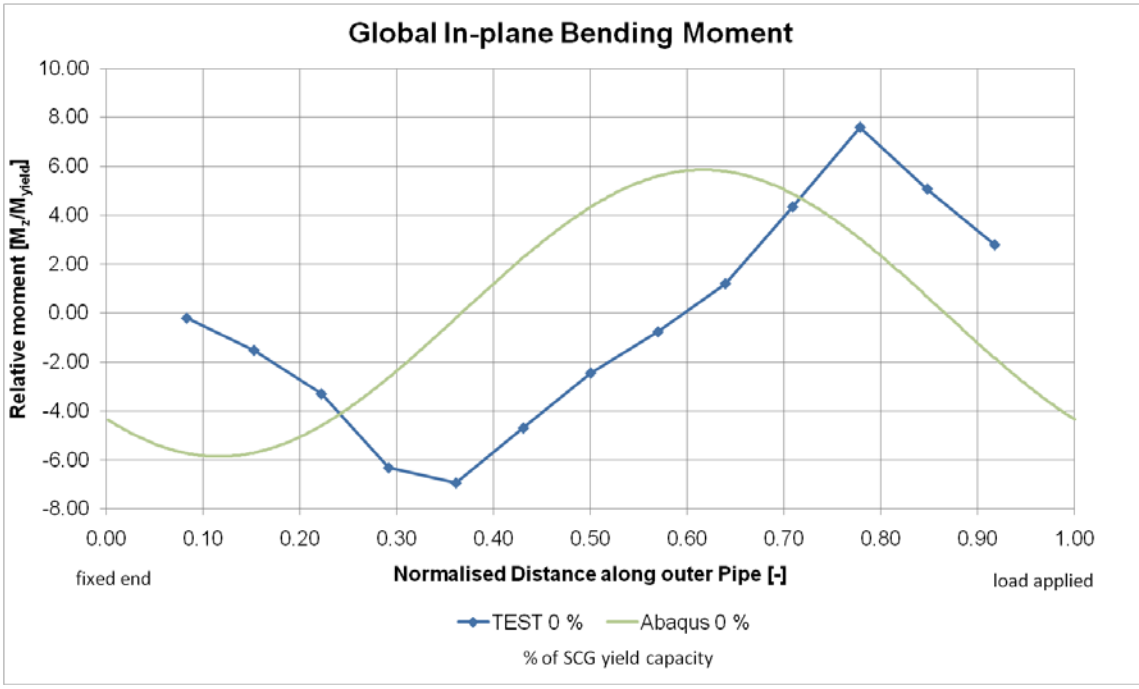

Figure 8.4: Phase 3, comparison of global in-plane moment for 45° bend

A comparison of the calculated global bending moment and the measured in the model test is given in Figure 8.4. It can be seen that the magnitude of both plots matches to a reasonable extent, although in this test the measured relative moment is higher than the calculated one. This is most probably due the smaller radius of curvature in the model test compared to the smooth shape formed numerically. The large difference evolution along the outer pipe is due to different bend outs (see Figure 5.2) and is consistent with the respective formed shape.

8.3 Local Bending Moment $M_{z,l}$

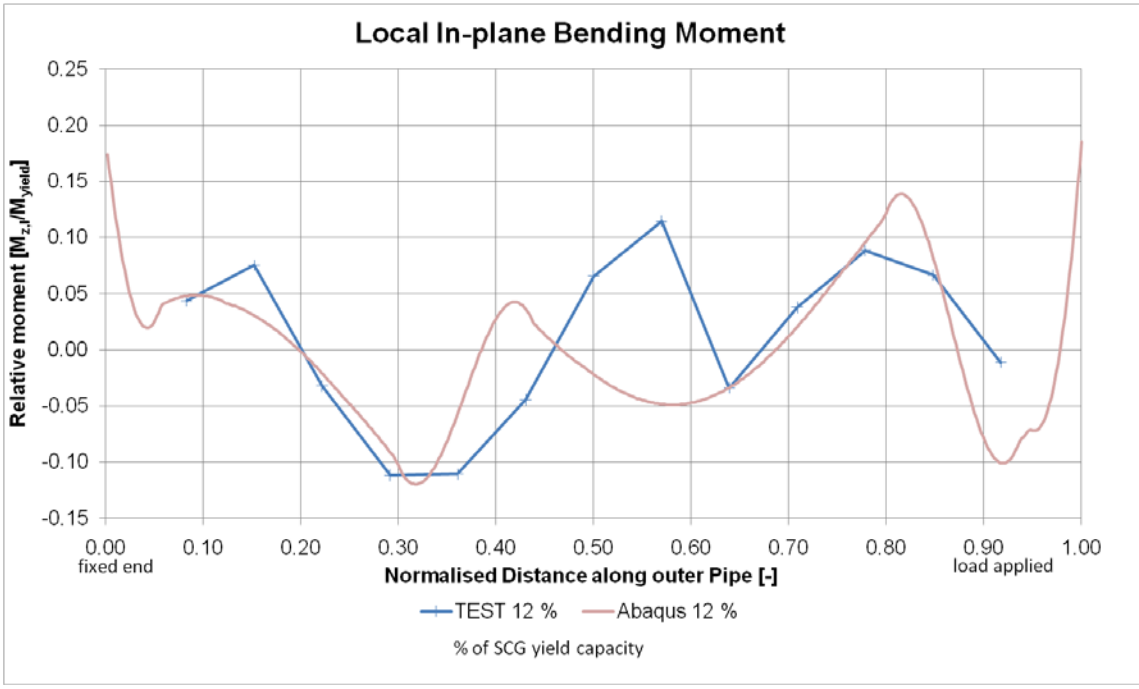

Figure 8.5: Phase 3, comparison of local in-plane bending moment for 45° bend and 12 % SMYS loading

For this case, the calculated local bending moment is partially in good accordance with the measured (Figure 8.5). In other tests the evolution along the pipe differs extensively, since it is very sensitive to how the shape is formed and how that affects the global bending moment. The magnitudes of local bending moments, however, are in all conducted tests reasonably close.

The maximum local bending moment increases at a faster rate in ABAQUS than in the model test as shown in Figure 8.6. This trend can be observed throughout the results.

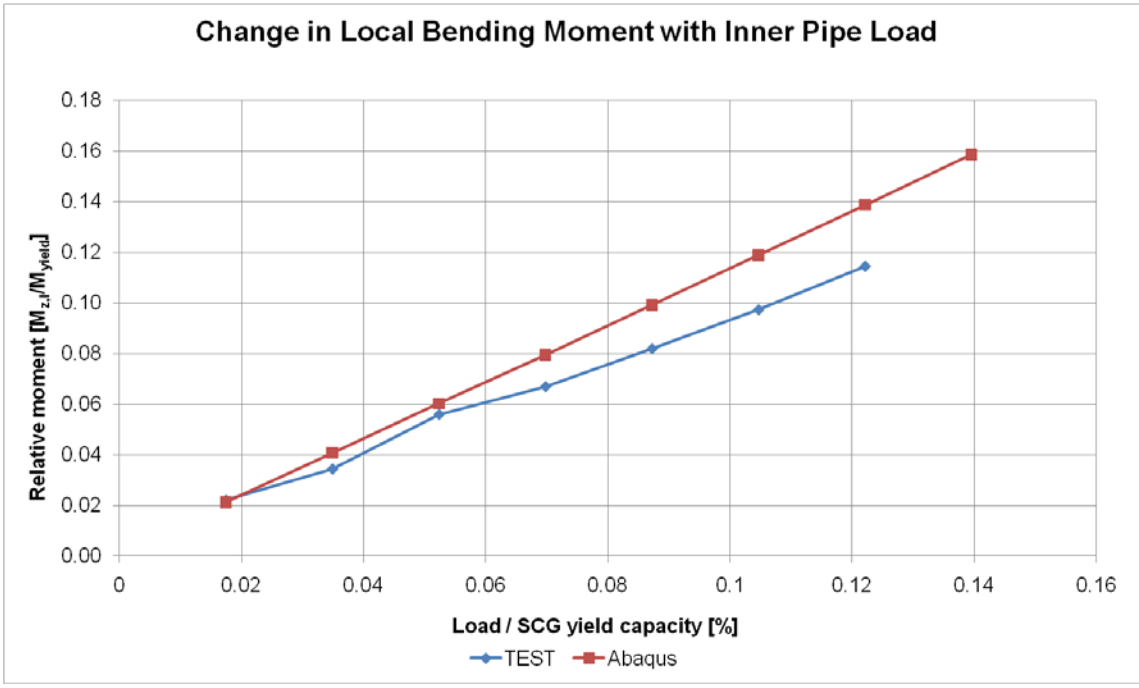

Figure 8.6: Phase 3, comparison change local bending moment $M_{z.l}$ with increasing load between the physical- and numerical model for 45° bend

Table 8-2: graph values of Figure 8.6

Load	2%	3%	5%	7%	9%	10%	12%	14%
abq	0.021	0.041	0.060	0.080	0.099	0.119	0.139	0.159
test	0.022	0.034	0.056	0.067	0.082	0.097	0.115	

9 Conclusion

The results of the conducted work on the present project lead to the conclusion, that load transfer due to geometric interaction in the pipe in pipe system, can be quantified as follows:

Peak compression in the guide can reach up to 1.3 times the applied load. It is independent of the interradial gap between the inner- and outer pipe, and does not change for inclination angles between 30° and 60° in the S-shape section.

Local bending moment in the outer pipe is proportional to the applied load and the interradial gap. It can be estimated by equation (6.6) for the stated range of gap to diameter ratio. The magnitude of local bending moment is constant for inclination angles between 30° and 60°.

Numerical calculations tend to underestimate the peak compression in the guide, while the maximum local bending moment was found to be higher in the numerical calculations than it was measured in the model tests. The most severe limitation by comparing physical model test- and numerical results is the shape difference, which cannot be influenced in both cases.

The resulting stress in the outer pipe due to geometric interactions can for the applied load of up to 400 kN be considered to be in a safe range for the state of the art design, and hence no local buckling is expected to occur.

The reader is nevertheless encouraged to act conservatively and to apply safety factors according to ISO 13628-7:2005 or equivalent.

10 Limitations and Further Research

It was pleasant that the investigation could be undertaken within the agreed timeframe. Extensive discussions have been made about the test setup, until it was decided that a horizontal pipe alignment is most suitable for the purpose of the investigation, and additionally it accelerates the process and hence the requested results can be delivered earlier.

A horizontal test setup, however, is suitable for in plane measurements and an installed pipe-in-pipe system. Significant force measurements in the guide during the inserting or pulling out of the inner pipe can only be undertaken on a vertical setup, since there gravity plays an important role. The same applies to the out of plane bending, which can only be meaningful quantified in a vertical setup.

To replace the inner pipe with a wire was the only possibility to increase the interradial gap in respect to the 12.7 mm outer pipe. The results have shown though that a wire transfers less friction force than a rigid pipe does, which consequently affected the consistency of the axial load transfer results compared to the two pipe-in-pipe systems.

Although the strain gauge spacing along the pipe was narrow compared to its length, the possibility of missing out some local maximum force cannot be excluded. But since the measured peaks in local bending and relative tension are matching the numerical results within an acceptable range, it can be assumed that no significant peak forces were missed.

Further experiments could repeat a similar test in a vertical setup, which would allow to measure bending in both planes, and make it possible to detect a helical shape when the offset is small. The setup should be designed in a way that the inner pipe is loaded by a

calibrated hydraulic pump, which would make the loading process and hence measurements more efficient. Desirably, investigations of the interradial gap should be conducted with exclusively pipe-in-pipe systems, since it has been noted that responses from a loaded wire implement small differences. Although the installing of Coiled Tubing is not expected to cause any problems, it would be interesting to model it and to examine the influence of residual bending of both, the guide pipe and the CT, in combination with the SCG's inclination angle. Since the so far conducted physical- and numerical models were only in 2D, a vertical 3D physical experiment could be used to benchmark and to validate previous results.

References

Archer,J.S., Wall,C.G. (1986). *Petroleum Engineering, Principle and Practice.* London: Graham and Trotman.

Bai, Y. (2001). *Pipelines and Risers.* Stavangar: Elsevier.

Brown, R.J., Palmer, A.C. (2007). *Developing Innovative Deep Water Pipelines Construction Techniques with Physical Models.* Transactions, American Society of Mechanical Engineers 129 56-60.

Chakrabarti, S. (2005). *Handbook of Offshore Engineering.* Oxford: Elsevier.

Daly, Roland, Bell, Mike. (2002). Reeling Strain Analysis of a Dynamic Pipe in Pipe Riser . *Offshore Technology Conference* . Houston.

Ishida,K., Otomo,K., Hirayama,H., Okamoto,N., Nishigaki,M., Ozaki,M. (2001). An FPSO with Surface Wells and Workover System in Deepwater. *Offshore Technology Conference* . Houston.

Kuroiwa,T., Nishigaki,M., Okamoto,N., Hirayama,H., Ihara,M., Ishida,K., Otomo,K. (2002). Interaction between Riser and Tubing in CVAR System. *International Conference on Ocean, Offshore and Arctic Engineering.* Kitakyushu.

Luk, C.H.Y., Rakshit, T. (2009). Pipe-in-Pipe Substructure Modeling in Deepwater Riser Design Analysis. *International Conference on Ocean, Offshore and Arctic Engineering.* Honolulu.

Mitchell, R. (1997). Effects of Well Deviation on Helical Buckling. SPE.

Mitchell, R. (1986). Simple Friction Analysis of Helical Buckling of Tubing. SPE.

Mitchell, R. (2007). The Effect of Friction on Initial Buckling of Tubing and Flowlines . Miami: SPE.

Mungall,C., Haverty,K., Bhat,S., Andersen,D., Sarkar,I., Wu,J., Martensson,N. (2004).

Semisubmersible Based Dry Tree Platform with Compliant Vertical Access Risers. *Offshore Technology Conference.* Houston.

O Zeitoun,H., Tornes,K., Li,J., Wong,S., Brevet,R., Willcocks,J. (2009). Advanced Dynamic Stability Analysis. *International Conference on Ocean, Offshore and Arctic Engineering.* Honolulu.

Oceanide. (2007). *SCG System - Model Test Report.* La Seyne.

Okamoto,N., Ishida,K., Otomo,K., Hirayama,H., Nishigaki,M. (2002). Competitive CVAR-FPSO concepts with Dry trees in ultra-deepwate; Weathervaning CVAR-FPSO for Brazil and Indonesia vs. Non-weathervaning for West Africa. *Offshore Technology Conference.* Houston.

Palmer, A.C. (2008). *Dimensional Analysis and Intelligent Experimentation.* Singapore: World Scientific Publishing.

Palmer, A.C. (1975). Technical and analytical aspects of pipelaying in deep water. *Joint Conference on Pipelaying in the North Sea* (pp. 6-11). London: Institute of Marine Engineers/ Society for Underwater Technology.

Palmer, A.C., Hutchinson, G., Ells,J.E. (1974). Configuration of submarine pipelines during laying operations. *American Society of Mechanical Engineers, Journal of Engineering for Industry* , 1112-1118.

Palmer, A.C., Roger King. (2004). *Subsea Pipeline Engineering.* Tulsa.

Principia. (2008). *SCG Stress and Buckling Analysis.* Singapore

Schlumberger Oilfield (S) Pte Ltd. (Confidential Report). *Pipe-in-Pipe Interaction Using ABAQUS.*

Schlumberger Oilfield (S) Pte Ltd. (August 2008, Confidential Report). *Properties of Coiled Tubing.*

Schlumberger Oilfield (S) Pte Ltd. (September 2008, Revision 02, Confidential Report). *SCG Design Basis - West of Africa, 1500m Water Depth.*

Schlumberger Oilfield (S) Pte. Ltd. (March 2009, Confidential Report). *Analytical Investigation of Pipe-in-Pipe Interaction.*

Yergin, D. (1990). *The Price: the epic quest for oil, money and power.* New York: Free Press.

Appendix A: Physical Model Test Results

Phase 1

12.7 mm Outer Pipe, 6 mm Inner Pipe

30° Inclination Angle

Pipe in Pipe Interaction using Physical Model

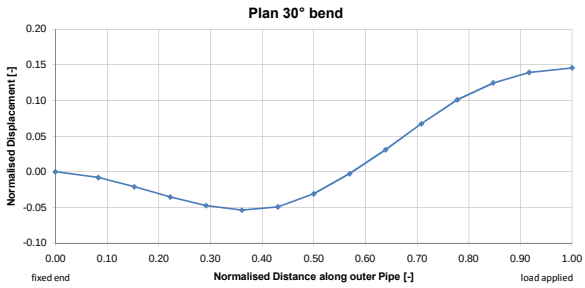

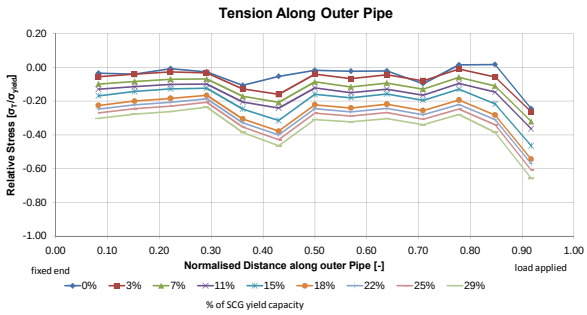

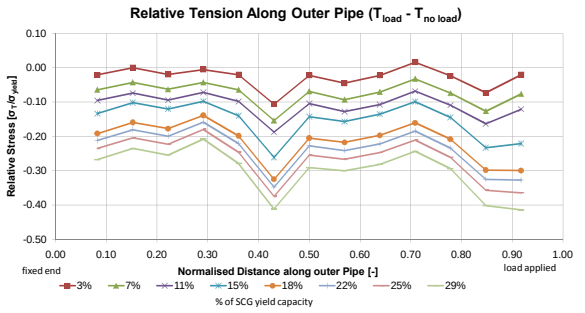

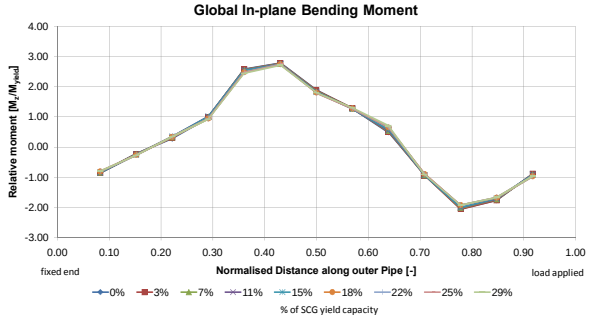

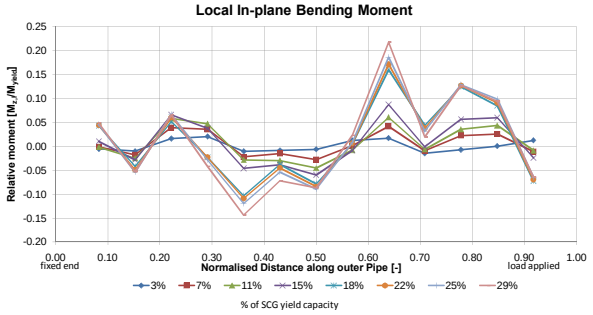

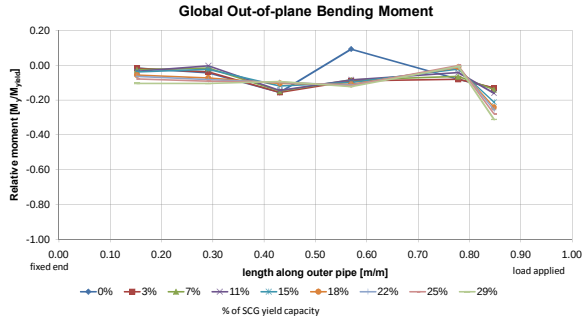

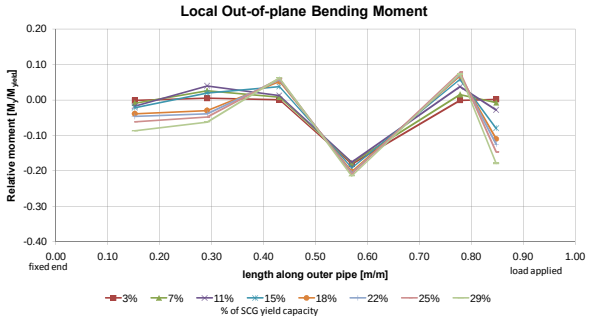

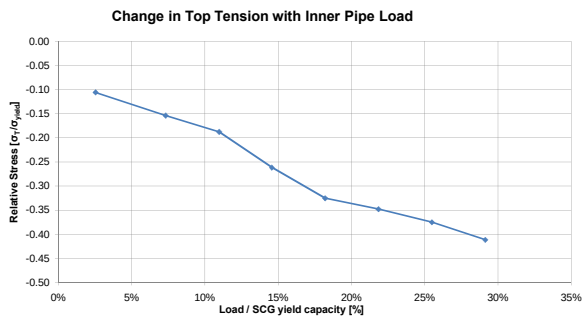

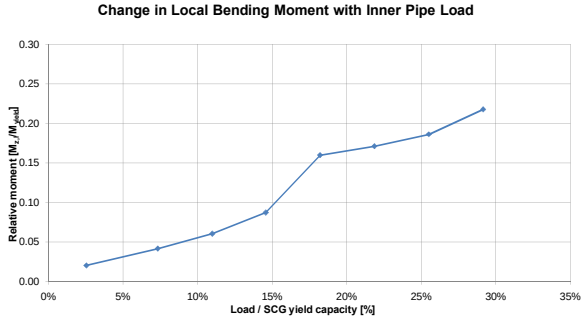

Phase 1

12.7 mm Outer Pipe, 6 mm Inner Pipe

45° Inclination Angle

Pipe in Pipe Interaction using Physical Model

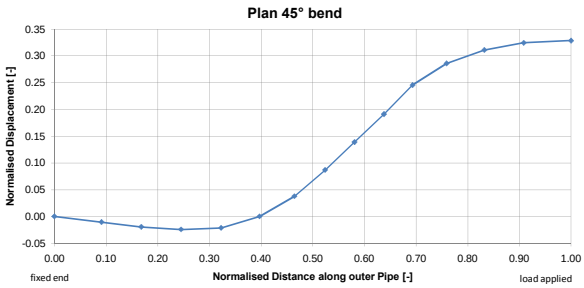

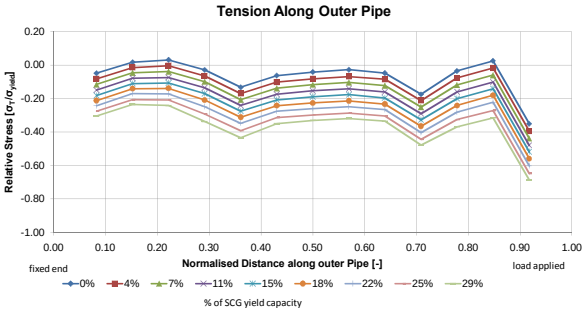

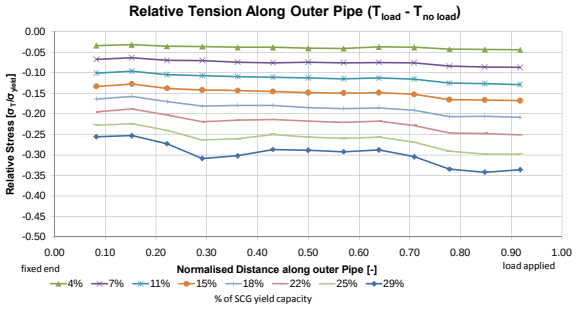

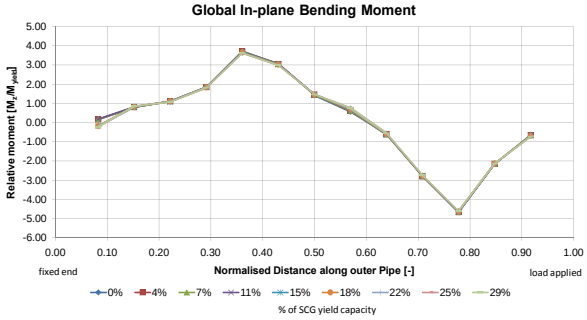

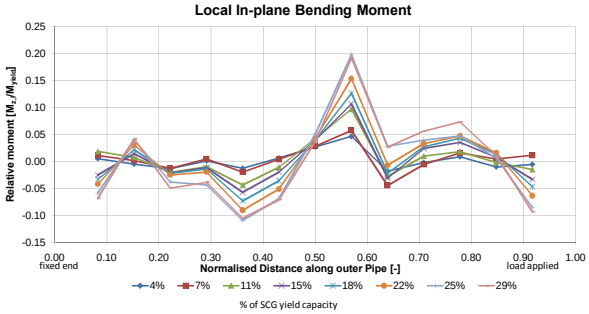

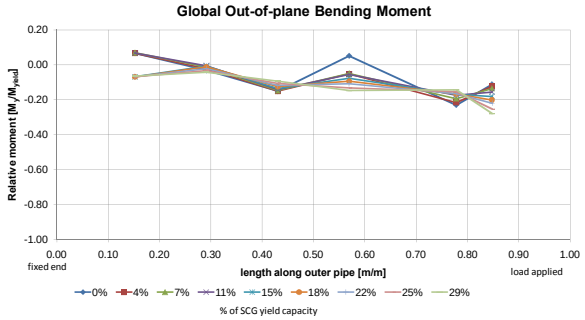

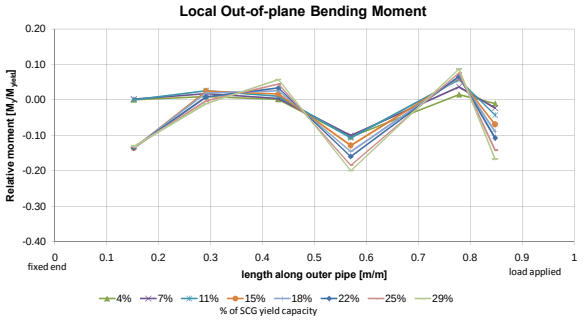

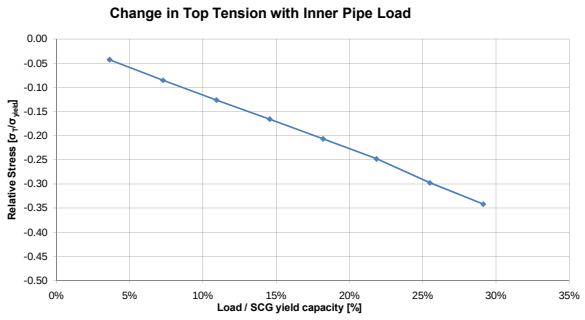

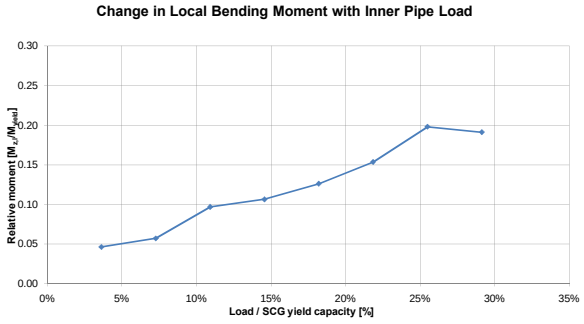

Phase 1

12.7 mm Outer Pipe, 6 mm Inner Pipe

60° Inclination Angle

Pipe in Pipe Interaction using Physical Model

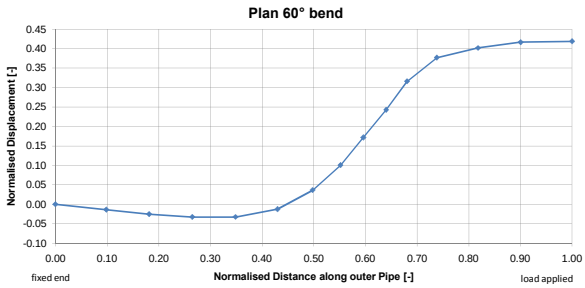

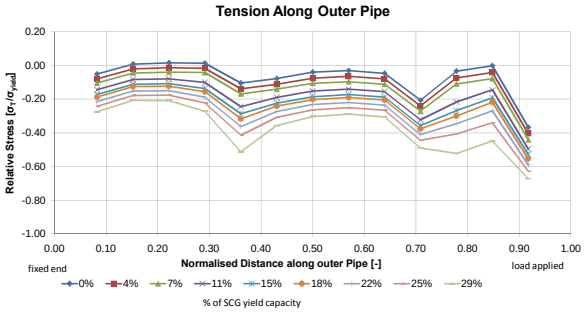

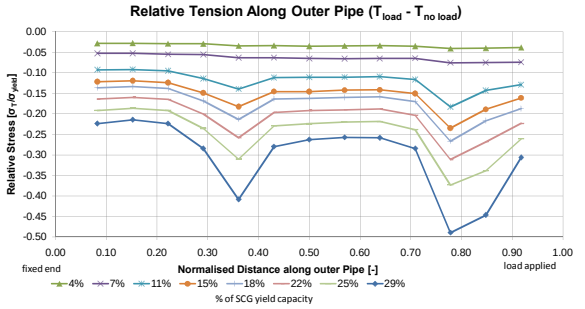

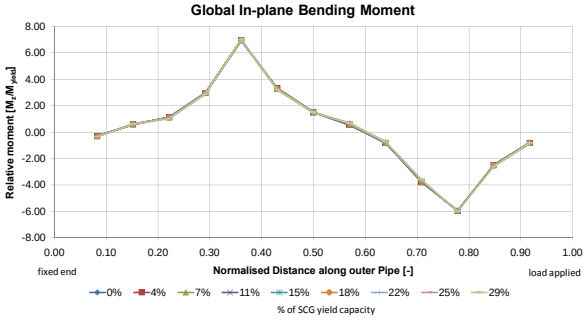

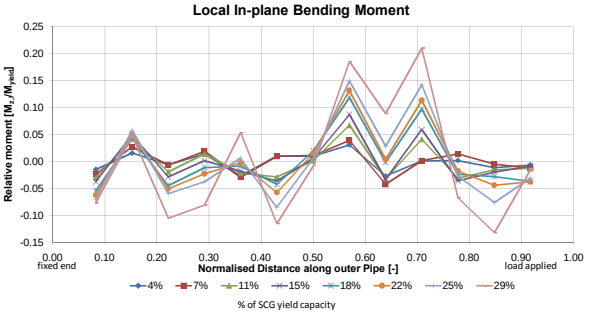

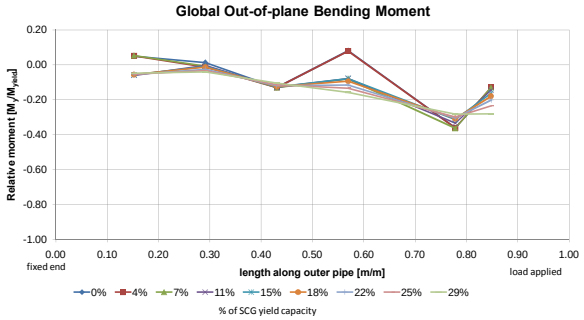

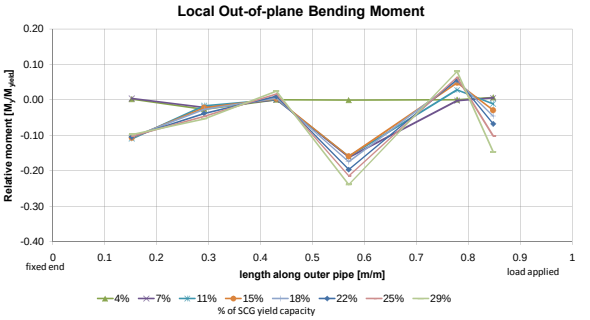

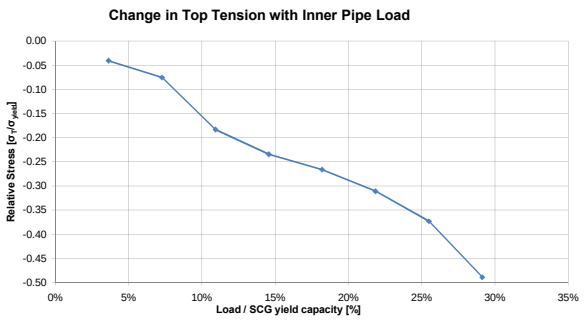

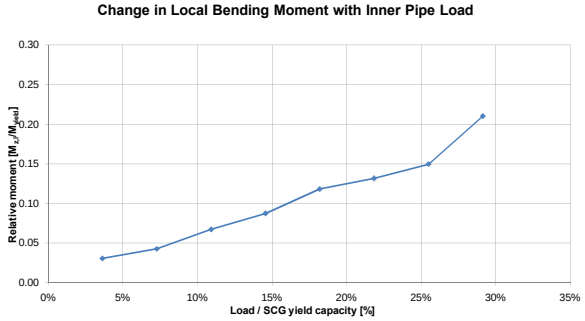

Phase 2

12.7 mm Outer Pipe, 2 mm Wire

30° Inclination Angle

Pipe in Pipe Interaction using Physical Model

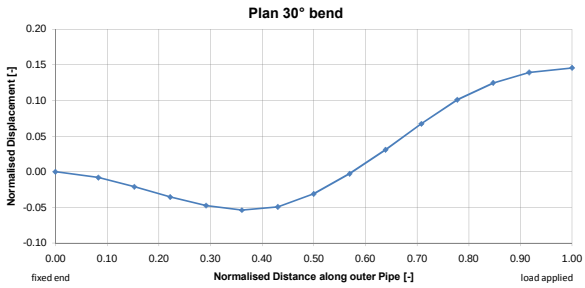

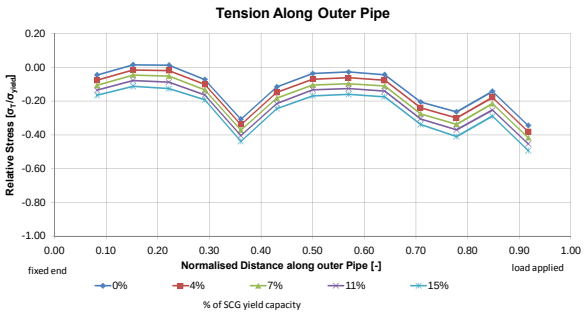

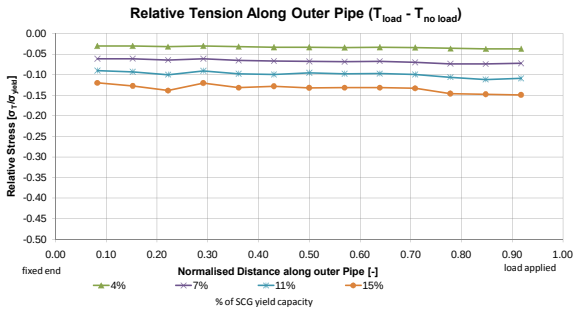

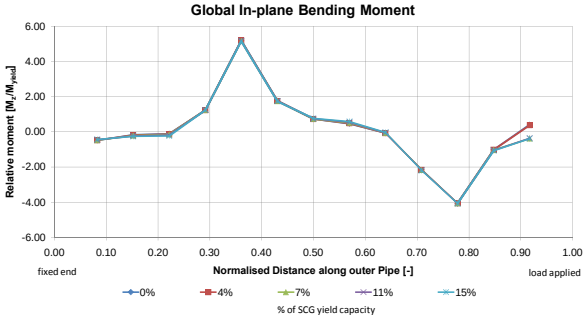

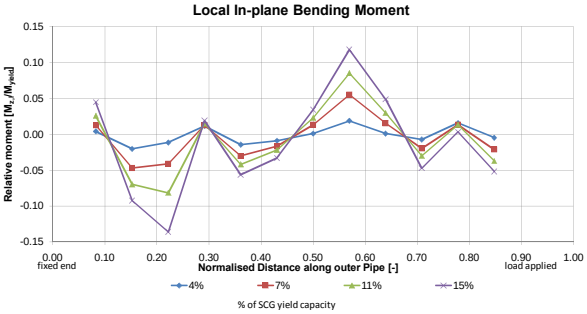

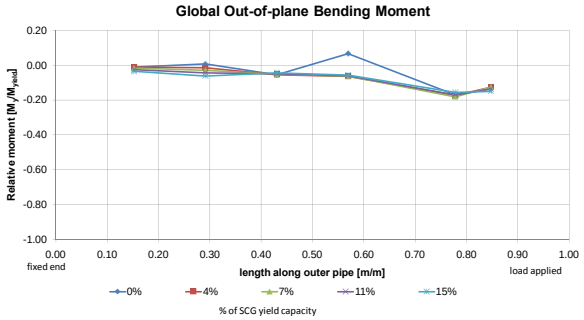

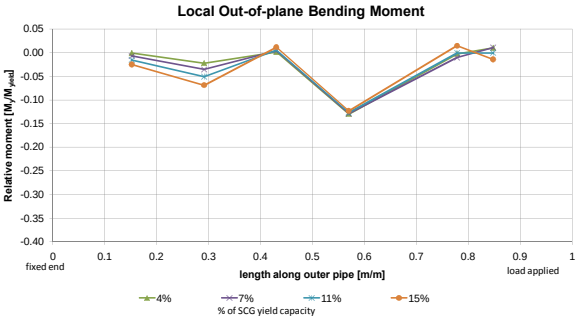

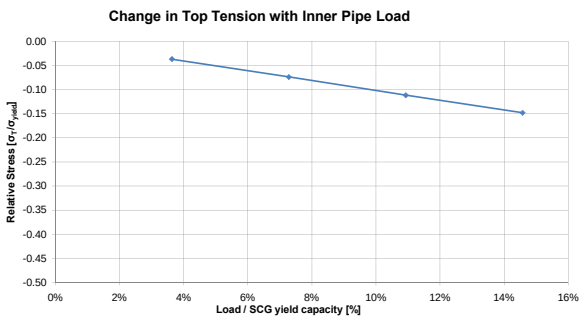

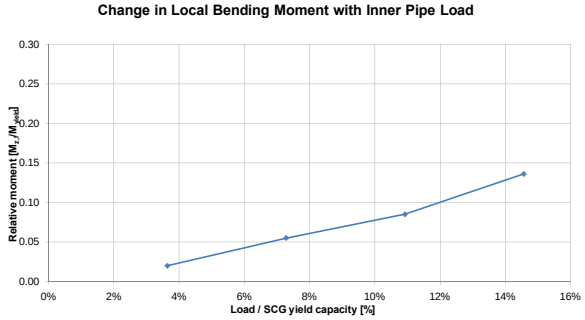

Phase 2

12.7 mm Outer Pipe, 2 mm Wire

45° Inclination Angle

Pipe in Pipe Interaction using Physical Model

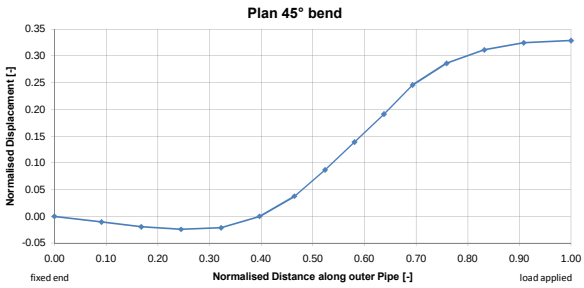

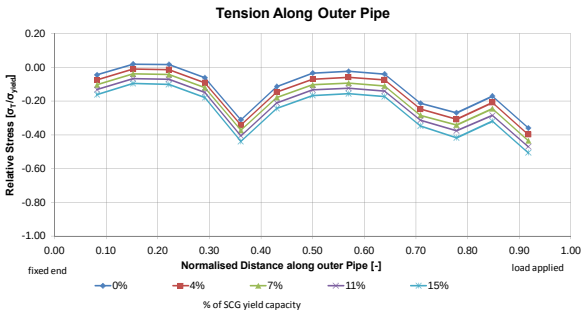

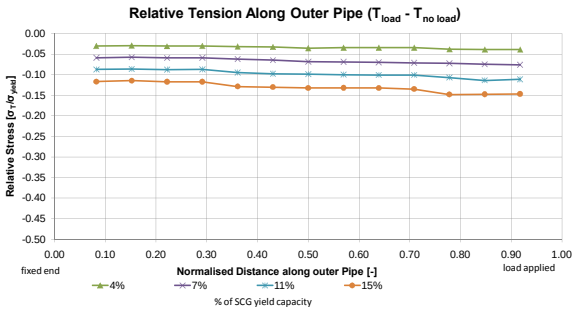

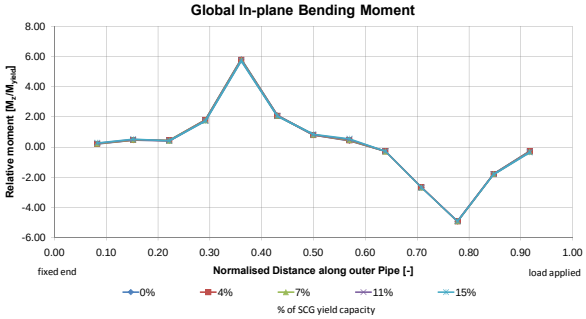

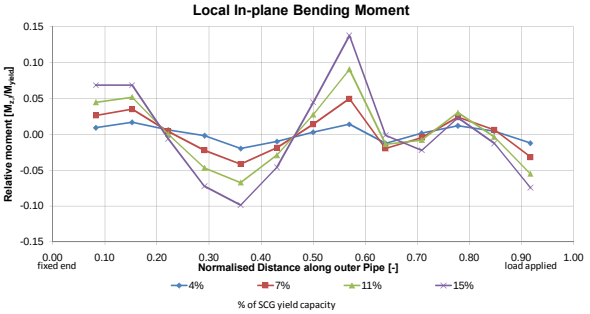

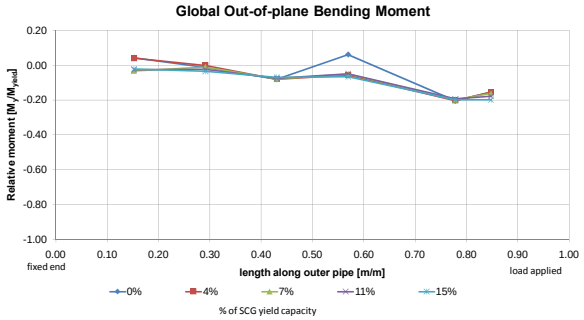

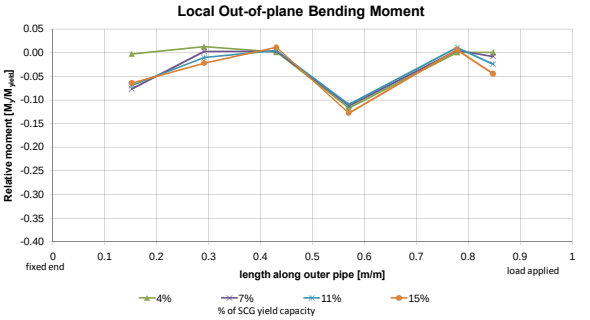

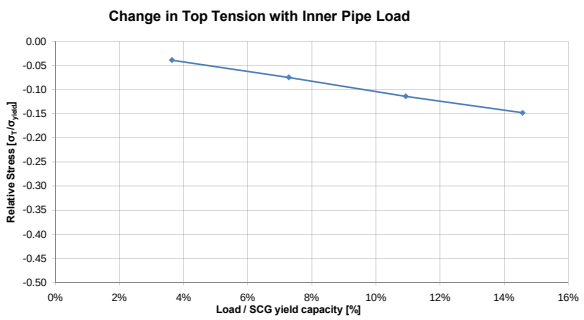

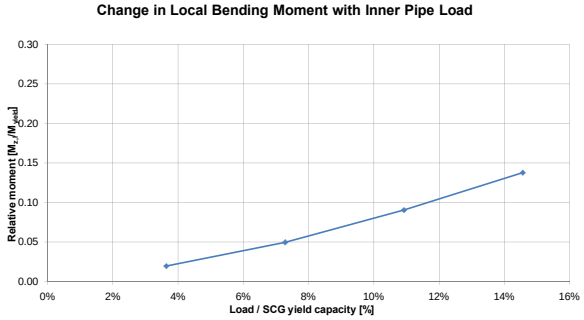

Phase 2

12.7 mm Outer Pipe, 2 mm Wire

60° Inclination Angle

Pipe in Pipe Interaction using Physical Model

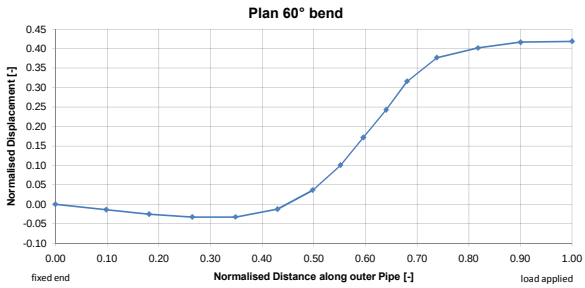

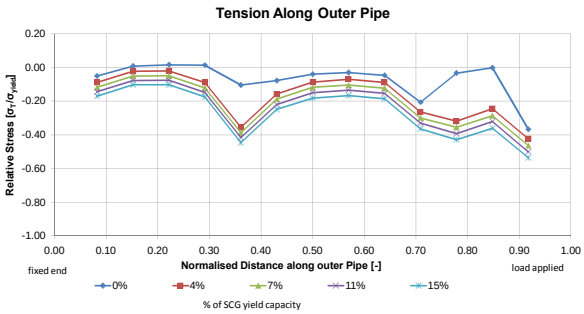

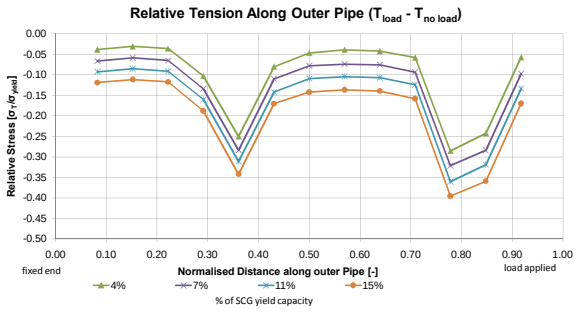

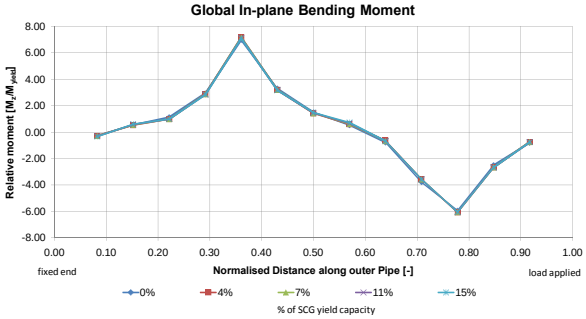

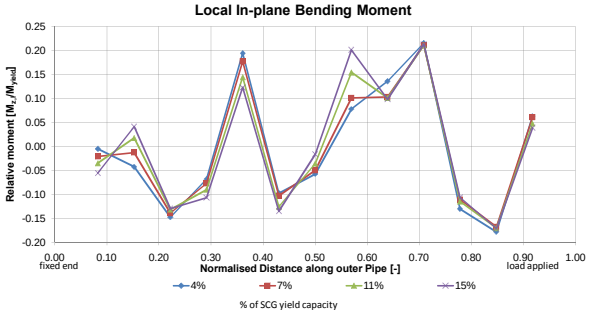

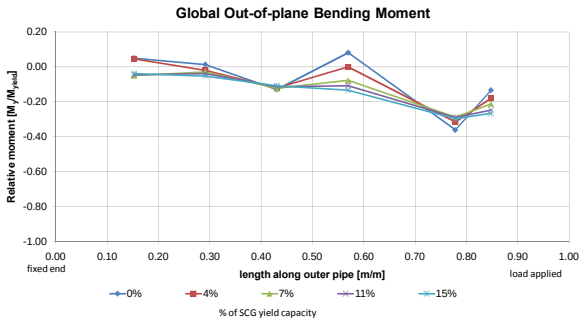

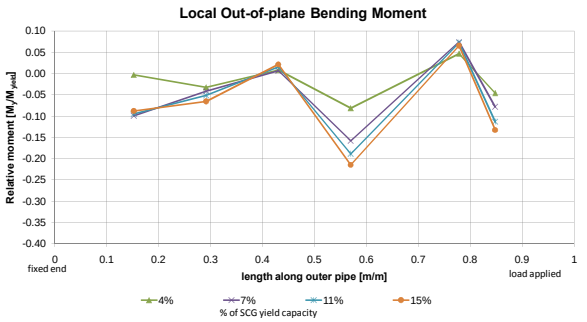

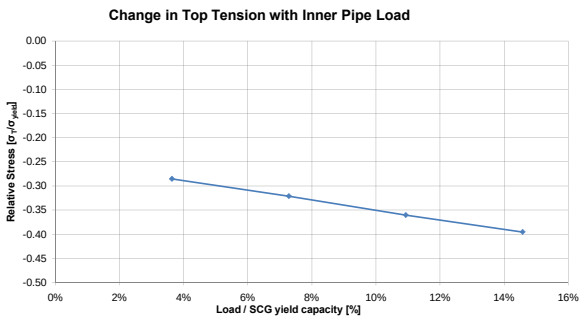

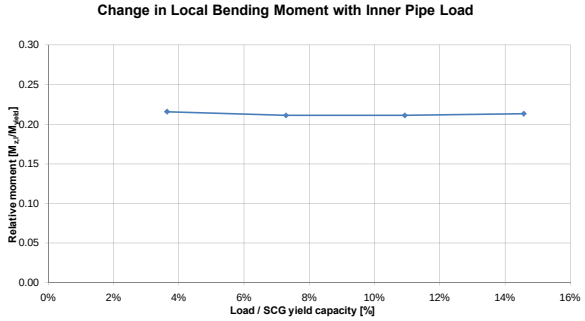

Phase 3

25.4 mm Outer Pipe, 6 mm Inner Pipe

30° Inclination Angle

Pipe in Pipe Interaction using Physical Model

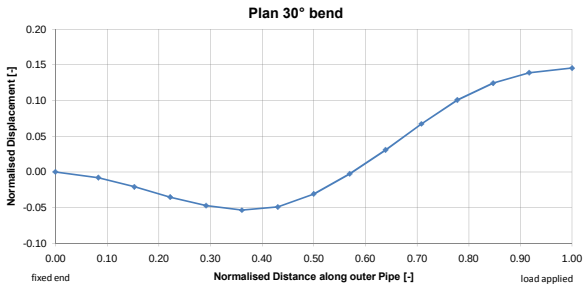

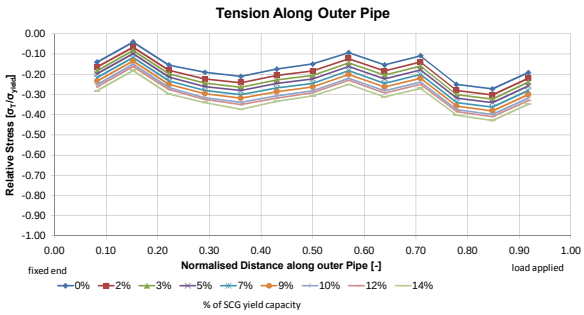

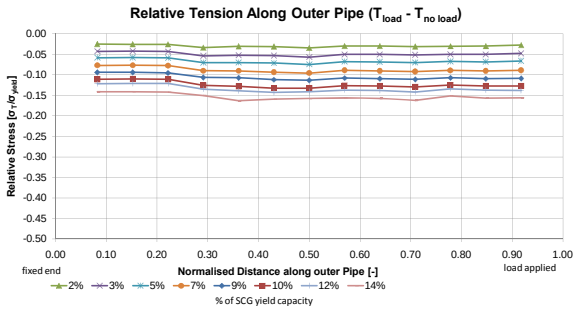

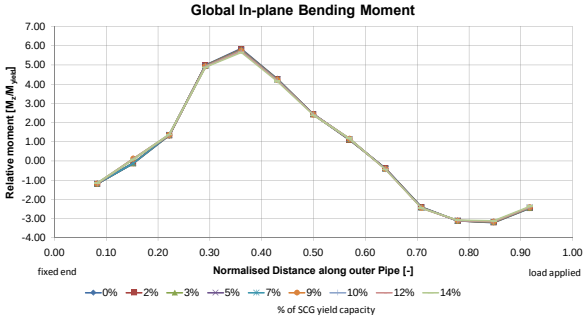

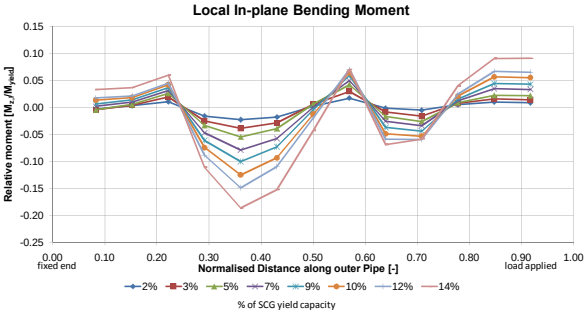

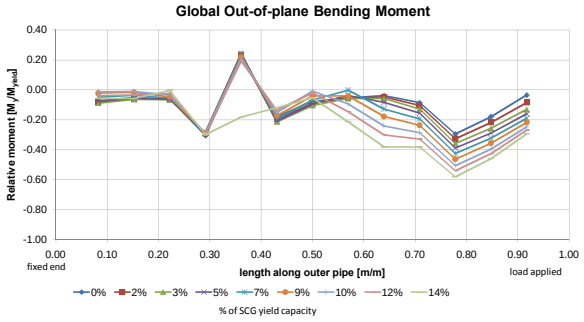

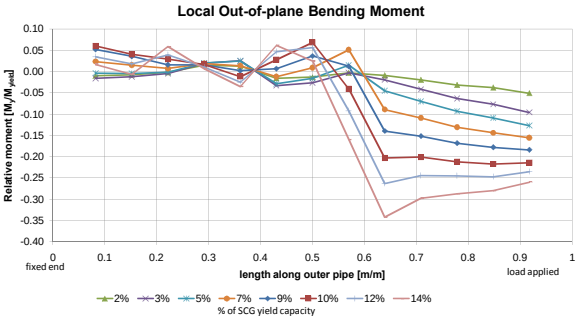

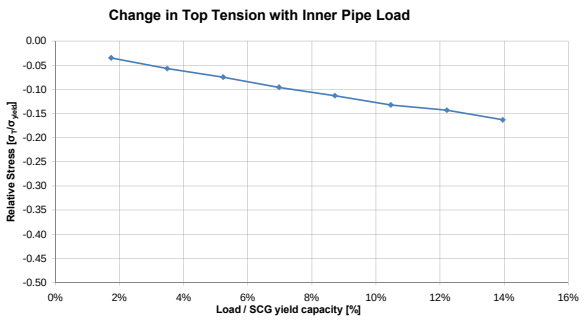

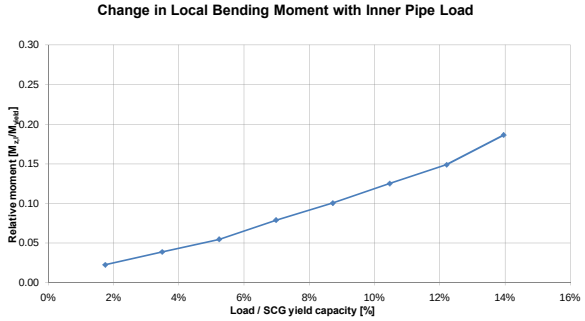

Phase 3

25.4 mm Outer Pipe, 6 mm Inner Pipe

45° Inclination Angle

Pipe in Pipe Interaction using Physical Model

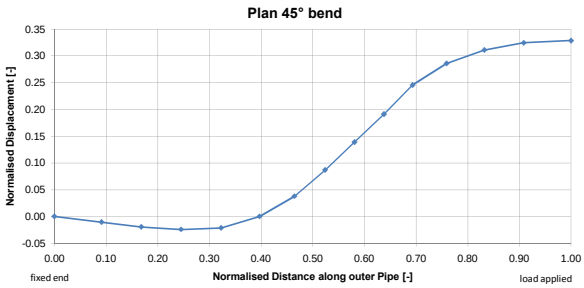

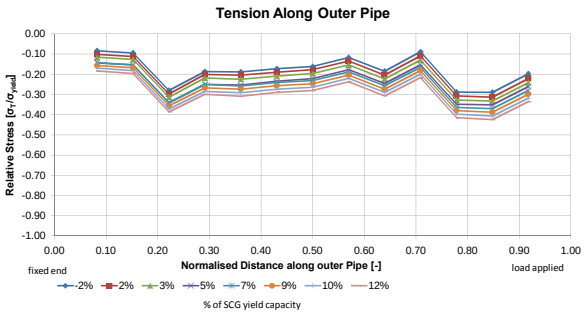

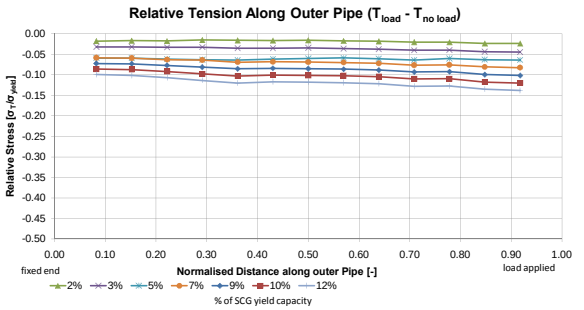

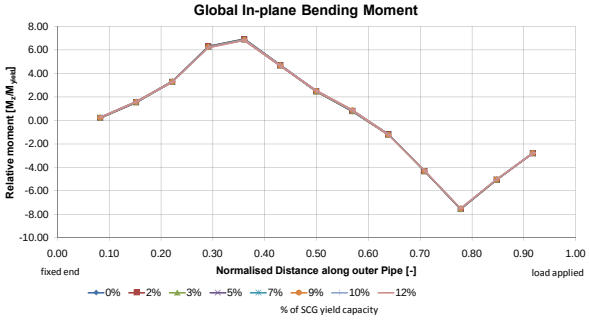

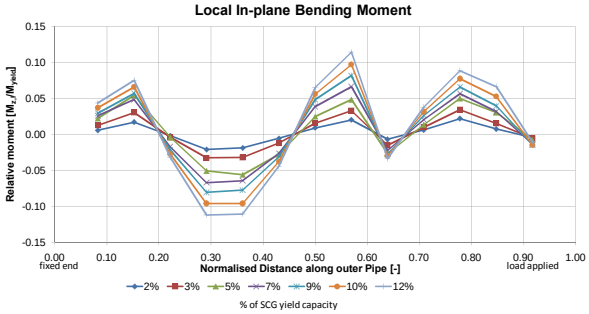

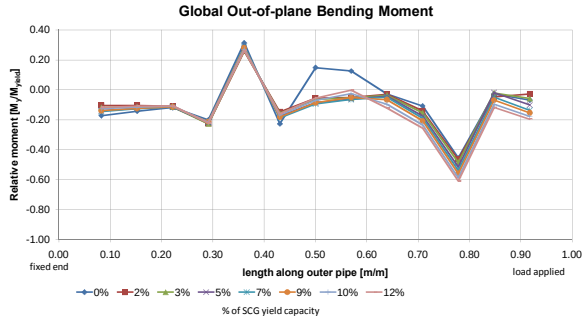

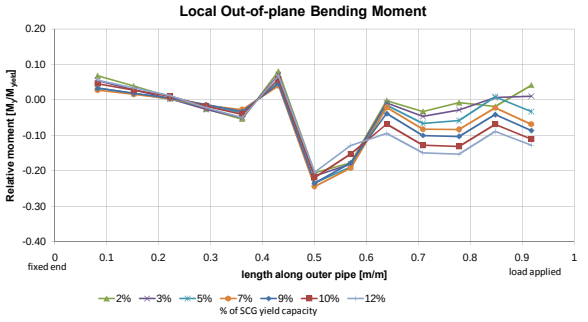

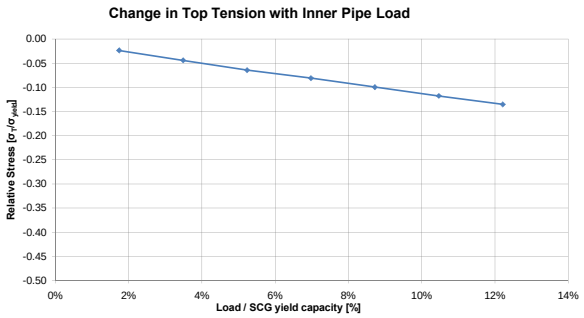

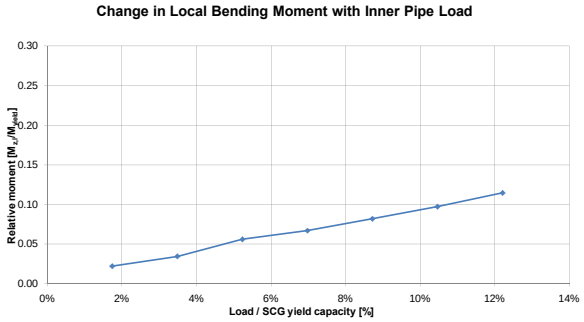

Phase 3

25.4 mm Outer Pipe, 6 mm Inner Pipe

60° Inclination Angle

Pipe in Pipe Interaction using Physical Model

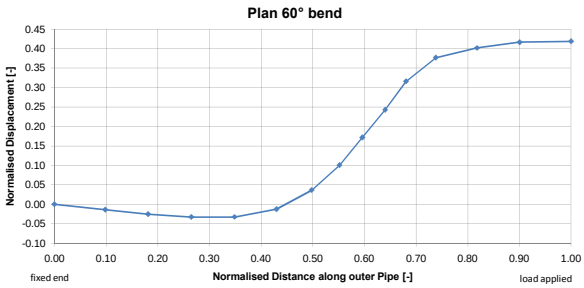

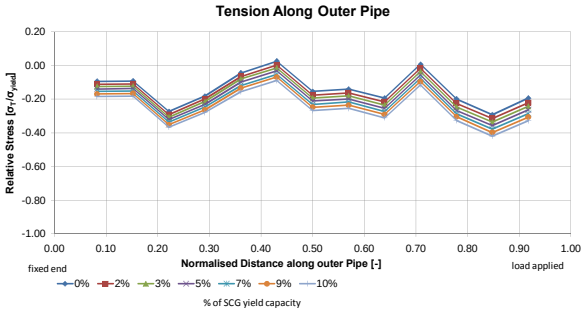

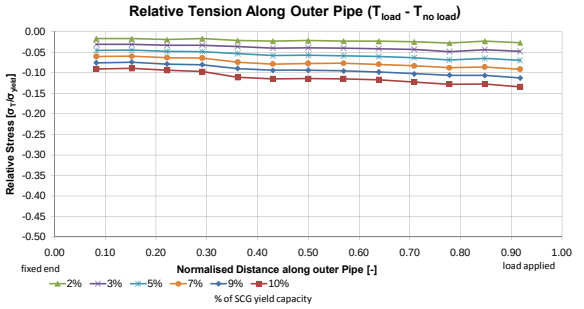

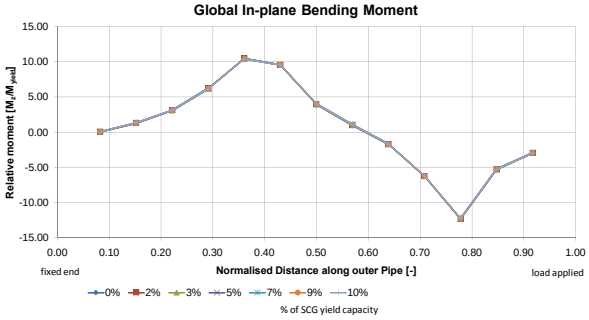

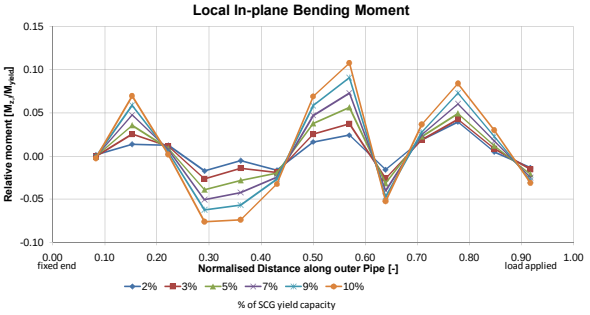

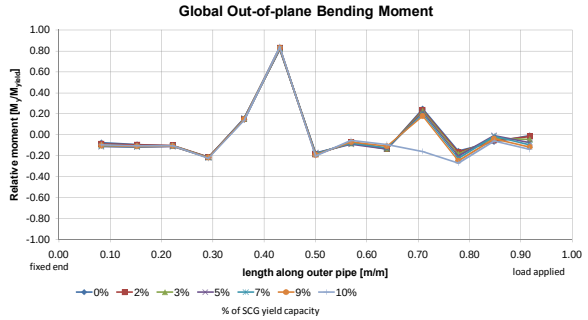

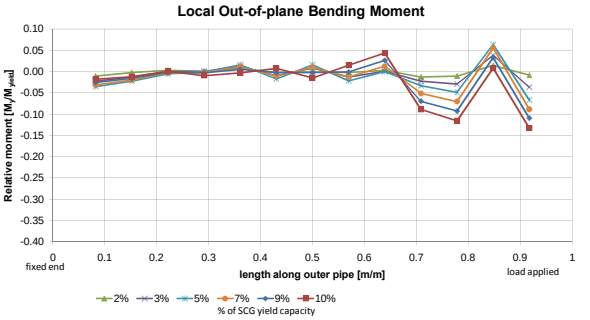

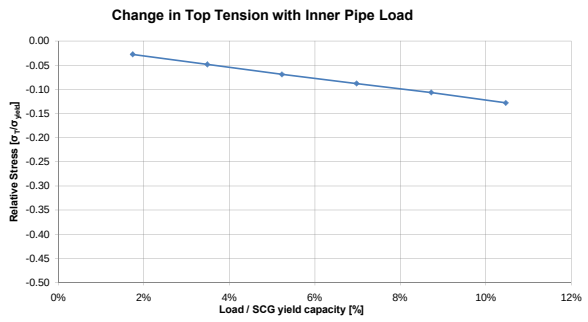

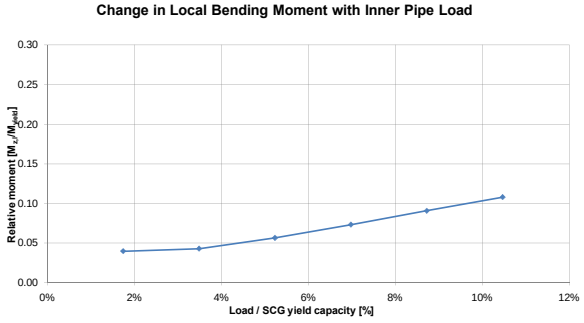

Phase 4

25.4 mm Outer Pipe, 2 mm Wire

30° Inclination Angle

Pipe in Pipe Interaction using Physical Model

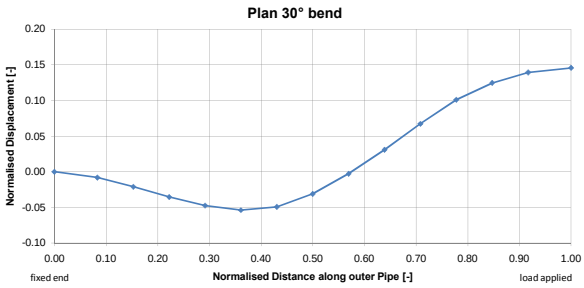

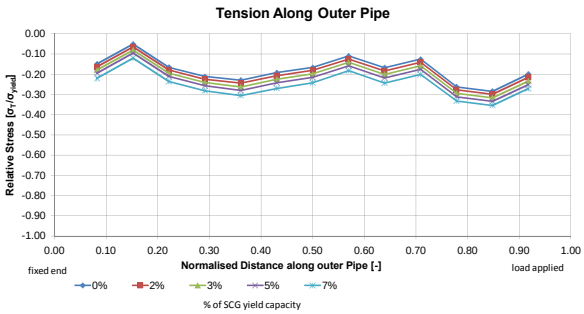

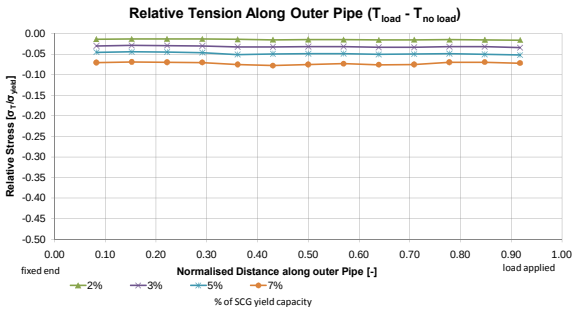

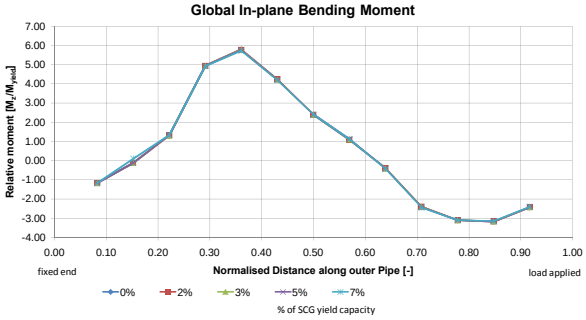

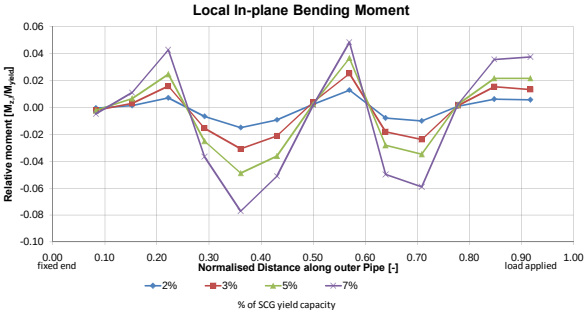

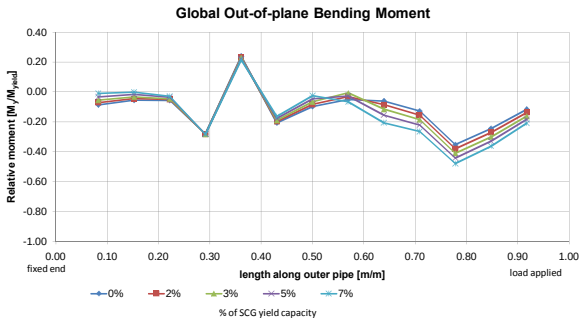

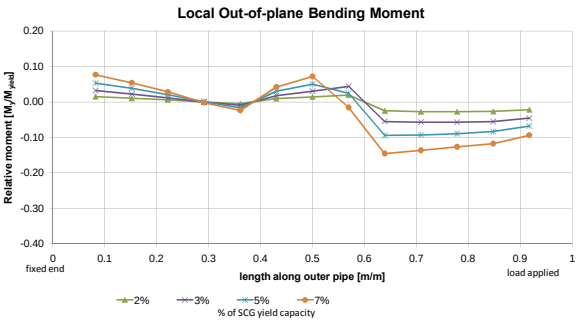

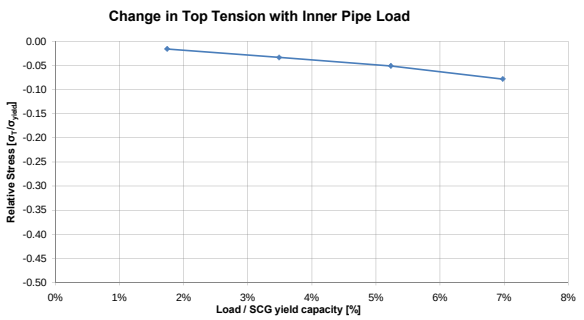

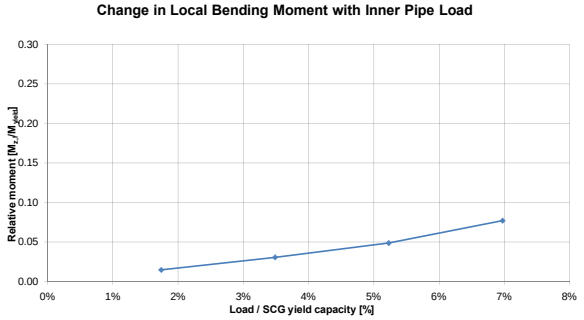

Phase 4

25.4 mm Outer Pipe, 2 mm Wire

45° Inclination Angle

Pipe in Pipe Interaction using Physical Model

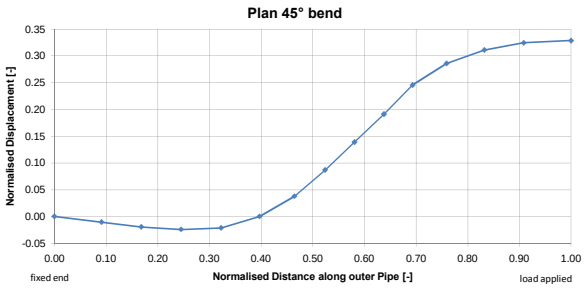

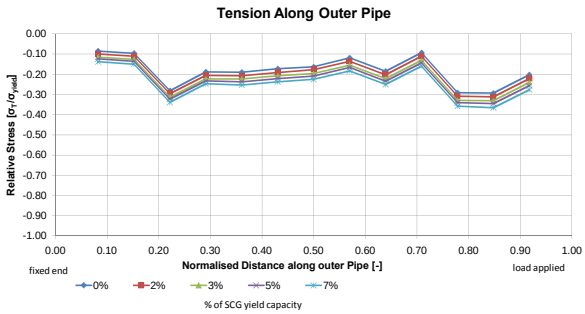

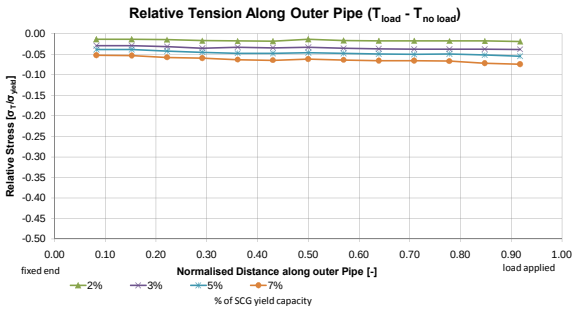

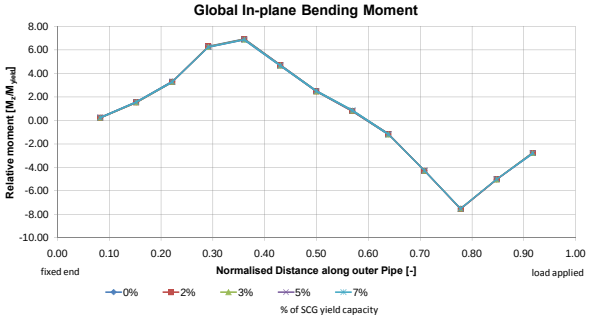

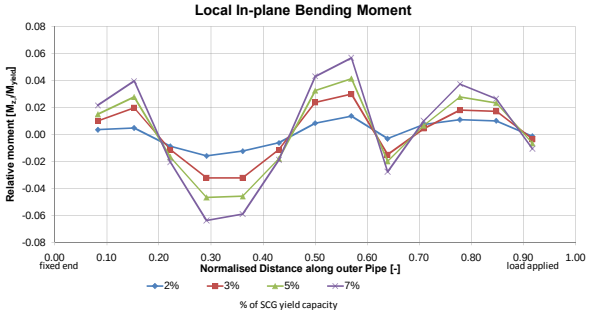

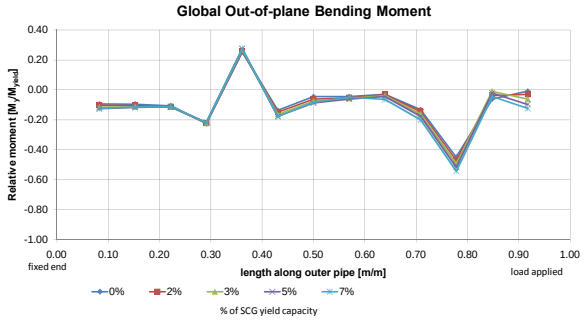

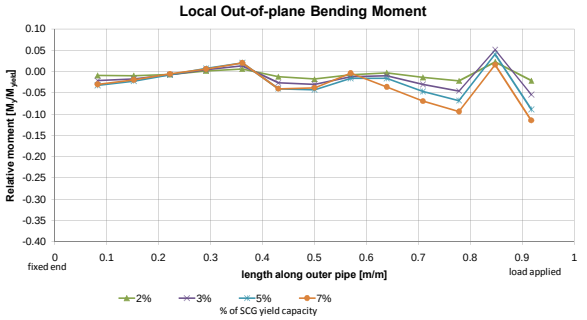

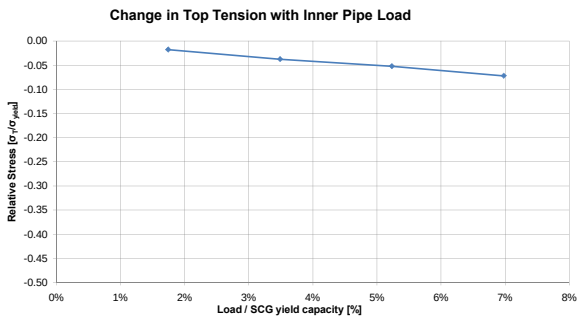

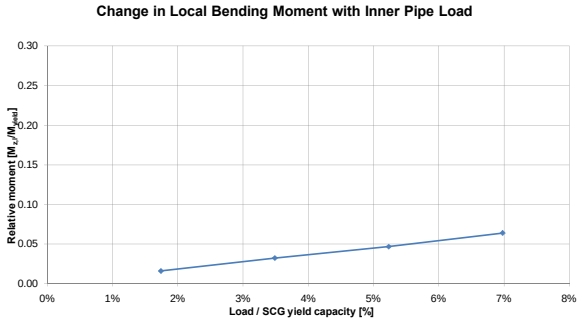

Phase 4

25.4 mm Outer Pipe, 2 mm Wire

60° Inclination Angle

Pipe in Pipe Interaction using Physical Model

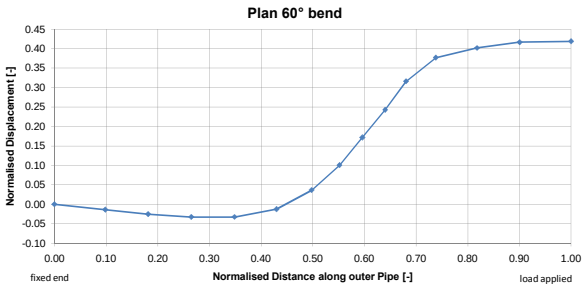

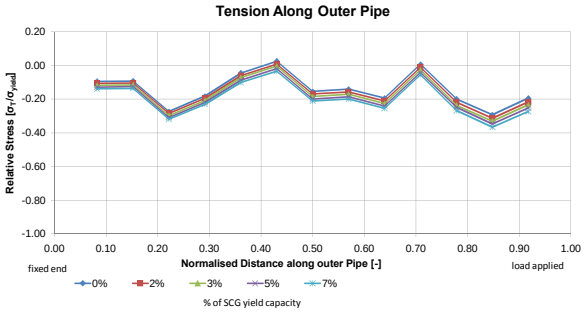

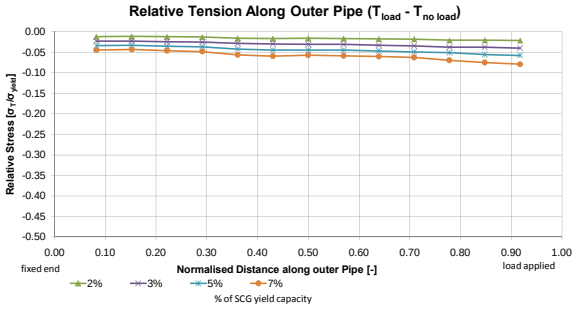

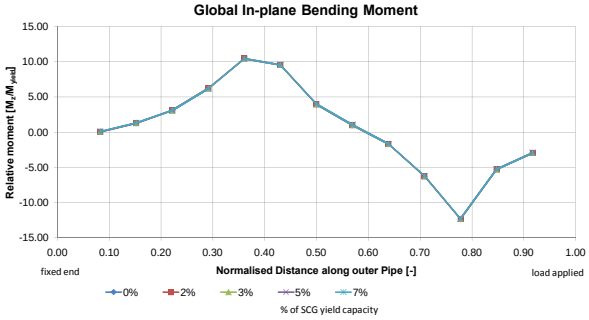

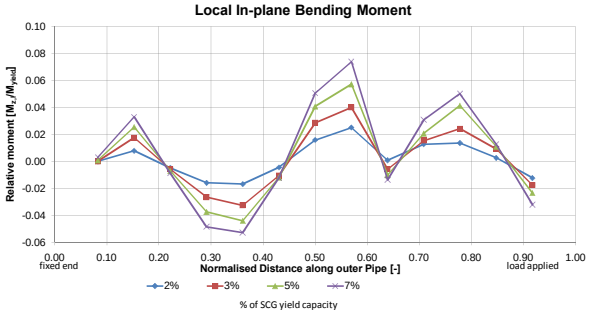

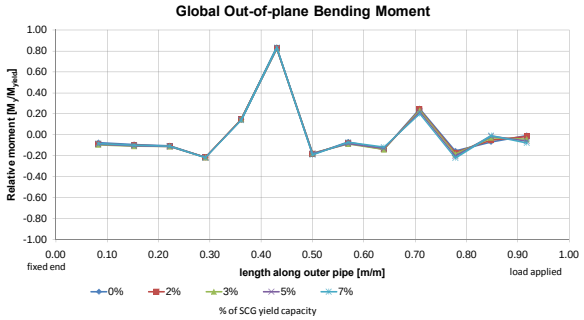

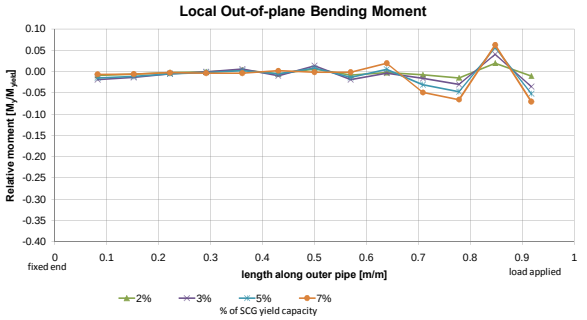

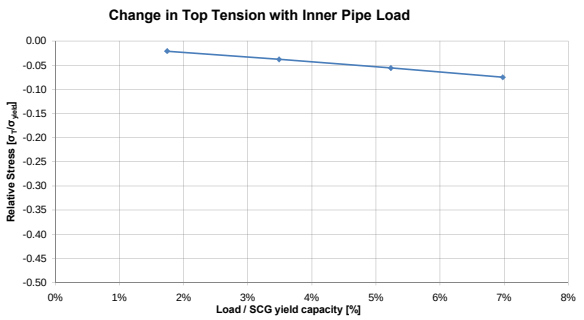

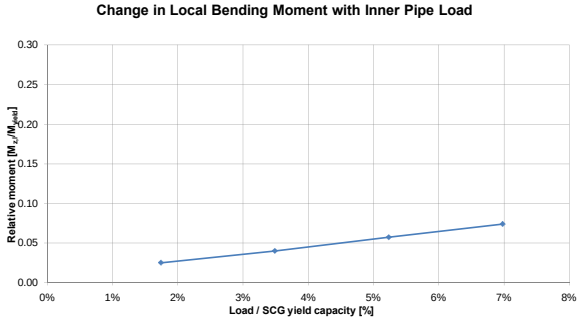

Appendix B: Physical Model Test – Comparison of different Pipe in Pipe Diameter Ratios

30° Inclination Angle

Comparison of different Pipe in Pipe Diameter Ratios

Pipe in Pipe Interaction using Physical Model

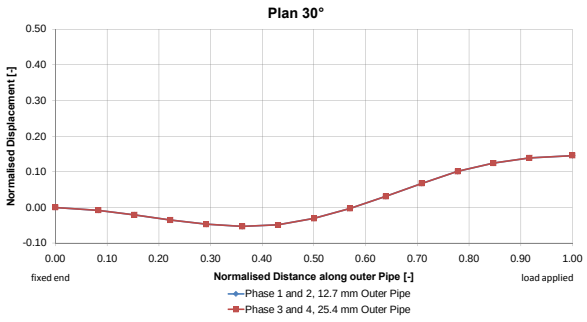

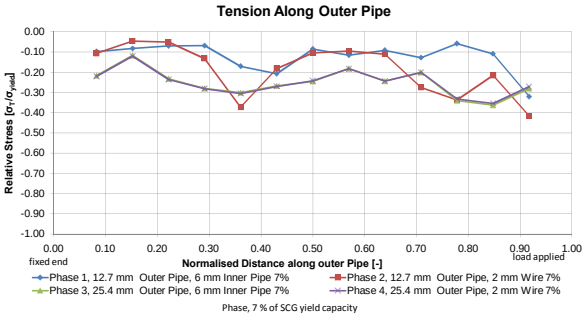

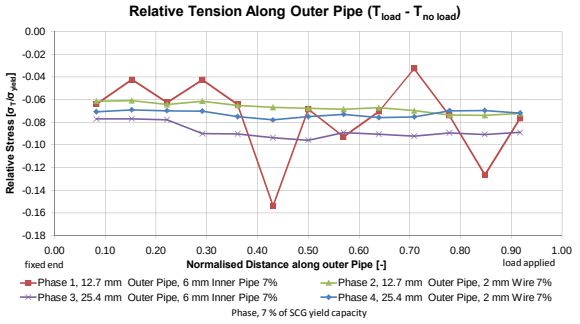

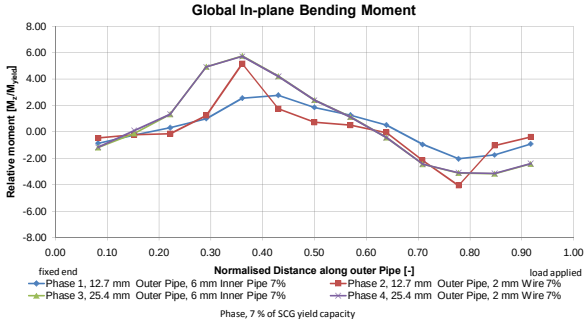

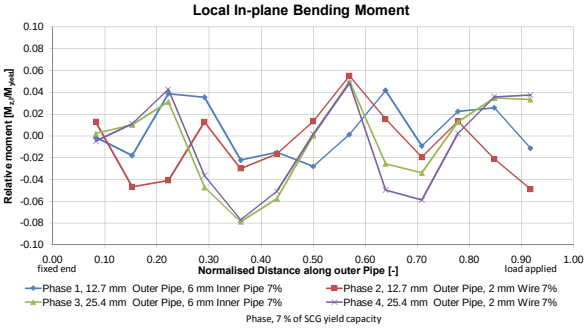

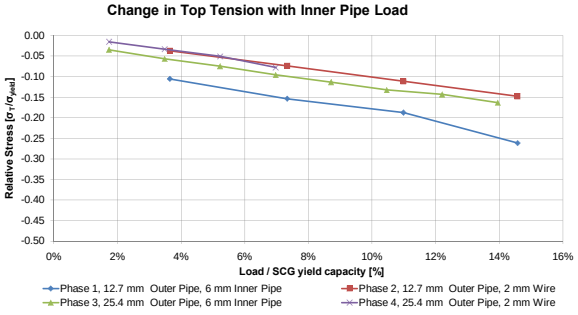

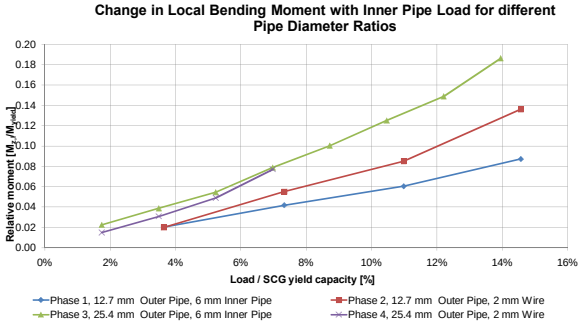

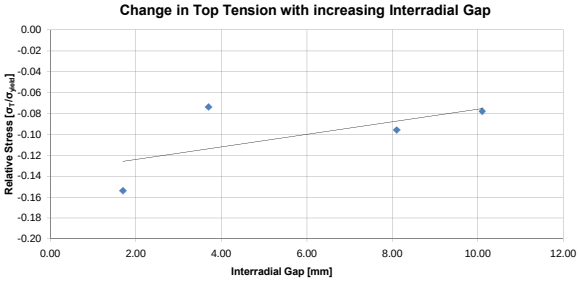

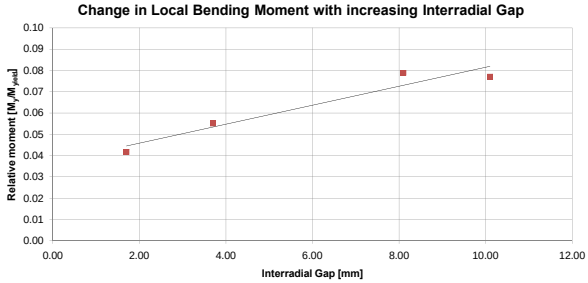

45° Inclination Angle

Comparison of different Pipe in Pipe Diameter Ratios

Pipe in Pipe Interaction using Physical Model

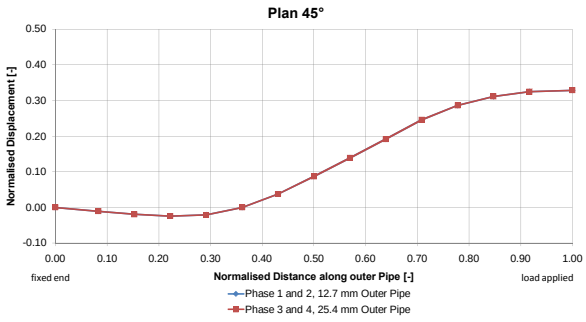

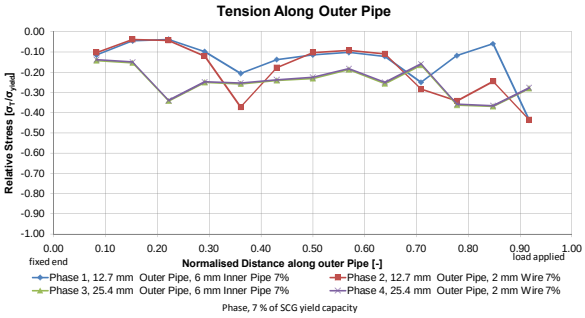

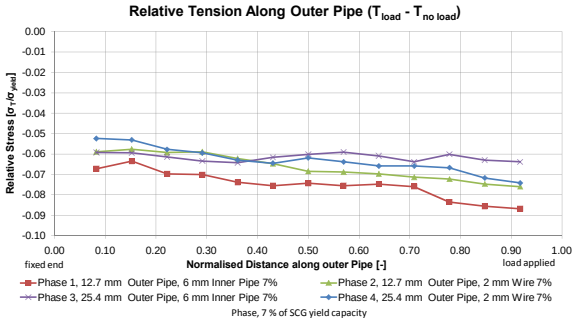

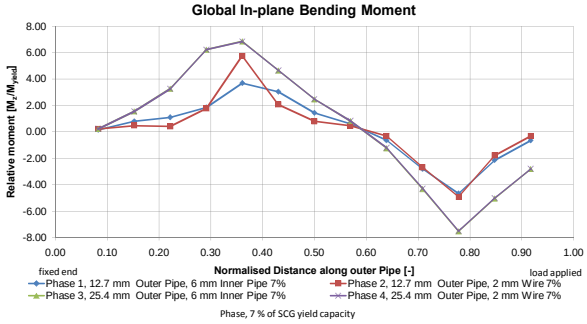

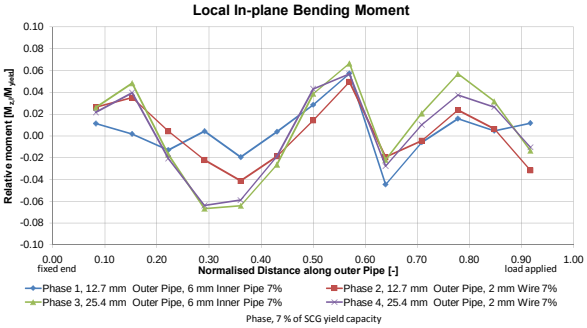

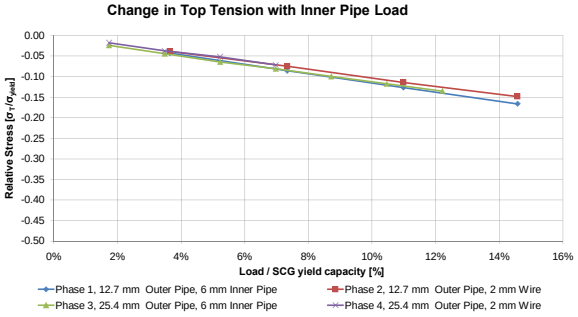

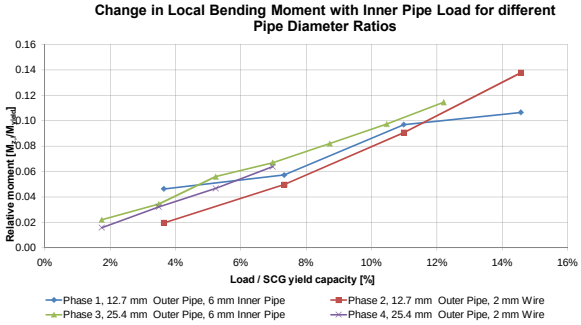

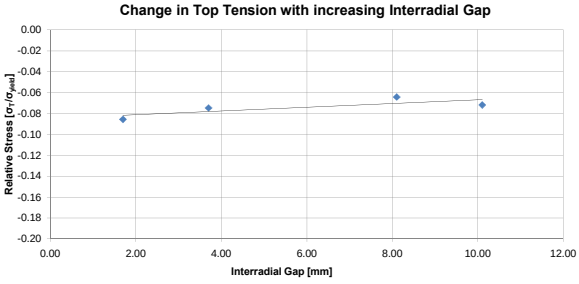

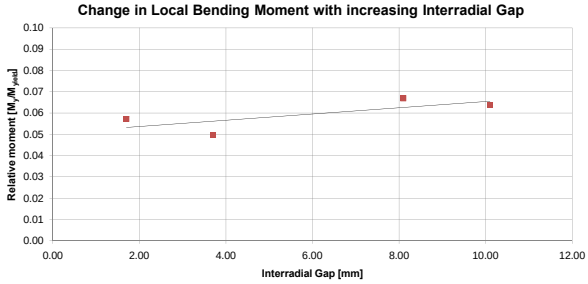

60° Inclination Angle

Comparison of different Pipe in Pipe Diameter Ratios

Pipe in Pipe Interaction using Physical Model

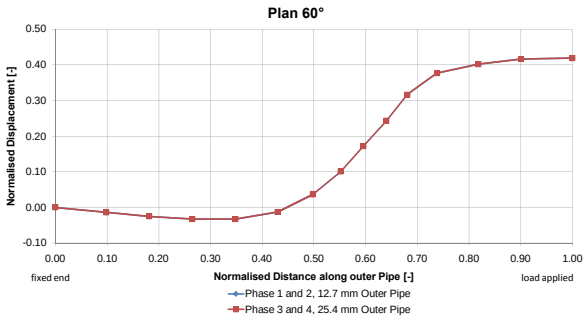

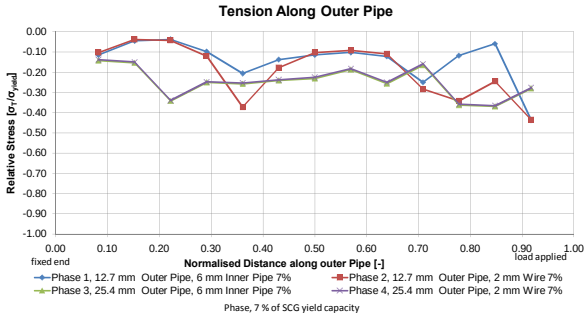

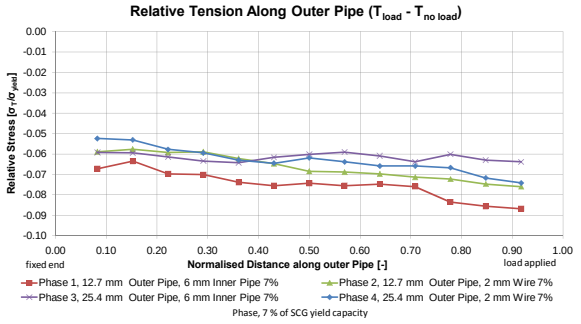

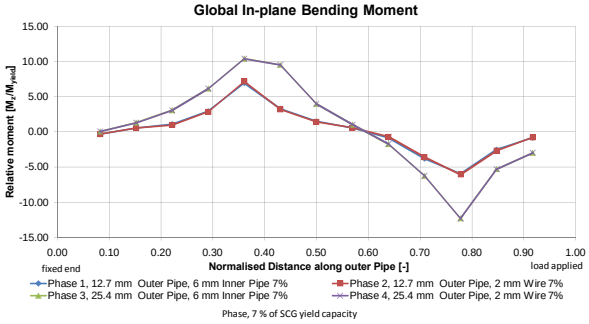

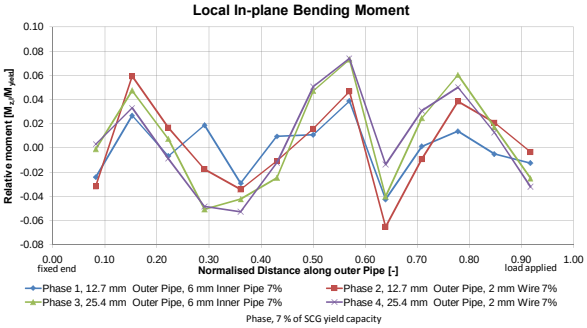

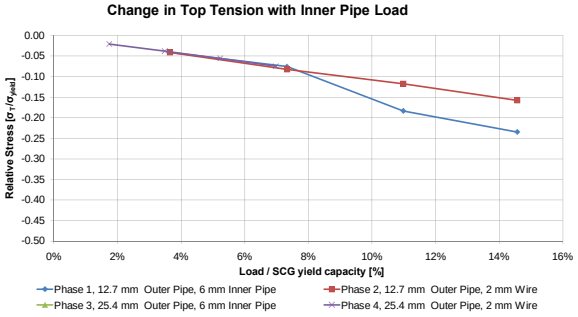

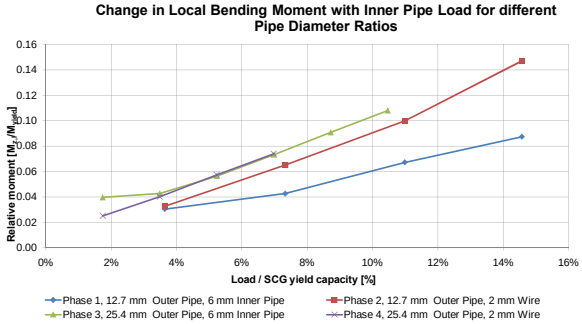

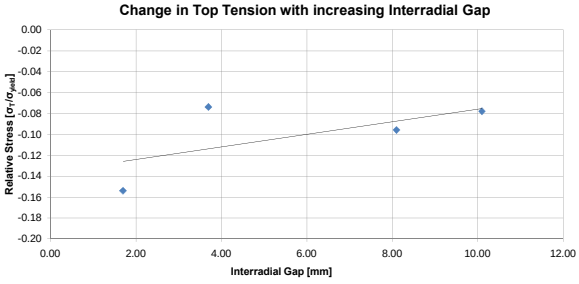

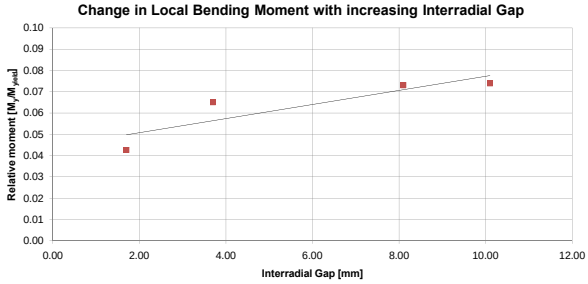

Appendix C: Physical Model Test – Comparison of different Inclination Angles

Phase 1

12.7 mm Outer Pipe, 6 mm Inner Pipe

Comparison of different Inclination Angles

Pipe in Pipe Interaction using Physical Model

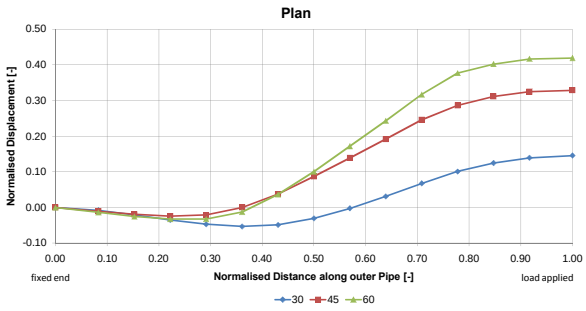

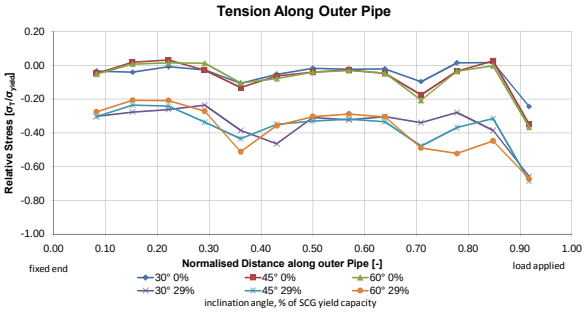

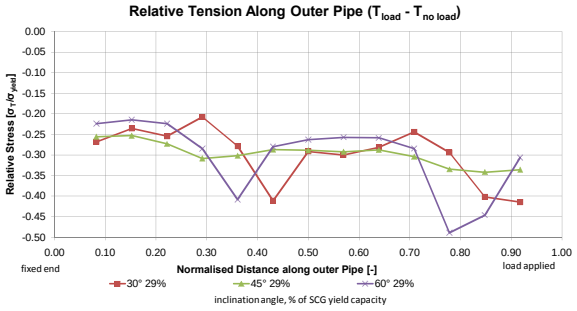

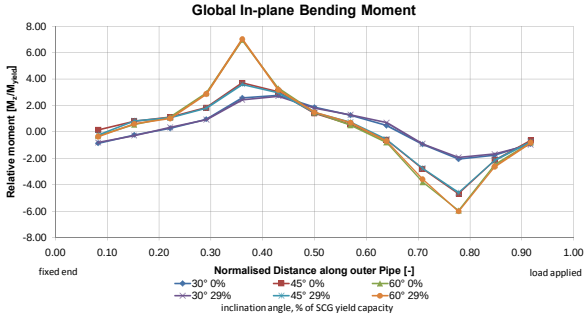

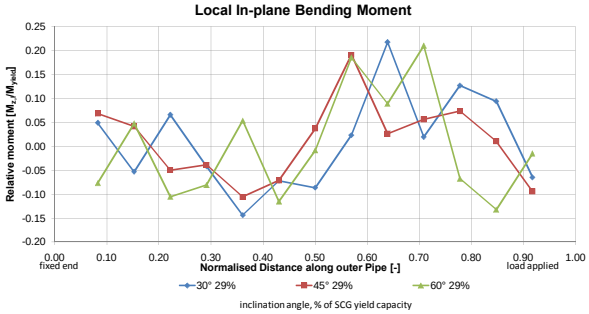

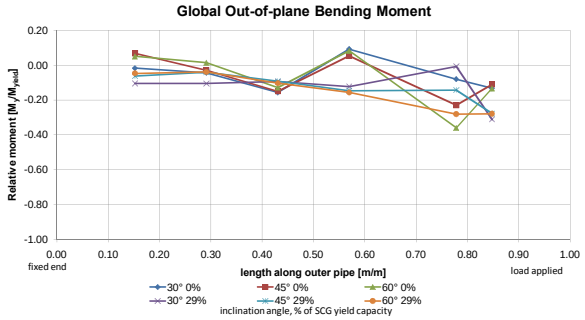

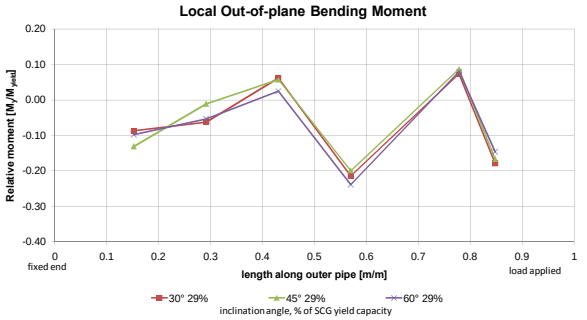

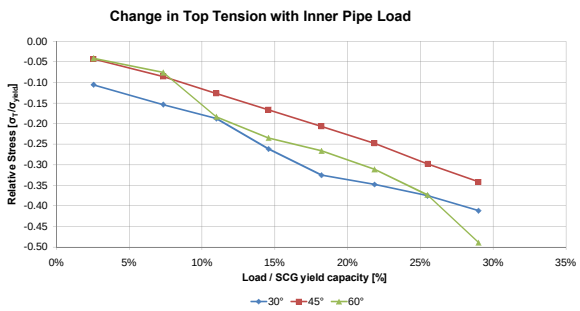

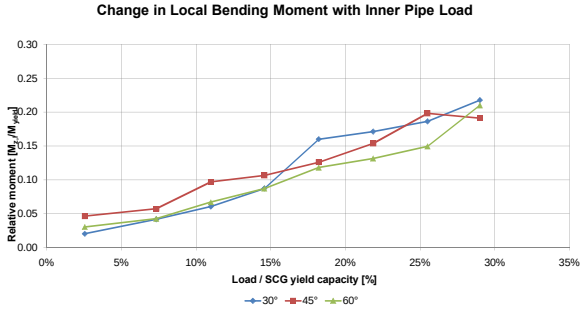

Phase 2

12.7 mm Outer Pipe, 2 mm Wire

Comparison of different Inclination Angles

Pipe in Pipe Interaction using Physical Model

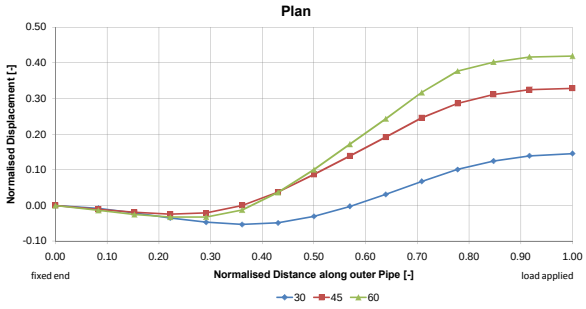

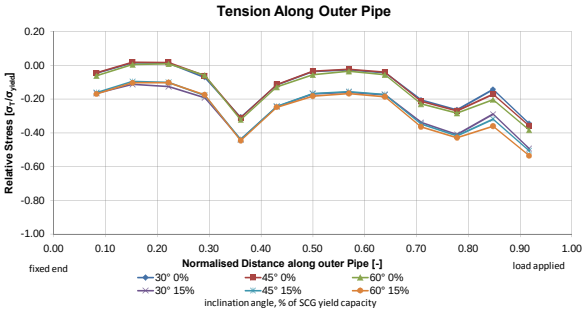

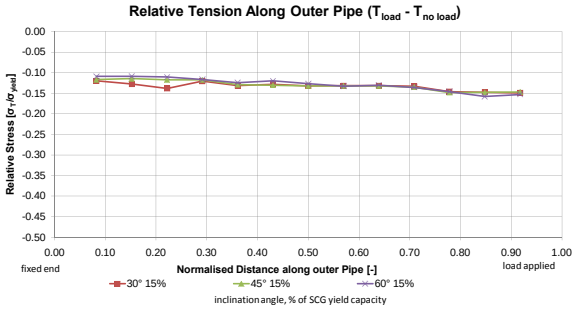

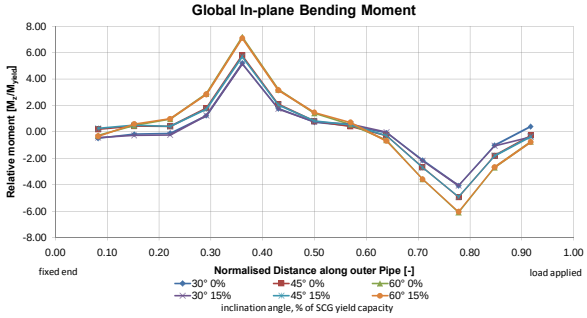

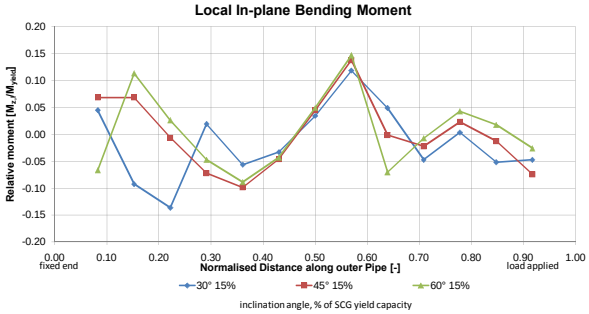

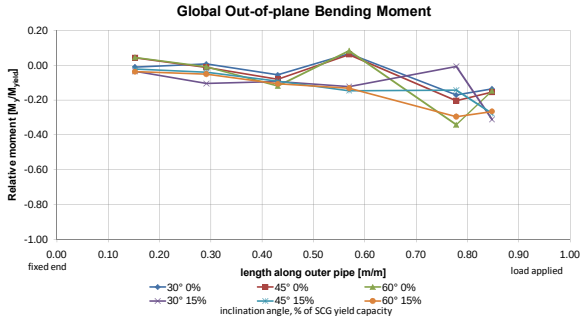

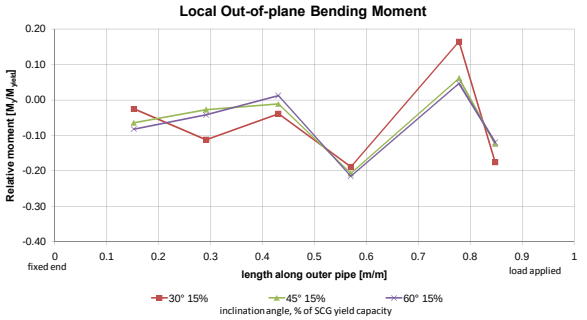

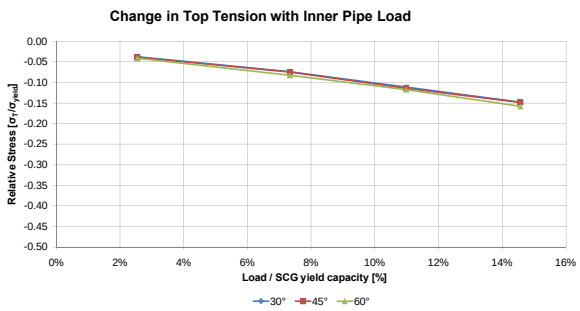

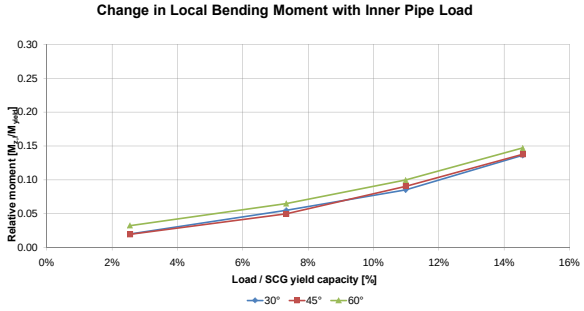

Phase 3

25.4 mm Outer Pipe, 6 mm Inner Pipe

Comparison of different Inclination Angles

Pipe in Pipe Interaction using Physical Model

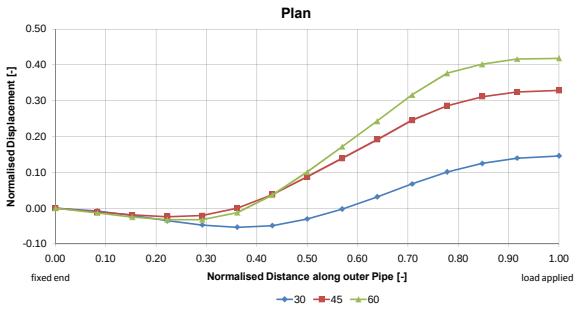

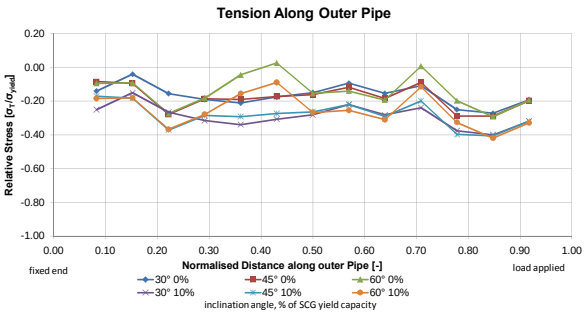

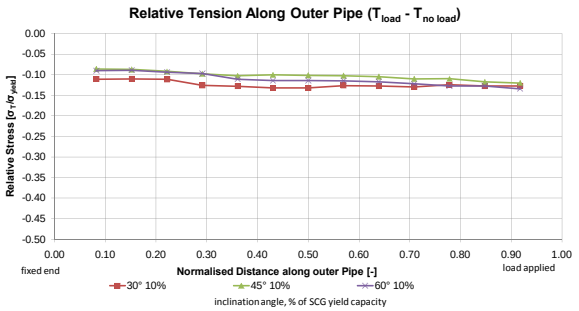

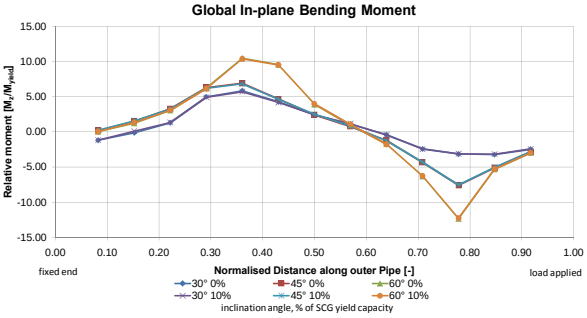

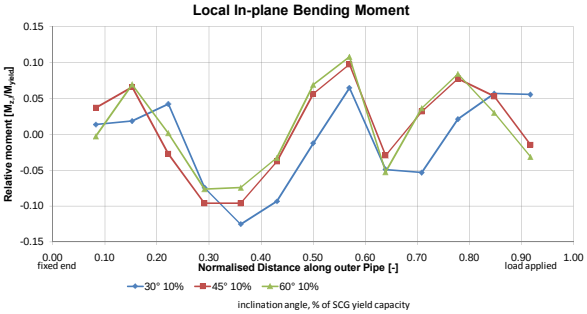

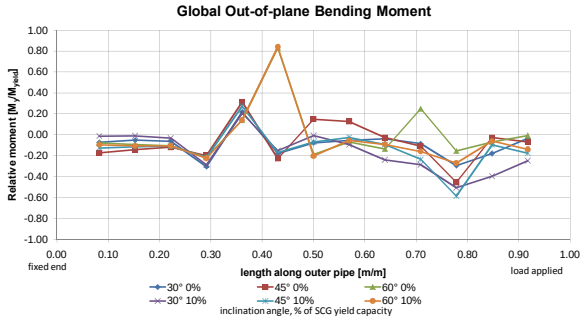

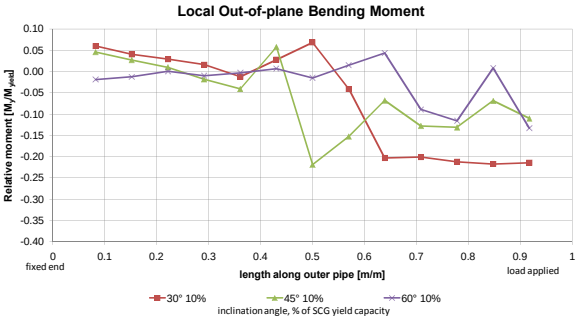

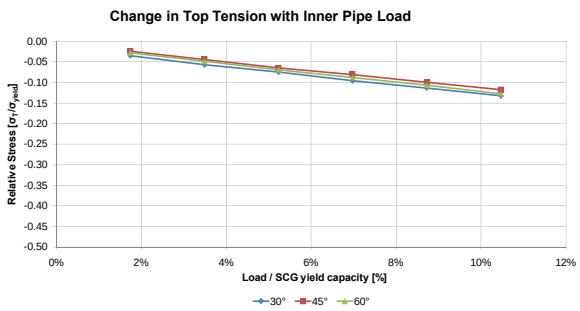

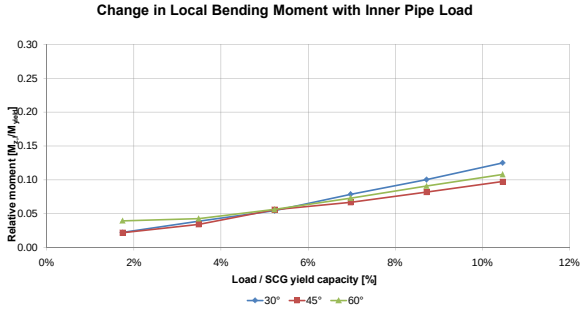

Phase 4

25.4 mm Outer Pipe, 2 mm Wire

Comparison of different Inclination Angles

Pipe in Pipe Interaction using Physical Model

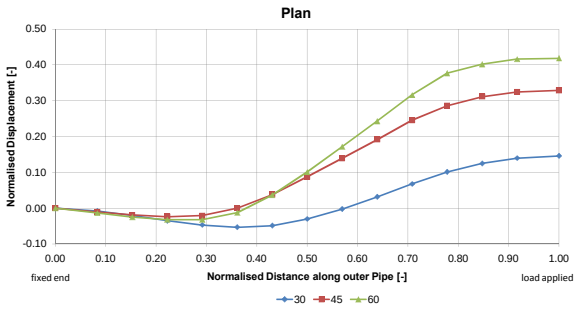

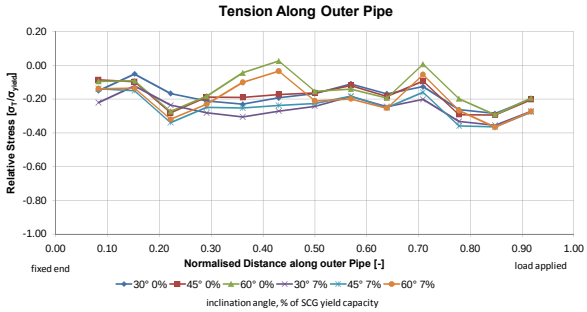

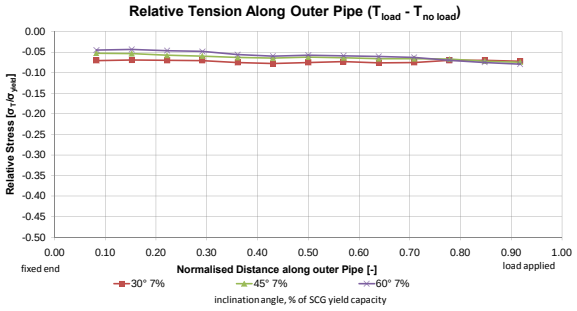

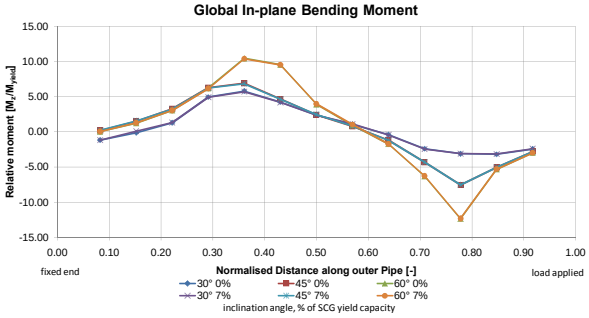

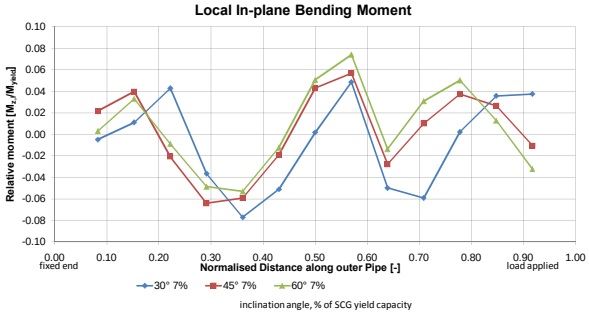

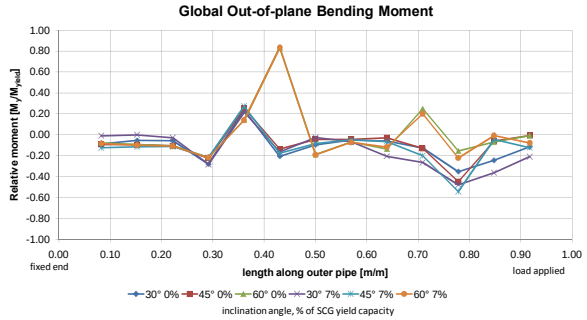

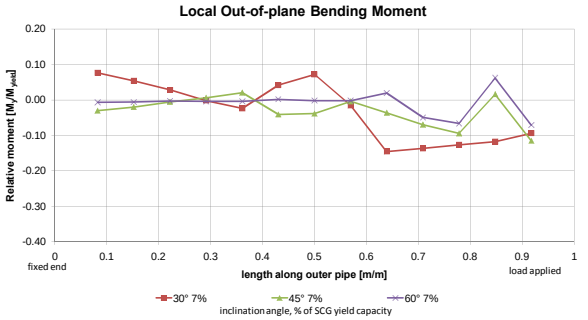

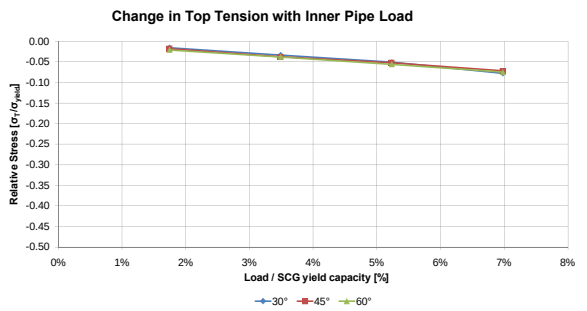

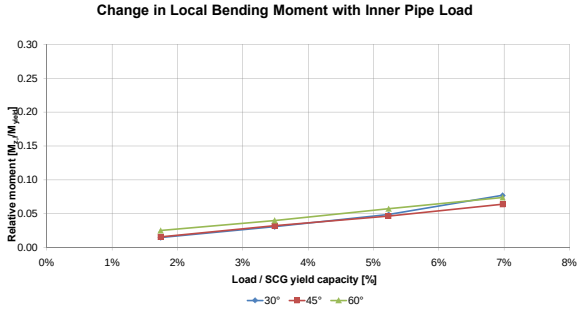

Appendix D: Numerical Model Test Results

D.1 Abaqus Input File sample

```
**-----------------------------------------------------------------
** Title: SCG Model Test, Phase 1, 30º bend
** Date: 2009 03 12
** Author: Simon Falser
**-----------------------------------------------------------------
*HEADING
 NUS Small Scale Local Bending Model
**
*RESTART, WRITE, FREQUENCY=1000
**
**-----------------------------------------------------------------
** Node Number, X (In-line), Y (Transverse), Z (Verticle)
**-----------------------------------------------------------------
*NODE
** SCG
 1, 0.0, 0.0, 0.0
 575, 5.75, 0.0, 0.0
**
** CT
 3001, 0.0, 0.0, 0.0
 3575, 5.75, 0.0, 0.0
**
*NGEN
  1, 575, 1
  3001, 3575, 1
**
**-----------------------------------------------------------------
** Element Definitions
**-----------------------------------------------------------------
*ELEMENT, TYPE=B31
  1, 1, 2
  3001, 3001, 3002
**
*ELGEN, ELSET=OuterPipe
  1, 574, 1
**
*ELGEN, ELSET=InnerPipe
  3001, 574, 1
**
*ELEMENT, TYPE=ITT31
  6001, 3001
*ELGEN, ELSET=PIP_Contact
  6001, 574, 1
**
**-----------------------------------------------------------------
** Element Properties
**-----------------------------------------------------------------
** Outer Diameter, Wall Thickness, (NL) Directional Cosigns,
(NL) Youngs Modulus, Torsional Shear,
**
*BEAM GENERAL SECTION, SECTION=PIPE,
DENSITY=7850.0, ELSET=OuterPipe
 0.00635, 0.00165,
 0.0, -1.0, 0.0
 207.00E9, 79.62E9
**
*BEAM GENERAL SECTION, SECTION=PIPE,
DENSITY=7850.0, ELSET=InnerPipe
 0.003, 0.001,
 0.0, -1.0, 0.0
 207.00E9, 79.62E9
**
**
**-----------------------------------------------------------------
** Pipe-in-pipe contact
**-----------------------------------------------------------------
*SLIDE LINE, TYPE=LINEAR, ELSET=PIP_Contact,
GENERATE
  1, 575, 1
*NODE PRINT, FREQUENCY=1
**
*Output, history, variable=PRESELECT
**
*INTERFACE, ELSET=PIP_Contact
  0.00335
*FRICTION
  0.3
**
**=======================================
** STEP 1
** Set up model pipe with initial boundry conditions
**=======================================
*STEP, NLGEOM, INC=100
*STATIC
  0.01, 1.0
**
** Boundary conditions
**-----------------------------------------------------------------
*BOUNDARY
  1, ENCASTRE
  3001, ENCASTRE
**
        575, 1, 1, 0.0
        575, 2, 2, 0.0
        575, 3, 3, 0.0
        575, 5, 5, 0.0
        575, 6, 6, 0.0
**
        3575, 2, 2, 0.0
        3575, 3, 3, 0.0
        3575, 5, 5, 0.0
        3575, 6, 6, 0.0
**
  57, 3, 3, 0.0
  115, 3, 3, 0.0
  172, 3, 3, 0.0
  230, 3, 3, 0.0
  287, 3, 3, 0.0
  345, 3, 3, 0.0
  402, 3, 3, 0.0
  460, 3, 3, 0.0
  517, 3, 3, 0.0
**
** Top tension (for initial problem setup with straight pipe)
** CLOAD  (Node, DOF, Magnitude)
*CLOAD
  575, 1, 1.0e2
 3575, 1, 1.0e2
**
*DLOAD
** Gravity
**-----------------------------------------------------------------
  , GRAV, 9.806, -0.01, 0.0, -1.0
**
*MONITOR, NODE=575, DOF=1
**
**-----------------------------------------------------------------
** Results
** Ensure results are recorded in the database
**-----------------------------------------------------------------
**
*OUTPUT, OP=NEW, FIELD, FREQUENCY=1
*ELEMENT OUTPUT
  SF, COORD, ESF1
*NODE OUTPUT
  U, COORD
**
**-----------------------------------------------------------------
** Print selected results to a results file
**-----------------------------------------------------------------
**


*END STEP
**
**=======================================
** STEP 2
```

```
** Move top of SCG to far vessel position
**=======================================
*STEP, NLGEOM, INC=100
*STATIC
 0.05, 1.0
**
*BOUNDARY
 575, 2, 2, 0.8
 3575, 2, 2, 0.8
**
*MONITOR, NODE=500, DOF=2
*END STEP
**
**=======================================
** STEP 3
** Release top tension and move top of guide to sea level, bending guide
**=======================================
*STEP, NLGEOM, INC=1000
*STATIC
 0.001, 1.0
**
*BOUNDARY
 575, 1, 1, -0.25
**
*MONITOR, NODE=500, DOF=1
*END STEP
**
**=======================================
** STEP 4
** Apply tension to inner pipe 343 N
**=======================================
*STEP, NLGEOM, INC=1000
*STATIC
 0.001, 1.0
**
*CLOAD
 3575, 1, 343.0
**
*MONITOR, NODE=500, DOF=1
*END STEP
**
**
**=======================================
** STEP 5
** Apply tension to inner pipe 986 N
**=======================================
*STEP, NLGEOM, INC=1000
*STATIC
 0.001, 1.0
**
*CLOAD
 3575, 1, 986.0
**
*MONITOR, NODE=500, DOF=1
*END STEP
**
**
**
**=======================================
** STEP 6
** Apply tension to inner pipe 1478 N
**=======================================
*STEP, NLGEOM, INC=1000
*STATIC
 0.001, 1.0
**
*CLOAD
 3575, 1, 1478.0
**
*MONITOR, NODE=500, DOF=1
*END STEP
**
**
**=======================================
** STEP 7
** Apply tension to inner pipe 1961 N
**=======================================
*STEP, NLGEOM, INC=1000
*STATIC
 0.001, 1.0
**
*CLOAD
 3575, 1, 1961.0
**
*MONITOR, NODE=500, DOF=1
*END STEP
**
**=======================================
** STEP 8
** Apply tension to inner pipe 2451 N
**=======================================
*STEP, NLGEOM, INC=1000
*STATIC
 0.001, 1.0
**
*CLOAD
 3575, 1, 2451.0
**
*MONITOR, NODE=500, DOF=1
*END STEP
**
**=======================================**
STEP 9
** Apply tension to inner pipe 2941 N
**=======================================
*STEP, NLGEOM, INC=1000
*STATIC
 0.001, 1.0
**
*CLOAD
 3575, 1, 2941.0
**
*MONITOR, NODE=500, DOF=1
*END STEP
**
**=======================================
** STEP 10
** Apply tension to inner pipe 3432 N
**=======================================
*STEP, NLGEOM, INC=1000
*STATIC
 0.001, 1.0
**
*CLOAD
 3575, 1, 3432.0
**
*MONITOR, NODE=500, DOF=1
*END STEP
**
**=======================================
** STEP 11
** Apply tension to inner pipe 3922 N
**=======================================
*STEP, NLGEOM, INC=1000
*STATIC
 0.001, 1.0
**
*CLOAD
 3575, 1, 3922.0
**
*MONITOR, NODE=500, DOF=1
*END STEP
**
```

Phase 1 N

12.7 mm Outer Pipe, 6 mm Inner Pipe

30° Inclination Angle

Pipe in Pipe Interaction using Numerical Model

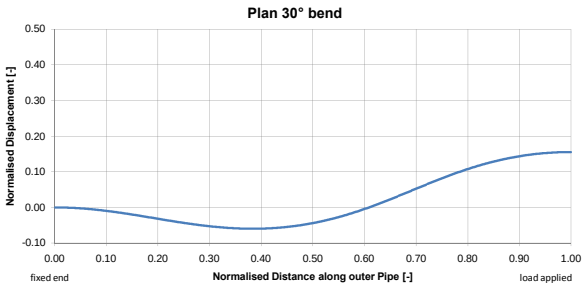

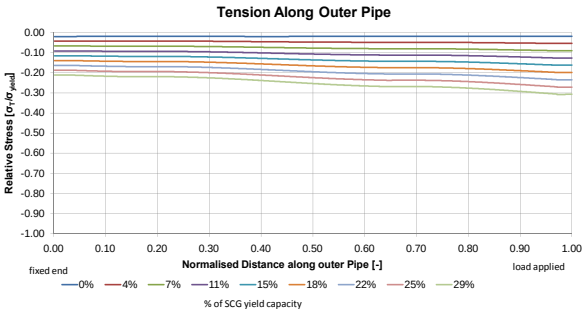

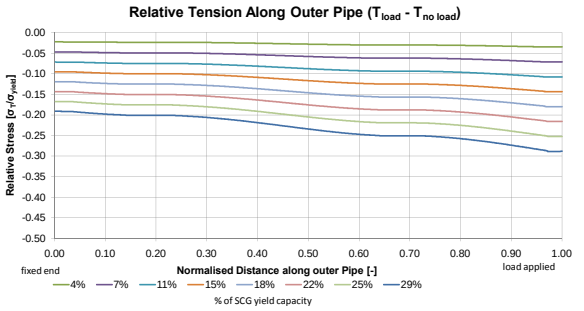

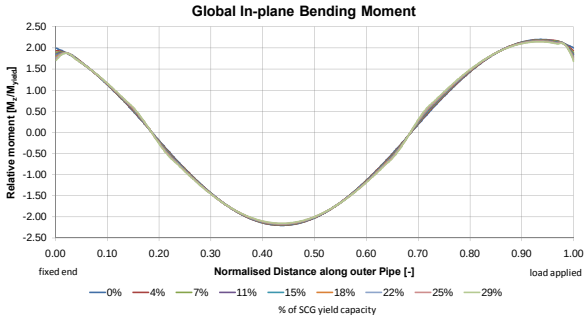

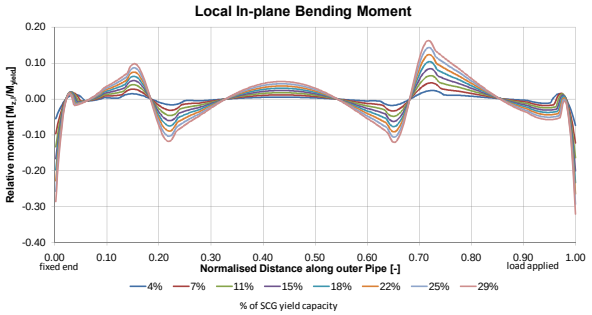

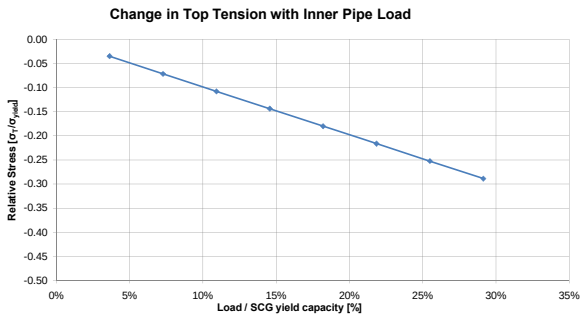

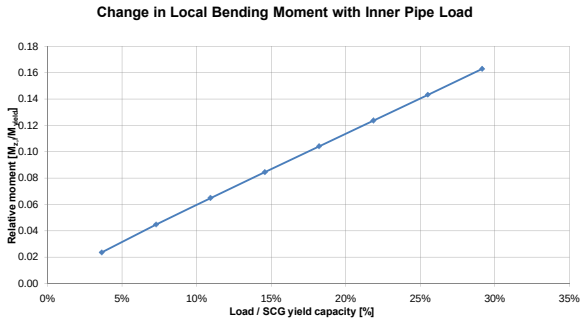

Phase 1 N

12.7 mm Outer Pipe, 6 mm Inner Pipe

45° Inclination Angle

Pipe in Pipe Interaction using Numerical Model

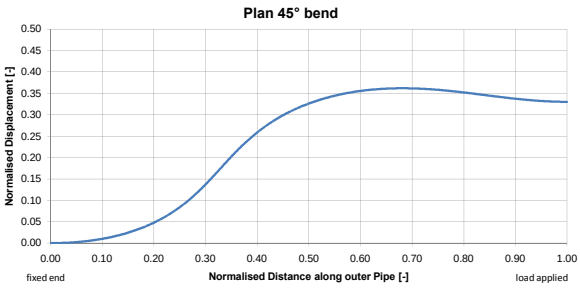

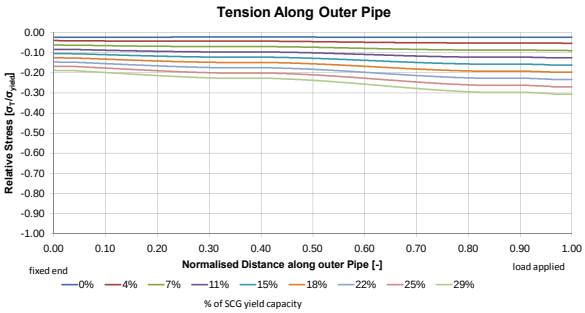

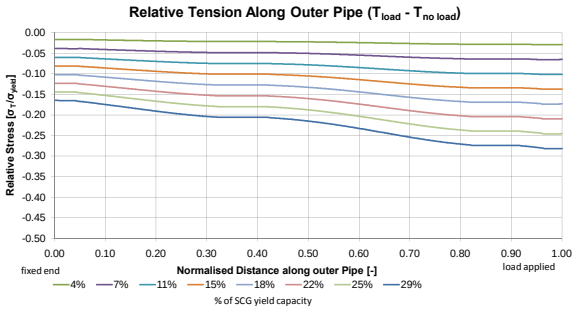

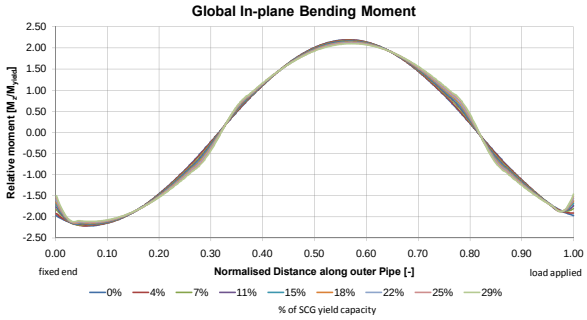

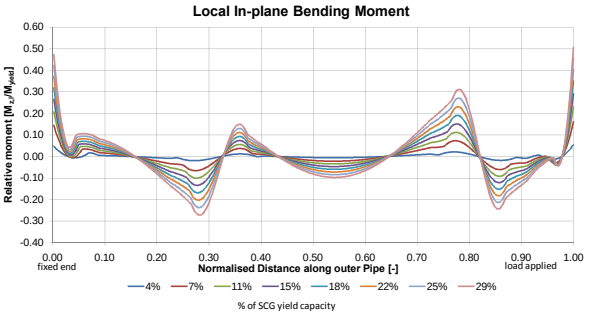

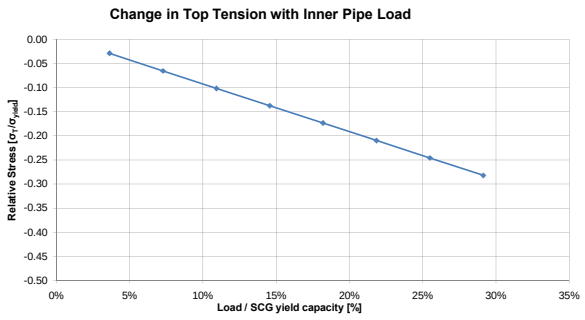

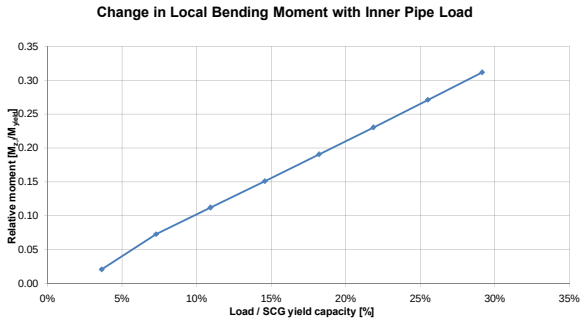

Phase 1 N

12.7 mm Outer Pipe, 6 mm Inner Pipe

60° Inclination Angle

Pipe in Pipe Interaction using Numerical Model

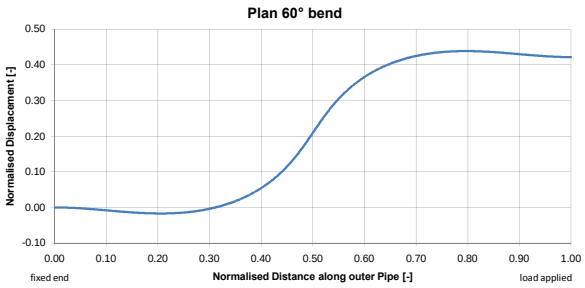

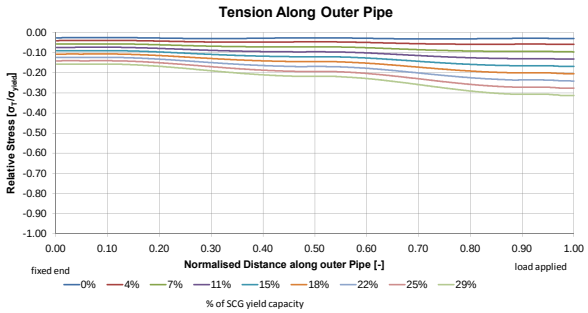

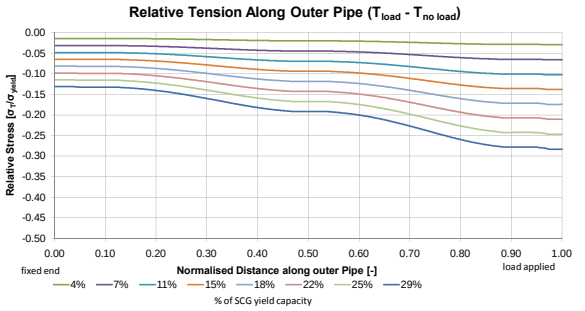

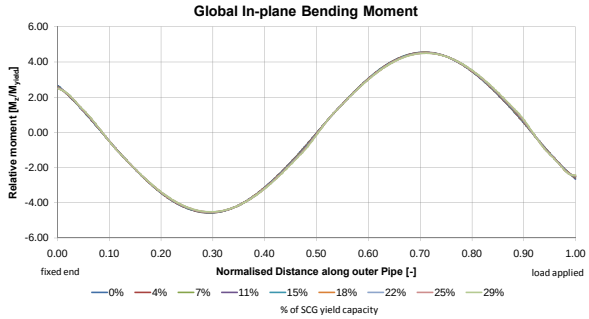

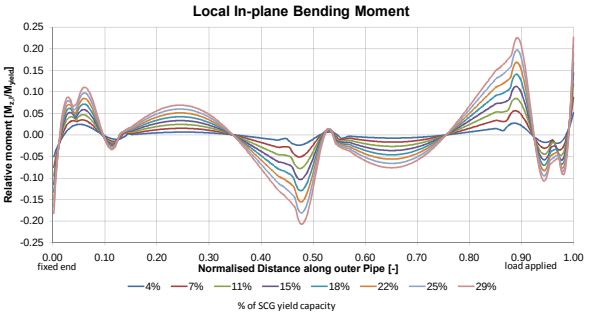

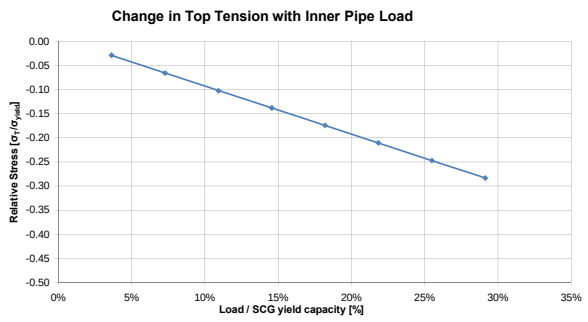

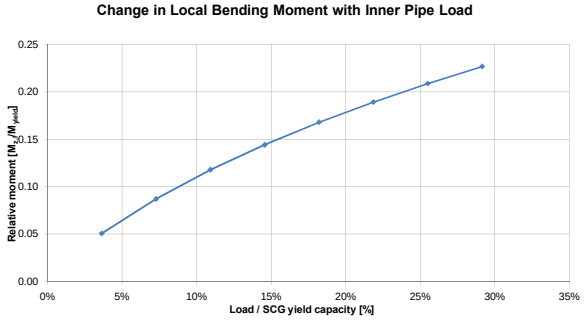

Phase 2 N

12.7 mm Outer Pipe, 2 mm Wire

30° Inclination Angle

Pipe in Pipe Interaction using Numerical Model

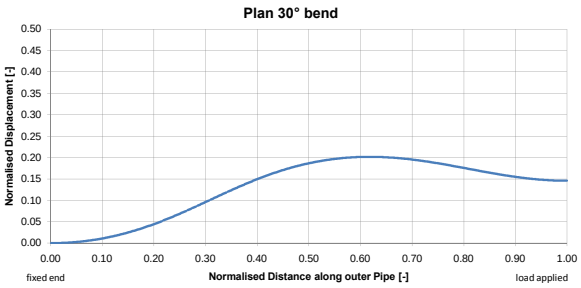

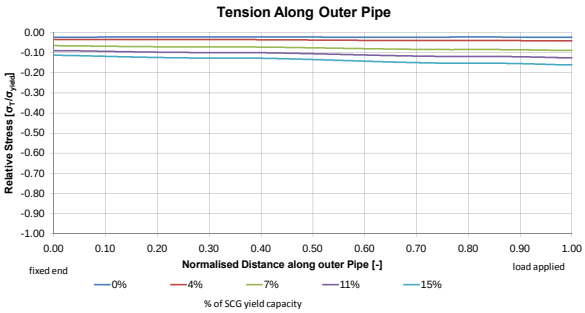

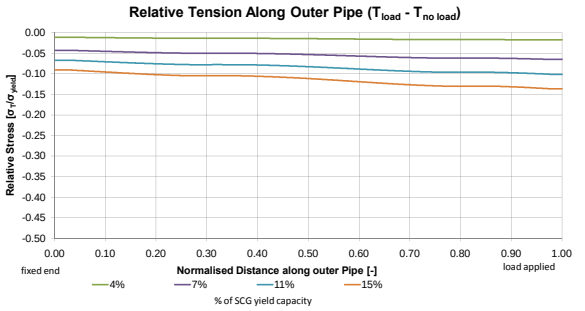

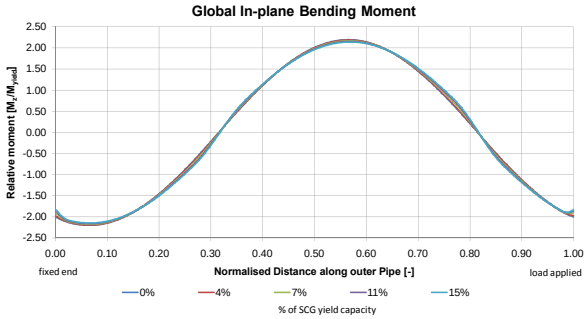

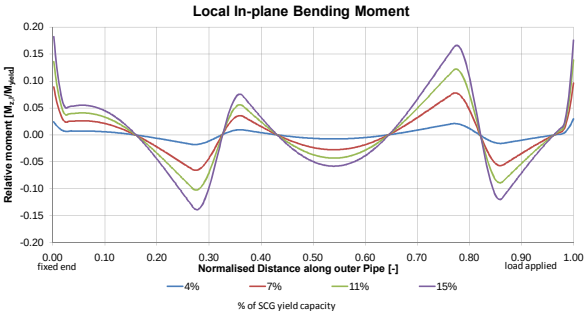

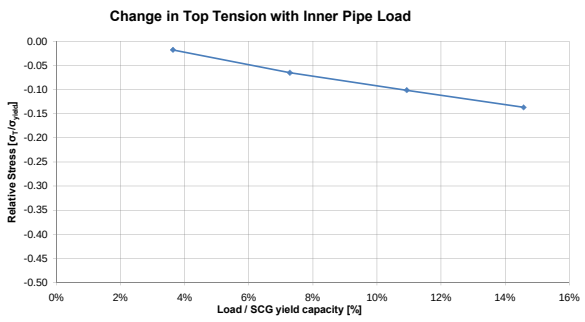

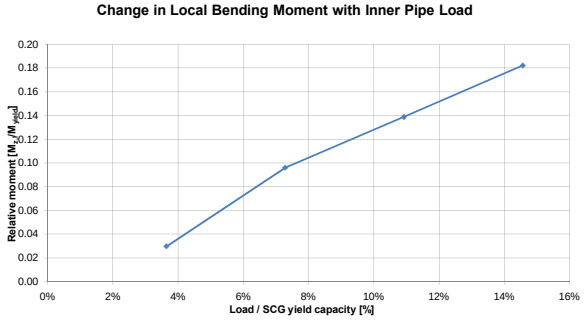

Phase 2 N

12.7 mm Outer Pipe, 2 mm Wire

45° Inclination Angle

Pipe in Pipe Interaction using Numerical Model

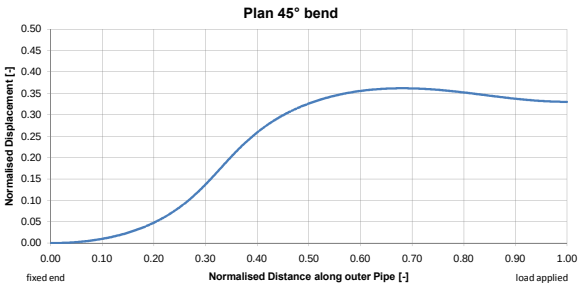

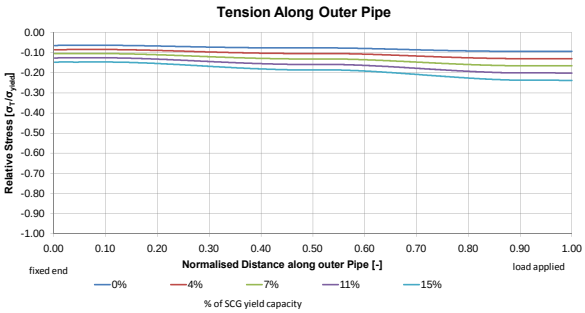

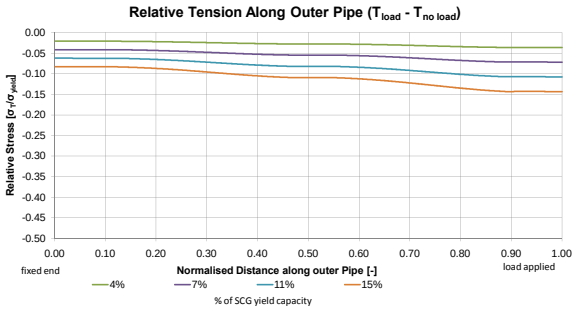

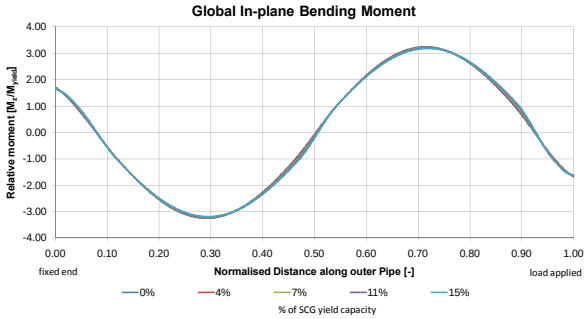

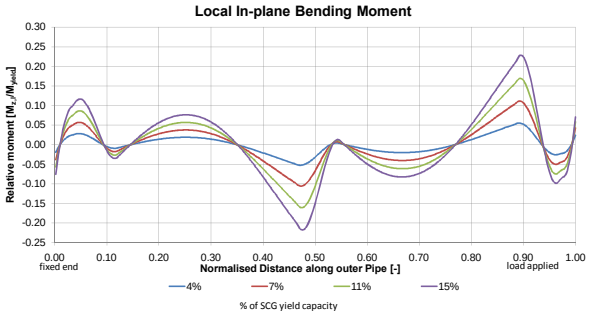

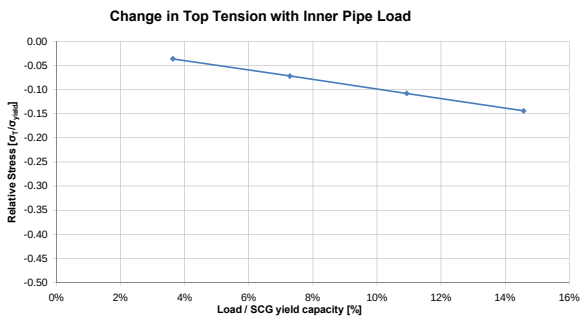

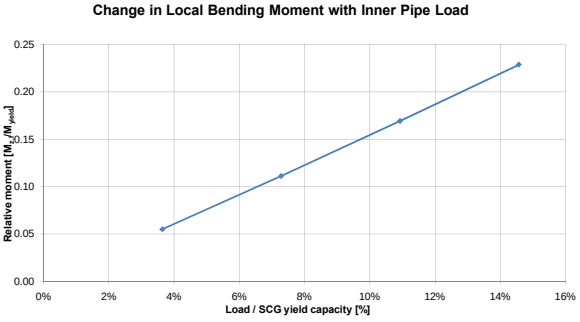

Phase 2 N

12.7 mm Outer Pipe, 2 mm Wire

60° Inclination Angle

Pipe in Pipe Interaction using Numerical Model

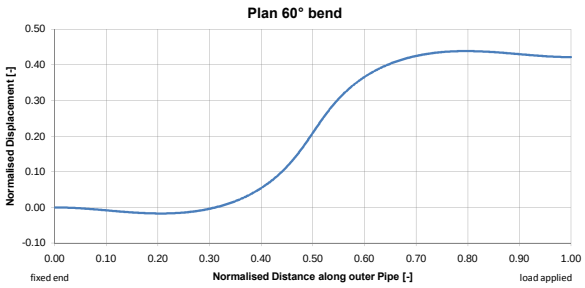

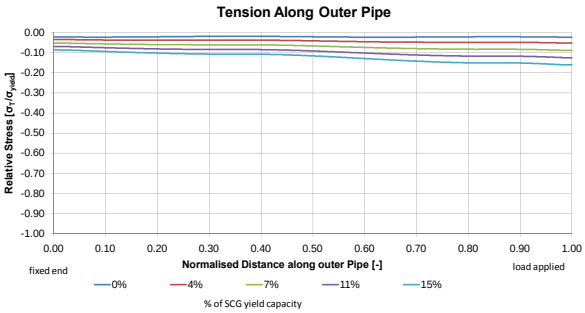

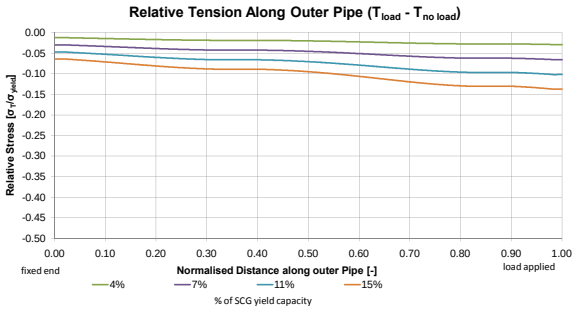

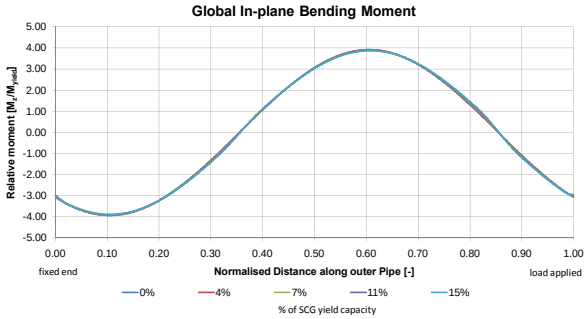

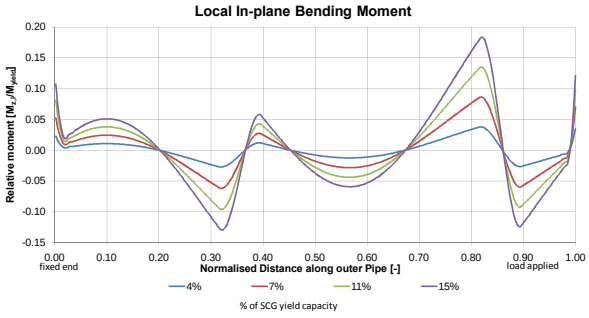

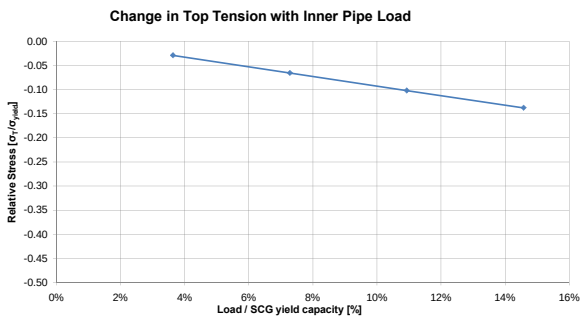

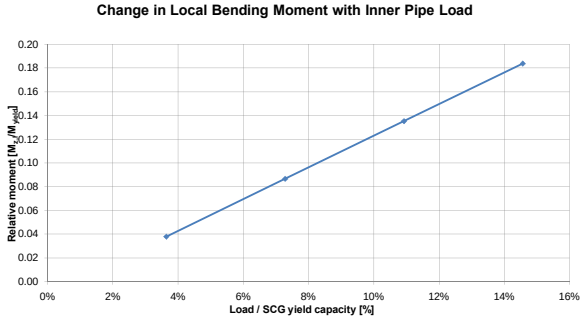

Phase 3 N

25.4 mm Outer Pipe, 6 mm Inner Pipe

30° Inclination Angle

Pipe in Pipe Interaction using Numerical Model

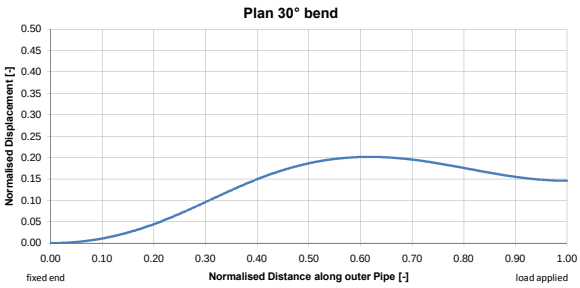

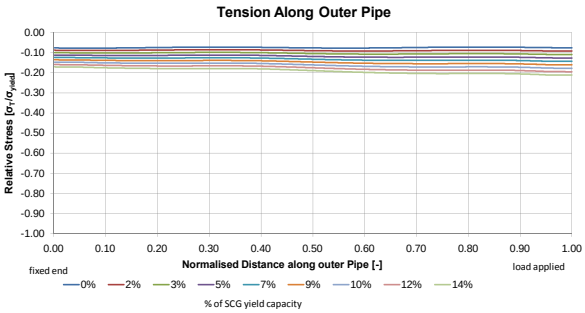

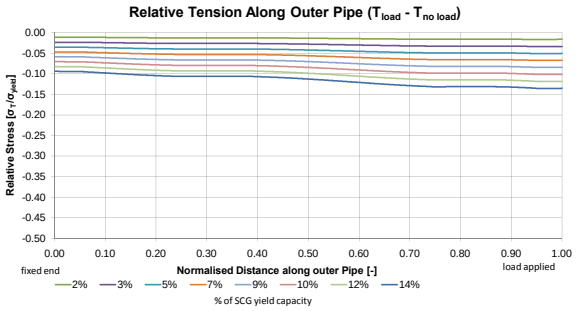

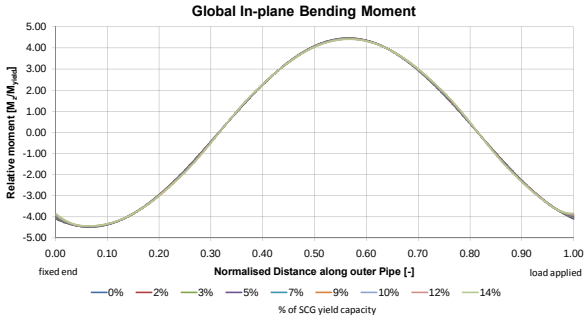

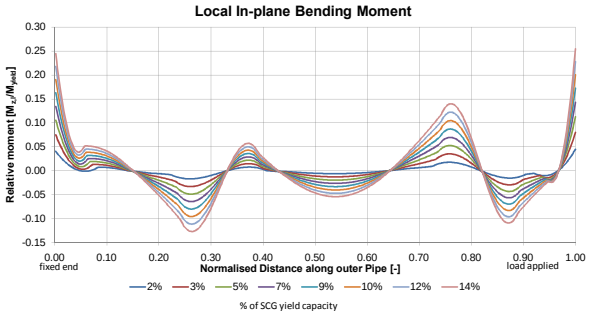

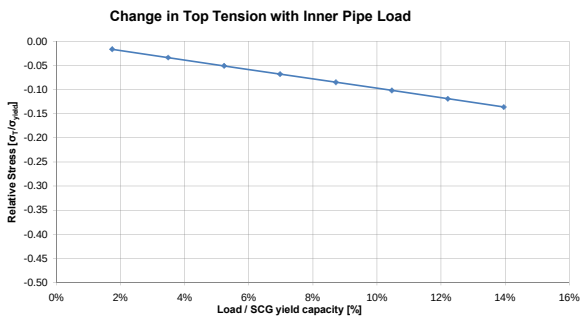

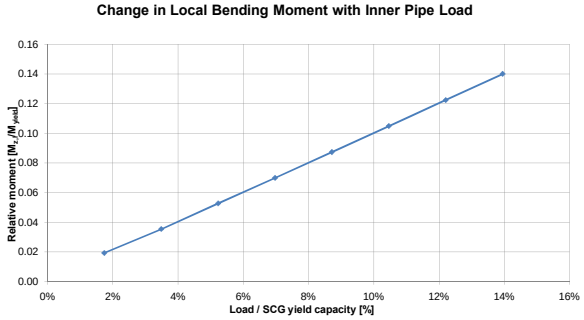

Phase 3 N

25.4 mm Outer Pipe, 6 mm Inner Pipe

45° Inclination Angle

Pipe in Pipe Interaction using Numerical Model

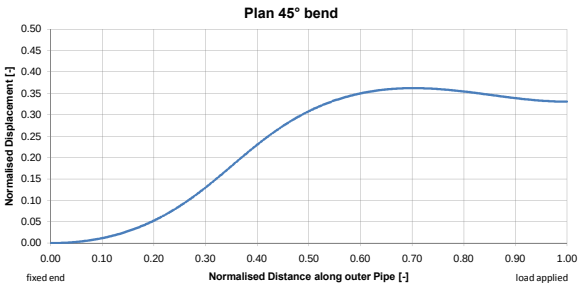

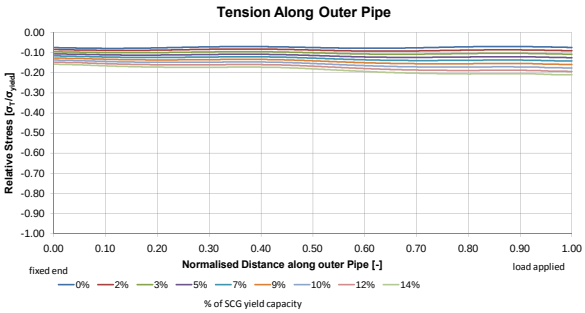

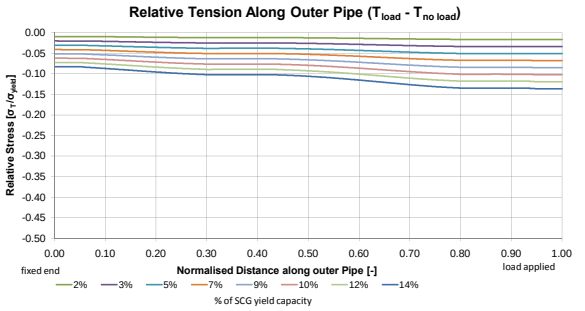

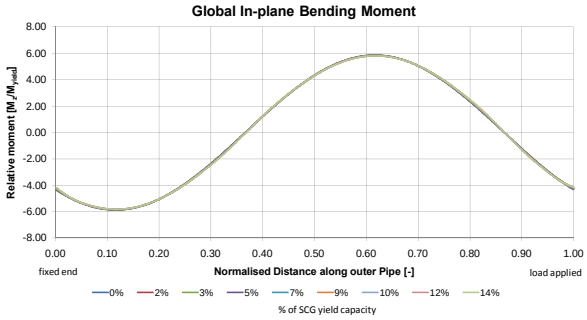

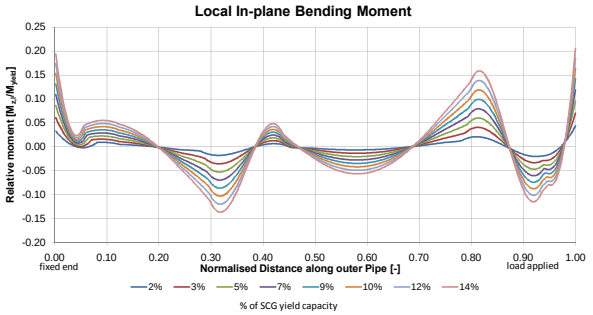

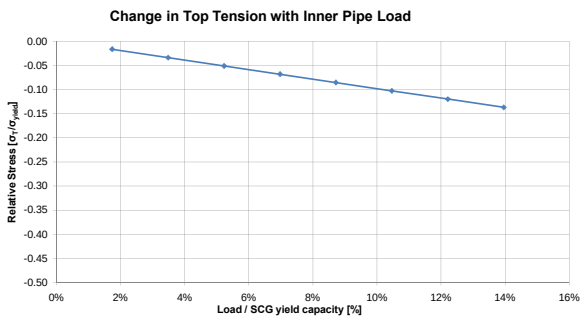

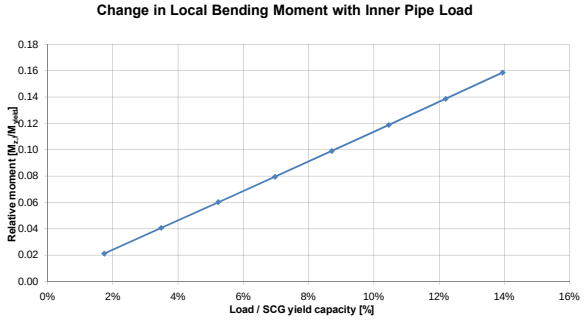

Phase 3 N

25.4 mm Outer Pipe, 6 mm Inner Pipe

60° Inclination Angle

Pipe in Pipe Interaction using Numerical Model

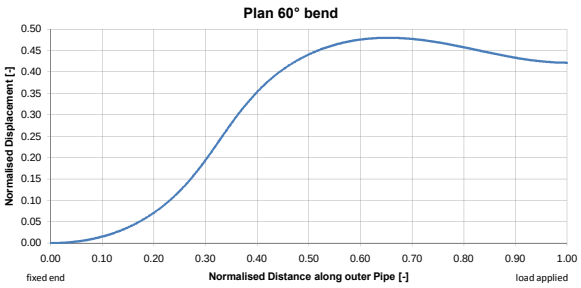

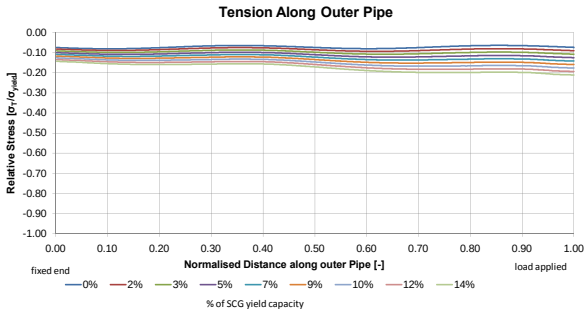

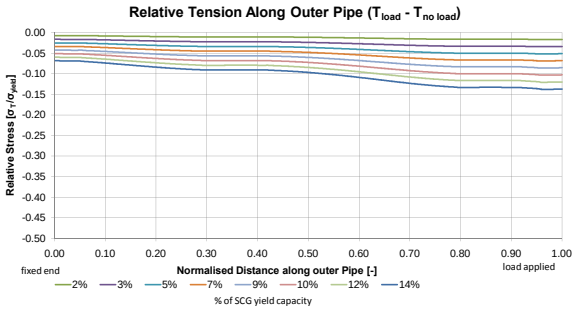

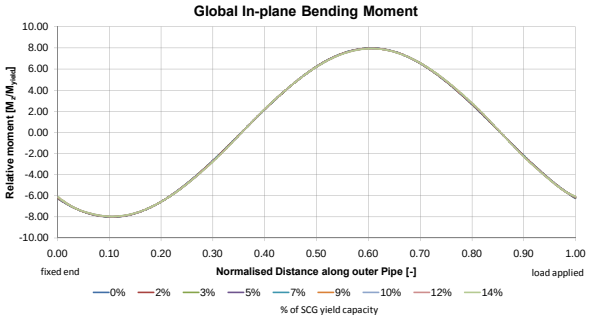

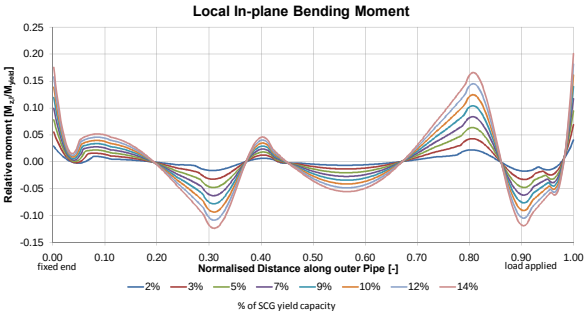

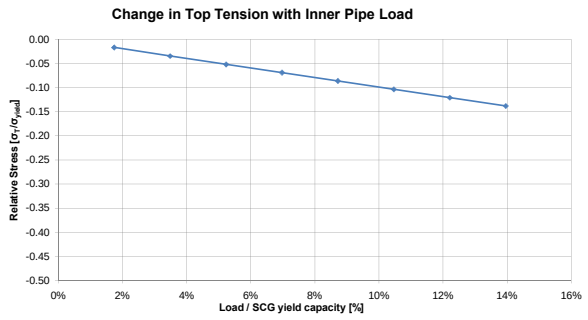

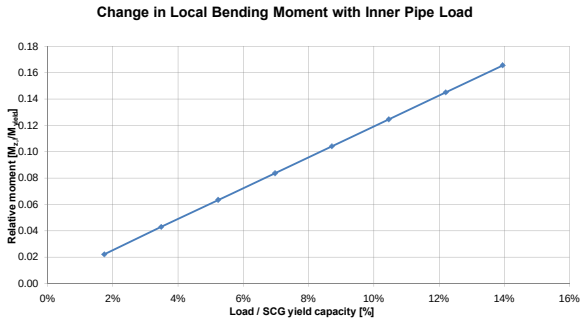

Phase 4 N

25.4 mm Outer Pipe, 2 mm Wire

30° Inclination Angle

Pipe in Pipe Interaction using Numerical Model

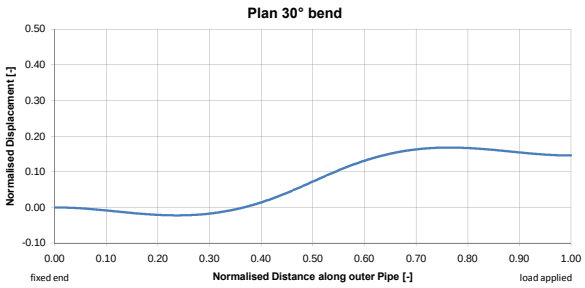

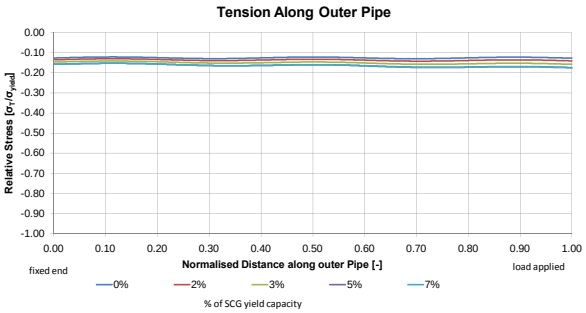

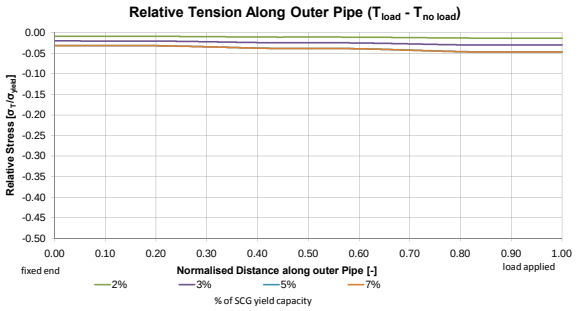

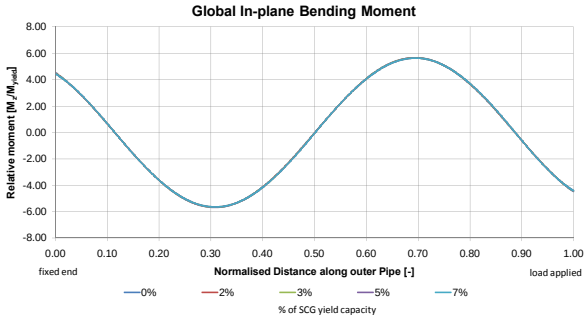

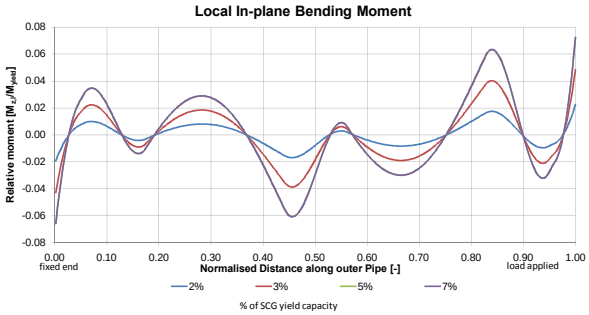

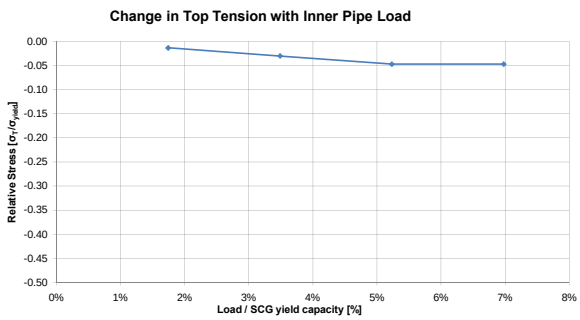

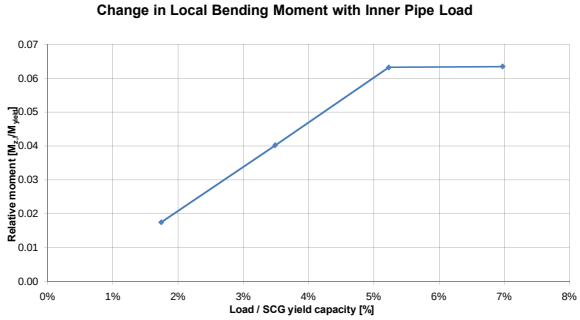

Phase 4 N

25.4 mm Outer Pipe, 2 mm Wire

45° Inclination Angle

Pipe in Pipe Interaction using Numerical Model

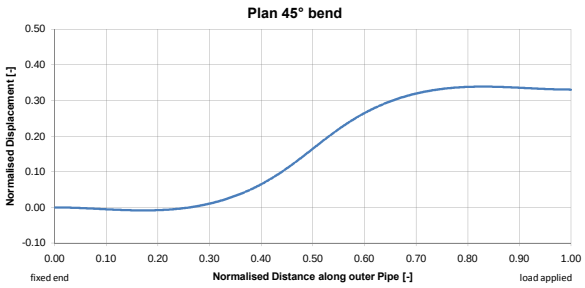

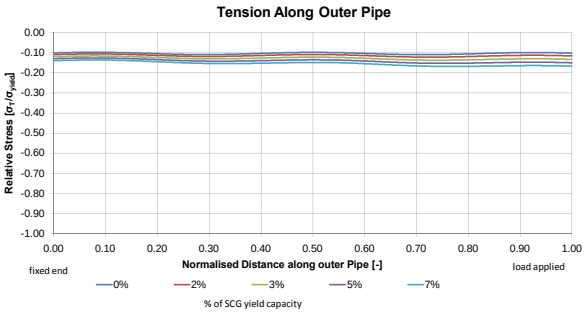

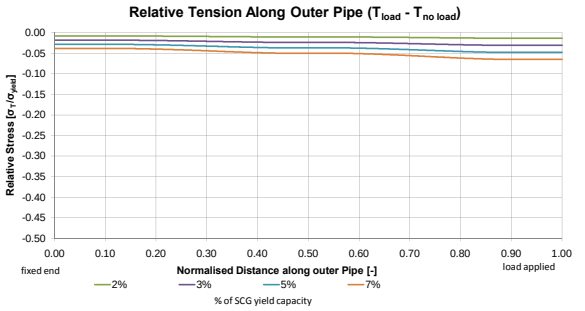

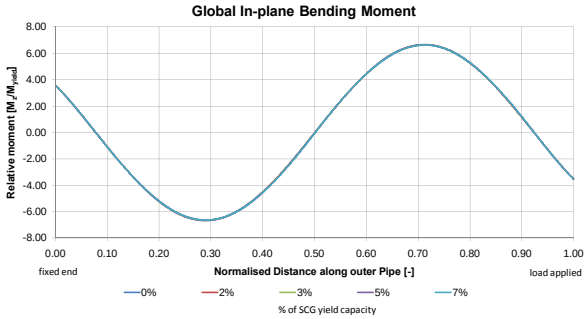

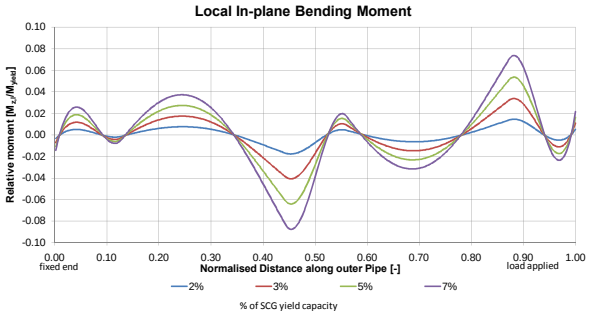

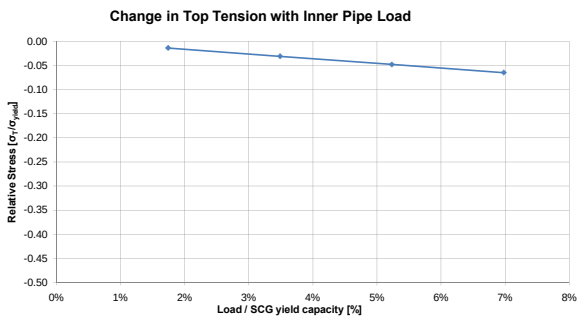

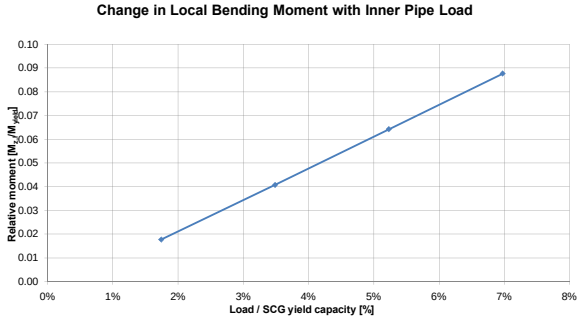

Phase 4 N

25.4 mm Outer Pipe, 2 mm Wire

60° Inclination Angle

Pipe in Pipe Interaction using Numerical Model

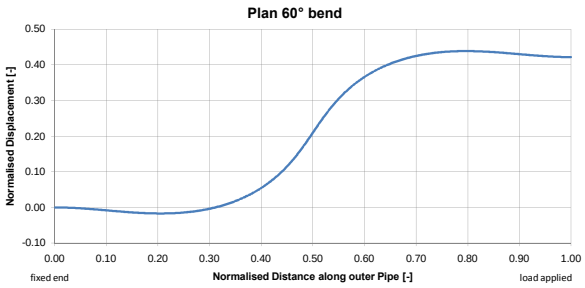

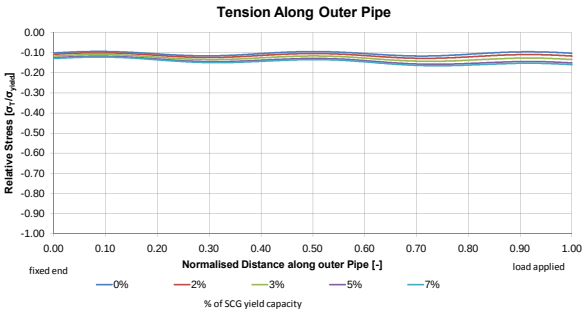

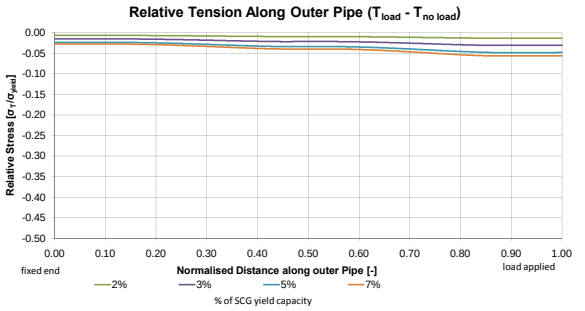

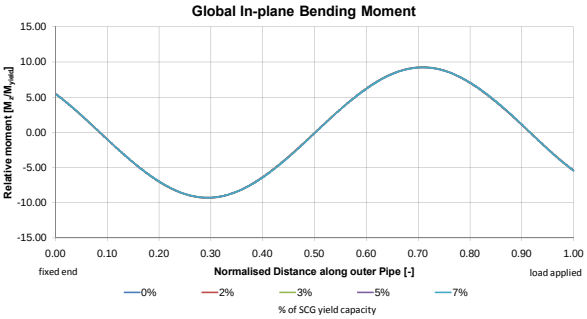

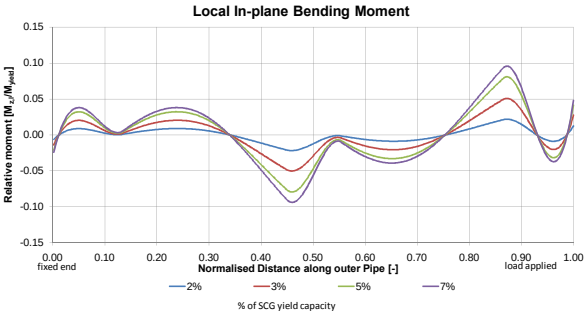

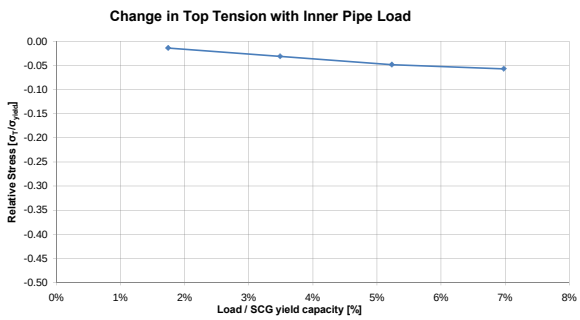

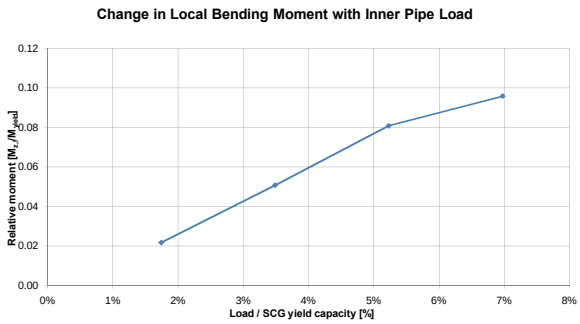

Appendix E: Numerical Model Test – Comparison of different Pipe-in-Pipe Diameter Ratios

30° Inclination Angle

Comparison of different Pipe in Pipe Diameter Ratios

Pipe in Pipe Interaction using Numerical Model

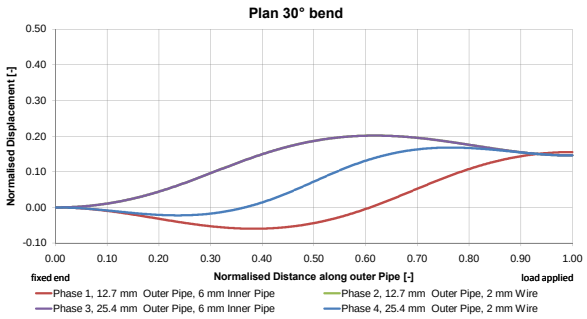

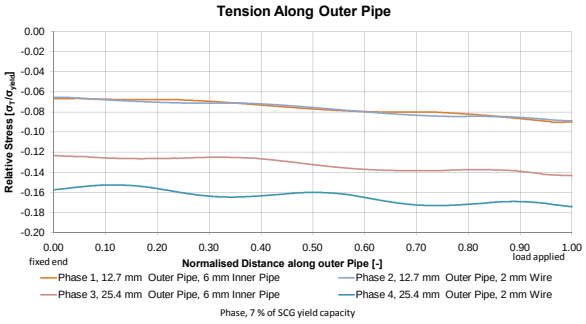

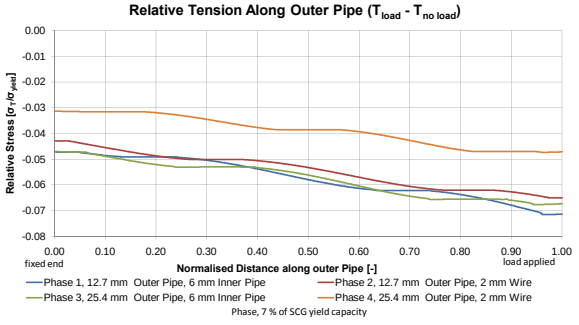

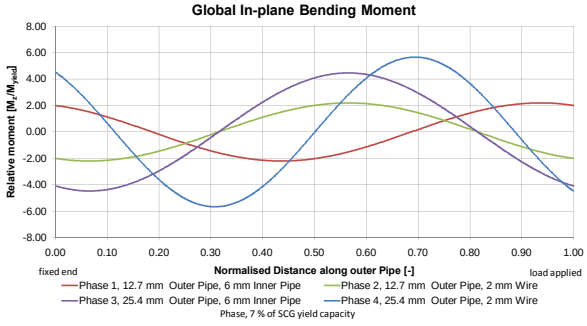

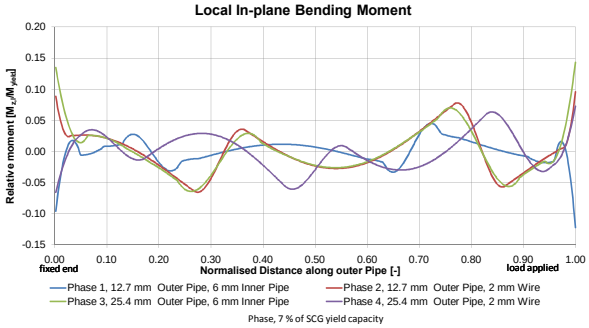

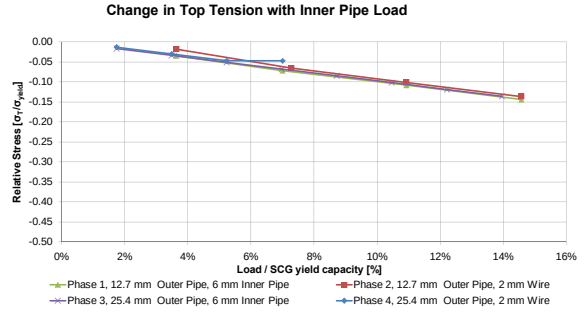

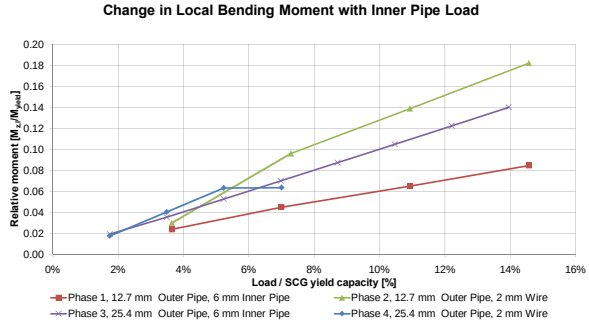

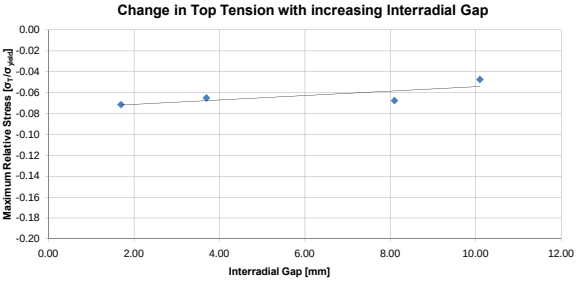

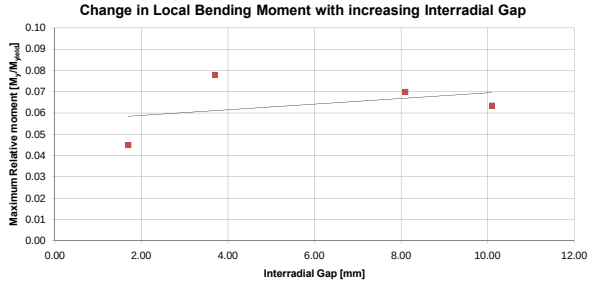

45° Inclination Angle

Comparison of different Pipe in Pipe Diameter Ratios

Pipe in Pipe Interaction using Numerical Model

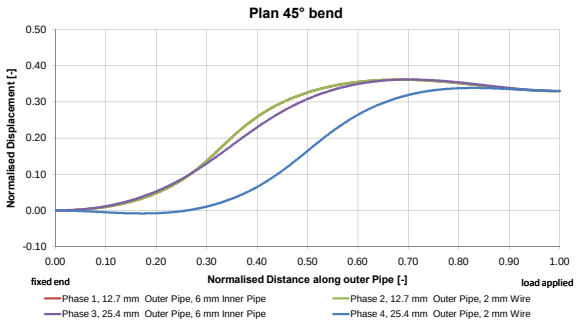

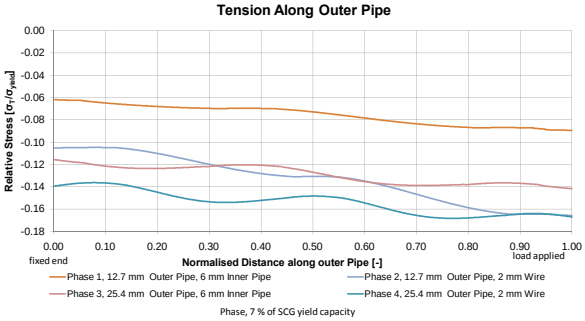

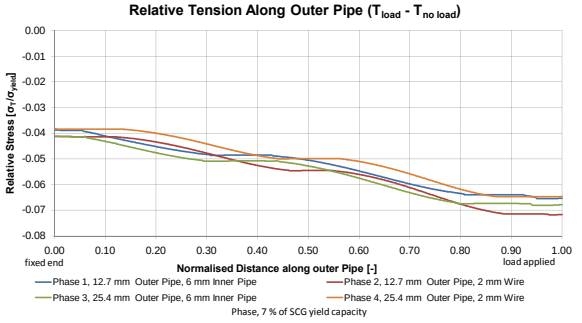

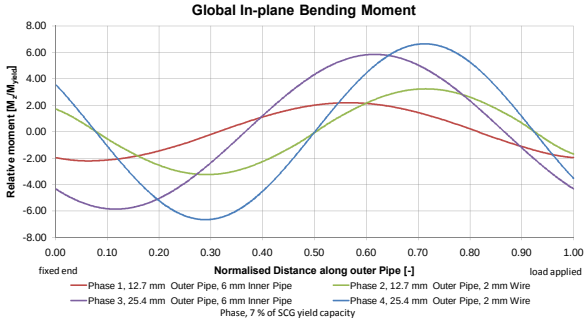

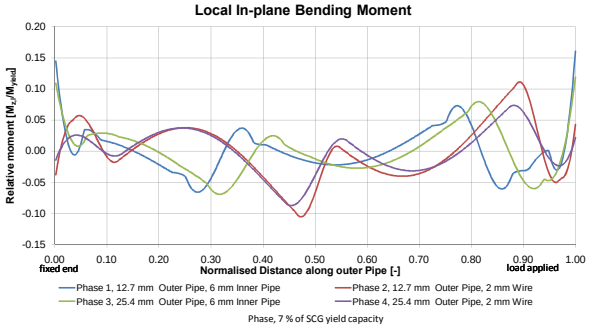

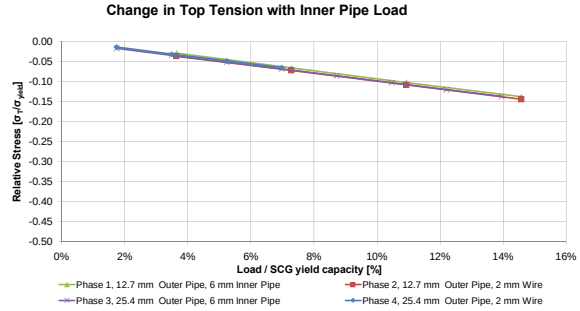

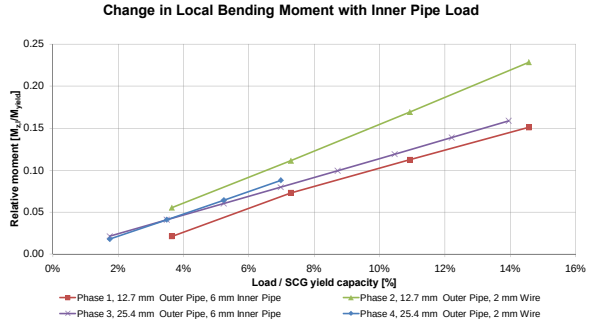

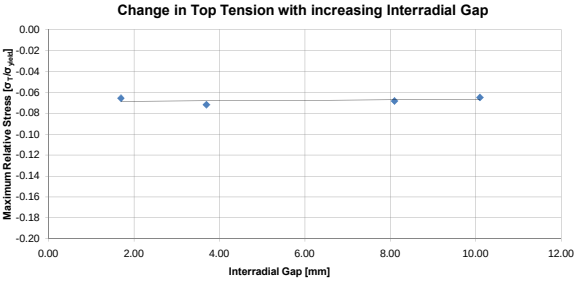

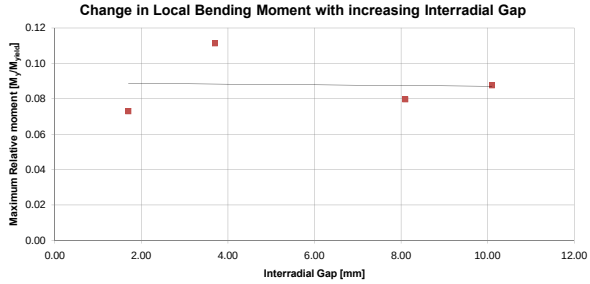

60° Inclination Angle

Comparison of different Pipe in Pipe Diameter Ratios

Pipe in Pipe Interaction using Numerical Model

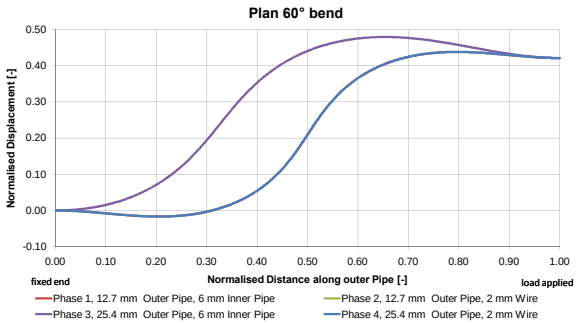

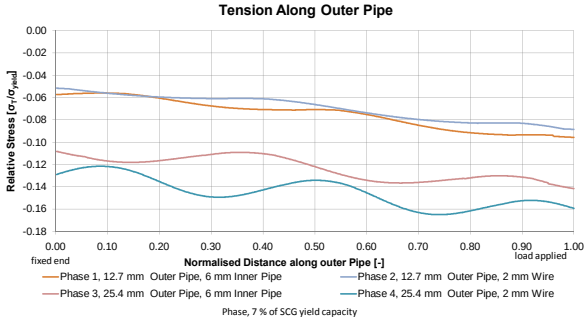

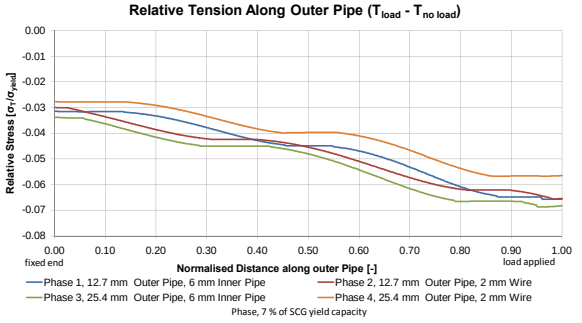

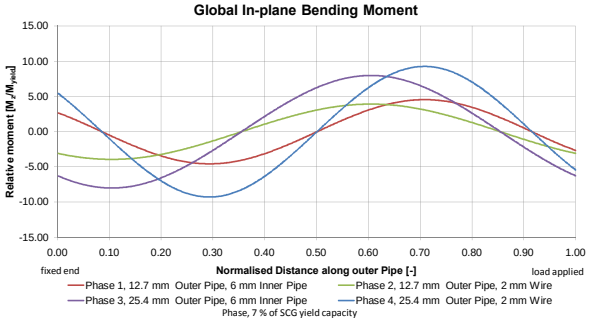

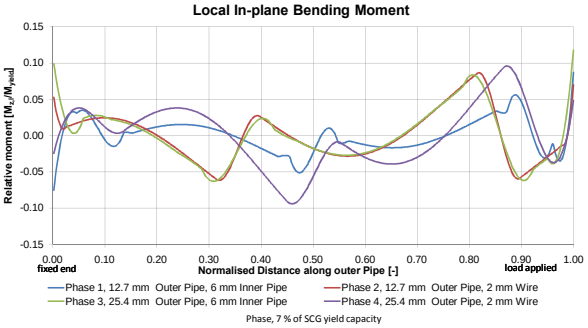

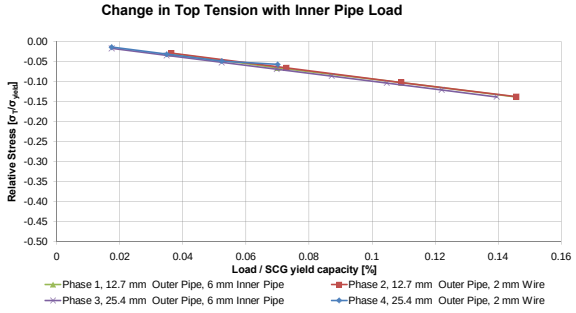

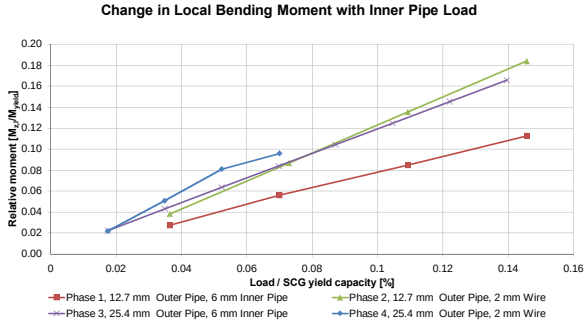

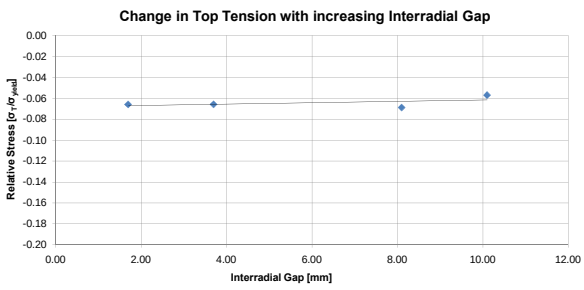

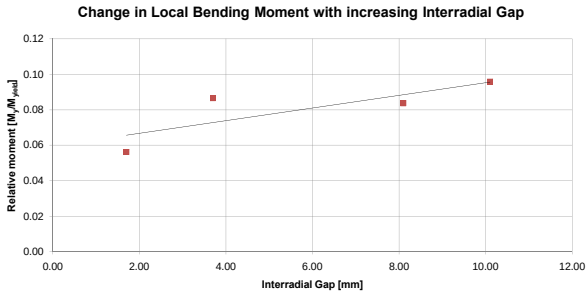

Appendix F: Comparison of Physical- and Numerical Test Results

Phase 1

12.7 mm Outer Pipe, 6 mm Inner Pipe

30° Inclination Angle

Comparison between Physical- and Numerical Model

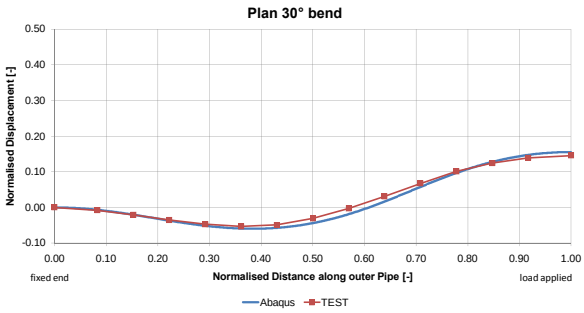

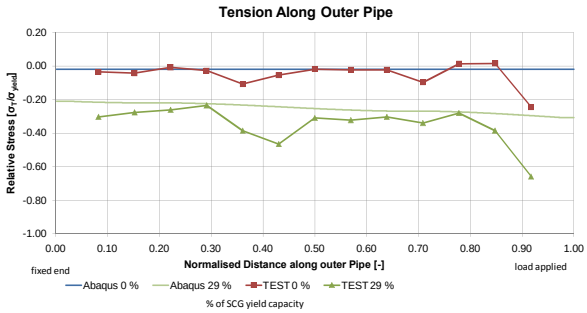

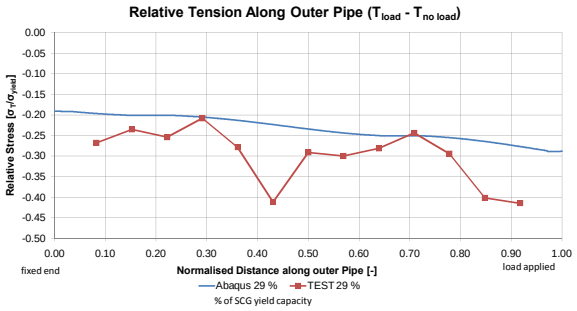

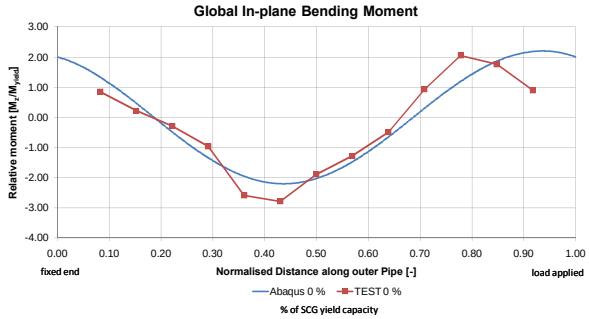

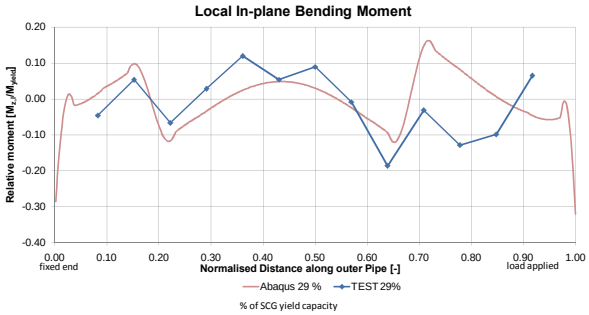

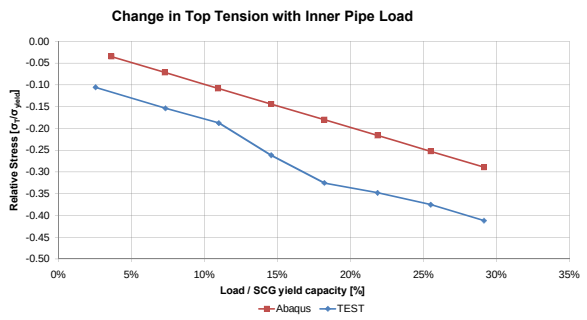

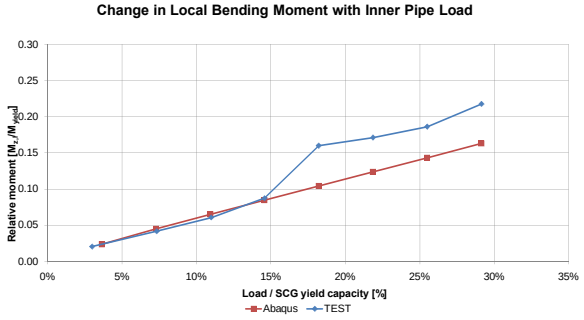

Phase 1

12.7 mm Outer Pipe, 6 mm Inner Pipe

45° Inclination Angle

Comparison between Physical- and Numerical Model

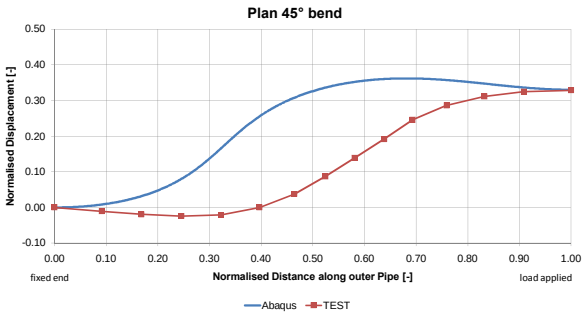

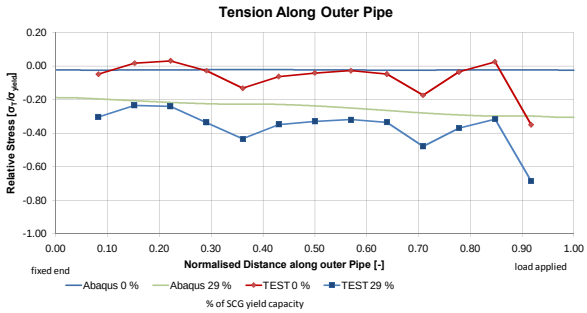

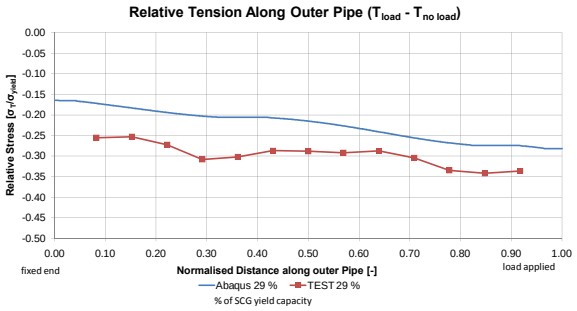

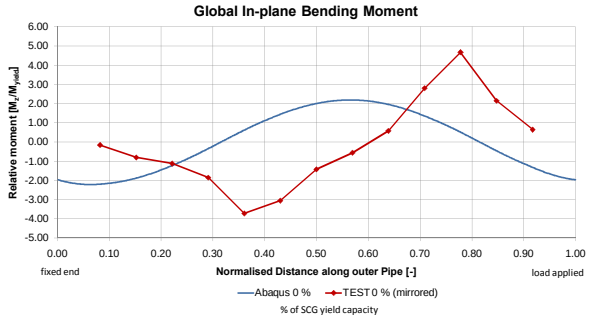

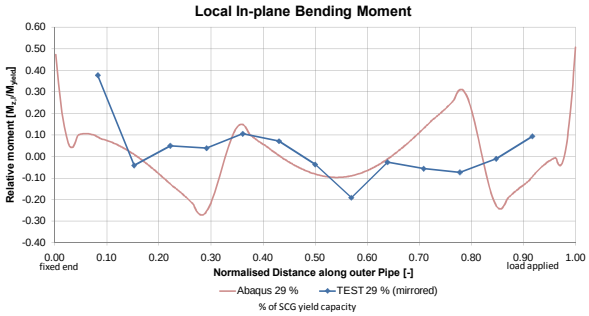

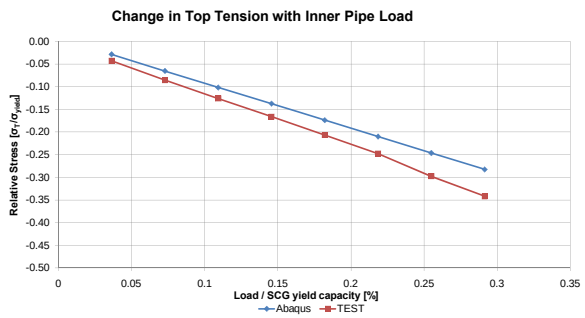

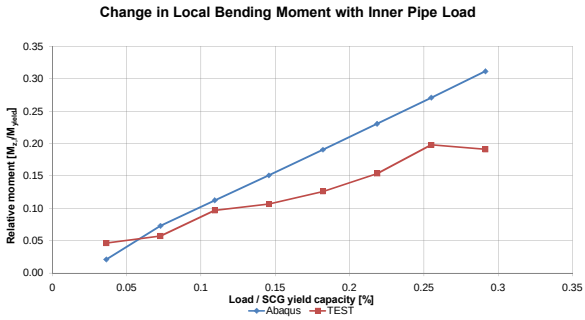

Phase 1

12.7 mm Outer Pipe, 6 mm Inner Pipe

60° Inclination Angle

Comparison between Physical- and Numerical Model

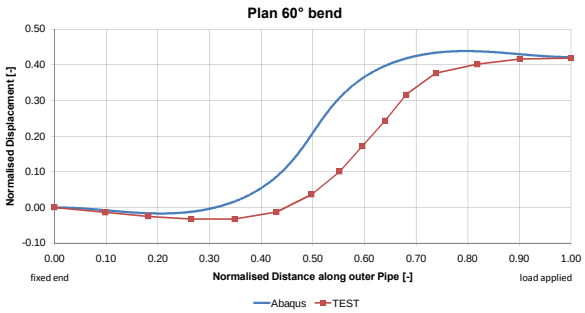

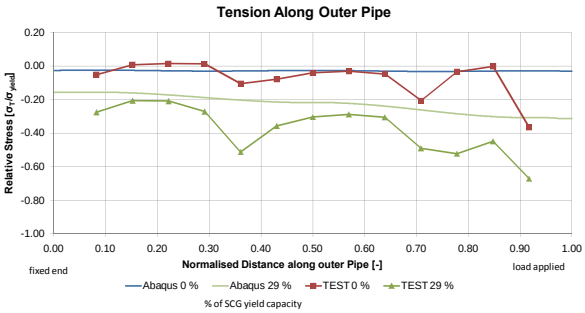

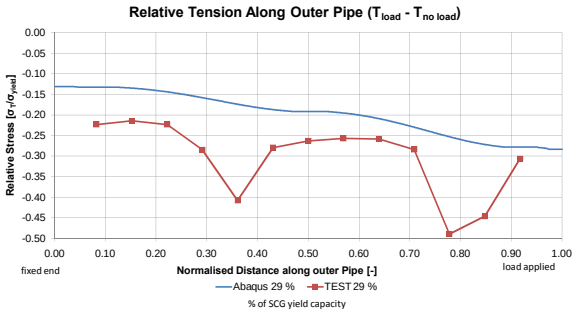

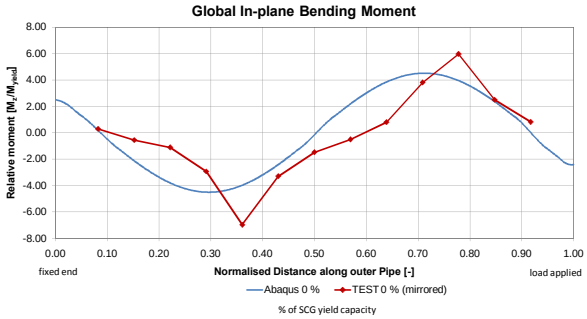

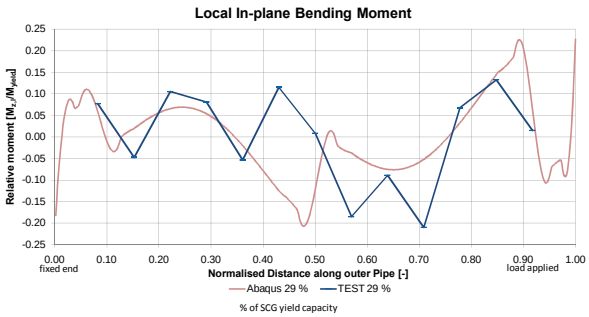

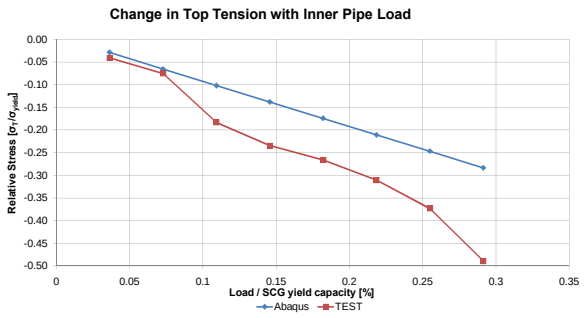

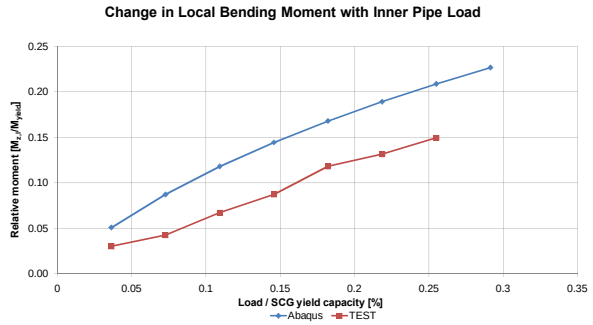

Phase 2

12.7 mm Outer Pipe, 2 mm Wire

30° Inclination Angle

Comparison between Physical- and Numerical Model

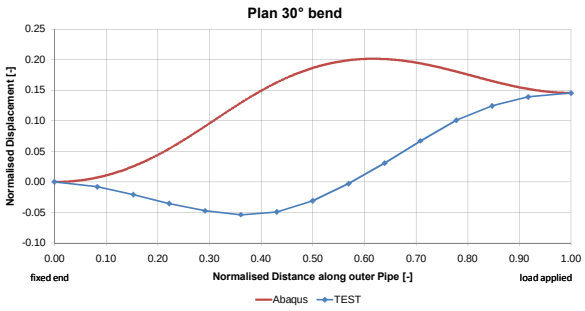

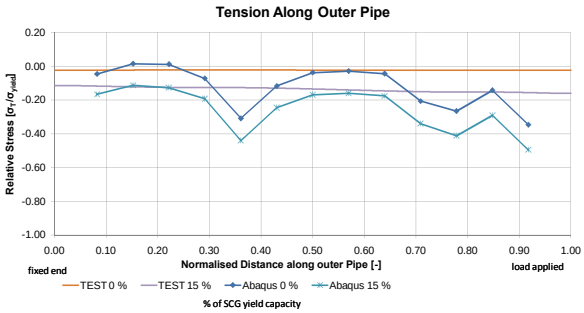

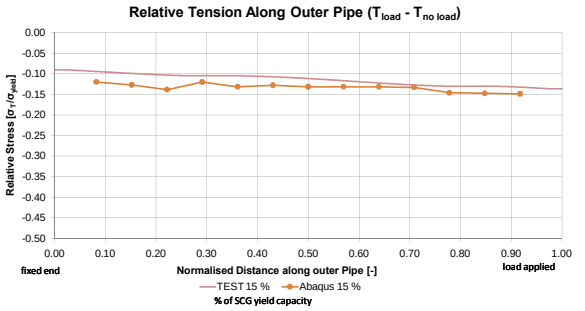

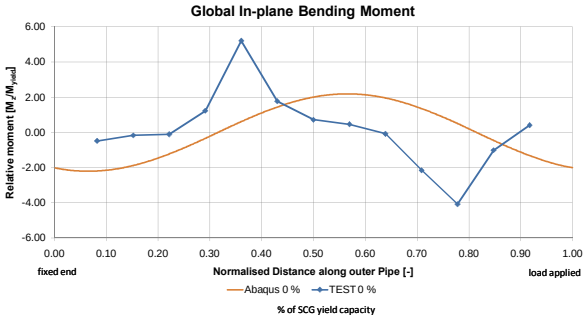

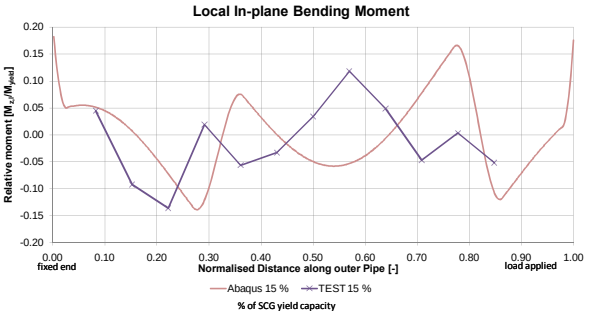

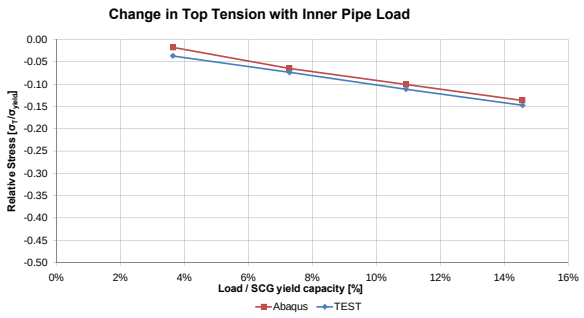

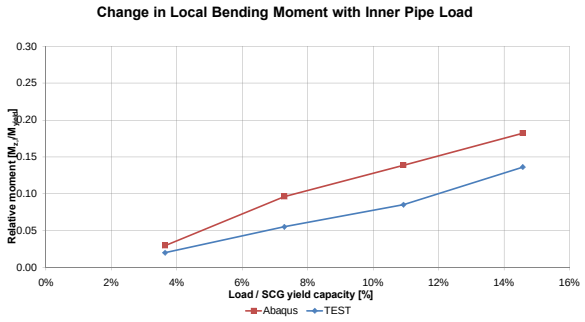

Phase 2

12.7 mm Outer Pipe, 2 mm Wire

45° Inclination Angle

Comparison between Physical- and Numerical Model

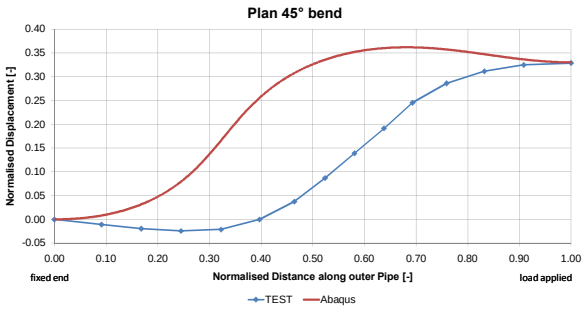

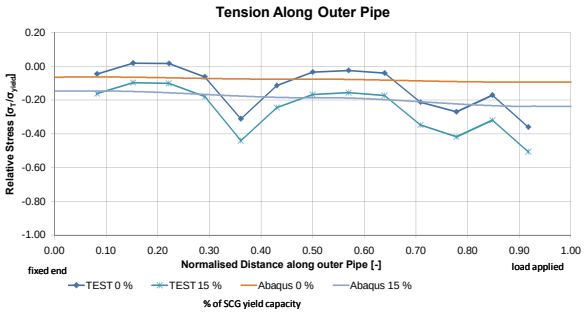

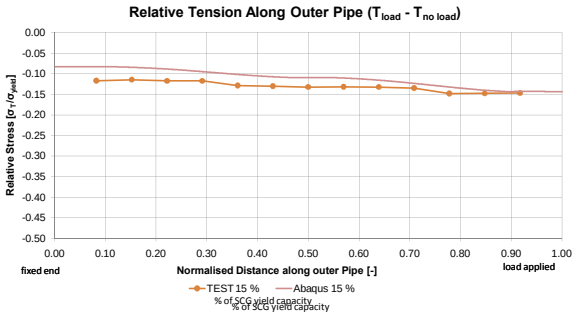

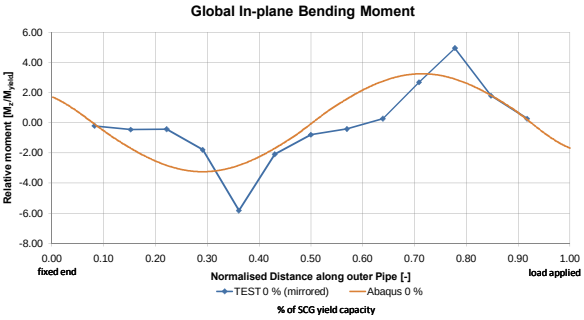

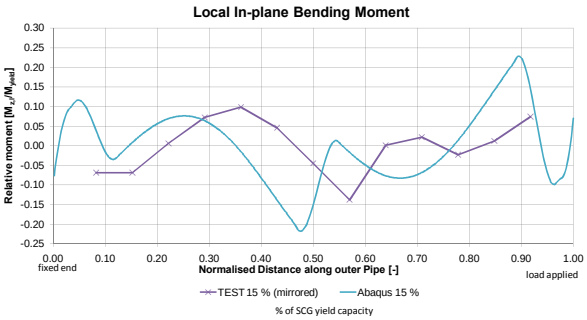

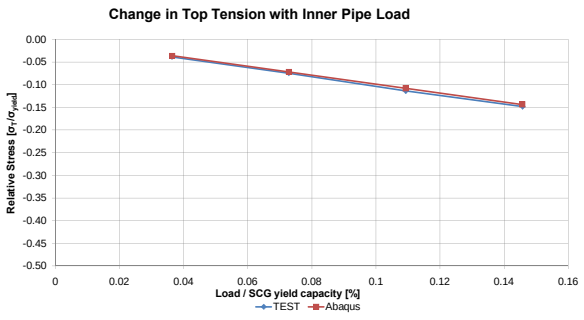

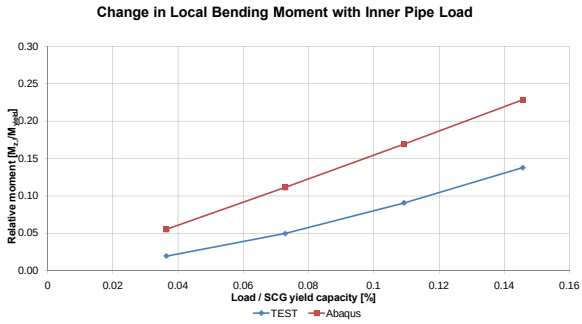

Phase 2

12.7 mm Outer Pipe, 2 mm Wire

60° Inclination Angle

Comparison between Physical- and Numerical Model

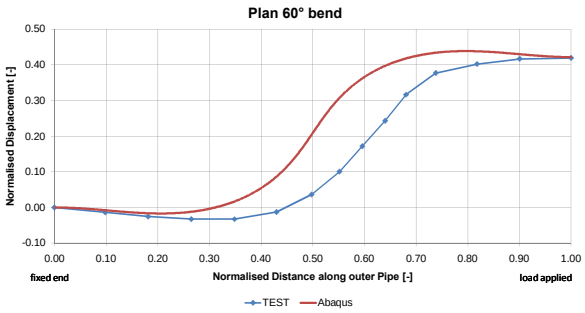

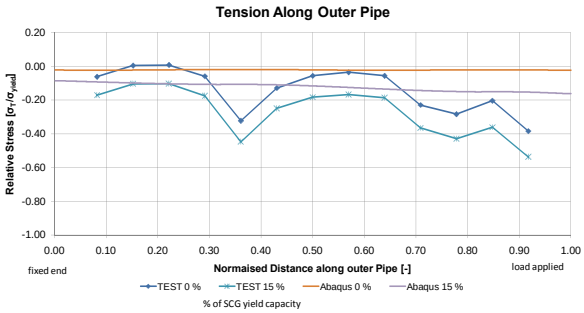

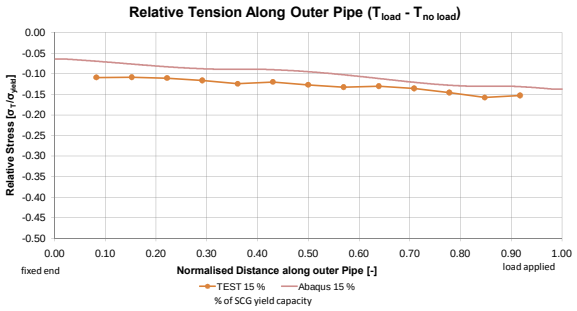

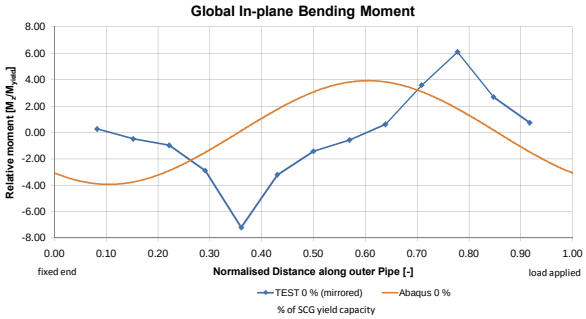

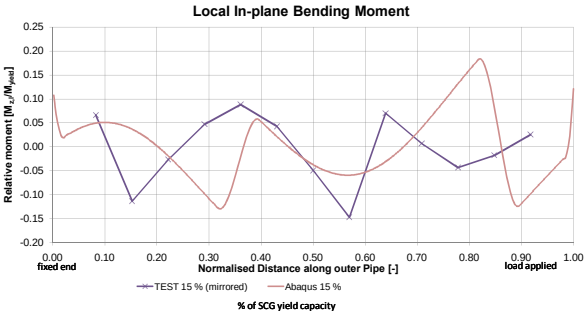

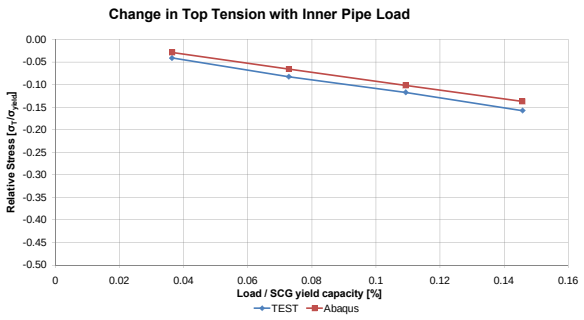

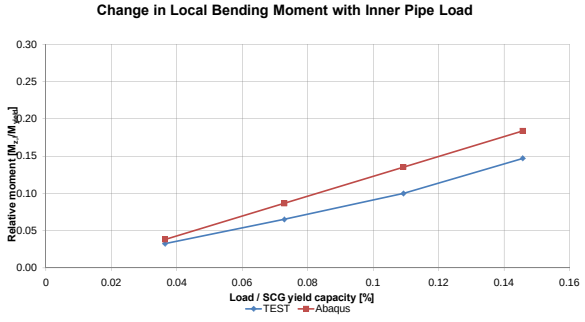

Phase 3

25.4 mm Outer Pipe, 6 mm Inner Pipe

30° Inclination Angle

Comparison between Physical- and Numerical Model

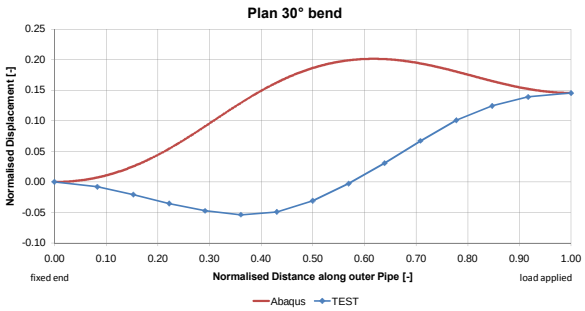

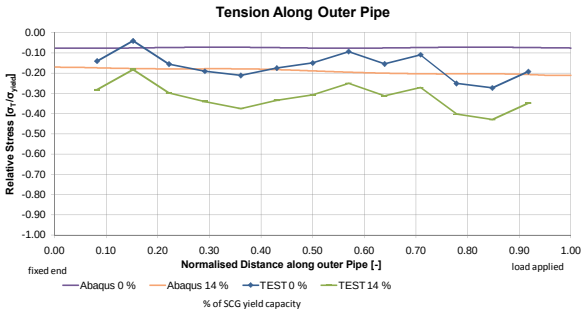

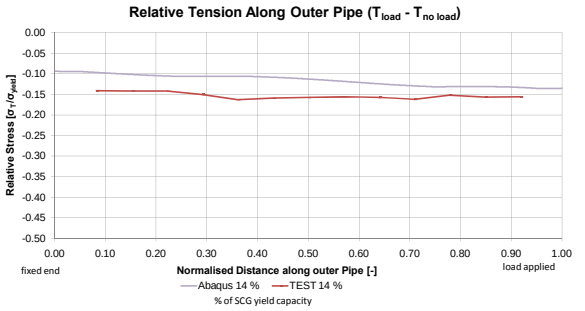

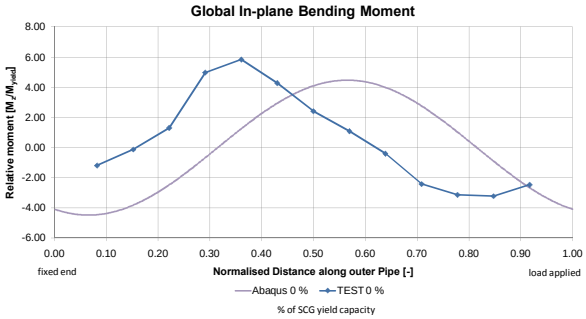

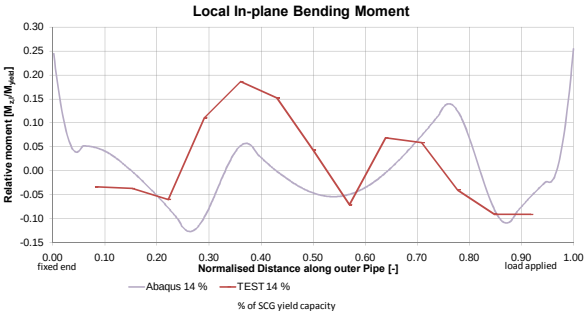

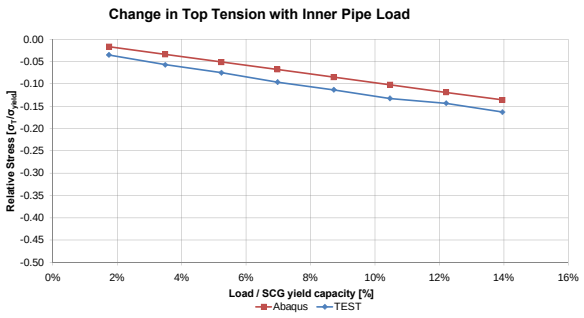

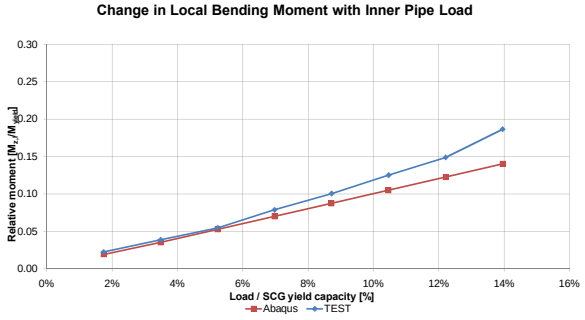

Phase 3

25.4 mm Outer Pipe, 6 mm Inner Pipe

45° Inclination Angle

Comparison between Physical- and Numerical Model

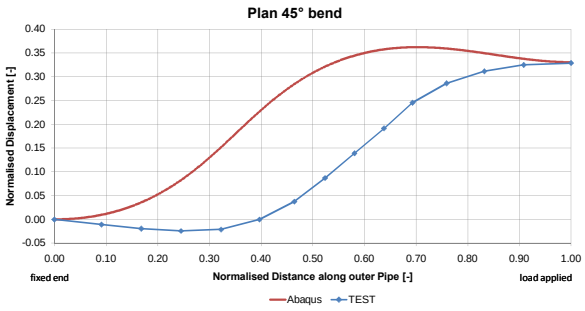

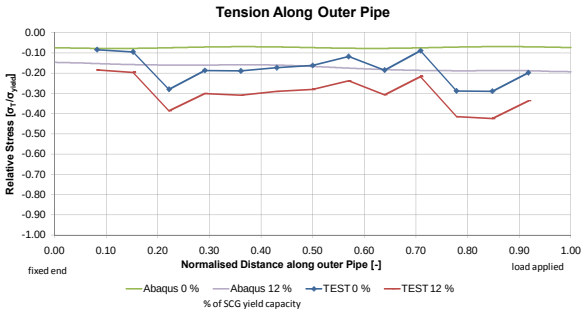

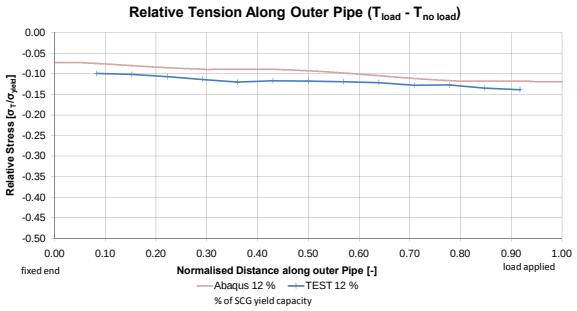

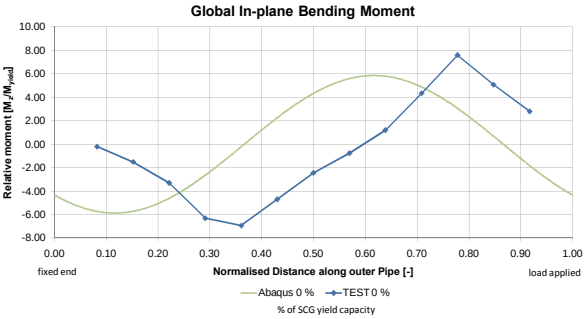

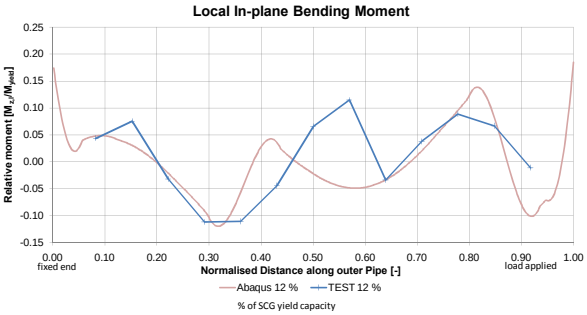

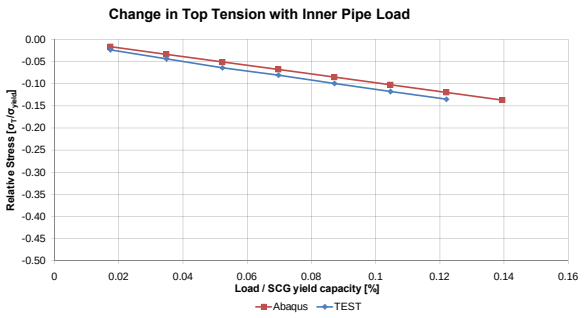

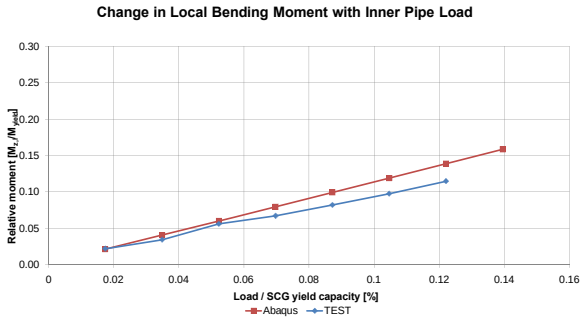

Phase 3

25.4 mm Outer Pipe, 6 mm Inner Pipe

60° Inclination Angle

Comparison between Physical- and Numerical Model

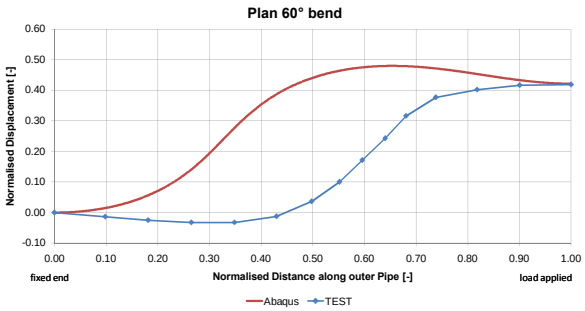

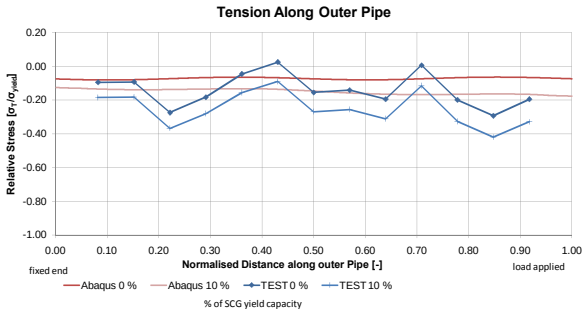

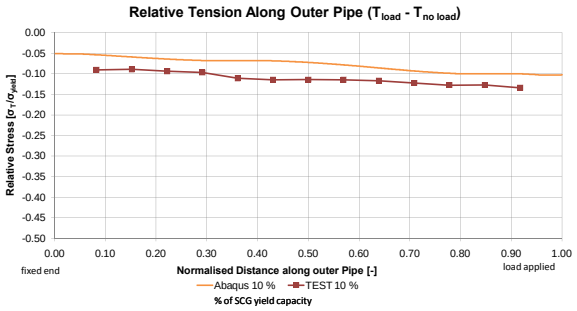

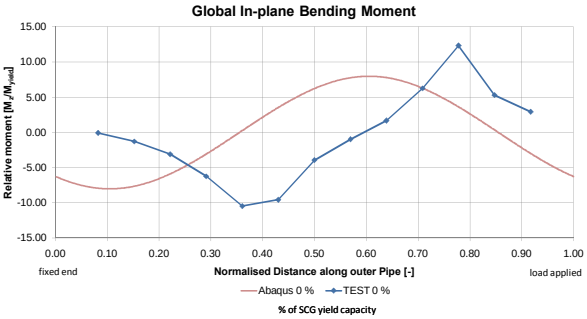

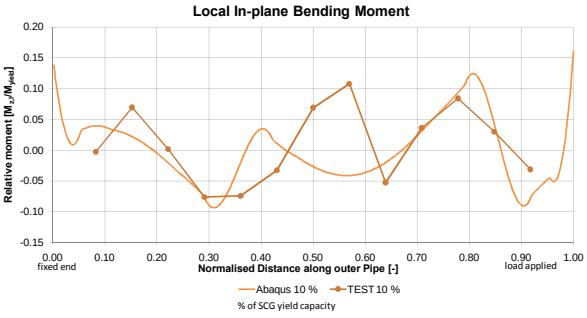

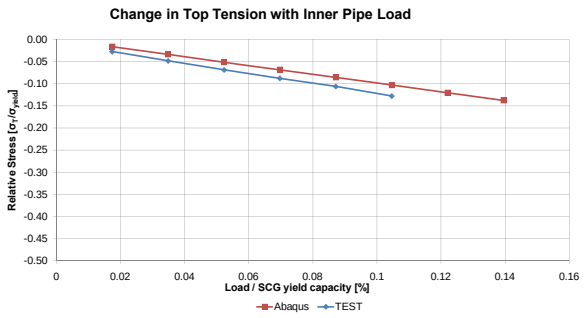

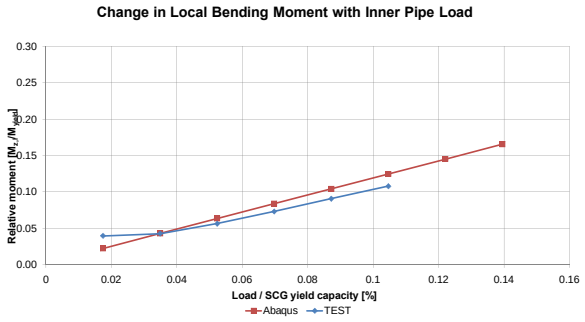

Phase 4

25.4 mm Outer Pipe, 2 mm Wire

30° Inclination Angle

Comparison between Physical- and Numerical Model

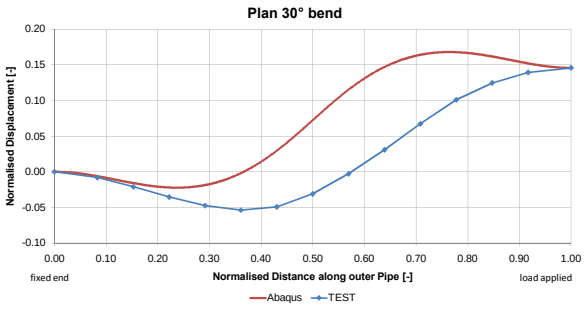

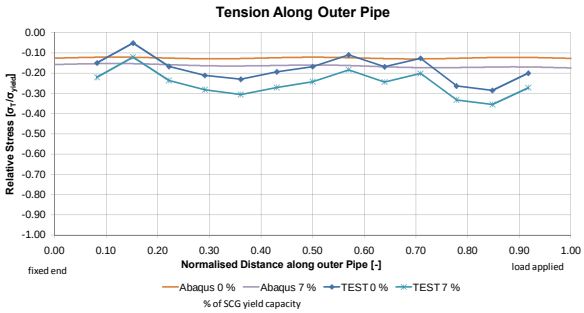

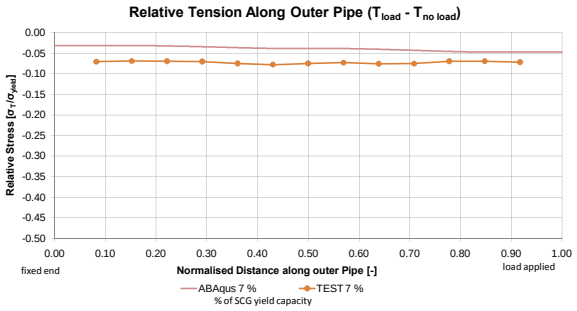

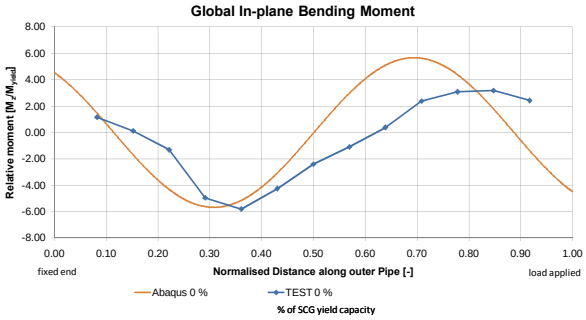

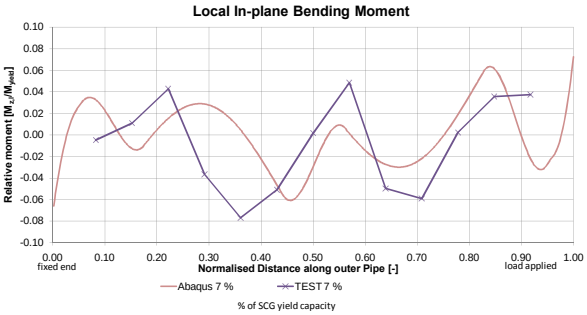

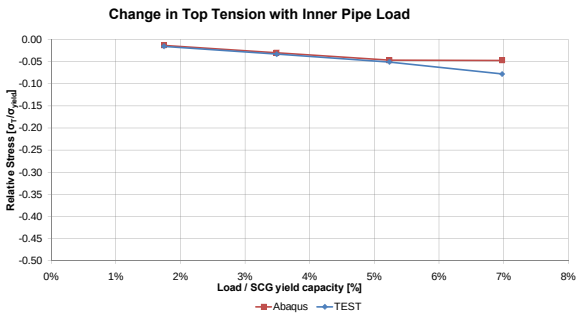

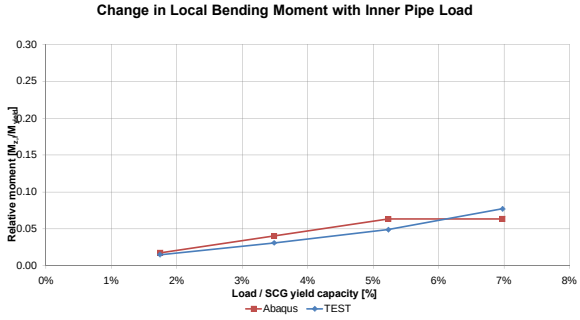

Phase 4

25.4 mm Outer Pipe, 2 mm Wire

45° Inclination Angle

Comparison between Physical- and Numerical Model

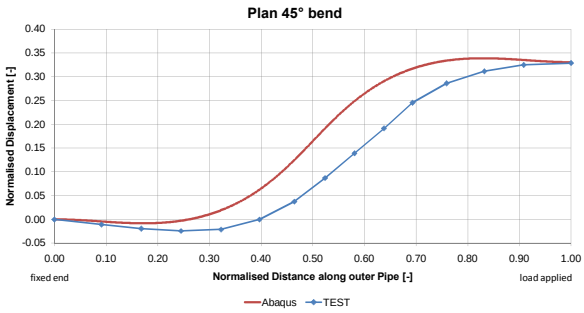

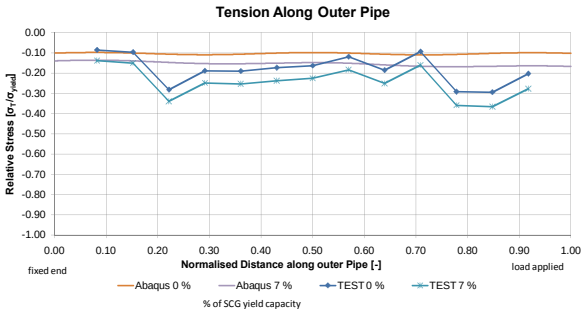

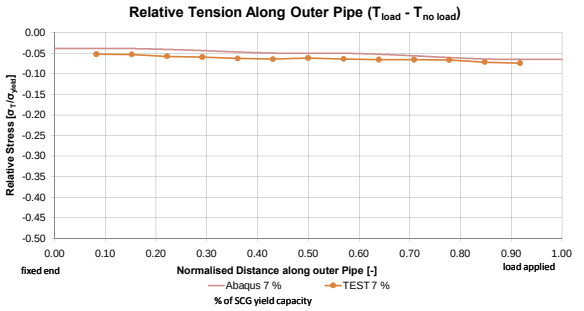

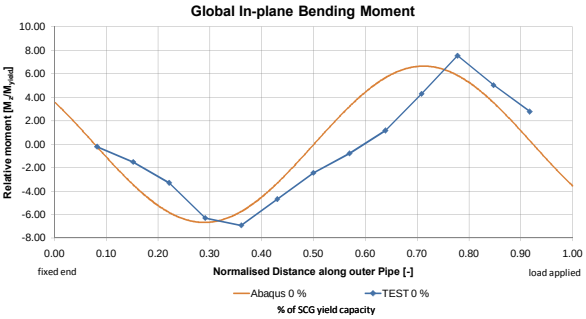

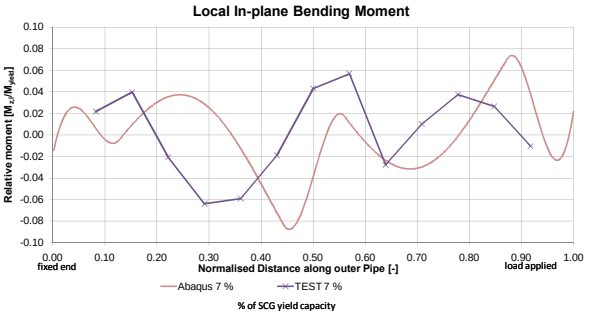

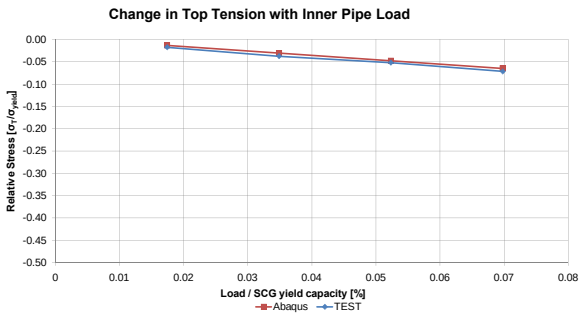

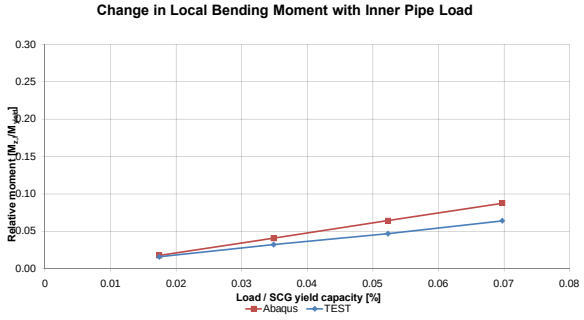

Phase 4

25.4 mm Outer Pipe, 2 mm Wire

60° Inclination Angle

Comparison between Physical- and Numerical Model

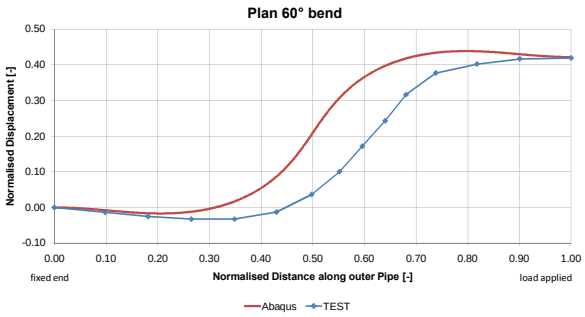

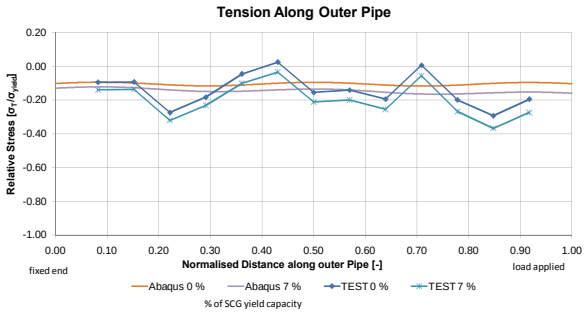

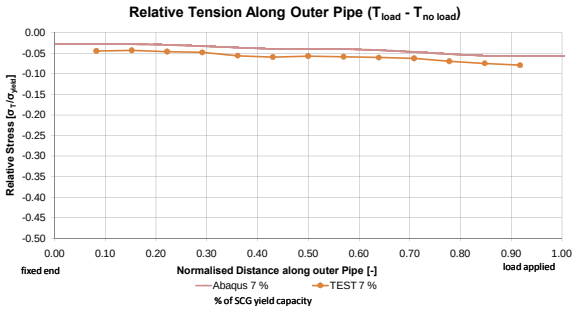

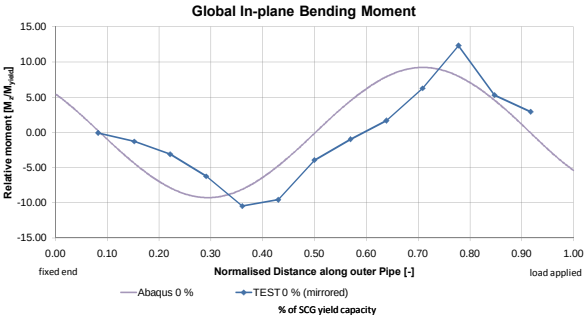

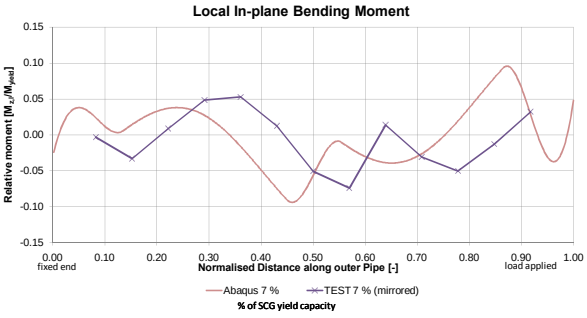

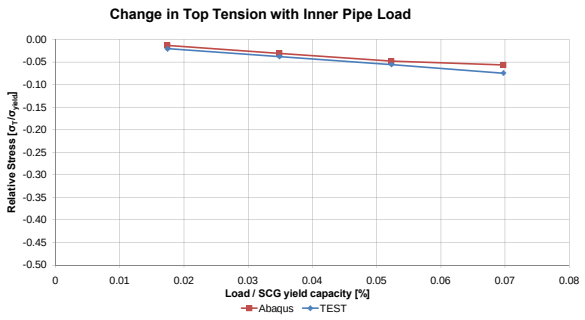

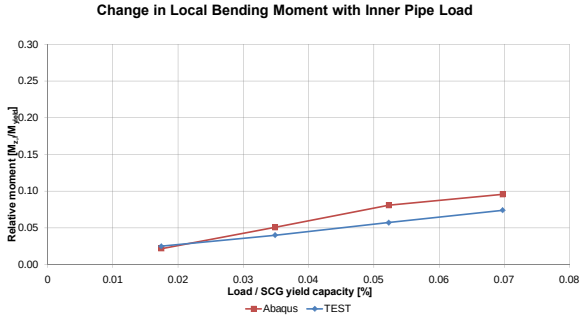

Comparison of different Pipe in Pipe Diameter Ratios

for Physical- and Numerical Model

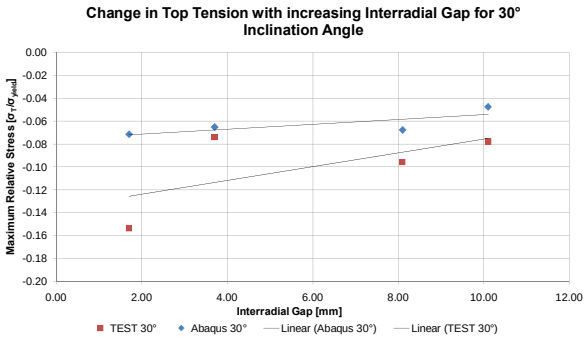

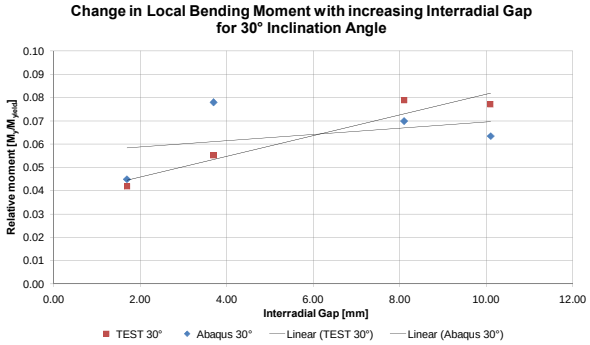

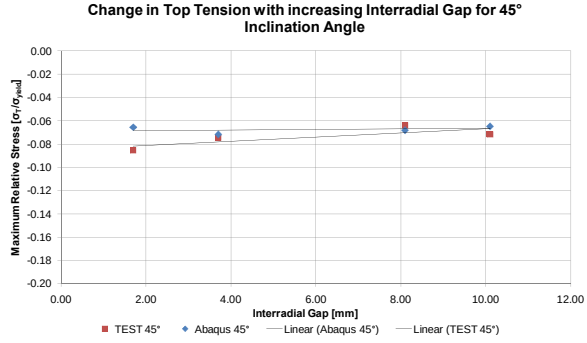

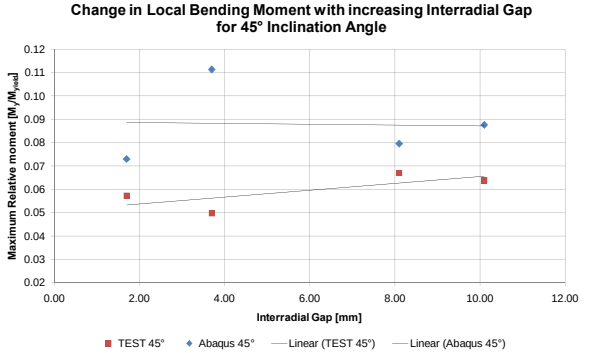

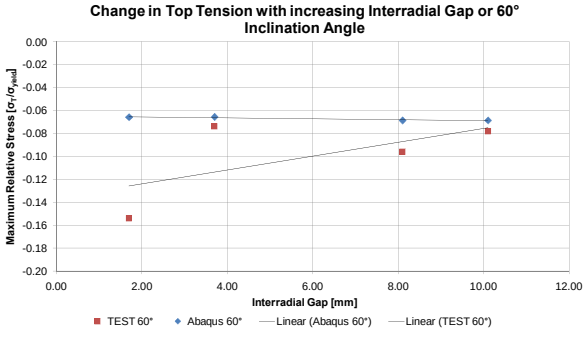

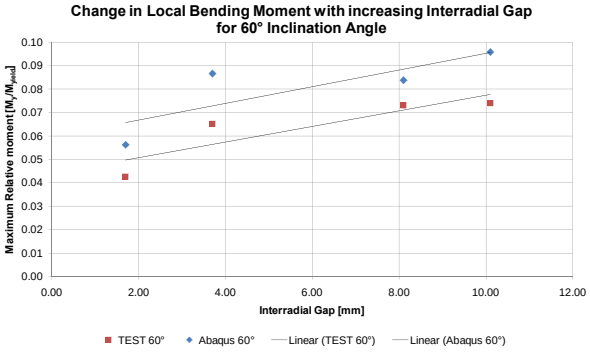

Appendix G: Physical Model Test: Equipment Drawings

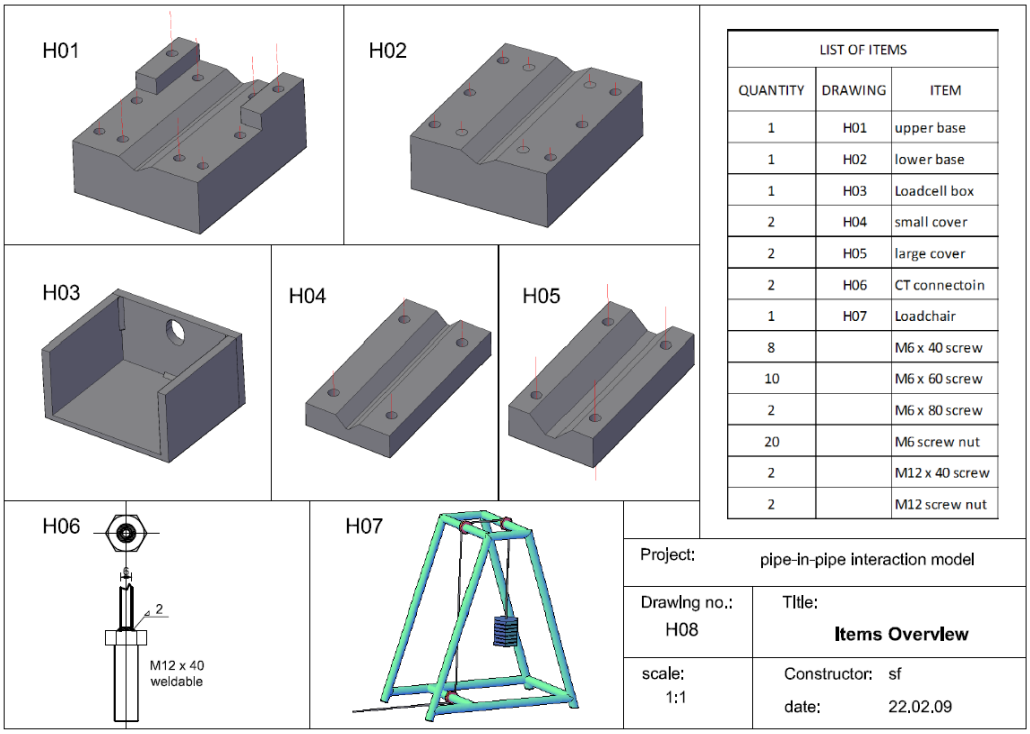

Figure G.1: Overview of items used to cuonduct the model tests

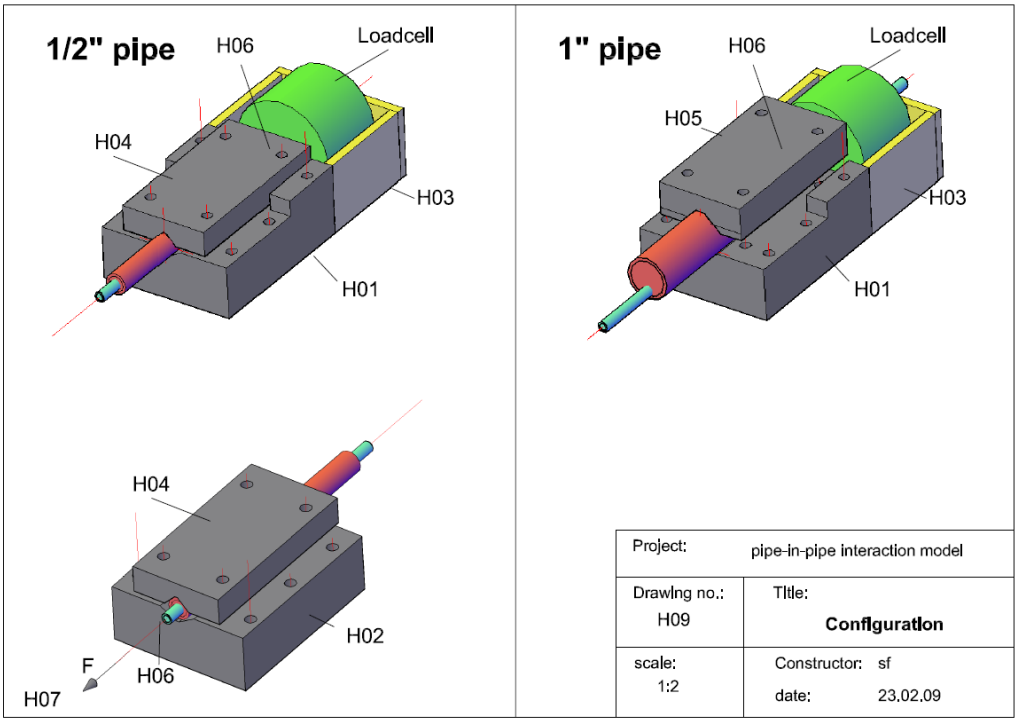

Figure G.2: Clamp configuration

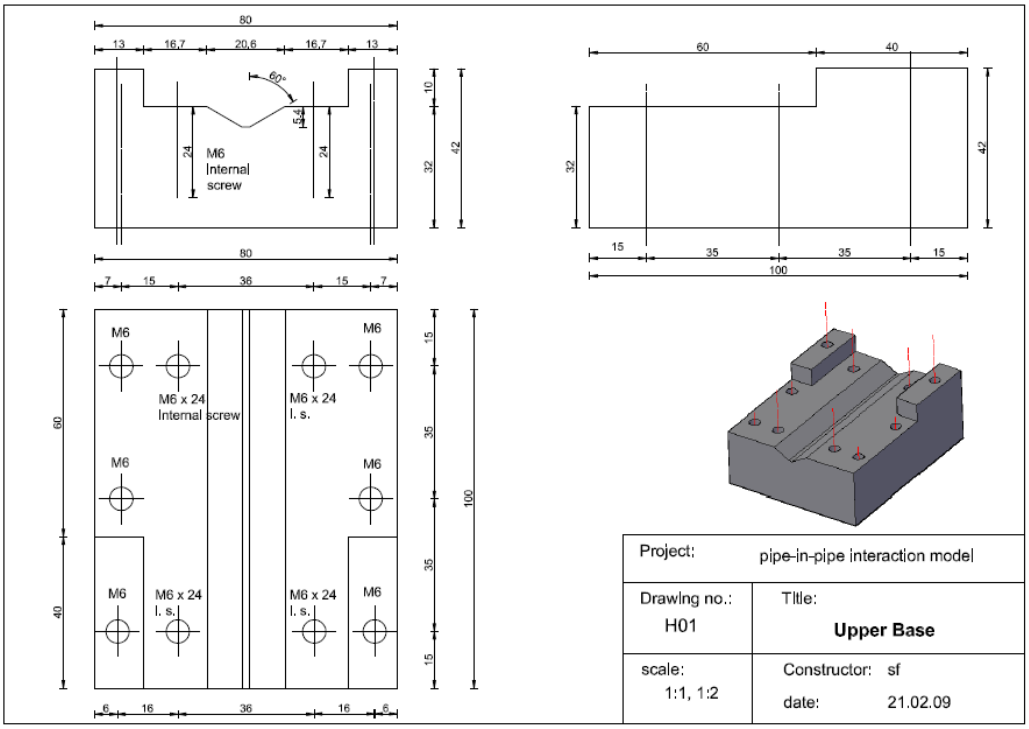

Figure G.3: Detail upper base

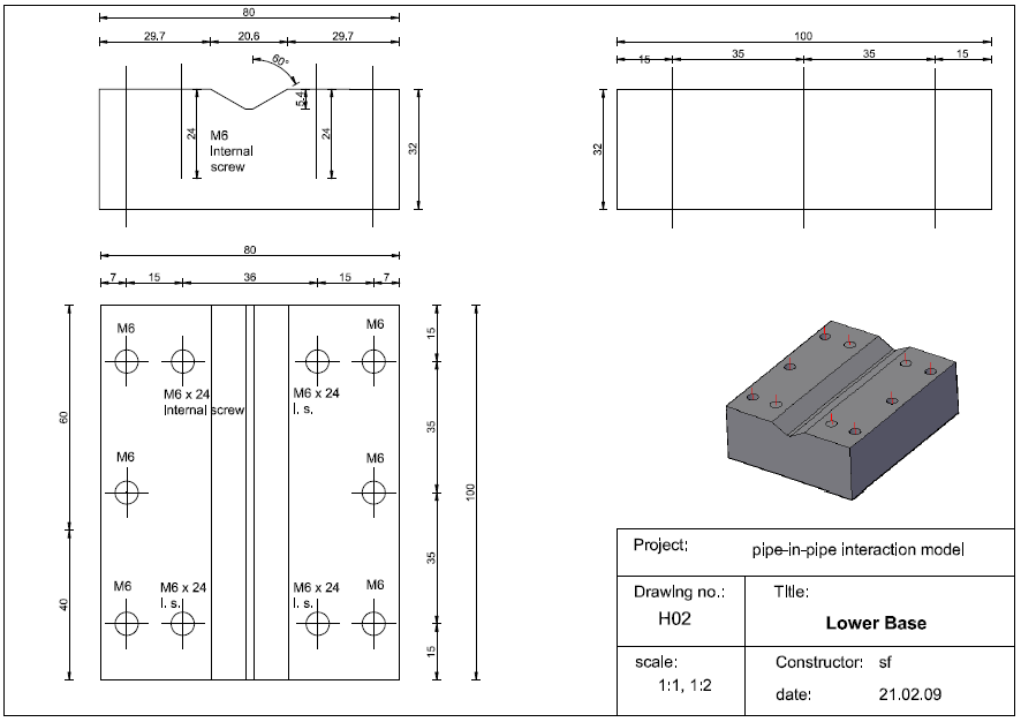

Figure G.4: Detail lower base

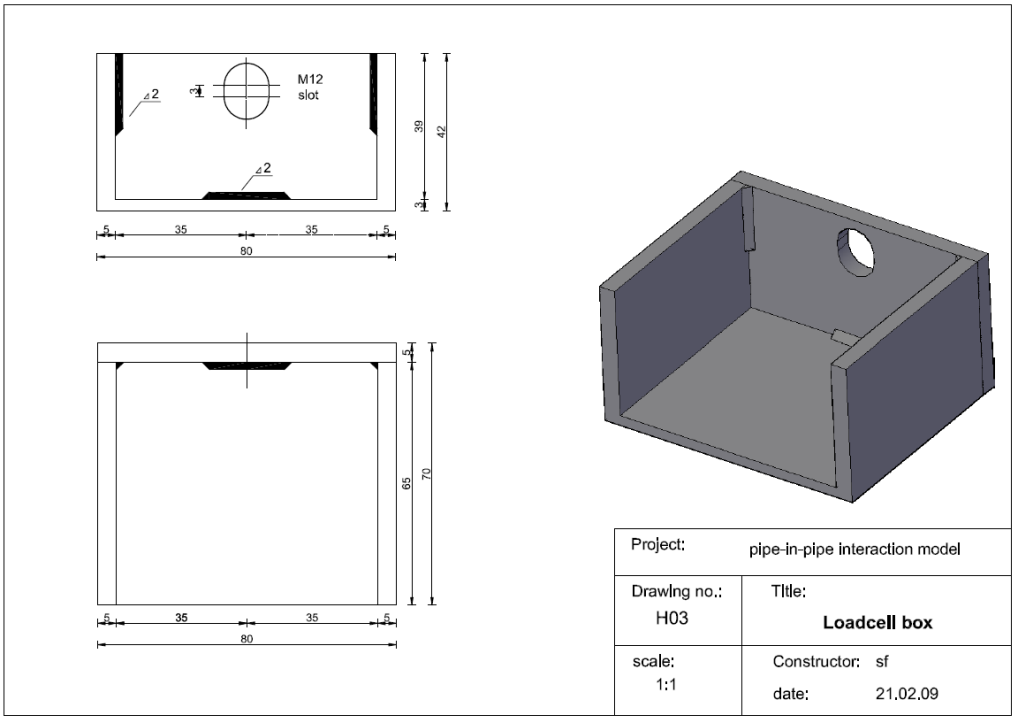

Figure G.5: Detail loadcell box

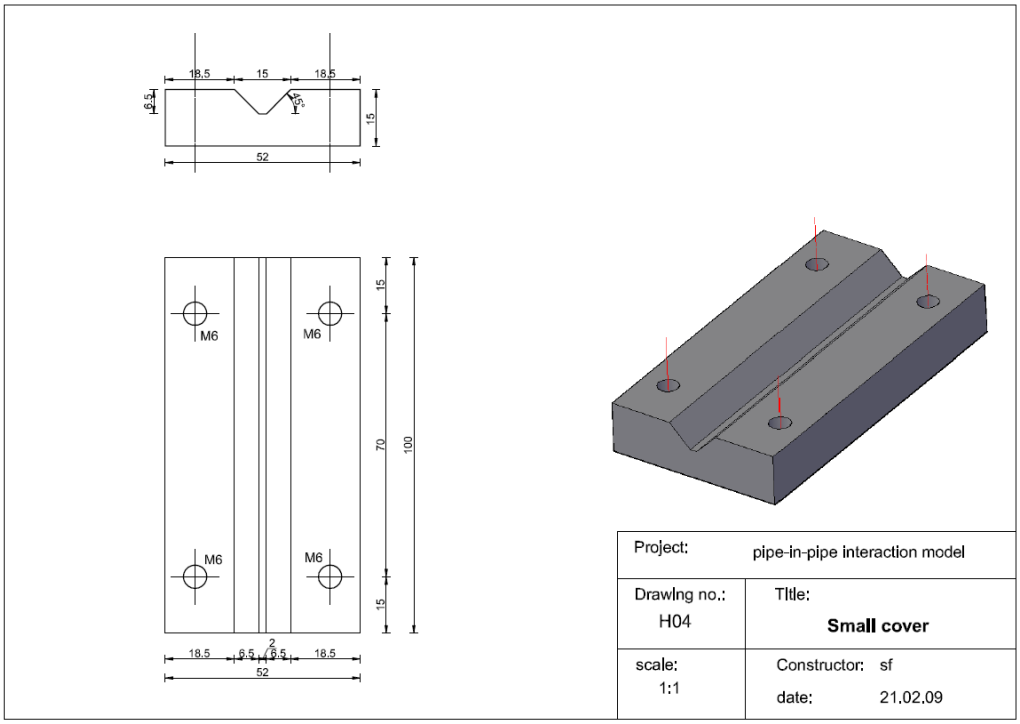

Figure G.6: Detail 1/2" cover

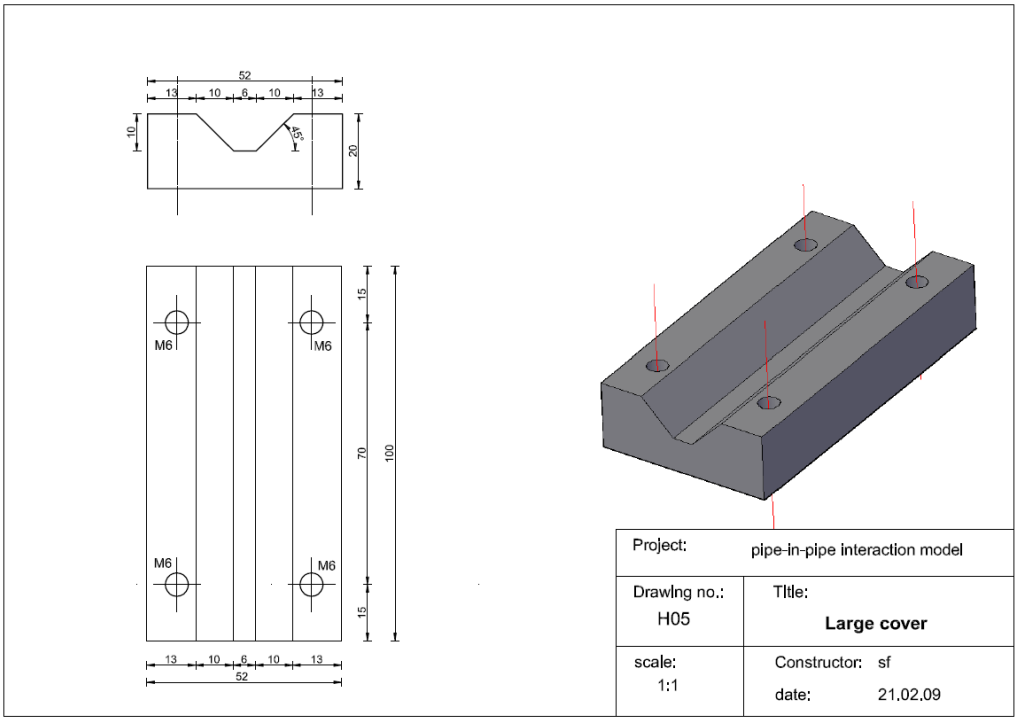

Figure G.7: Detail 1" cover

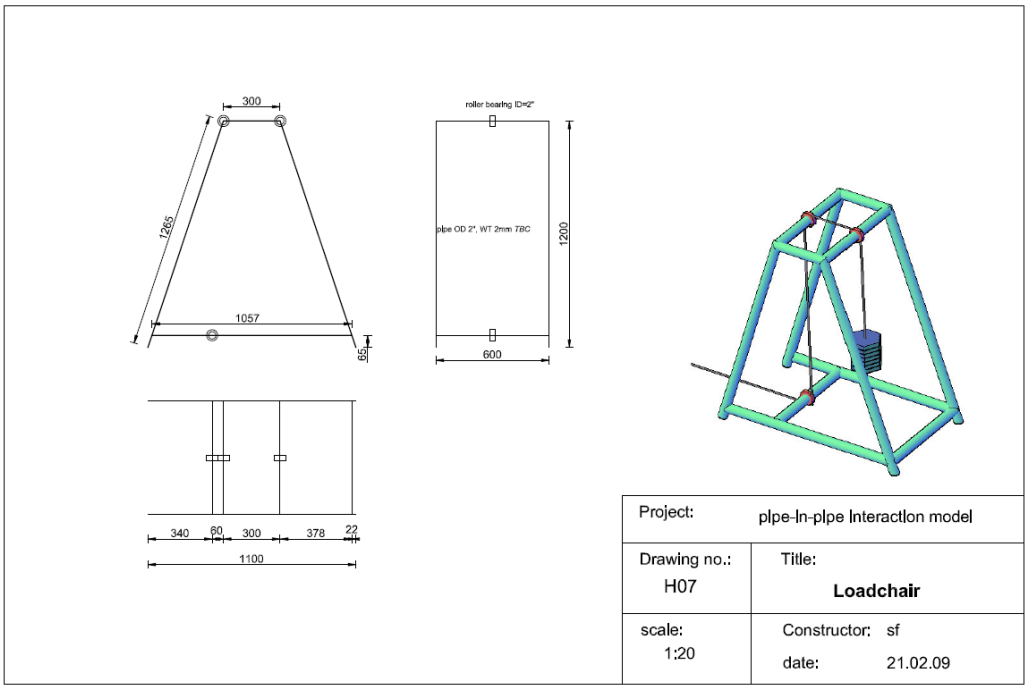

Figure G.8: detail loadchair

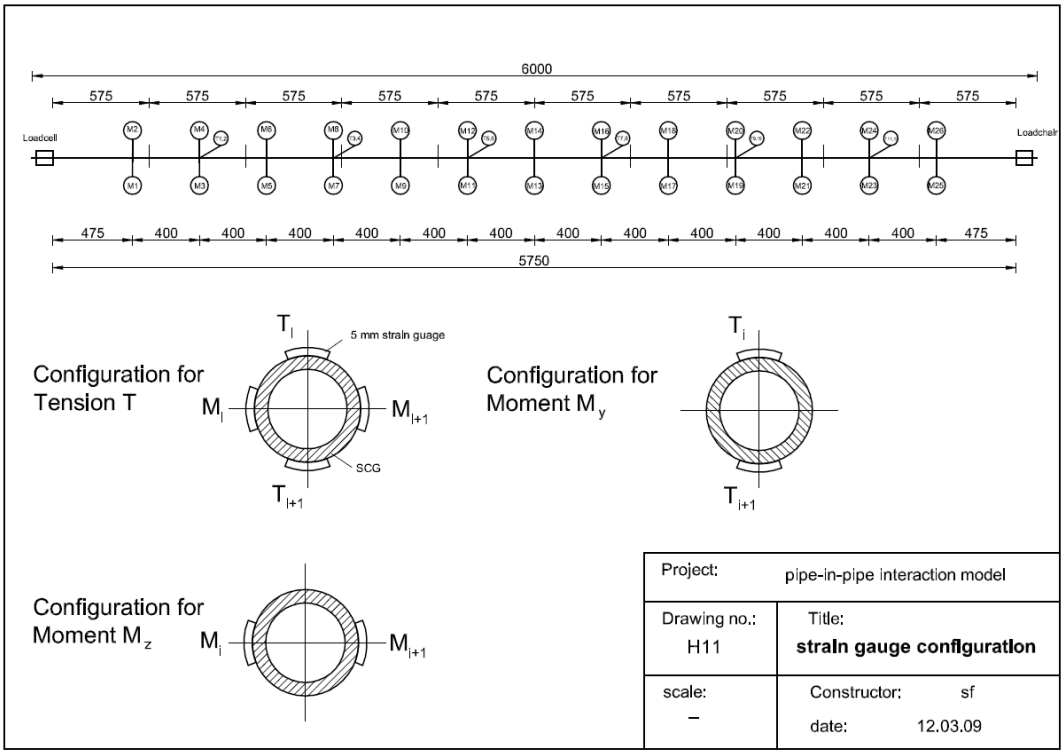

Figure G.9: Strain gauge configuration

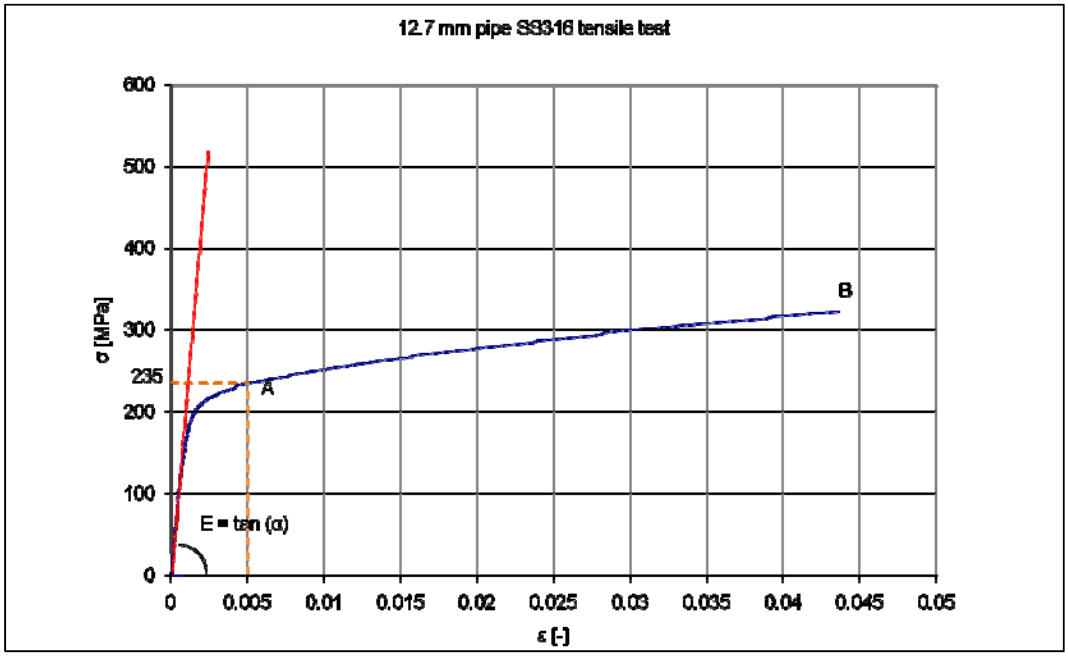

Figure G.10: Tensile test of OD 1/2" pipe used in Phase 1 and 2